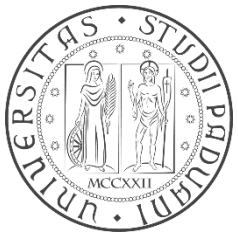

University of Padova

Department of Chemical Sciences

Doctoral Course in Molecular Sciences

PhD Thesis

M-N-C electrocatalysts supported on engineered carbon materials for the reduction of Oxygen

Director: Prof. Leonard Prins

Supervisor: Prof. Christian Durante

Student: Marco Mazzucato

35° Cycle

Index

Symbols

$\Delta\tilde{\nu}$	Raman Shift	cm^{-1}
I_n	n-th band intensity	u.a.
ν_i	i-th frequency	s^{-1}
λ	Wavelength	nm
A_n	n-th band area	cm^{-1}
p	System pressure	Pa
p^0	Saturation pressure	Pa
p/p^0	Relative pressure	-
$Q.ta\ ads.$	Adsorbed amount of gas	mmol g^{-1}
S_{BET}	Surface area from BET model	$m^2\ g^{-1}$
S_μ	Surface area of micropore	$m^2\ g^{-1}$
S_{meso}	Surface area of mesopore	$m^2\ g^{-1}$
V_μ	Volume of micropore	$cm^3\ g^{-1}$
V_{meso}	Volume of mesopore	$cm^3\ g^{-1}$
V_{tot}	Total pore volume	$cm^3\ g^{-1}$
E_p	Peak potential	V
E_{onset}	Onset potential	V
$E_{1/2}$	Half-wave potential	V
$i(E)$	Current	mA
i_p	Peak current	mA
j_L	Limiting current density	mA cm^{-2}
j_k	Kinetic current	A g^{-1}
n	Number of transferred electron	#
n_{kl}	Number of transferred electrons from K-L	#
$\%H_2O_2$	Percentage of Hydrogen peroxide produced	%
N	Collection efficiency (RRDE)	%
v	Scan rate	mV s^{-1}
ω	Rotation speed	rpm
D_{O2}	Diffusion coefficient of O_2	$cm^2\ s^{-1}$
C_{O2}	Concentration of O_2	mol cm^{-3}
v	Cinematic viscosity	$cm^2\ s^{-1}$
F	Faraday constant	C
i_d	Disk current	mA
i_r	Ring current	mA
η	Overpotential	V
Q_{strip}	Stripping Charge	C
Δ_{ik}	Kinetic current difference	A g^{-1}
E_b	Binding Energy	eV
E_k	Kinetic energy	eV o J
Φ	Work function	eV
d	Interplanar distance	Å
θ	Incidence angle	rad
Abs	Absorbance	-
T	Transmittance	-
$\varepsilon(\lambda)$	Molar extinction coefficient	$M^{-1}\ cm^{-1}$

Acronymous

AFC	Alkalyne Fuel Cell
BE	Binding Energy
BET	Brunauer–Emmet–Teller
BJH	Barrett-Joyner-Halenda
CA	Chronoamperometry
CE	Counter Electrode
CB	Carbon Black
CV	Cyclic Voltammetry
DFT	Density Functional Theory
DLC	Diamondlike Carbon
DMF	Dimethylformamide
DMFC	Direct Methanol Fuel Cell
EC-STM	Electrochemical STM
FC	Fuel Cell
FWHM	Full width at half maximum
GC	Glassy Carbon
GDL	Gas diffusion Layer
ICP-MS	Inductively Coupled Plasma Mass Spectrometry
IUPAC	International Union of Pure and Applied Chemistry
K-L	Kouteky-Levich
LSV	Linear Sweep Voltammetry
MCFC	Molten Carbonates Fuel Cell
MEA	Membrane Electrode Assembly
MC	Mesoporous Carbon
MOF	Metal–organic framework
MSD	Site density
NLDFT	Non-linear DFT
NP	Nanoparticles
ORR	Oxygen Reduction Reaction
PAFC	Phosphoric Acid Fuel Cell
PEEK	Polyether Ether Ketone
PEMFC	Proton Exchange Membrane Fuel Cell
PGM	Platinum Group Metal
Phen	1,10-Phenanthroline
RDE	Rotating Disk Electrode
RE	Reference Electrode
RHE	Reversible Hydrogen Electrode
RRDE	Rotating Ring-Disk Electrode
SCE	Saturated Calomel Electrode
SAFC	Solid acid fuel cell
SOFC	Solid Oxide Fuel Cell
STM	Scanning Tunnelling microscopy
T-K	Tuinstra-Koenig
TOF	Turnover frequency

UHV	Ultra High Vacuum
UV-Vis	Ultraviolet–visible
WE	Working Electrode
WE2	Second Working Electrode
XAS	X-ray Absorption Spectroscopy
XPS	X-ray Photoelectron Spectroscopy
XRD	X-ray Diffraction
ZIF	Zeolitic imidazolate framework

Abstract

Fuel cells represent a valid alternative to traditional energy sources that contain the use of fossil fuels, since H_2 and O_2 are respectively used as fuel and oxidant in a reaction that mainly produce H_2O. The reaction of oxygen reduction at the cathode, due to the tetra-electron mechanism, has a slow and sluggish kinetics and therefore requires large quantities of catalyst. For a commercialization of these devices the traditional catalysts based on platinum supported on mesoporous carbon must be replaced with cheaper materials. Carbonaceous supports with a discrete porous structure, doped with nitrogen and with transition metals such as Fe, have proven to be able to catalyse the reduction of O_2 with performances that can approach Pt-based materials. Although numerous studies have been conducted on the subject, there is still a strong debate on nature of active sites in these systems and, in particular, on which the experimental conditions of synthesis that allow to control their formation. One of the fixed points of these studies, which normally still combine spectroscopic techniques with electrochemical techniques, is that the primary centres of oxygen reduction to water are the FeN_4 sites, however the conditions that lead to the formation of these sites and the quantification require one in-depth study.

In this PhD project different M-N-C based materials have been studied to evaluate the influence of the porosity of the carbonaceous support on the formation of the Fe-N and C-N sites and consequently on the electrocatalytic activity. Also the effect of the precursors of Fe and N was studied showing that $Fe(phen)_3Cl_2$ is a good choice. Later Bimetallic systems were studied, by adding Sn in the mixture and finally the study of C-N group was achieved by grafting of organic molecule on the surface.

One big part of the project was to show that gas diffusion electrode setup are perfectly suitable for these materials and allow to complete the information obtained with typical rotating electrode analysis. All materials were studied by deeply combining physico-chemical and electrochemical characterization techniques.

1. Introduction

The well-being development has always contributed to the technological improvement of the level of life and to the human being, which is why we are interested in continuing to progress in this field. One of the objectives of research in the technological field, especially in recent times, is to progress in the field of energy production (or more correctly conversion) in order to reduce pollution levels and at the same time ensure an improvement in the quality of life. Smart research must also be focused on producing quality products that are durable and that can be recycled in order to reduce the consumption of materials and energy that production processes require. As mentioned, one of the reasons that pushes to develop new energy conversion systems is the increasing air pollution, in fact in 2018 the greenhouse gases (mainly carbon dioxide, methane and nitrous oxide) released into the atmosphere reached new records. The global average concentration of CO_2 on the surface for 2017 was 405.0 ppm and in 2019 it was higher than 410 ppm, the highest ever recorded in the era also considering the land surface of the concentration in ice dating back to 800 000 years ago. Figure 1.1) [1].

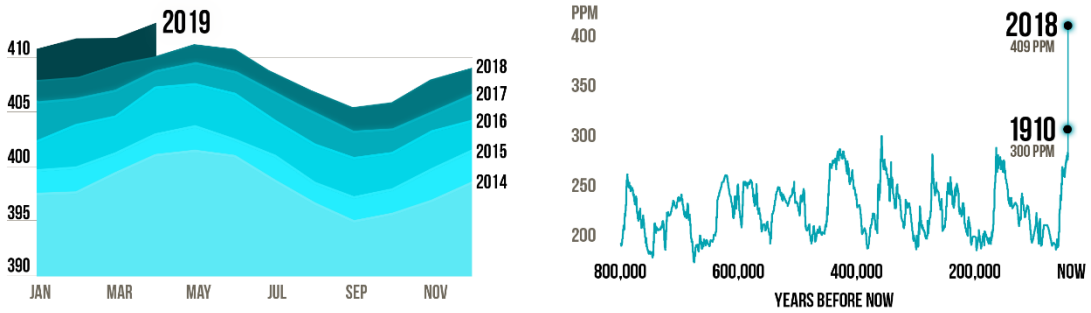

Figure 1.1. CO_2 concentration in ppm in the atmosphere: temporal evolution [2]

In December 2015, in an attempt to take global action to reduce harmful emissions, the Paris Agreement was signed, which is an agreement between the member states of the United Nations Convention on Climate Change (UNFCCC) regarding the reduction of greenhouse gas emissions starting from the year 2020. As of March 2019, 195 members of the UNFCCC signed the agreement and 186 decided to join it [3]. The long-term goal of the Agreement is to contain the rise in temperature by limiting it to 1.5 ° C. The growing attention to the health of the planet is also reflected in the data reported in the "Renewables 2018 Global Status Report" [4], where it is highlighted that investments in renewable energy are growing again after a decline in 2016, in particular with regard to the "production" of energy with solar radiation and in the wind sector. A good step forward has also been made in the transport sector which accounts for about a third of global energy consumption. In fact, in 2017, five countries announced their intention to ban the sales of new diesel and petrol cars, by 2030 in India, the Netherlands and Slovenia and by 2040 in France and the United Kingdom. In the transport sector there are basically two possibilities, the first is to use combustion engines that burn biofuels (biodiesel), the second is to use electricity stored in batteries or "produced" by fuel cells. However, it is good to remember that electric cars, even if with zero emissions, to be recharged use, to date, mainly energy derived from non-renewable sources, consequently a change is also necessary on this front. Another important issue is, for example, the recycling of lithium batteries used in electric or hybrid vehicles, development is also needed in this field [5]. Parallel to the pollution issue there is undoubtedly also that of technological progress, in the field of transport, for example, the replacement of combustion engines with electric motors or batteries, leads to a reduction in noise pollution in cities, cars are also more durable, or they require

less maintenance and are safer [6]. In addition to the field of transport, the development of devices for the production of energy would allow for example to decentralize the production of energy or to make isolated structures independent, an example is the San Giuliano refuge, which uses excess hydroelectric energy to produce hydrogen in a cogeneration plant, to be used later to produce energy when necessary, reducing or eliminating the use of diesel generators [7].
Starting from the 90s of the last centuries, the research and technological innovation of new generation batteries has inevitably led to interest in other similar devices such as fuel cells. The latter are cells capable of causing the combustion reaction (fuel + oxygen) to take place without the intermediate intervention of a thermal cycle, allowing higher conversion efficiencies than conventional devices:

- The efficiency of these devices is double that of a combustion engine, about 60% considering the losses due to process activation, ohmic drops and those due to mass transport.
- Such devices are also easily scalable since devices can be combined in series or in parallel to obtain the desired voltage or current.
- If powered by hydrogen and air they do not produce harmful emissions, as long as the hydrogen does not come from reforming

However, there are limitations related above all to costs, durability and the production and storage of hydrogen, in fact this is often produced by steam reforming (since it is the cheapest method) and its storage presents problems in terms of capacity and safety.
Despite some limitations, prototypes and commercial vehicles have been created with the use of hydrogen-powered fuel cells. Some examples, shown in figure 1.2 are the Hyundai Nexo and the Coradia iLint produced by Alstom which is the first hydrogen-powered passenger train, operating in Germany between Cuxhaven and Buxtehude, a line on which a total of 16 iLint trains will be operational from 2021 against an expense of 81 million euros [8].

Figure 1.2. Hyundai Nexo on the left and the Coradia iLint on the right, two vehicles powered by fuel cells

The increase in vehicles based on such devices is promising but is still hampered by the high costs of production, maintenance, and not always high efficiencies, in addition to the improvements required to obtain good chemical and mechanical stability. These problems can be overcome by developing innovative materials and optimizing those in use. In fuel cells, a fundamental component is that linked to the carbonaceous materials used to the electrodes as supports for catalysts (generally metal phases such as Platinum), in particular the cathode branch is the most problematic since the catalysis of the oxygen reduction reaction requires large quantities of catalyst, and that is why research is concentrated in the synthesis of catalysts based on Pt and/or other metals to seek the best compromise between cost and performance of the cell. This thesis will evaluate different

aspects effects on the formation of active sites on Fe-N-C-based materials for the catalysis of oxygen reduction by evaluating chemical-physical and electrochemical aspects.

1.1. Fuel cells

Fuel cells (FC) are chemically rechargeable primary energy sources (or batteries) that allow you to convert chemical energy into electricity (and heat). They are able to supply energy as long as a fuel and an oxidant are introduced into the anode and cathode compartments, respectively. The most used fuel is hydrogen, sometimes mixed with carbon monoxide, while the oxidant is oxygen or air.
There are numerous types of fuel cells which differ in terms of: fuel used, temperature of use, electrode, and electrolytic materials, but all share three fundamental elements:

- Anode: element on which the oxidation of the fuel occurs.
- Electrolyte: solid or liquid allows the migration of ionic species from the anode to the cathode or vice versa, it is therefore an ionic conductor, but an electrical insulator.
- Cathode: element on which the oxidizer is reduced.

Based on the temperature of use and consequently also in the materials that compose them, the cells are divided into:

- Polymer electrolyte cells (PEMFC)
- Alkaline fuel cells (AFC)
- Molten carbonate cells (MCFC)
- Direct methanol cells (DMFC)
- Solid oxide cells (SOFC)
- Phosphoric acid cells (PAFC)

The development of different types of cells derives from the various possible applications, among which we remember the production of stationary and decentralized energy, consumer electronics, the replacement of fossil fuel power plants and the automotive sector, in particular for the latter category. PEMFC cells are by far the most promising for their low operating temperature (<100 ° C), for their low or zero CO2 emissions, for their versatility and scalability, as well as for their high power density.

1.1.1. PEMFC

The proton exchange membrane cells are characterized by a perfluoro-sulphonic polymeric membrane (Nafion) which allows the transfer of protons from the anode to the cathode (Figure 1.3 and 1.4), these protons are generated at the anode according to reaction 1.1, they migrate through the membrane to the cathode where they participate in the oxygen reduction reaction (1.2) forming water:

$$H_2 \rightarrow 2H^+ + 2e^- \quad E^0_{H^+/H_2} = 0\,V \tag{1.1}$$

$$\frac{1}{2}O_2 + 2H^+ + 2e^- \rightarrow H_2O \quad E^0_{O_2/H_2O} = 1.23\,V \tag{1.2}$$

The global reaction is consequently that of the formation of water from hydrogen and oxygen (1.3):

$$H_2 + {}^1/_2\, O_2 \rightarrow H_2O \qquad (1.3)$$

This type of cells work at low temperatures, between 60 and 120 °C, very low temperatures if compared to those necessary for the operation of SOFCs (600-1000 °C) or MCFCs (≈ 650 °C). Their power density per unit area is around 0.5 W cm^{-2}, among the best compared to other types of cells. As mentioned, being powered by pure H_2 and air, they produce little or no CO_2 emissions. The electrolyte used is not dangerous and being a solid allows the devices to be mounted in any orientation, plus a solid electrolyte is better manageable than liquid electrolytes as happens in PAFC (H_3PO_4 at 85%) and AFC (KOH at 35 -50%). Finally, they are very scalable (in size) and can be put in series or in parallel as needed.

As shown in Figure 1.3 there are various components in the cell, the main ones are:

- Gas diffusion layer
- Catalyst layer
- Membrane
- Bipolar plate
- Electrical connection

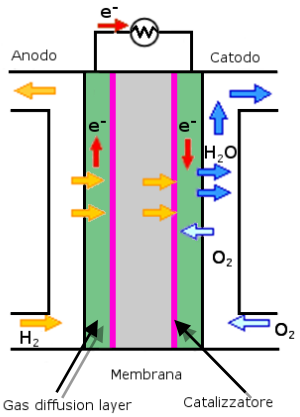

Figure 1.3. Scheme for a generic PEMFC in which the components are highlighted

The gas diffusion layer (GDL) is a porous and conductive layer that allows the gas to be conveyed (to both electrode compartments) towards the catalytic layer that promotes oxidation and reduction reactions, in particular to the cathode compartment it is important to have the so-called " three-phase zone ", i.e., the gas diffusion layer, the catalyst and the electrolyte must be in contact for the reaction between protons, oxygen and electrons to take place.
The membrane, as mentioned, is composed of a polymer, Nafion, which is made of Teflon modified with sulphonic groups linked to the side chains, these, in the presence of water, are able to favour proton transport, in fact the presence of water allows the dissociation of sulphonic acid and in the presence of an electric field the protons are able to move between the various zones with the conduction mechanism of Grotthus. The Nafion is also advantageous for poor electrical conduction and a low gas crossover phenomenon, phenomena that cause the devices efficiency to drop.

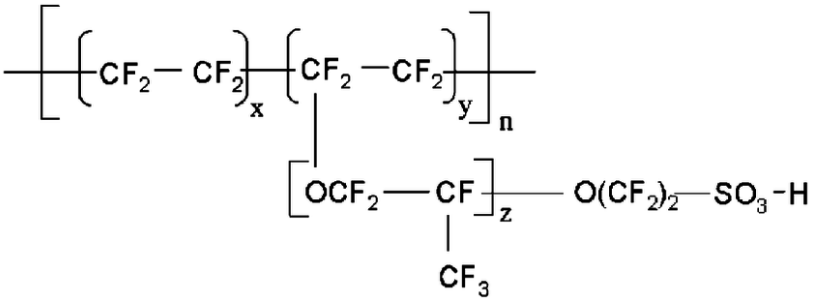

Figure 1.4. Chemical structure of Nafion, the most common material in membranes

Another fundamental component are the bipolar plates, generally made of graphite or metal alloys, they allow to evenly distribute the fuels on the GDL, they also guarantee a good electrical contact and allow the dissipation of the heat produced, they are also fundamental for the construction of cells in series or in parallel to obtain the desired voltages or currents. The last component is the catalytic layer which allows to lower the activation energy of the anodic and cathodic reactions, and in the ideal cell it is for both electrodes Pt supported on meso/microporous carbon; the distribution of the porosity allows to guarantee: the diffusion of the gases, the electrical conductivity, and the dispersion of the catalyst. Of the two reactions, the most problematic is the oxygen reduction reaction since it involves a four-electron mechanism that requires a large amount of catalyst, which affects the final price of the stack by up to 50% [9]. Generally, the GDLs, the catalytic materials and the membrane are assembled to form the Membrane electrode assembly (MEA) with two methods: the first involves depositing the catalyst on the two GDLs and then assembling them with the membrane; the second involves depositing the catalyst on the membrane and then adding the GDL.

1.2. Oxygen Reduction Reaction [10]

The Oxygen Reduction Reaction is one of the most studied reactions in the field of electrocatalysis in the last decades because of the importance in energy conversion technologies such as fuel cells and metal-air batteries. In aqueous solution ORR could follow different mechanisms, depending on pH and electronicity, but in general the reduction to water involves a multi electron/proton transfer, making this a very sluggish reaction if compared to hydrogen evolution reaction. The overall reaction of reduction of oxygen to water can be expressed as (in acidic electrolytes):

$$O_2 + 4\,H^+ + 4\,e^- \rightarrow 2\,H_2O \qquad E° = 1.23\ V \tag{1.4}$$

at the same time, a 2 step mechanism could lead to water by production of peroxide as intermediate according to the following reaction:

$$O_2 + 2H^+ + 2\,e^- \rightarrow H_2O_2 \qquad E° = 0.68\ V \tag{1.5}$$

$$H_2O_2 + 2\,H^+ + 2\,e^- \rightarrow 2\,H_2O \qquad E° = 1.776\ V \tag{1.6}$$

where the latter reaction could also be the chemical decomposition of peroxide:

$$2H_2O_2 \rightarrow O_2 + 2H_2O \tag{1.7}$$

If we pass to alkaline media the reaction is clearly different involving OH^- species as follow:

$$O_2 + 2H_2O + 4\,e^- \rightarrow 4OH^- \qquad E° = 0.401\ V \tag{1.8}$$

Or by indirect route:

$$O_2 + H_2O + 2\,e^- \rightarrow HO_2^- + OH^- \qquad E° = 0.08\ V \tag{1.9}$$

$$HO_2^- + H_2O + 2e^- \rightarrow 3OH^- \qquad E° = 0.880\ V \tag{1.10}$$

The actual mechanism has been a matter of debate for lots of year, which is not surprising for such a complex reaction featuring an interplay of electrochemical and purely chemical steps. A scheme that summarize the possible step have been proposed in 1976 by Wroblowa et al. [11,12] and is reported in Figure 1.5:

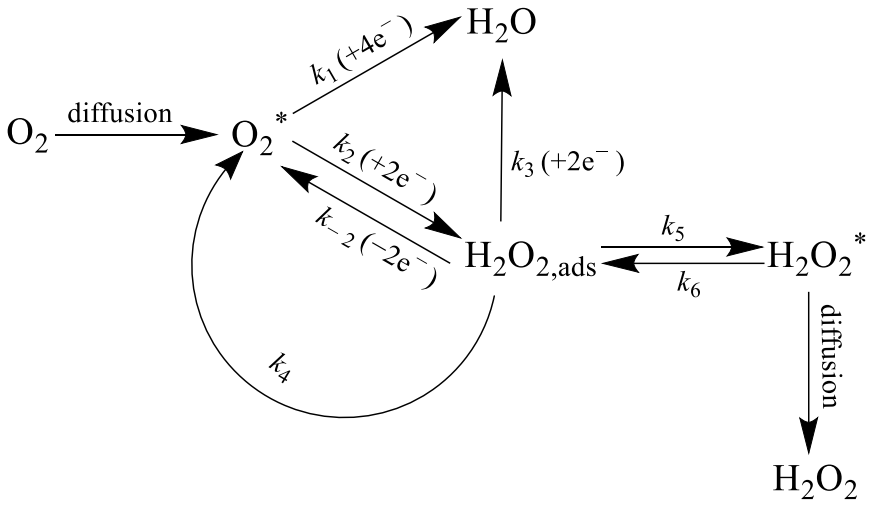

Figure 1.5. Scheme of possible chemical and electrochemical reaction that could occur during oxygen reduction. * means near the surface.

Even if not totally accurate, for example the adsorbed H_2O_2 seems to be unrealistic from experimental data, this scheme summarizes the possible paths. First of all, there is the adsorption of oxygen (depending on the adsorption sites, both side-on and end-on configuration are possible) then one possible route is the direct four-electron reaction from O_2 to H_2O (k_1), secondly the redox equilibrium between O_2 and intermediate H_2O_2 ($k_{\pm 2}$) and thirdly the electrochemical reduction of H_2O_2 to H_2O (k_3). Eventually, desorption (k_5) and adsorption of H_2O_2 (k_6) from/onto the electrode is also to be considered. The chemical H_2O_2 decomposition to H_2O and O_2 (k_4) could also occur in parallel with the electrochemical reduction of H_2O_2 to H_2O.

A lot of research has been directed towards the understanding of the ORR mechanism on various electrode materials. Already in 1959, Frumkin et al. [13] proposed to use a rotating ring disk electrode (RRDE, see 10.1.2) for detecting stable intermediates formed at the working electrode in the course of complex electrochemical reactions. For ORR detection of H_2O_2 at the ring, electrode gives evidence that the ORR tends to follow an indirect route. The technique was very solid and still nowadays is one of the standard procedures to characterize ORR catalysts; also, various ring electrode materials have been proposed, for example for CO_2 reduction where CO is detected on Au ring even if quantitative analysis is still challenging [14,15].

The ORR is therefore almost always studied under conditions of controlled hydrodynamics, ideally by performing a Koutecky-Levich (K-L) analysis and RRDE experiments, with the latter which is more reliable for different reason (i.e., the derivation of the K-L implies a first-order reaction and a

constant *n* value) that's why coupling the two analysis is always a good approach to study ORR catalysts. The combination of H_2O_2 detection at the ring electrode and Tafel slope analysis have highlighted that, in acidic media, ORR at a polycrystalline Pt electrode is a four-electron process with traces (1%) of H_2O_2 being formed at low overpotentials; this result does not exclude very fast 2+2 electron pathway, and that is why there are still lots of studies that try to elucidate better the mechanism on different material, on different nanostructure or even on different crystalline plane. Material such as mercury, graphite, gold, the majority of metal oxides and oxide-covered metals tend indeed to proceeds through the 2 electrons mechanism.
On the regard of fuel cells, the ORR is the cathodic reaction, and its catalysis is fundamental due to the slow kinetic, so the introduction of electrocatalyst is used to accelerate the kinetic and induce four-electron reduction of O_2 to water by utilizing the protons that permeate through a membrane from the anode. On the other hand, H_2O_2 is also obtaining attention as energy carrier alternative to H_2 in fuel cell [16,17]. The production of H_2O_2 is of historical importance due to its large role in environmentally friendly methods in the chemical industry. H_2O_2 is a widespread disinfectant and bleach product used in cosmetics, in house holding, in manufacture industry and in water treatment [18]. A common environmental application of H_2O_2 is in the Fenton's reagent, an aqueous mixture of H_2O_2 and Fe^{2+}, that under acidic conditions, generates the highly oxidant hydroxyl radicals [19–21]. For these reasons alternatives to the anthraquinone process are of interest and that means that both 4 electron and 2 electron ORR are of interest in the field of electrocatalysis [22,23]. For the record, also the chemical production from hydrogen and oxygen has been proposed on palladium-based catalysts [24].
Pt is the electrocatalyst that is currently used for ORR reactions, as it is practically the only commercially available catalyst with sensible activity and stability for PEMFCs, although it offers limited commercialization of fuel cells due to its limited availability and high cost. Enormous efforts have been made to reduce the cost of cathodic compartment, which impact a lot on final fuel cells cost by (i) using the low-Pt approach that consists of using other metal to enhance activity and therefore reduce the amount of Pt (i.e, PtY_x alloy) [25–30]; (ii) work on engineered nanoparticle shapes or (iii) working with support properties such as carbon nanotube or carbon fibres, which impact on electronic properties and therefore on activity. Other approaches try to develop more cheap material that could replace Pt, even if in larger amount, but with a lower total cost. A brief list of ORR catalysts is proposed below, while a pictorial view of carbon based catalyst is given in Figure 1.6.

- Pt or Pt alloys, commonly supported on carbon.
- Pt-group material as Pd also in this case pure or in alloy form supported on carbonaceous substrate [27,31–33].
- Metal-free pyrolyzed carbon or Metal-Nitrogen-Carbon pyrolyzed materials, the presence of nitrogen and metal-nitrogen functionalities are at the base of ORR activity. They are cheaper than Pt-base catalysts, and with comparable activities in alkaline environment. Some of these are also commercially available and used as benchmark in research [34,35].
- Metal Chalcogenides [36].
- Metal Nitride, Metal Carbide, Metal oxides and combination of that such as oxynitrides, and carbonitrides [37].

As said parallel to fuel cell, the H_2O_2 production is another crucial aspect in green chemistry industry. Novel and cleaner methods for the production of H_2O_2 are being explored and the

development of electrolyzes for the *in situ* generation of H_2O_2 represents one viable way [38]. Many catalysts have been proposed for the direct generation of the H_2O_2, unfortunately, catalysts for the direct synthesis of H_2O_2 are also effective for its subsequent decomposition to water. Hence, there is an increasing interest in developing catalysts for the ORR that selectively promote H_2O_2. Some examples are carbon materials both as support and to produce peroxide [39–41], for example mesoporous carbons (MCs) are materials with large surface area, tunable pore structure, uniform and adjustable pore size, mechanical stability, and good conductivity. The advantage of working with mesoporous materials is a favourable mass transport: therefore, the chemical intermediates can be released within a relatively short contact time, avoiding subsequent reactions which would lower the process selectivity [42], that is in a similar way what append when performing RRDE analysis, i.e., the peroxide production depends on catalyst loading since for high loading, H_2O_2 remains trapped inside pores and further reduced [43]. In addition, surface modification can promote both the electrochemical activity and the wettability needed for the implementation of an electrode to be employed in an electrolyser. From this perspective, MC activity can be tailored (enhanced) through surface modification with heteroatoms such as nitrogen, sulphur, boron, phosphorus and so on, obtaining a cheap and metal-free catalyst [39,44]. Also, some metal containing catalysts (mainly Cobalt) are attractive for H_2O_2 production [45,46] .

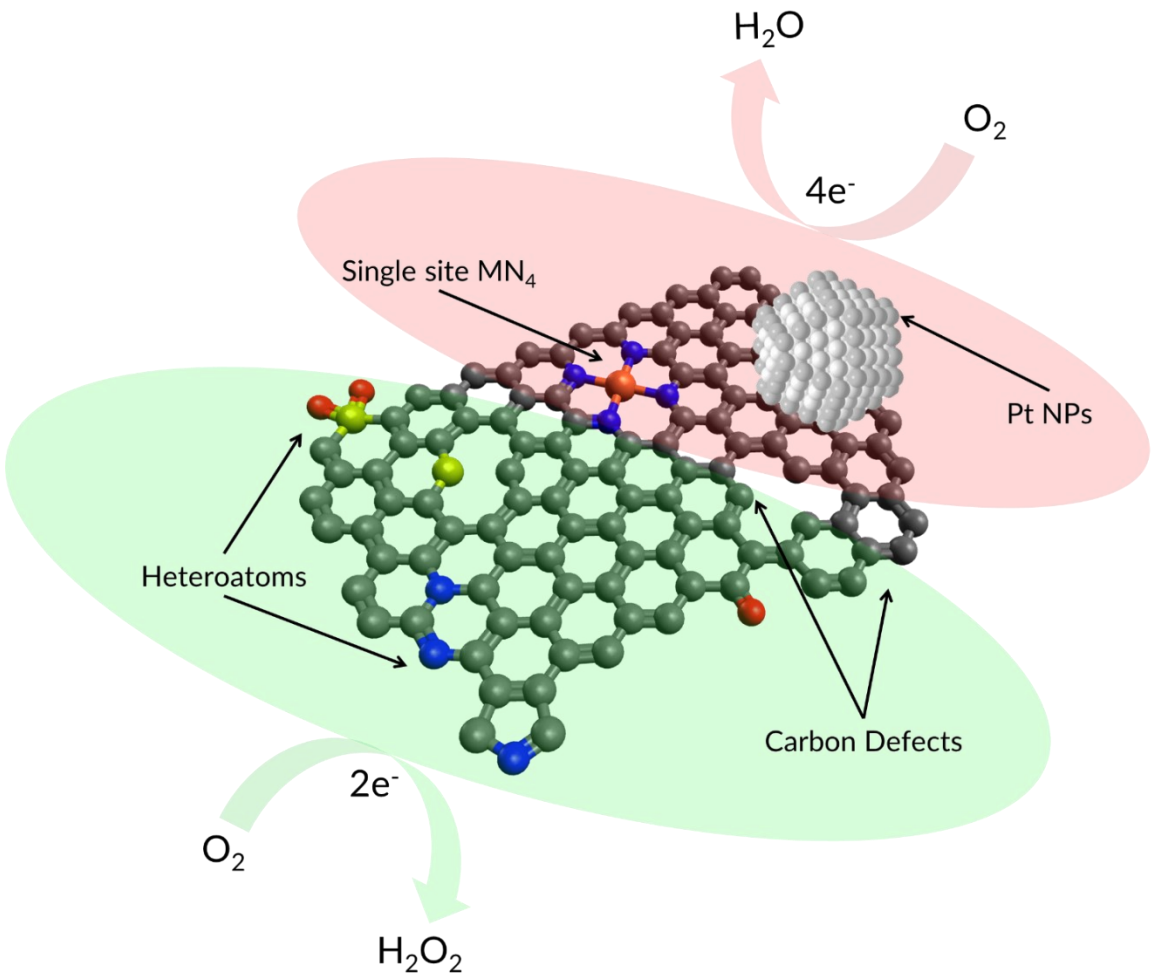

Figure 1.6. Pictorial representation of carbon based catalysts for ORR

1.3. Non-PGM catalyst

As explained before the main drawback of fuel cell application and hydrogen peroxide production are the expensive catalysts required and the non-environmentally friendly media for the reaction respectively. Catalysts based on doped carbon with or without on transition metal represent a good alterative, in one case to reduce cost of the device an on the other to carry the reaction in aqueous media. For the two application basically active and selective material are required, namely a four electron reaction is needed for fuel cell, while a two electron reaction is needed for H_2O_2 production.
Of all class of catalysts, it can be observed that generally metal free catalyst tend to produce more hydrogen peroxide and therefore could be optimized with this aim, while metal based one, with some exception, tend to catalyse the reduction to water. For this reason, in the following paragraphs some examples of metal free catalyst will be given looking at H_2O_2 production, while for metal based some examples are reported for fuel cell applications (Figure 1.7)

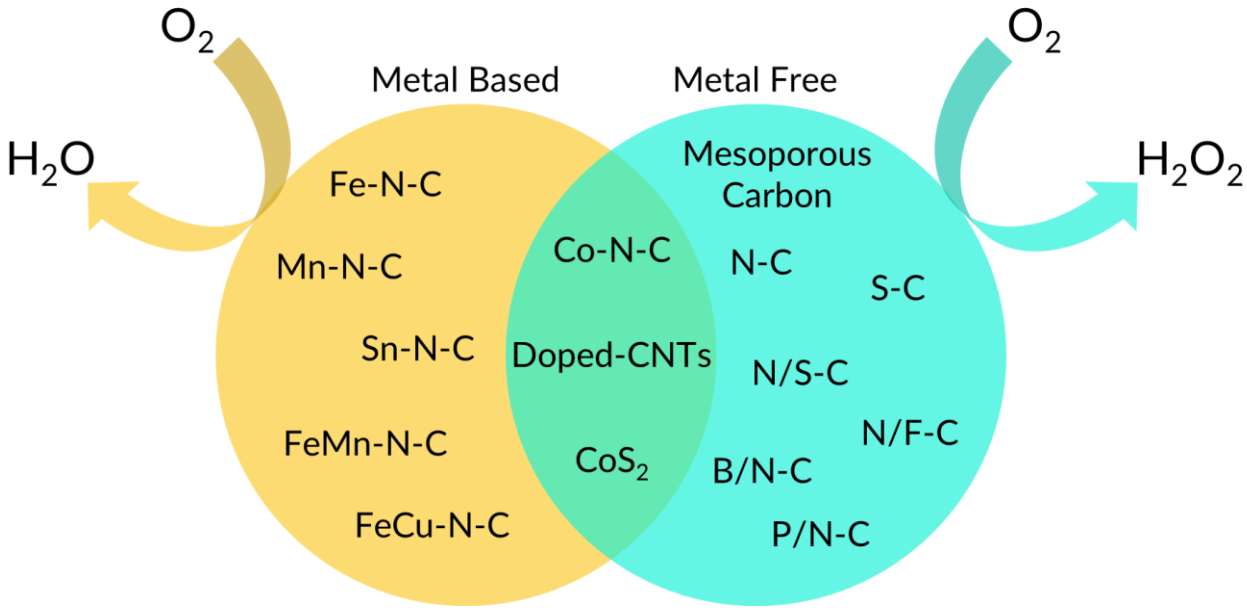

Figure 1.7. Schematic representation of material for ORR.

1.3.1. Metal free

The main drawback on metal-based catalysts is the expensiveness of some of those and the difficulty on scalability for industrial production. On the contrary metal free carbon materials has received a special attention owing to their low-cost and diversified ways of production, favourable selectivity, and good chemical stability [47]. Among carbon-based materials, mesoporous carbon doped or co-doped with nitrogen, boron, phosphorus, or sulfur showed interesting electroactivity in oxygen reduction to hydrogen peroxide [48–51]. The current challenge about those materials is to understand how textural properties such as micro and mesopore surface and volume or defects of graphene plane/edge influences the activity and selectivity, i.e., the precise role of the various type of N species, i.e., pyridinic and pyrrolic nitrogen, need to be understand as for the role of other heteroatoms. The following paragraphs give a quick overview about that.

1.3.2. Carbon based catalysts

Carbon itself has low catalytic activity toward ORR, but the not ideality of carbon matrix generally increase that. Defects (Figure 1.8) in all fashion are generally observed to have their own catalytic activity. Porosity and defects are clearly linked since the latter are found on graphitic edge or plane, but in general they have to be exposed to be reached by oxygen. For that reason, the control of porosity is linked to activity of carbon-sole catalysts. Porous carbon materials with tailorable pore size and surface area can be prepared by template methods, which involves the pyrolysis of a carbon precursor and the utilization of a hard or a soft template [41,52–54], and the textural properties can be modulated by means of thermal treatments in different feeding gases including CO_2, H_2O and NH_3 [55]. In this context, mesoporous carbons have the benefit of better exposing the active sites and favouring the mass transport, therefore, the chemical intermediates (H_2O_2) can be released within a relatively short contact time, avoiding subsequent reactions which would lower the process selectivity [42,56,57]. One example of carbon-based catalyst was proposed by Wang at al. [58] that prepared defective commercial carbon black with a one-step plasma method. In detail they prepare the material by exposing commercial CB materials to an O_2 plasma environment, which is known to generate carbon defects and oxygen-containing groups in carbon material, by removing oxygen by annealing the also shows that the main selectivity, which in 0.1 M KOH at around 0.55 V vs. RHE reaches almost 100%, comes from carbon defect. The role of defect was also observed by Chen et al. [59] in 2018 where two carbon materials were prepared, one microporous and one mesoporous. Both catalysts performed well for ORR in KOH with selectivity up to 70%, but the mesoporous one demonstrated greater electrochemical accessibility and also activity, selectivity, and stability better than those of microporous carbon. This difference arise from the different pore sizes of the two materials, given their similar characteristics otherwise, which in other word is related to a different accessibility or differentiation of carbon defect which are the active site since in absence of other heteroatom. In another paper, Xu ad co-worker observed from a series of CO_2 activated carbon that the growing surface area well correlate with the activity in term of onset potential or mass current, while the H_2O_2 peroxide production slightly decrease with higher micropore fraction, this was explained with a trapping effect of peroxide in pore that allow a further reduction [60].

If on one hand carbon-only materials are attractive, on the other to work at lower overpotential generally doping with some heteroatoms is useful; in addition, looking at materials derived from waste like biomass, the presence of heteroatom such as oxygen and nitrogen are unavoidable.

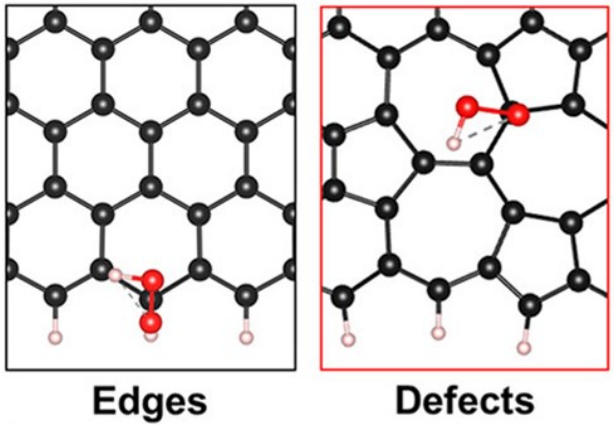

Figure 1.8. Types of carbon defects

1.3.3. Doped carbon catalysts

Heteroatom doped carbons are mainly prepared by thermal treatments of a carbon material or by pyrolysis of suitable precursors or additives containing nitrogen, sulfur, or other hetero-elements such as natural, artificial, or synthetic molecules, polymers, ionic liquids, and biomasses [61,62]. The important parameters to control are the type and content of dopant (heteroatoms functional groups or structure defects) and the textural properties, even if it is worth to mention that available synthetic procedures, for scalable catalyst, are poorly selective versus the type of functional group that can be pinned into the carbon material, whereas the capability to fine tune the textural properties is more manageable. The doping of carbon materials is attractive because it lowers the overpotential of the oxygen reduction reaction, furthermore the capability to be as precise as possible in the types of functionalities introduced allows also to increase the selectivity versus the 2e-ORR or the 4e-ORR. In some cases, the presence of heteroatoms such as oxygen and nitrogen are unavoidable because inherently present in the carbon precursors.

Oxygen functional groups helps activity and selectivity, it is in fact sufficient to think that the quinone groups are the basis of the current industrial processes for the production of hydrogen peroxide [63,64]. A clear example was reported by Lu et al. who reported a nearly linear correlation between the ORR activity and O content in oxidized CNTs [65], i.e., the overpotential drastically lowered by ~130 mV at 0.2 mA compared with standard CNTs while simultaneously increasing the selectivity up to 90%. The origin of the high activity comes from the –COOH functional group in the armchair edge as well as the C–O–C functional group in the basal plane of the graphene (Figure 1.9). As last example, recently San Romani et al. [66] show that the zigzag edge sites with high carbonyl group coverage, as well as other edge configurations with a similar local coordination environment, enables selective, 2e-ORR in graphene-based materials.

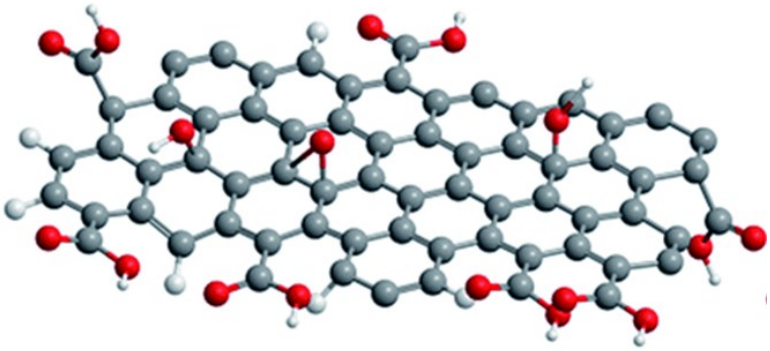

Figure 1.9. Oxygen defect on carbon graphitic plane

Similar to oxygen, nitrogen has a larger electronegativity than carbon, enabling N-doping to be a method to redistribute electrons as well as active sites in the carbon framework [64]. The experimental and theoretical results demonstrated that N atoms facilitated the adsorption of O_2, on the nitrogen itself or on the adjacent carbon, thus enhancing the catalytic activity for the ORR.

Activity boosting are attributed to different sites, for example graphitic nitrogen [67,68], pyrrolic [69–71] and sometimes pyridinic (Figure 1.10). Whether it is widely demonstrated that the nitrogen doping content scales linearly with the catalytic activity versus ORR, much less clear is the effect of the different functionalities [72]. For example, pyridinic-N is claimed to be active for the reduction of peroxide to water [56,71] but its role in catalysing the first bi-electronic reduction step cannot be excluded especially when present in the protonated form [50,68]. Graphitic-N groups appear to be catalytically active in neutral and alkaline conditions. The role of pyrrolic group was specifically identified for promoting the 2e-ORR and a clear example is reported by Li et al. who demonstrated a linear dependence between pyrrolic functional group concentration and the H_2O_2 yield [70].

Actually, the C atoms neighbouring N-doped carbons is considered the actual active site, but in any case the presence of N-functionalities is fundamental to facilitate the charge transfer from the π orbital to the antibonding orbital in O_2 to weaken the O–O bond because of its delocalized lone pair electrons [73].

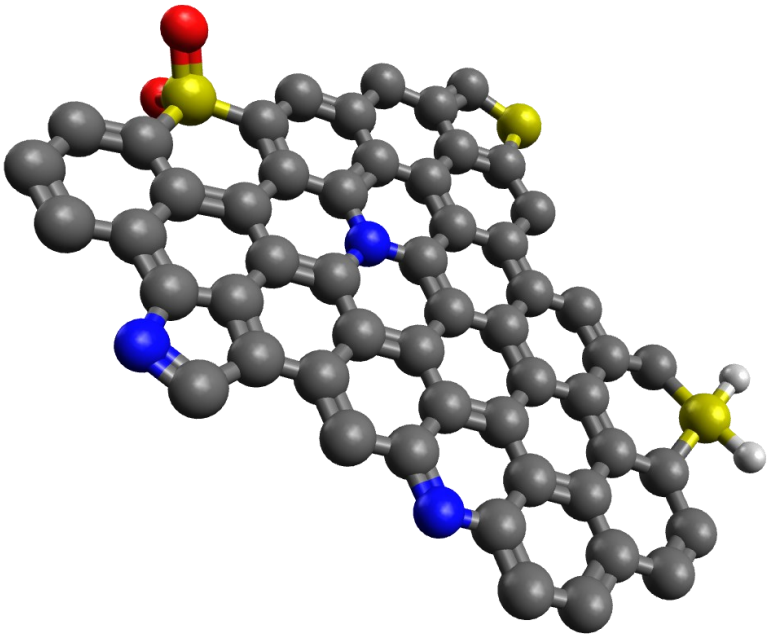

Figure 1.10. Heteroatoms defects of Nitrogen (•) and Sulphur (•)

Among different dopant heteroatoms, boron is considered the best candidate to improve the overpotentials needed to deliver industrial relevant currents, while maintaining high H_2O_2 selectivity [51]. In fact, the B 2p electrons play an essential role in the adsorption of HOO* intermediates, owing to its strong interaction with the O 2s electrons. Sulfur (Figure 1.10) is another element commonly employed for the doping of carbon materials, but actually according to the free Gibbs energy profile it favours too much the adsorption of O_2 [51,74] which leads to a decrease of both the catalytic activity and selectivity. In fact, there are experimental evidence reporting the decrease of activity with the increasing of sulfur content. This behaviour seems to be favourable in the presence of metal, like iron in Fe-N-C where the active site is not sulphur itself, and some examples will be given later.

Much less investigations are devoted to phosphorous doped carbon. For example, Strasser and Co. report on a P-doped carbon exhibiting considerable catalytic activity for the ORR but mostly for the 4e-ORR rather than 2e-ORR [75]. This can be explicated on the base of an unfavourable formation energy of H_2O_2. According to Xia et al. there is no energy barrier for the formation of *O originated from dissociation of the O–O bond. Thus, the $4e^-$ pathway becomes more favourable with respect to H_2O_2 formation, which, as said, is an advantage or a disadvantage depending on application.

A step forward is to add a secondary doping and usually this is done together with nitrogen as a primary dopant. Sulfur is one of the most common choices where S could help the “end-on” O_2 adsorption which facilitates the peroxide production [41,74], or by stabilizing the O-O favouring the formation of peroxide. Other less conventional doping are made with boron [51,76], phosphorus [77–79] or even fluorine. The latter was done by Jia et al. [48] who prepare N, F co-doped carbon nanocages for electrosynthesis of H_2O_2 in both alkaline and acid electrolytes. Whether N promote the adsorption of O_2, the F atoms promoted the desorption of *OOH, causing a high selectivity for H_2O_2 electroproduction.

1.3.4. Grafting

Chemical functionalization represents a valuable and alternative approach to the nitrogen decoration of complex carbon nanostructures by means of tailored “edge-type” N-containing functionalities. Compared with the classical CVD approach, chemical functionalization offers a unique tool for the rationalization of the fundamental structure−reactivity relationship of N-doped carbon nanomaterials active in the ORR [80,81].

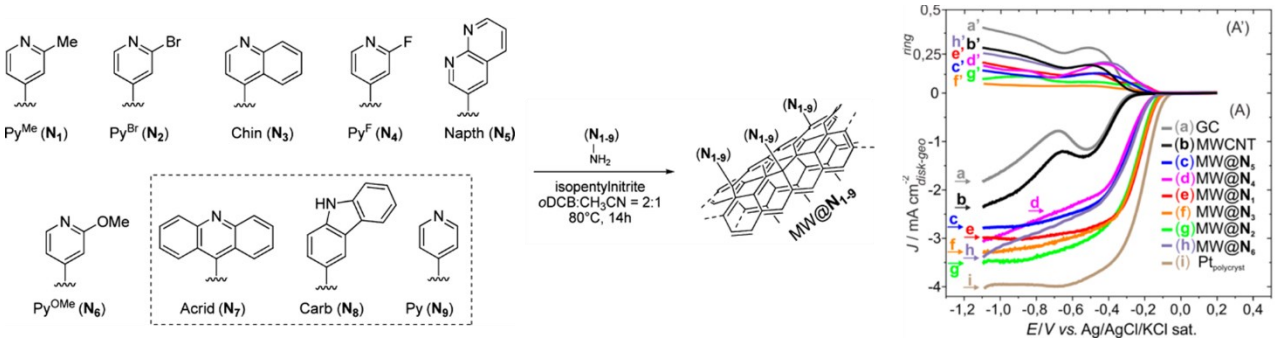

Figure 1.11. Molecule with N-group grafted by Tuci et al. [80] with LSV in alkaline media.

The synthesis through the grafting procedure is basically the introduction of specifical functional group on a carbon support. Grafting means that a molecule is bonded on the surface via covalent bond onto a certain surface, a carbon in this case. The foundations of this reaction are explainable with a Tour-like reaction (Figure 1.12) in which an in-situ generated aryldiazonium cation or introduced as salt react spontaneously with a conjugated system, as the carbon surface:

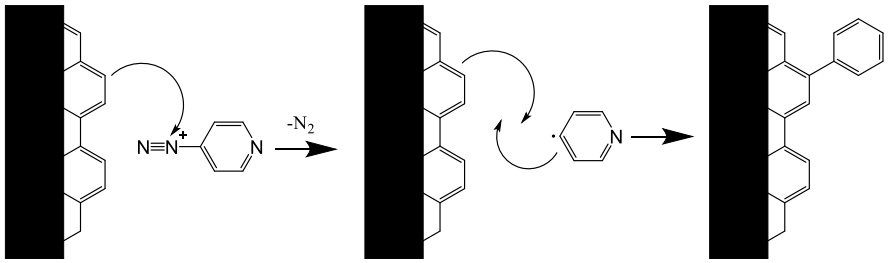

Figure 1.12. Dediazotation by Nucleophilic Attack of the Carbon Surface on the Benzene-diazonium Cation Followed by the Heterolytic Formation of a Covalent C-C Bond Between the Surface and the Aryl Group

The great advantages of this synthesis are that could be conducted in water, are occurring spontaneously and are in principle controllable with the time and temperature of grafting. Some notable examples are from the author that gave the name to Tour reaction, which study the functionalization of nanotube in ionic liquid [82] and in water [83]. On carbon black the reaction was successfully carried out by Toupin et al. [84,85] by generating in situ diazonium salt that consequently generate the aryl radical, as already explained in Figure 1.12.

1.3.5. Iron-Nitrogen doped carbon (Fe-N-C)

Fe-N-C has emerged as the best metal based single atom catalyst for the oxygen reduction as alternative to Pt-based catalysts. In the following paragraph some feature of these catalysts will be given. In general, they consist in single atom of iron that coordinates nitrogen functionalities on

carbon surface, namely on N-doped graphene layer (The Plurality of Active Sites Observed in Fe-N-C Electrocatalysts [93]).

1.3.5.1.Active sites

The possible active sites present on Fe-N-C materials could be summarized as shown in Figure 1.13. This can be classified in three categories:

- Carbon-Nitrogen functionalities
- Iron-Nitrogen functionalities
- Iron Inorganic Phases

For the first are valid the consideration made above regarding metal free catalysts, while for the other two some insights are given. The carbon defect or oxygen functionalities are generally not considered due to low contribution of difficulty to discriminate the influence.

Mixing observation, hypothesis, and calculation different type of FeN_x sites have been identified FeN_2, FeN_3, FeN_{2+2}, FeN_4, N-FeN_4, FeN_{4+1} and Fe-N_xC_{4-x} [86–92].

Fe-containing nanoparticles are also formed, but generally removed by acid washing. Some of them could remain and have impact on activity, selectivity, and durability. These are usually, magnetic α- and γ-Fe and Fe-carbides and nitrides [91,92].

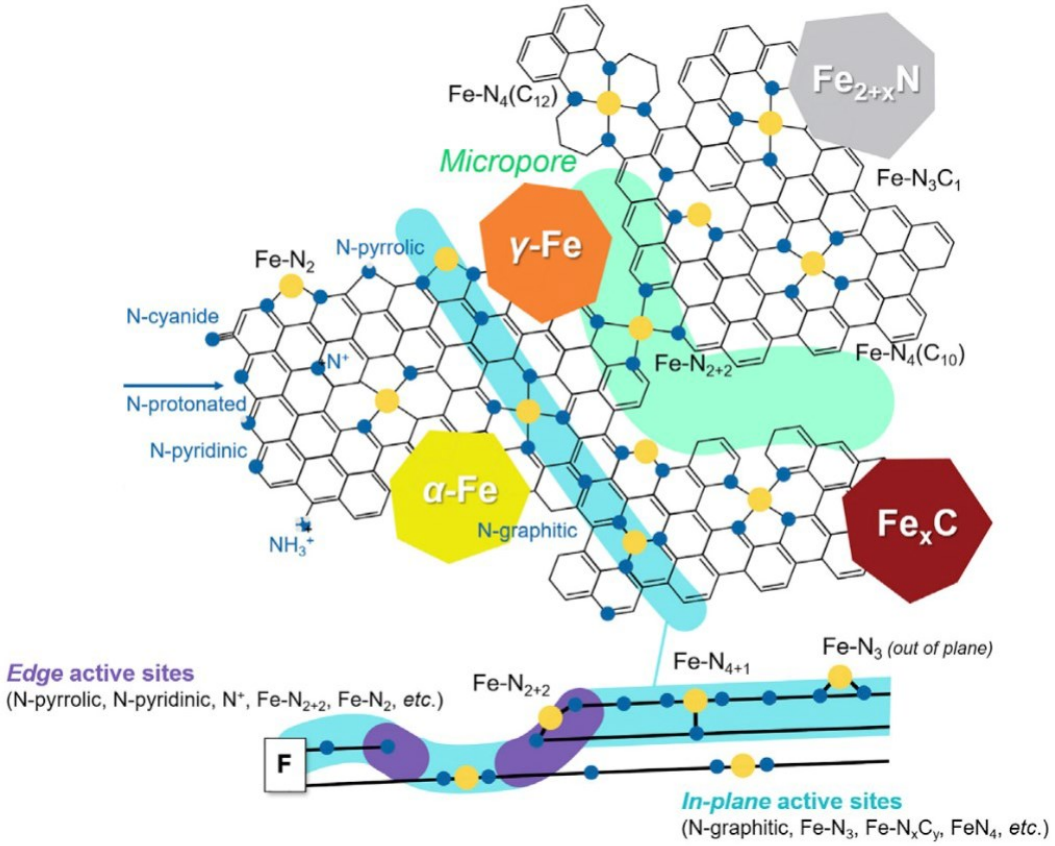

Figure 1.13. The Plurality of Active Sites Observed in Fe-N-C Electrocatalysts [93]

The Fe-N_x moieties differ by electronic structure (electronic orbital filling), coordination, environment, and therefore activity for the ORR. The latter is affected by the O_2 binding onto Fe-N_x. Some of those (FeN_{2+2}) from consideration on orbital filling after O_2 binding are considered inactive, but the complex structure of those catalyst and the influence of surrounding atom made

difficult to give certain conclusion. The configuration of the carbons surrounding the Fe-N_4 moieties has been investigated by density functional theory (DFT) assuming both pyridinic (FeN_4C_{10}) and pyrrolic (FeN_4C_{12}) coordinating nitrogen since the first is in theory the favoured, but also the second was experimentally observed by EXAFS [91]. In substance, Fe-N_4 and Fe-N_{4+1} are believed to be the main Fe-containing active sites for the ORR with the help of FeN_x ($x < 4$) sites [93].
Fe-based nanoparticles were sometimes considered as an ORR active site for example Tylus et al. [94] proposed the role of Fe/FeO_x encapsulated under carbon layer, while Strickland at al. prepared a non-iron-nitrogen coordinated catalyst with good activity [95]. However, it has been recently evidenced that their preferential oxidation during Fe-N-C electrocatalysts aging resulted in no decay in activity in an acid environment, hence suggesting that such nanoparticles are inactive for the ORR at low pHs [96] in opposition to alkaline environments [97].
The influence of pH is indeed present for all sites. For example, the N-pyridinic has a pKa of 6.5, hence, a shift from acidic to alkaline media would result in a change of protonation influencing the adsorption of O_2 species [98,99] The pH also impacts the overall ORR mechanism on Fe-N-C electrocatalysts, i.e., the specific adsorption of OH^- in a strong alkaline block the Fe-containing moieties and results in an outer-sphere electron transfer mechanism. This facilitates H_2O_2 formation, which is also unstable in this media, therefore not suitable for peroxide production.
Figure 1.14 summarize the role of active moieties in Fe-N-C catalysts.

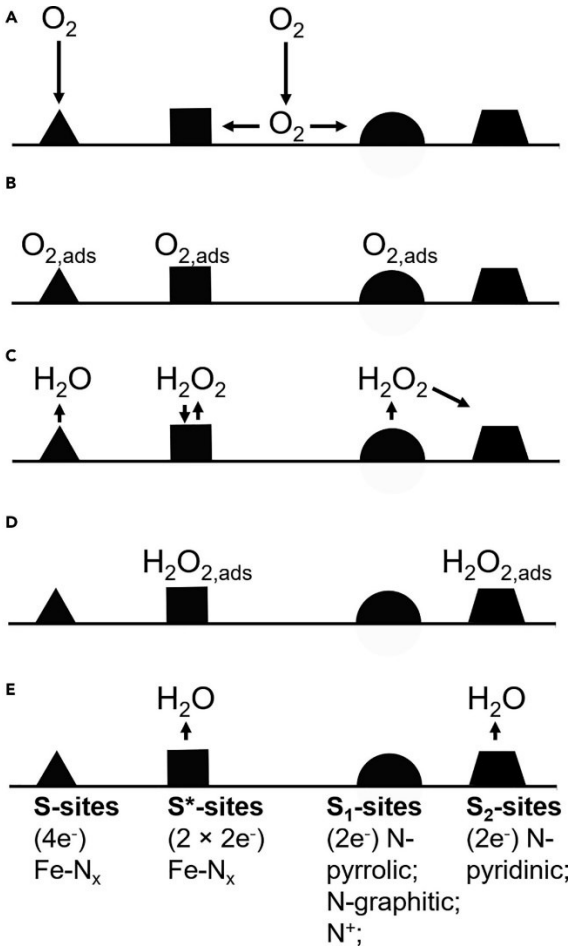

Figure 1.14. Oxygen reduction reaction mechanism on the different active sites (S, S*, S_1,and S_2) commonly observed in Fe-N-C electrocatalysts: (a) O_2 in solution or surface diffusion to the active sites. (b) O_2 adsorption on the different active sites. (c) O_2 reduction to H_2O (on S sites) or H_2O_2 (on S* or S_1 sites) followed by diffusion in solution. (d) re-adsorption on S* or S_2 sites. (e) H_2O_2 reduction to H_2O, followed by diffusion in solution [93].

1.3.5.2.Parameter in play

The type of sites formed, and their activity are influenced by the precursor, the synthesis condition, and the final properties of the carbon matrix. As a main topic of this thesis several parameters will be investigated, i.e., carbon support morphology the iron-nitrogen precursor and so on.

For example, FeN_4 tend to form inside micropore [100], but the accessibility to them require a more open structure of mesopore, in other words both dimensional range of pore are needed.

With regard to the FeN_4 moieties, the reactivity depends on the carbon basal plane electronic properties, impacting the Fe^{III}/Fe^{II} redox transition potential, i.e., the shift from an out-of-plane $Fe^{II}N_4$ to an in-plane $HO\text{-}Fe^{III}N_4$ [93]. This transition is believed to be partly responsible for the enhanced reactivity of the pyrolyzed electrocatalysts compered to molecular catalysts, and the out-of-plane $Fe^{II}N_4$ is believed to be the main ORR catalytic site [93,94,101].

The redox transition potential is dependent on the *p*-electron delocalization in the carbon basal plane, this effect is very evident if the redox potential of a typical iron macrocycle (porphyrin like) is compared with a pyrolyze catalyst, the shift is indeed around 0.7 V toward more positive potential. As said this is influenced by the presence of defect the make the p-electron system defective, hence increasing its electron withdrawing nature. This impact the strength of oxygen on iron centre which is a descriptor of the activity (in term of turn over frequency) of the sites [93,102]. This is basically a Sabatier principle-like description and therefore it is important to optimize the structural defects' density in the carbon basal plane to achieve an optimal binding energy on the Fe(II)-N4 moieties, schematically represented in Figure 1.15. This means that not only porosity control is fundamental to have sites formation but also to determine the optimal activity. This is perfectly in line with observation made by us on steam activated sample (see chapter 4) with tuned porosity [55]. This means that too defective carbon will result in weak binding of oxygen, without forget that defect will also impact the durability since they are preferential corrosion sites.

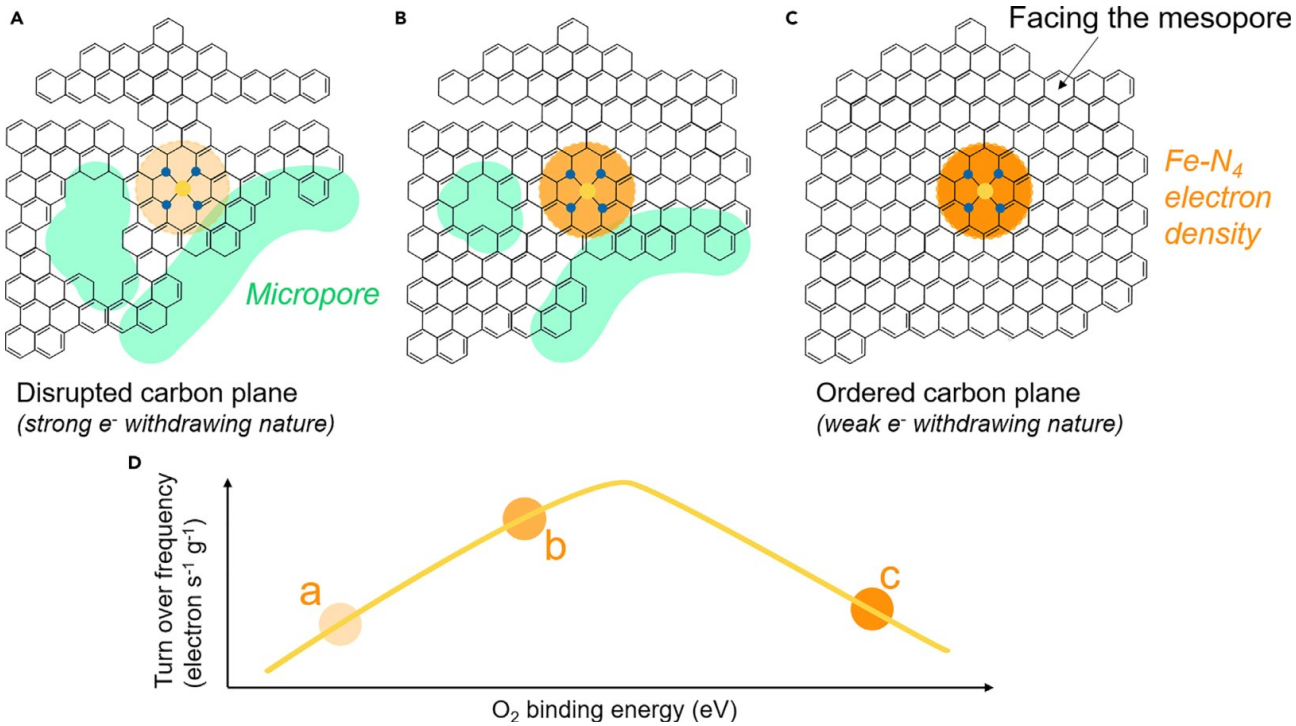

Figure 1.15. Qualitative Representation of the Carbon Basal Plane Defectivity on the O_2 Binding Energy. (A) Highly defective carbon basal plane, (B) low-defectivity carbon basal plane, (C) ordered carbon basal plane, and (D) turnover frequency for the ORR versus the O_2 binding energy, with three qualitative examples corresponding to (A)–(C) [93].

1.3.6. Other metal

More or less all d-transition metal of 4th period have been used to prepare M-N-C materials [103–105]. Therefore, Cr [104,106], Mn, Co, Ni, Cu [105,107,108] and Zn [109,110] have been used to produce catalyst. If on one hand Cr and Zn are less studied, the first probably for toxicity, the other have been wildly studied for both oxygen reduction and carbon dioxide reduction. Iron seem to remain the most active and selective, but for other applications a part of the fuel cells, other metal are also attractive, also for their higher stability. Gao et al. [107] shows by combing experimental and DFT results, show that Co is the best candidate to H_2O_2 production, while Fe and Mn for the tetra-electronic reduction of oxygen (Figure 1.16). Similar result was observed by Sun et al. [105] with Co that has the higher selectivity toward H_2O_2.

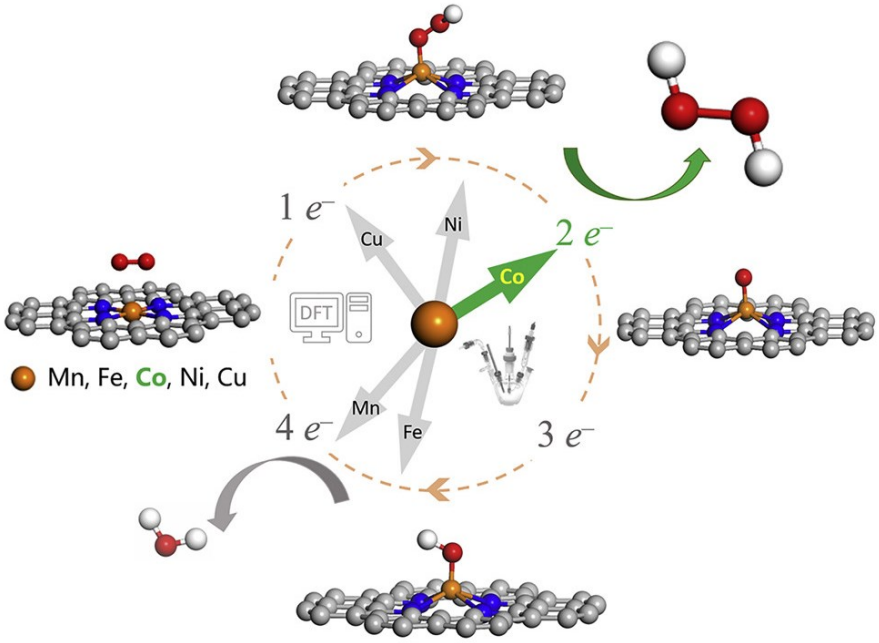

Figure 1.16. Schematic of ORR along the 2 e^- or 4 e^- pathway on transition metal SACs (M = Mn, Fe, Co, Ni, and Cu) anchored in N-doped graphene [57].

1.3.7. Bimetallic and co-doping with other heteroatoms

Choosing the right carbon matrix is the turning point to improve catalytic performance. Indeed, increasing the density of the active sites is not sufficient to enhance the catalyst activity, since it is also necessary to rationally design the textural and porous properties of the carbon support to facilitate the mass transport between micropores and the bulk solution [55,111,112]. Moreover, the catalytic enhancement can be obtained by the incorporation of heteroatoms like N, S, P or B or another metal to form bimetallic system [113–115].

For example, Sun et al. [114] show that incorporation of phosphorus helps the performance of Fe-N-C both in term of activity and stability (Figure 1.17). The idea underlying the doping process is the capability of heteroatoms to modulate the electronic structure of the carbon plane via the delocalization of the π-electrons when pinned into the carbon framework, improving the catalyst activity [116]. Considering instead the S doping, the high electron spin density of doped S atoms enhances the electrocatalytic activity, in particular the asymmetric charge density distribution creates adsorption sites enhancing the performance for ORR [117]. Other study demonstrates that

S doping activates carbon atoms next to graphitic N becoming ORR active sites [118]. ORR activity of a single Fe-N_x catalytic site as said for carbon defect is influenced by electron-withdrawing/donating groups, so only oxidized S functionality (-SO_x) should induce an increase of ORR [119]. However, it has been demonstrated that the main incorporated S-structure is thiophene-like (C-S-C) and that its beneficial effect in ORR was observed to be dependent on the distance between the iron centre and the S atom [120]. So, in general an effect is expected but difficult to control and understand.

Bimetallic N-doped carbon have been less studied due to the already complex nature of the monometallic system. Despite that, the addition of a second metal, generally to Fe-N-C catalysts, could have an impact of site formation [121], final activity [122], or stability [123]. For example, the addition of Ni to the precursor mixture results in a lower number of sites, due to competition mechanisms during the pyrolysis [121], while the addition of Mn (Figure 1.17) shows an activity improvement in alkaline environment [122], and the use of copper seems to be beneficial to activity [124]. Recently also Zr was used to improve the activity of Fe-N-C. In this case the effect was induced by a synergistic effect between Fe-N_x site and ZrO_x present on the carbon surface [125]. *d*-group metals (4th period) are generally the only used to fabricate M-N-C catalysts, because of their better performances. Indeed, other metal are less interesting due to the inability to form nitrogen coordinating single sites materials (in pyrolytic condition) or to the tendency of forming NPs instead of isolated metal-nitrogen sites [126,127]. Other metals are too pricy or are more prone to catalyse other reactions, such as the homogeneous CO_2 reduction [128–132]. In a recent paper, Strasser et Co. showed the possible role of Sn in oxygen reduction reaction (ORR) in real fuel cell system [123]. Sn is a *p*-block element that was substantially [133] never studied in the single sites catalyst shape, conversely to other transition metals such as Fe or Co [134,135]. In fact, Sn is typically used as catalyst in nanoparticle form [136,137].

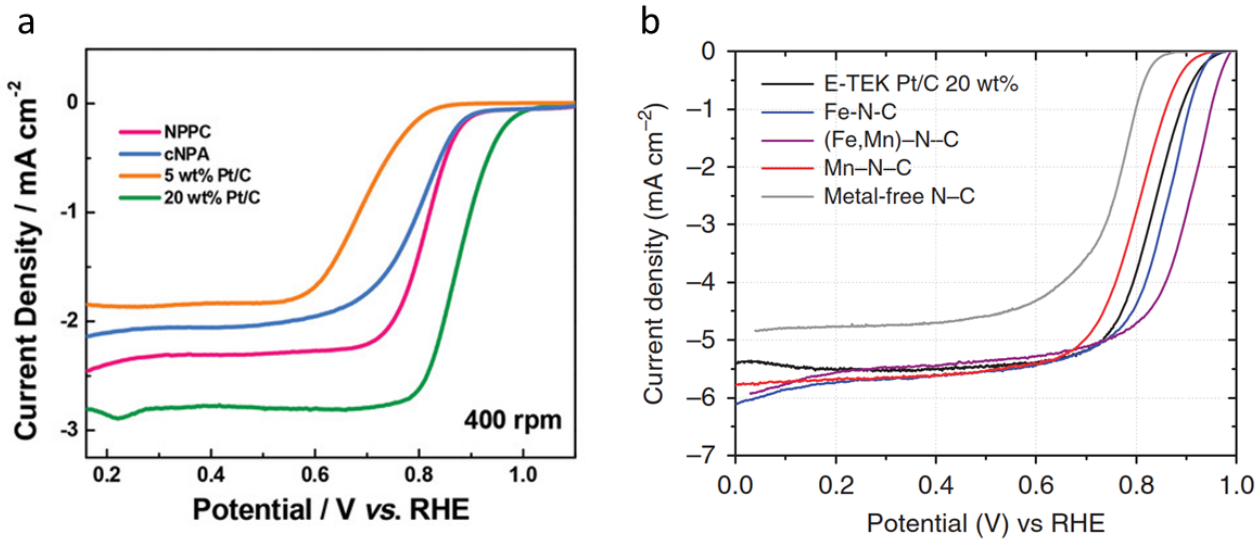

Figure 1.17. a) Effect of P addition and b) effect of Mn addition on Fe-N-C [114]

1.4. Bibliography

[1] D.S. Arndt, R.J.H. Dunn, T. Li, Special Supplement to the STATE OF THE CLIMATE IN 2017, 99 (2018). https://doi.org/10.1175/2018BAMSStateoftheClimate.1.

[2] https://www.climatecentral.org (accessed June 29, 2019).

[3] UNTC - Paris Agreement, (accessed June 23, 2019).

[4] Renewables 2018 Global Status Report, http://www.ren21.net/gsr-2018/ (accessed June 12, 2019).

[5] M. Chen, Z. Zheng, Q. Wang, Y. Zhang, X. Ma, C. Shen, D. Xu, J. Liu, Y. Liu, P. Gionet, I. O'Connor, L. Pinnell, J. Wang, E. Gratz, R. Arsenault, Y. Wang, Closed Loop Recycling of Electric Vehicle Batteries to Enable Ultra-high Quality Cathode Powder, Sci. Rep. 9 (2019) 1654. https://doi.org/10.1038/s41598-018-38238-3.

[6] Benefit Of Electric Cars, (n.d.). https://www.ergon.com.au/network/smarter-energy/electric-vehicles/benefits-of-electric-vehicles (accessed August 17, 2019).

[7] Rifugio san Giuliano, https://www.rainews.it/tgr/trento/video/2019/07/tnt-rifugio-idrogeno-San-Giuliano-energie-rinnovabili-e17f3f76-c6d0-4e90-9ef9-5cfb7542c22a.html (accessed September 6, 2019).

[8] iLint, https://www.agi.it/blog-italia/energia-e-sostenibilta/treni_idrogeno_economia_solare-4390105/post/2018-09-18/ (accessed June 29, 2019).

[9] J. Wang, H. Wang, Y. Fan, Techno-Economic Challenges of Fuel Cell Commercialization, Engineering. 4 (2018) 352–360. https://doi.org/10.1016/j.eng.2018.05.007.

[10] C. Durante, M. Mazzucato, M. Bellardita, F. Parrino, Fundamentals of photoelectrocatalysis, in: L. Palmisano, S. Yurdakal (Eds.), PHOTOELECTROCATALYSIS Fundam. Appl., 1st ed., ELSEVIER, 2022: p. 362. https://doi.org/10.1016/B978-0-12-823989-6.00003-5.

[11] H.S. Wroblowa, Yen-Chi-Pan, G. Razumney, Electroreduction of oxygen, J. Electroanal. Chem. Interfacial Electrochem. 69 (1976) 195–201. https://doi.org/10.1016/s0022-0728(76)80250-1.

[12] C.F. Zinola, Fundamental aspects of electrocatalysis, Electrocatal. Comput. Exp. Ind. Asp. (2010) 43–75. https://doi.org/10.1201/9781420045451.

[13] A. Frumkin, L. Nekrasov, B. Levich, J. Ivanov, Die anwendung der rotierenden scheibenelektrode mit einem ringe zur untersuchung von zwischenprodukten elektrochemischer reaktionen, J. Electroanal. Chem. 1 (1959) 84–90. https://doi.org/10.1016/0022-0728(59)80012-7.

[14] A. Goyal, G. Marcandalli, V.A. Mints, M.T.M. Koper, Competition between CO2Reduction and Hydrogen Evolution on a Gold Electrode under Well-Defined Mass Transport Conditions, J. Am. Chem. Soc. 142 (2020) 4154–4161. https://doi.org/10.1021/jacs.9b10061.

[15] K.H. Wu, Q. Zhang, Y. Lin, M.A. Ali, S. Zhao, S. Heumann, G. Centi, Real-Time Carbon Monoxide Detection using a Rotating Gold Ring Electrode: A Feasibility Study, ChemElectroChem. 7 (2020) 4417–4422. https://doi.org/10.1002/celc.202001263.

[16] A.E. Sanli, A. Aytaç, Response to Disselkamp: Direct peroxide/peroxide fuel cell as a novel type fuel cell, Int. J. Hydrogen Energy. 36 (2011) 869–875. https://doi.org/10.1016/j.ijhydene.2010.09.038.

[17] Y. Yamada, M. Yoneda, S. Fukuzumi, High and robust performance of H 2 O 2 fuel cells in the presence of scandium ion, Energy Environ. Sci. 8 (2015) 1698–1701. https://doi.org/10.1039/C5EE00748H.

[18] J.M. Campos-Martin, G. Blanco-Brieva, J.L.G. Fierro, Hydrogen peroxide synthesis: an outlook beyond the anthraquinone process, Angew. Chemie Int. Ed. 45 (2006) 6962–84. https://doi.org/10.1002/anie.200503779.

[19] C. Durante, M. Cuscov, A.A. Isse, G. Sandonà, A. Gennaro, Advanced oxidation processes coupled with electrocoagulation for the exhaustive abatement of Cr-EDTA, Water Res. 45 (2011) 2122–2130. https://doi.org/10.1016/j.watres.2010.12.022.

[20] G. Daniel, Y. Zhang, S. Lanzalaco, F. Brombin, T. Kosmala, G. Granozzi, A. Wang, E. Brillas, I. Sirés, C. Durante, Chitosan-Derived Nitrogen-Doped Carbon Electrocatalyst for a Sustainable

Upgrade of Oxygen Reduction to Hydrogen Peroxide in UV-Assisted Electro-Fenton Water Treatment, ACS Sustain. Chem. Eng. 8 (2020) 14425–14440. https://doi.org/10.1021/acssuschemeng.0c04294.
[21] I. Sirés, E. Brillas, Upgrading and expanding the electro-Fenton and related processes, Curr. Opin. Electrochem. 27 (2021). https://doi.org/10.1016/j.coelec.2020.100686.
[22] J.K. Edwards, B. Solsona, E. Ntainjua N, A.F. Carley, A.A. Herzing, C.J. Kiely, G.J. Hutchings, Switching off hydrogen peroxide hydrogenation in the direct synthesis process., Science. 323 (2009) 1037–1041. https://doi.org/10.1126/science.1168980.
[23] S. Ranganathan, V. Sieber, Recent advances in the direct synthesis of hydrogen peroxide using chemical catalysis—a review, Catalysts. 8 (2018). https://doi.org/10.3390/catal8090379.
[24] X. Ji, D. Chen, L. Peng, F. Frison, C.D. Valle, C. Tubaro, M. Zecca, P. Centomo, D. Ye, P. Chen, Sustainable direct H2O2 synthesis over Pd catalyst supported on mesoporous carbon: The effect of surface nitrogen functionality, Catal. Today. 376 (2021) 1–8. https://doi.org/10.1016/j.cattod.2020.12.036.
[25] M. Escudero-Escribano, P. Malacrida, M.H. Hansen, U.G. Vej-Hansen, A. Velazquez-Palenzuela, V. Tripkovic, J. Schiotz, J. Rossmeisl, I.E.L. Stephens, I. Chorkendorff, Tuning the activity of Pt alloy electrocatalysts by means of the lanthanide contraction, Science. 352 (2016) 73–76. https://doi.org/10.1126/science.aad8892.
[26] P. Hernandez-Fernandez, F. Masini, D.N. McCarthy, C.E. Strebel, D. Friebel, D. Deiana, P. Malacrida, A. Nierhoff, A. Bodin, A.M. Wise, J.H. Nielsen, T.W. Hansen, A. Nilsson, I.E.L. Stephens, I. Chorkendorff, Mass-selected nanoparticles of Ptx y as model catalysts for oxygen electroreduction, Nat. Chem. 6 (2014) 732–738. https://doi.org/10.1038/nchem.2001.
[27] J. Greeley, I.E.L. Stephens, A.S. Bondarenko, T.P. Johansson, H.A. Hansen, T.F. Jaramillo, J. Rossmeisl, I. Chorkendorff, J.K. Nørskov, Alloys of platinum and early transition metals as oxygen reduction electrocatalysts, Nat. Chem. 1 (2009) 552–556. https://doi.org/10.1038/nchem.367.
[28] C. Cui, L. Gan, M. Heggen, S. Rudi, P. Strasser, Compositional segregation in shaped Pt alloy nanoparticles and their structural behaviour during electrocatalysis., Nat. Mater. 12 (2013) 765–71. https://doi.org/10.1038/nmat3668.
[29] R. Brandiele, C. Durante, E. Grądzka, G.A. Rizzi, J. Zheng, D. Badocco, P. Centomo, P. Pastore, G. Granozzi, A. Gennaro, One step forward to a scalable synthesis of platinum–yttrium alloy nanoparticles on mesoporous carbon for the oxygen reduction reaction, J. Mater. Chem. A. 4 (2016) 12232–12240. https://doi.org/10.1039/C6TA04498K.
[30] R. Brandiele, A. Guadagnini, L. Girardi, G. Dražić, M.C. Dalconi, G.A. Rizzi, V. Amendola, C. Durante, Climbing the oxygen reduction reaction volcano plot with laser ablation synthesis of Pt x Y nanoalloys, Catal. Sci. Technol. 10 (2020) 4503–4508. https://doi.org/10.1039/D0CY00983K.
[31] M. Escudero-Escribano, A. Verdaguer-Casadevall, P. Malacrida, U. Grønbjerg, B.P. Knudsen, A.K. Jepsen, J. Rossmeisl, I.E.L. Stephens, I. Chorkendorf, Pt 5 Gd as a Highly Active and Stable Catalyst for Oxygen Electroreduction, J. Am. Chem. Soc. 134 (2012) 16476–16479. https://doi.org/dx.doi.org/10.1021/ja306348d.
[32] Y.-J. Wang, N. Zhao, B. Fang, H. Li, X.T. Bi, H. Wang, Carbon-Supported Pt-Based Alloy Electrocatalysts for the Oxygen Reduction Reaction in Polymer Electrolyte Membrane Fuel Cells: Particle Size, Shape, and Composition Manipulation and Their Impact to Activity, Chem. Rev. 115 (2015) 3433–3467. https://doi.org/10.1021/cr500519c.
[33] R. Brandiele, V. Amendola, A. Guadagnini, G.A. Rizzi, D. Badocco, P. Pastore, A.A. Isse, C. Durante, A. Gennaro, Facile synthesis of Pd_3Y alloy nanoparticles for electrocatalysis of the oxygen reduction reaction, Electrochim. Acta. 320 (2019) 134563–134572. https://doi.org/10.1016/j.electacta.2019.134563.
[34] T.J. Stephenson, P. Short, Pajarito Powder, (2021). https://pajaritopowder.com/ (accessed September 3, 2021).

[35] M. Primbs, Y. Sun, A. Roy, D. Malko, A. Mehmood, M.T. Sougrati, P.Y. Blanchard, G. Granozzi, T. Kosmala, G. Daniel, P. Atanassov, J. Sharman, C. Durante, A. Kucernak, D. Jones, F. Jaouen, P. Strasser, Establishing reactivity descriptors for platinum group metal (PGM)-free Fe-N-C catalysts for PEM fuel cells, Energy Environ. Sci. 13 (2020) 2480–2500. https://doi.org/10.1039/d0ee01013h.

[36] H.M.A. Amin, U.P. Apfel, Metal-Rich Chalcogenides as Sustainable Electrocatalysts for Oxygen Evolution and Reduction: State of the Art and Future Perspectives, Eur. J. Inorg. Chem. 2020 (2020) 2679–2690. https://doi.org/10.1002/ejic.202000406.

[37] D.H. Youn, G. Bae, S. Han, J.Y. Kim, J.W. Jang, H. Park, S.H. Choi, J.S. Lee, A highly efficient transition metal nitride-based electrocatalyst for oxygen reduction reaction: TiN on a CNT-graphene hybrid support, J. Mater. Chem. A. 1 (2013) 8007–8015. https://doi.org/10.1039/c3ta11135k.

[38] S. Siahrostami, A. Verdaguer-Casadevall, M. Karamad, D. Deiana, P. Malacrida, B. Wickman, M. Escudero-Escribano, E.A. Paoli, R. Frydendal, T.W. Hansen, I. Chorkendorff, I.E.L. Stephens, J. Rossmeisl, Enabling direct H2O2 production through rational electrocatalyst design., Nat. Mater. 12 (2013) 1137–1143. https://doi.org/10.1038/nmat3795.

[39] V. Perazzolo, C. Durante, R. Pilot, A. Paduano, J. Zheng, G.A. Rizzi, A. Martucci, G. Granozzi, A. Gennaro, Nitrogen and sulfur doped mesoporous carbon as metal-free electrocatalysts for the in situ production of hydrogen peroxide, Carbon. 95 (2015) 949–963. https://doi.org/10.1016/j.carbon.2015.09.002.

[40] V. Perazzolo, C. Durante, A. Gennaro, Nitrogen and sulfur doped mesoporous carbon cathodes for water treatment, J. Electroanal. Chem. 782 (2016) 264–269. https://doi.org/10.1016/j.jelechem.2016.10.037.

[41] V. Perazzolo, G. Daniel, R. Brandiele, L. Picelli, G.A. Rizzi, A.A. Isse, C. Durante, PEO-b-PS Block Copolymer Templated Mesoporous Carbons: A Comparative Study of Nitrogen and Sulfur Doping in the Oxygen Reduction Reaction to Hydrogen Peroxide, Chem. – A Eur. J. 27 (2021) 1002–1014. https://doi.org/10.1002/chem.202003355.

[42] J. Park, Y. Nabae, T. Hayakawa, M.A. Kakimoto, Highly selective two-electron oxygen reduction catalyzed by mesoporous nitrogen-doped carbon, ACS Catal. 4 (2014) 3749–3754. https://doi.org/10.1021/cs5008206.

[43] A. Bonakdarpour, M. Lefevre, R. Yang, F. Jaouen, T. Dahn, J.P. Dodelet, J.R. Dahn, Impact of loading in RRDE experiments on Fe-N-C catalysts: Two- or four-electron oxygen reduction?, Electrochem. Solid-State Lett. 11 (2008) 105–108. https://doi.org/10.1149/1.2904768.

[44] H.-X. Zhang, S.-C. Yang, Y.-L. Wang, J.-C. Xi, J.-C. Huang, J.-F. Li, P. Chen, R. Jia, Electrocatalyst derived from fungal hyphae and its excellent activity for electrochemical production of hydrogen peroxide, Electrochim. Acta. 308 (2019) 74–82. https://doi.org/10.1016/j.electacta.2019.04.011.

[45] A. Lenarda, M. Bevilacqua, C. Tavagnacco, L. Nasi, A. Criado, F. Vizza, M. Melchionna, M. Prato, P. Fornasiero, Selective Electrocatalytic H 2 O 2 Generation by Cobalt@N-Doped Graphitic Carbon Core–Shell Nanohybrids, ChemSusChem. 12 (2019) 1664–1672. https://doi.org/10.1002/cssc.201900238.

[46] B.-Q. Li, C.-X. Zhao, J.-N. Liu, Q. Zhang, Electrosynthesis of Hydrogen Peroxide Synergistically Catalyzed by Atomic Co–N x –C Sites and Oxygen Functional Groups in Noble-Metal-Free Electrocatalysts, Adv. Mater. 1808173 (2019) 1–8. https://doi.org/10.1002/adma.201808173.

[47] V. Perazzolo, E. Grądzka, C. Durante, R. Pilot, N. Vicentini, G.A. Rizzi, G. Granozzi, A. Gennaro, Chemical and Electrochemical Stability of Nitrogen and Sulphur Doped Mesoporous Carbons, Electrochim. Acta. 197 (2016) 251–262. https://doi.org/10.1016/j.electacta.2016.02.025.

[48] N. Jia, T. Yang, S. Shi, X. Chen, Z. An, Y. Chen, S. Yin, P. Chen, N,F-Codoped Carbon Nanocages: An Efficient Electrocatalyst for Hydrogen Peroxide Electroproduction in Alkaline and Acidic Solutions, ACS Sustain. Chem. Eng. 8 (2020) 2883–2891. https://doi.org/10.1021/acssuschemeng.9b07047.

[49] Y. Sun, I. Sinev, W. Ju, A. Bergmann, S. Dresp, S. Kühl, C. Spöri, H. Schmies, H. Wang, D. Bernsmeier, B. Paul, R. Schmack, R. Kraehnert, B. Roldan Cuenya, P. Strasser, Efficient Electrochemical Hydrogen Peroxide Production from Molecular Oxygen on Nitrogen-Doped Mesoporous Carbon Catalysts, ACS Catal. 8 (2018) 2844–2856. https://doi.org/10.1021/acscatal.7b03464.
[50] D. Iglesias, A. Giuliani, M. Melchionna, S. Marchesan, A. Criado, L. Nasi, M. Bevilacqua, C. Tavagnacco, F. Vizza, M. Prato, P. Fornasiero, N-Doped Graphitized Carbon Nanohorns as a Forefront Electrocatalyst in Highly Selective O2 Reduction to H2O2, Chem. 4 (2018) 106–123. https://doi.org/10.1016/j.chempr.2017.10.013.
[51] Y. Xia, X. Zhao, C. Xia, Z.Y. Wu, P. Zhu, J.Y. Kim, X. Bai, G. Gao, Y. Hu, J. Zhong, Y. Liu, H. Wang, Highly active and selective oxygen reduction to H2O2 on boron-doped carbon for high production rates, Nat. Commun. 12 (2021). https://doi.org/10.1038/s41467-021-24329-9.
[52] M. Mazzucato, G. Daniel, V. Perazzolo, R. Brandiele, G.A. Rizzi, A.A. Isse, A. Gennaro, C. Durante, Mesoporosity and nitrogen doping: The leading effect in oxygen reduction reaction activity and selectivity at nitrogen-doped carbons prepared by using polyethylene oxide-block-polystyrene as a sacrificial template, Electrochem. Sci. Adv. (2022) 1–18. https://doi.org/10.1002/elsa.202100203.
[53] R. Brandiele, M. Zerbetto, M.C. Dalconi, G.A. Rizzi, A.A. Isse, C. Durante, A. Gennaro, Mesoporous Carbon with Different Density of Thiophenic-Like Functional Groups and Their Effect on Oxygen Reduction, ChemSusChem. 12 (2019) 4229–4239. https://doi.org/10.1002/cssc.201901568.
[54] R. Brandiele, F. Poli, L. Picelli, R. Pilot, G.A. Rizzi, F. Soavi, C. Durante, Nitrogen doped mesoporous carbon electrodes prepared from templating propylamine functionalized silica, ChemElectroChem. 92 (2020) 455–459. https://doi.org/10.1002/celc.202000098.
[55] M. Mazzucato, G. Daniel, A. Mehmood, T. Kosmala, G. Granozzi, A. Kucernak, C. Durante, Effects of the induced micro- and meso-porosity on the single site density and turn over frequency of Fe-N-C carbon electrodes for the oxygen reduction reaction, Appl. Catal. B Environ. 291 (2021) 120068. https://doi.org/10.1016/j.apcatb.2021.120068.
[56] G.A. Ferrero, K. Preuss, A.B. Fuertes, M. Sevilla, M.M. Titirici, The influence of pore size distribution on the oxygen reduction reaction performance in nitrogen doped carbon microspheres, J. Mater. Chem. A. 4 (2016) 2581–2589. https://doi.org/10.1039/c5ta10063a.
[57] D. Barrera, M. Florent, K. Sapag, T.J. Bandosz, Insight into the Mechanism of Oxygen Reduction Reaction on Micro/Mesoporous Carbons: Ultramicropores versus Nitrogen-Containing Catalytic Centers in Ordered Pore Structure, ACS Appl. Energy Mater. 2 (2019) 7412–7424. https://doi.org/10.1021/acsaem.9b01427.
[58] Z. Wang, Q.K. Li, C. Zhang, Z. Cheng, W. Chen, E.A. McHugh, R.A. Carter, B.I. Yakobson, J.M. Tour, Hydrogen peroxide generation with 100% faradaic efficiency on metal-free carbon black, ACS Catal. 11 (2021) 2454–2459. https://doi.org/10.1021/acscatal.0c04735.
[59] S. Chen, Z. Chen, S. Siahrostami, T.R. Kim, D. Nordlund, D. Sokaras, S. Nowak, J.W.F.F. To, D. Higgins, R. Sinclair, J.K. Nørskov, T.F. Jaramillo, Z. Bao, Defective Carbon-Based Materials for the Electrochemical Synthesis of Hydrogen Peroxide, ACS Sustain. Chem. Eng. 6 (2018) 311–317. https://doi.org/10.1021/acssuschemeng.7b02517.
[60] H. Xu, X. Lv, H. Wang, J. Ye, J. Yuan, Y. Wang, Z. Zhou, S. Sun, Impact of Pore Structure on Two-Electron Oxygen Reduction Reaction in Nitrogen-Doped Carbon Materials: Rotating Ring-Disk Electrode vs. Flow Cell, ChemSusChem. 202102587 (2022) 1–10. https://doi.org/10.1002/cssc.202102587.
[61] K.S. Lakhi, D.H. Park, K. Al-Bahily, W. Cha, B. Viswanathan, J.H. Choy, A. Vinu, Mesoporous carbon nitrides: Synthesis, functionalization, and applications, Chem. Soc. Rev. 46 (2017) 72–101. https://doi.org/10.1039/c6cs00532b.
[62] E. Antolini, Nitrogen-doped carbons by sustainable N- and C-containing natural resources as nonprecious catalysts and catalyst supports for low temperature fuel cells, Renew. Sustain.

Energy Rev. 58 (2016) 34–51. https://doi.org/10.1016/j.rser.2015.12.330.
[63] B. Wang, B. Liu, L. Dai, Non-N-Doped Carbons as Metal-Free Electrocatalysts, Adv. Sustain. Syst. 5 (2021). https://doi.org/10.1002/adsu.202000134.
[64] Z. Wang, D.K. James, J.M. Tour, Metal-Free Electrocatalysts for Oxygen Reduction to Hydrogen Peroxide, Adv. Energy Sustain. Res. 2 (2021) 2100021. https://doi.org/10.1002/aesr.202100021.
[65] Z. Lu, G. Chen, S. Siahrostami, Z. Chen, K. Liu, J. Xie, L. Liao, T. Wu, Di. Lin, Y. Liu, T.F. Jaramillo, J.K. Nørskov, Y. Cui, High-efficiency oxygen reduction to hydrogen peroxide catalysed by oxidized carbon materials, Nat. Catal. 1 (2018) 156–162. https://doi.org/10.1038/s41929-017-0017-x.
[66] D. San Roman, D. Krishnamurthy, R. Garg, H. Hafiz, M. Lamparski, N.T. Nuhfer, V. Meunier, V. Viswanathan, T. Cohen-Karni, Engineering Three-Dimensional (3D) Out-of-Plane Graphene Edge Sites for Highly Selective Two-Electron Oxygen Reduction Electrocatalysis, ACS Catal. 10 (2020) 1993–2008. https://doi.org/10.1021/acscatal.9b03919.
[67] J. Liu, P. Song, M. Ruan, W. Xu, Catalytic properties of graphitic and pyridinic nitrogen doped on carbon black for oxygen reduction reaction, Cuihua Xuebao/Chinese J. Catal. 37 (2016) 1119–1126. https://doi.org/10.1016/S1872-2067(16)62456-7.
[68] Y. Sun, S. Li, Z.P. Jovanov, D. Bernsmeier, H. Wang, B. Paul, X. Wang, S. Kühl, P. Strasser, Structure, Activity, and Faradaic Efficiency of Nitrogen-Doped Porous Carbon Catalysts for Direct Electrochemical Hydrogen Peroxide Production, ChemSusChem. 11 (2018) 3388–3395. https://doi.org/10.1002/cssc.201801583.
[69] M. Tian, Y. Zhu, D. Zhang, M. Wang, Y. Chen, Y. Yang, S. Gao, Pyrrolic-nitrogen-rich biomass-derived catalyst for sustainable degradation of organic pollutant via a self-powered electro-Fenton process, Nano Energy. 64 (2019) 103940–103947. https://doi.org/10.1016/j.nanoen.2019.103940.
[70] L. Li, C. Tang, Y. Zheng, B. Xia, X. Zhou, H. Xu, S.Z. Qiao, Tailoring Selectivity of Electrochemical Hydrogen Peroxide Generation by Tunable Pyrrolic-Nitrogen-Carbon, Adv. Energy Mater. 10 (2020) 1–10. https://doi.org/10.1002/aenm.202000789.
[71] S. Kabir, K. Artyushkova, A. Serov, P. Atanassov, Role of Nitrogen Moieties in N-Doped 3D-Graphene Nanosheets for Oxygen Electroreduction in Acidic and Alkaline Media, ACS Appl. Mater. Interfaces. 10 (2018) 11623–11632. https://doi.org/10.1021/acsami.7b18651.
[72] A. Martucci, Nitrogen and Sulfur Doped Mesoporous Carbon as Metal-Free Electrocatalysts for the in Situ Production of Hydrogen Peroxide, Carbon. 95 (2015) 949–963. https://doi.org/10.1016/j.carbon.2015.09.002.
[73] B. Zhang, W. Xu, Z. Lu, J. Sun, Recent Progress on Carbonaceous Material Engineering for Electrochemical Hydrogen Peroxide Generation, Trans. Tianjin Univ. 26 (2020) 188–196. https://doi.org/10.1007/s12209-020-00240-0.
[74] Y. Zhu, F. Deng, S. Qiu, F. Ma, Y. Zheng, R. Lian, Enhanced electro-Fenton degradation of sulfonamides using the N, S co-doped cathode: Mechanism for H2O2 formation and pollutants decay, J. Hazard. Mater. 403 (2021) 123950. https://doi.org/10.1016/j.jhazmat.2020.123950.
[75] J. Wu, Z. Yang, X. Li, Q. Sun, C. Jin, P. Strasser, R. Yang, Phosphorus-doped porous carbons as efficient electrocatalysts for oxygen reduction, J. Mater. Chem. A. 1 (2013) 9889. https://doi.org/10.1039/c3ta11849e.
[76] X. Li, X. Wang, G. Xiao, Y. Zhu, Identifying active sites of boron, nitrogen co-doped carbon materials for the oxygen reduction reaction to hydrogen peroxide, J. Colloid Interface Sci. 602 (2021) 799–809. https://doi.org/10.1016/j.jcis.2021.06.068.
[77] F.Y. Zheng, R. Li, S. Ge, W.R. Xu, Y. Zhang, Nitrogen and phosphorus co-doped carbon networks derived from shrimp shells as an efficient oxygen reduction catalyst for microbial fuel cells, J. Power Sources. 446 (2020) 227356. https://doi.org/10.1016/j.jpowsour.2019.227356.
[78] M. Li, K. Wang, Q. Lv, N,P-co-Doped Graphdiyne as Efficient Metal-free Catalysts for Oxygen Reduction Reaction, Chem. Res. Chinese Univ. 37 (2021) 1283–1288.

https://doi.org/10.1007/s40242-021-1256-6.
[79] Y. Sun, S. Li, B. Paul, L. Han, P. Strasser, Highly efficient electrochemical production of hydrogen peroxide over nitrogen and phosphorus dual-doped carbon nanosheet in alkaline medium, J. Electroanal. Chem. 896 (2021) 115197. https://doi.org/10.1016/j.jelechem.2021.115197.
[80] G. Tuci, C. Zafferoni, A. Rossin, A. Milella, L. Luconi, M. Innocenti, L. Truong Phuoc, C. Duong-Viet, C. Pham-Huu, G. Giambastiani, Chemically Functionalized Carbon Nanotubes with Pyridine Groups as Easily Tunable N-Decorated Nanomaterials for the Oxygen Reduction Reaction in Alkaline Medium, Chem. Mater. 26 (2014) 3460–3470. https://doi.org/10.1021/cm500805c.
[81] G. Tuci, C. Za, P.D. Ambrosio, S. Caporali, M. Ceppatelli, A. Rossin, T. Tsou, M. Innocenti, G. Giambastiani, Tailoring Carbon Nanotube N - Dopants while Designing Metal-Free Electrocatalysts for the Oxygen Reduction Reaction in Alkaline Medium, (2013) 3–6.
[82] B.K. Price, J.L. Hudson, J.M. Tour, Green chemical functionalization of single-walled carbon nanotubes in ionic liquids, J. Am. Chem. Soc. 127 (2005) 14867–14870. https://doi.org/10.1021/ja053998c.
[83] B.K. Price, J.M. Tour, Functionalization of single-walled carbon nanotubes “on water,” J. Am. Chem. Soc. 128 (2006) 12899–12904. https://doi.org/10.1021/ja063609u.
[84] M. Toupin, D. Bélanger, Thermal stability study of aryl modified carbon black by in situ generated diazonium salt, J. Phys. Chem. C. 111 (2007) 5394–5401. https://doi.org/10.1021/jp066868e.
[85] M. Toupin, D. Bélanger, Spontaneous functionalization of carbon black by reaction with 4-nitrophenyldiazonium cations, Langmuir. 24 (2008) 1910–1917. https://doi.org/10.1021/la702556n.
[86] Y. Shao, J.P. Dodelet, G. Wu, P. Zelenay, PGM-Free Cathode Catalysts for PEM Fuel Cells: A Mini-Review on Stability Challenges, Adv. Mater. 31 (2019) 1–8. https://doi.org/10.1002/adma.201807615.
[87] U.I. Koslowski, I. Abs-Wurmbach, S. Fiechter, P. Bogdanoff, Nature of the catalytic centers of porphyrin-based electrocatalysts for the ORR: A correlation of kinetic current density with the site density of Fe-N4 centers, J. Phys. Chem. C. 112 (2008) 15356–15366. https://doi.org/10.1021/jp802456e.
[88] U.I. Kramm, M. Lefèvre, N. Larouche, D. Schmeisser, J.P. Dodelet, Correlations between mass activity and physicochemical properties of Fe/N/C catalysts for the ORR in PEM fuel cell via 57Fe Mössbauer spectroscopy and other techniques, J. Am. Chem. Soc. 136 (2014) 978–985. https://doi.org/10.1021/ja410076f.
[89] M. Lefèvre, E. Proietti, F. Jaouen, J.-P. Dodelet, Iron-Based Catalysts with Improved Oxygen Reduction Activity in Polymer Electrolyte Fuel Cells, Science. 324 (2009) 71–74. https://doi.org/10.1126/science.1170051.
[90] I. Matanovic, K. Artyushkova, P. Atanassov, Understanding PGM-free catalysts by linking density functional theory calculations and structural analysis: Perspectives and challenges, Curr. Opin. Electrochem. 9 (2018) 137–144. https://doi.org/10.1016/j.coelec.2018.03.009.
[91] A. Zitolo, V. Goellner, V. Armel, M.T. Sougrati, T. Mineva, L. Stievano, E. Fonda, F. Jaouen, Identification of catalytic sites for oxygen reduction in iron- and nitrogen-doped graphene materials, Nat. Mater. 14 (2015) 937–942. https://doi.org/10.1038/nmat4367.
[92] M. Ferrandon, A.J. Kropf, D.J. Myers, K. Artyushkova, U. Kramm, P. Bogdanoff, G. Wu, C.M. Johnston, P. Zelenay, Multitechnique characterization of a polyaniline-iron-carbon oxygen reduction catalyst, J. Phys. Chem. C. 116 (2012) 16001–16013. https://doi.org/10.1021/jp302396g.
[93] T. Asset, P. Atanassov, Iron-Nitrogen-Carbon Catalysts for Proton Exchange Membrane Fuel Cells, Joule. 4 (2020) 33–44. https://doi.org/10.1016/j.joule.2019.12.002.
[94] U. Tylus, Q. Jia, K. Strickland, N. Ramaswamy, A. Serov, P. Atanassov, S. Mukerjee, Elucidating oxygen reduction active sites in pyrolyzed metal-nitrogen coordinated non-precious-metal electrocatalyst systems, J. Phys. Chem. C. 118 (2014) 8999–9008.

https://doi.org/10.1021/jp500781v.
[95] K. Strickland, E. Miner, Q. Jia, U. Tylus, N. Ramaswamy, W. Liang, M.T. Sougrati, F. Jaouen, S. Mukerjee, Highly active oxygen reduction non-platinum group metal electrocatalyst without direct metal-nitrogen coordination, Nat. Commun. 6 (2015) 1–8. https://doi.org/10.1038/ncomms8343.
[96] C.H. Choi, C. Baldizzone, J.-P. Grote, A.K. Schuppert, F. Jaouen, K.J.J. Mayrhofer, Stability of Fe-N-C Catalysts in Acidic Medium Studied by Operando Spectroscopy, Angew. Chemie Int. Ed. 54 (2015) 12753–12757. https://doi.org/10.1002/anie.201504903.
[97] W.J. Jiang, L. Gu, L. Li, Y. Zhang, X. Zhang, L.J. Zhang, J.Q. Wang, J.S. Hu, Z. Wei, L.J. Wan, Understanding the High Activity of Fe-N-C Electrocatalysts in Oxygen Reduction: Fe/Fe3C Nanoparticles Boost the Activity of Fe-Nx, J. Am. Chem. Soc. 138 (2016) 3570–3578. https://doi.org/10.1021/jacs.6b00757.
[98] S. Rojas-Carbonell, K. Artyushkova, A. Serov, C. Santoro, I. Matanovic, P. Atanassov, Effect of pH on the Activity of Platinum Group Metal-Free Catalysts in Oxygen Reduction Reaction, ACS Catal. 8 (2018) 3041–3053. https://doi.org/10.1021/acscatal.7b03991.
[99] W. Zhong, Z. Wang, S. Han, L. Deng, J. Yu, Y. Lin, X. Long, M. Gu, S. Yang, Identifying the Active Sites of a Single Atom Catalyst with pH-Universal Oxygen Reduction Reaction Activity, Cell Reports Phys. Sci. 1 (2020) 100115. https://doi.org/10.1016/j.xcrp.2020.100115.
[100] F. Jaouen, M. Lefèvre, J.-P. Dodelet, M. Cai, Heat-Treated Fe/N/C Catalysts for O 2 Electroreduction: Are Active Sites Hosted in Micropores?, J. Phys. Chem. B. 110 (2006) 5553–5558. https://doi.org/10.1021/jp057135h.
[101] J. Li, S. Ghoshal, W. Liang, M.-T. Sougrati, F. Jaouen, B. Halevi, S. McKinney, G. McCool, C. Ma, X. Yuan, Z.-F. Ma, S. Mukerjee, Q. Jia, Structural and mechanistic basis for the high activity of Fe–N–C catalysts toward oxygen reduction, Energy Environ. Sci. 9 (2016) 2418–2432. https://doi.org/10.1039/C6EE01160H.
[102] N. Ramaswamy, U. Tylus, Q. Jia, S. Mukerjee, Activity descriptor identification for oxygen reduction on nonprecious electrocatalysts: Linking surface science to coordination chemistry, J. Am. Chem. Soc. 135 (2013) 15443–15449. https://doi.org/10.1021/ja405149m.
[103] L. Osmieri, Transition Metal–Nitrogen–Carbon (M–N–C) Catalysts for Oxygen Reduction Reaction. Insights on Synthesis and Performance in Polymer Electrolyte Fuel Cells, ChemEngineering. 3 (2019) 16. https://doi.org/10.3390/chemengineering3010016.
[104] Q. Liu, Q. Li, S. Chen, Metal–nitrogen coordination moieties in carbon for effective electrocatalytic reduction of oxygen, Curr. Opin. Electrochem. 21 (2020) 46–54. https://doi.org/10.1016/j.coelec.2020.01.002.
[105] Y. Sun, L. Silvioli, N.R. Sahraie, W. Ju, J. Li, A. Zitolo, S. Li, A. Bagger, L. Arnarson, X. Wang, T. Moeller, D. Bernsmeier, J. Rossmeisl, F. Jaouen, P. Strasser, Activity–Selectivity Trends in the Electrochemical Production of Hydrogen Peroxide over Single-Site Metal–Nitrogen–Carbon Catalysts, J. Am. Chem. Soc. 141 (2019) 12372–12381. https://doi.org/10.1021/jacs.9b05576.
[106] E. Luo, H. Zhang, X. Wang, L. Gao, L. Gong, T. Zhao, Z. Jin, J. Ge, Single-Atom Cr À N 4 Sites Designed for Durable Oxygen Reduction Catalysis in Acid Media, 230026 (2019) 12469–12475. https://doi.org/10.1002/anie.201906289.
[107] J. Gao, H. bin Yang, X. Huang, S.-F. Hung, W. Cai, C. Jia, S. Miao, H.M. Chen, X. Yang, Y. Huang, T. Zhang, B. Liu, Enabling Direct H2O2 Production in Acidic Media through Rational Design of Transition Metal Single Atom Catalyst, Chem. 6 (2020) 658–674. https://doi.org/10.1016/j.chempr.2019.12.008.
[108] H. Shang, X. Zhou, J. Dong, A. Li, X. Zhao, Q. Liu, Y. Lin, J. Pei, Z. Li, Z. Jiang, D. Zhou, L. Zheng, Y. Wang, J. Zhou, Z. Yang, R. Cao, R. Sarangi, T. Sun, X. Yang, X. Zheng, W. Yan, Z. Zhuang, J. Li, W. Chen, D. Wang, J. Zhang, Y. Li, Engineering unsymmetrically coordinated Cu-S1N3 single atom sites with enhanced oxygen reduction activity, Nat. Commun. 11 (2020) 1–12. https://doi.org/10.1038/s41467-020-16848-8.
[109] Q. Wang, T. Ina, W. Chen, L. Shang, F. Sun, S. Wei, D. Sun-waterhouse, S.G. Telfer, T. Zhang,

G.I.N. Waterhouse, Evolution of Zn (II) single atom catalyst sites during the pyrolysis-induced transformation of ZIF-8 to N-doped carbons, Sci. Bull. 65 (2020) 1743–1751. https://doi.org/10.1016/j.scib.2020.06.020.
[110] J. Li, S. Chen, N. Yang, M. Deng, S. Ibraheem, J. Deng, J. Li, Oxygen Reduction Reaction Hot Paper Ultrahigh-Loading Zinc Single-Atom Catalyst for Highly Efficient Oxygen Reduction in Both Acidic and Alkaline Media Angewandte, (2019) 7035–7039. https://doi.org/10.1002/anie.201902109.
[111] S.H. Lee, J. Kim, D.Y. Chung, J.M. Yoo, H.S. Lee, M.J. Kim, B.S. Mun, S.G. Kwon, Y.E. Sung, T. Hyeon, Design Principle of Fe-N-C Electrocatalysts: How to Optimize Multimodal Porous Structures?, J. Am. Chem. Soc. 141 (2019) 2035–2045. https://doi.org/10.1021/jacs.8b11129.
[112] Z. Shi, W. Yang, Y. Gu, T. Liao, Z. Sun, Metal-Nitrogen-Doped Carbon Materials as Highly Efficient Catalysts: Progress and Rational Design, Adv. Sci. 7 (2020) 2001069. https://doi.org/10.1002/advs.202001069.
[113] V. Perazzolo, C. Durante, R. Pilot, A. Paduano, J. Zheng, G.A. Rizzi, A. Martucci, G. Granozzi, A. Gennaro, Nitrogen and sulfur doped mesoporous carbon as metal-free electrocatalysts for the in situ production of hydrogen peroxide, Carbon. 95 (2015) 949–963. https://doi.org/10.1016/j.carbon.2015.09.002.
[114] Y.N. Sun, M.L. Zhang, L. Zhao, Z.Y. Sui, Z.Y. Sun, B.H. Han, A N, P Dual-Doped Carbon with High Porosity as an Advanced Metal-Free Oxygen Reduction Catalyst, Adv. Mater. Interfaces. 6 (2019) 1–9. https://doi.org/10.1002/admi.201900592.
[115] G. Daniel, M. Mazzucato, R. Brandiele, L. De Lazzari, D. Badocco, P. Pastore, T. Kosmala, G. Granozzi, C. Durante, Sulfur Doping versus Hierarchical Pore Structure: The Dominating Effect on the Fe-N-C Site Density, Activity, and Selectivity in Oxygen Reduction Reaction Electrocatalysis, ACS Appl. Mater. Interfaces. (2021). https://doi.org/10.1021/acsami.1c09659.
[116] Z. Lu, Z. Li, S. Huang, J. Wang, R. Qi, H. Zhao, Q. Wang, Y. Zhao, Construction of 3D carbon network with N,B,F-tridoping for efficient oxygen reduction reaction electrocatalysis and high performance zinc air battery, Appl. Surf. Sci. 507 (2020) 145154. https://doi.org/10.1016/j.apsusc.2019.145154.
[117] D. Kim, G. Kim, S. Oh, J. Park, S. Lee, S. Yoon, J. Lee, W. Lee, T.Y. Jeon, E. Cho, K. Sohn, D.K. Yang, J. Kim, Dual-Doping of Sulfur on Mesoporous Carbon as a Cathode for the Oxygen Reduction Reaction and Lithium-Sulfur Batteries, ACS Sustain. Chem. Eng. 8 (2020) 8537–8548. https://doi.org/10.1021/acssuschemeng.0c00628.
[118] G. Chao, L. Zhang, D. Wang, S. Chen, H. Guo, K. Xu, W. Fan, T. Liu, Activation of graphitic nitrogen sites for boosting oxygen reduction, Carbon. 159 (2020) 611–616. https://doi.org/10.1016/j.carbon.2019.12.052.
[119] Y. Mun, S. Lee, K. Kim, S. Kim, S. Lee, J.W. Han, J. Lee, Versatile Strategy for Tuning ORR Activity of a Single Fe-N 4 Site by Controlling Electron-Withdrawing/Donating Properties of a Carbon Plane, J. Am. Chem. Soc. 141 (2019) 6254–6262. https://doi.org/10.1021/jacs.8b13543.
[120] H. Shen, E. Gracia-Espino, J. Ma, K. Zang, J. Luo, L. Wang, S. Gao, X. Mamat, G. Hu, T. Wagberg, S. Guo, Synergistic Effects between Atomically Dispersed Fe–N–C and C–S–C for the Oxygen Reduction Reaction in Acidic Media, Angew. Chemie - Int. Ed. 56 (2017) 13800–13804. https://doi.org/10.1002/anie.201706602.
[121] F. Luo, S. Wagner, I. Onishi, S. Selve, S. Li, W. Ju, H. Wang, J. Steinberg, A. Thomas, U.I. Kramm, P. Strasser, Surface site density and utilization of platinum group metal (PGM)-free Fe–NC and FeNi–NC electrocatalysts for the oxygen reduction reaction, Chem. Sci. 12 (2021) 384–396. https://doi.org/10.1039/D0SC03280H.
[122] N.R. Sahraie, U.I. Kramm, J. Steinberg, Y. Zhang, A. Thomas, T. Reier, J.-P. Paraknowitsch, P. Strasser, Quantifying the density and utilization of active sites in non-precious metal oxygen electroreduction catalysts, Nat. Commun. 6 (2015) 8618. https://doi.org/10.1038/ncomms9618.

[123] F. Luo, A. Roy, L. Silvioli, D.A. Cullen, A. Zitolo, M.T. Sougrati, I.C. Oguz, T. Mineva, D. Teschner, S. Wagner, J. Wen, F. Dionigi, U.I. Kramm, J. Rossmeisl, F. Jaouen, P. Strasser, P-block single-metal-site tin/nitrogen-doped carbon fuel cell cathode catalyst for oxygen reduction reaction, Nat. Mater. (2020) 1–9. https://doi.org/10.1038/s41563-020-0717-5.
[124] J. Li, J. Chen, H. Wan, J. Xiao, Y. Tang, M. Liu, H. Wang, Boosting oxygen reduction activity of Fe-N-C by partial copper substitution to iron in Al-air batteries, Appl. Catal. B Environ. 242 (2019) 209–217. https://doi.org/10.1016/j.apcatb.2018.09.044.
[125] S. Guo, J. Hu, S. Luo, Y. Zhang, Z. Zhang, P. Dong, X. Zeng, M. Xu, L. Han, J. Yuan, C. Zhang, Y. Zhang, Zr enhanced Fe, N, S co-doped carbon-based catalyst for high-efficiency oxygen reduction reaction, Int. J. Hydrogen Energy. 47 (2022) 8348–8358. https://doi.org/10.1016/j.ijhydene.2021.12.209.
[126] H. Zhong, L. Duan, P. Ye, X. Li, A. Xu, Q. Peng, Synthesis of cobalt–nitrogen-doped mesoporous carbon from chitosan and its performance for pollutant degradation as Fenton-like catalysts, Res. Chem. Intermed. 45 (2019) 907–918. https://doi.org/10.1007/s11164-018-3655-y.
[127] A. Zitolo, N. Ranjbar-Sahraie, T. Mineva, J. Li, Q. Jia, S. Stamatin, G.F. Harrington, S.M. Lyth, P. Krtil, S. Mukerjee, E. Fonda, F. Jaouen, Identification of catalytic sites in cobalt-nitrogen-carbon materials for the oxygen reduction reaction, Nat. Commun. 8 (2017). https://doi.org/\.
[128] W. Ju, A. Bagger, G.P. Hao, A.S. Varela, I. Sinev, V. Bon, B. Roldan Cuenya, S. Kaskel, J. Rossmeisl, P. Strasser, Understanding activity and selectivity of metal-nitrogen-doped carbon catalysts for electrochemical reduction of CO2, Nat. Commun. 8 (2017) 1–9. https://doi.org/10.1038/s41467-017-01035-z.
[129] X.M. Hu, S.U. Pedersen, K. Daasbjerg, Supported molecular catalysts for the heterogeneous CO2 electroreduction, Curr. Opin. Electrochem. 15 (2019) 148–154. https://doi.org/10.1016/j.coelec.2019.05.006.
[130] M.L. Pegis, B.A. McKeown, N. Kumar, K. Lang, D.J. Wasylenko, X.P. Zhang, S. Raugei, J.M. Mayer, Homogenous Electrocatalytic Oxygen Reduction Rates Correlate with Reaction Overpotential in Acidic Organic Solutions, ACS Cent. Sci. 2 (2016) 850–856. https://doi.org/10.1021/acscentsci.6b00261.
[131] S. Sinha, R. Zhang, J.J. Warren, Low Overpotential CO2Activation by a Graphite-Adsorbed Cobalt Porphyrin, ACS Catal. 10 (2020) 12284–12291. https://doi.org/10.1021/acscatal.0c01367.
[132] A. Genoni, D.N. Chirdon, M. Boniolo, A. Sartorel, S. Bernhard, M. Bonchio, Tuning Iridium Photocatalysts and Light Irradiation for Enhanced CO2 Reduction, ACS Catal. 7 (2017) 154–160. https://doi.org/10.1021/acscatal.6b03227.
[133] U.I. Kramm, I. Herrmann-Geppert, J. Behrends, K. Lips, S. Fiechter, P. Bogdanoff, On an Easy Way To Prepare Metal–Nitrogen Doped Carbon with Exclusive Presence of MeN 4 -type Sites Active for the ORR, J. Am. Chem. Soc. 138 (2016) 635–640. https://doi.org/10.1021/jacs.5b11015.
[134] S. Samad, K.S. Loh, W.Y. Wong, W. Sudarsono, T.K. Lee, W.R. Wan Daud, Effect of various Fe/Co ratios and annealing temperatures on a Fe/Co catalyst supported with nitrogen-doped reduced graphene oxide towards the oxygen reduction reaction, J. Alloys Compd. 816 (2020) 152573. https://doi.org/10.1016/j.jallcom.2019.152573.
[135] S. Yuan, L. Cui, Z. Dou, X. Ge, X. He, W. Zhang, T. Asefa, Nonprecious Bimetallic Sites Coordinated on N-Doped Carbons with Efficient and Durable Catalytic Activity for Oxygen Reduction, Small. 16 (2020) 2000742. https://doi.org/10.1002/smll.202000742.
[136] E. Negro, A. Bach Delpeuch, K. Vezzù, G. Nawn, F. Bertasi, A. Ansaldo, V. Pellegrini, B. Dembinska, S. Zoladek, K. Miecznikowski, I.A. Rutkowska, M. Skunik-Nuckowska, P.J. Kulesza, F. Bonaccorso, V. Di Noto, Toward Pt-Free Anion-Exchange Membrane Fuel Cells: Fe-Sn Carbon Nitride-Graphene Core-Shell Electrocatalysts for the Oxygen Reduction Reaction, Chem. Mater. 30 (2018) 2651–2659. https://doi.org/10.1021/acs.chemmater.7b05323.

[137] X. Zhang, J. Liu, Y. Qiao, A. Kong, R. Li, Y. Shan, Fe-boosting Sn-based dual-shell nanostructures from new covalent porphyrin frameworks as efficient electrocatalysts for oxygen reduction and zinc-air batteries, Electrochim. Acta. 320 (2019) 134593. https://doi.org/10.1016/j.electacta.2019.134593.

2. Experimental technique

This chapter presents very briefly the investigation techniques and tools used in the thesis project. The chapter is divided into two sections, the first is dedicated to the theoretical and practical aspects of physico-chemical characterization techniques; the second, on the other hand, is dedicated to the theoretical and practical aspects of electrochemical techniques for the investigation of the catalytic activity of synthesized materials.

2.1. Physical chemical

2.1.1. Elemental Analysis

Elemental analyses were carried out on a Flash 2000 analyser (Thermo Scientific) schematize in Figure 2.1. This technique allow a screening of bulk content of nitrogen, hydrogen, carbon, and sulphur on the sample. The instrument is calibrated using the 2,5-Bis(5-tert-butyl-benzoxazol-2-yl)thiophene as standard. The sample is weighted on a tin cell with V_2O_5 that serve as catalyst for the following combustion where both the sample and the cell are burned.

The instrument is equipped with a CuO/Cu column which is heated to favour the combustion reaction, the element of interest, namely H, C, N and S produce respectively H_2O, CO_2, NO_X, and SO_X. Helium is used as carrier to drive the product through the column, when the gas reach the Copper section are reduced to SO_2, CO_2, H_2O and N_2, in particular to form the molecular nitrogen by removing the oxygen [1]. Then those gases reach a molecular exclusion chromatographic column bridged to a thermal coupled detector (TCD). The peak response are compared to the standard and the amount of C, H, N and S are obtained as peak area ratio.

Applied to carbon-based materials this technique is very useful to have a fast screening of doping successful or contamination. The first aspect regard the doping of carbonaceous material with nitrogen or sulfur, which fundamental in this field. The other aspects is about contamination of carbon, generally from sulphur in production plant or from other species not detected by the technique, this are mainly oxygen or element like Al, Si, Ca, Mg in the case of hard templating approach in carbon synthesis.

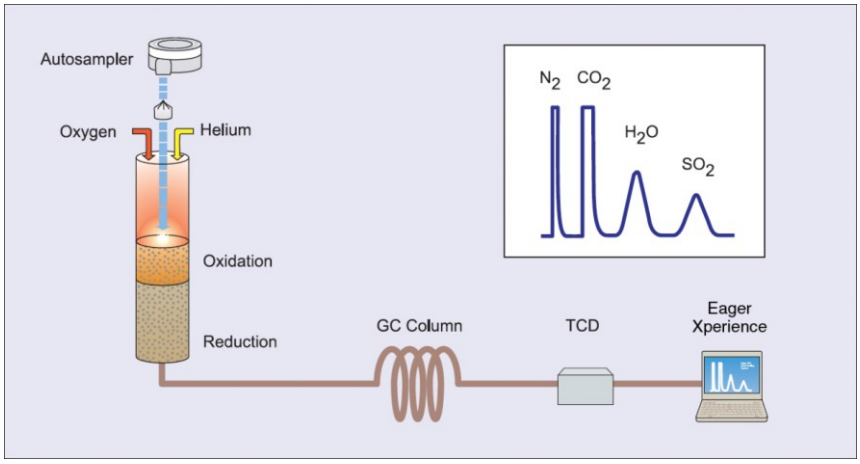

Figure 2.1. Scheme of CHNS analyser with an example of measurable signal [2]

2.1.2. Raman

Raman spectroscopy is one of the principal techniques in the field of vibration spectroscopy together with infrared. This exploits the phenomenon of inelastic diffusion of photons, called Raman diffusion. Whenever light (electromagnetic radiation) interact with a medium, many phenomena can occur. Leaving out the phenomena of absorption and other emissive phenomena (such as spontaneous emission), the phenomenon of diffusion occurs and consists in an emission of the incident light in directions other than that of propagation. If the incident radiation is monochromatic (frequency ν_L) like that of a laser and the scattered radiation is observed at a certain angle, two new components can be identified: one with a higher frequency than the incident one and one with a lower frequency deriving from processes inelastic. The first component is called Anti-Stokes, the second is called Stokes (Figure 2.2). In any case, most of the outgoing photons have the same frequency as the incident ones (Rayleigh elastic diffusion), only one photon in a million undergoes an inelastic process which leads to a change in frequency.

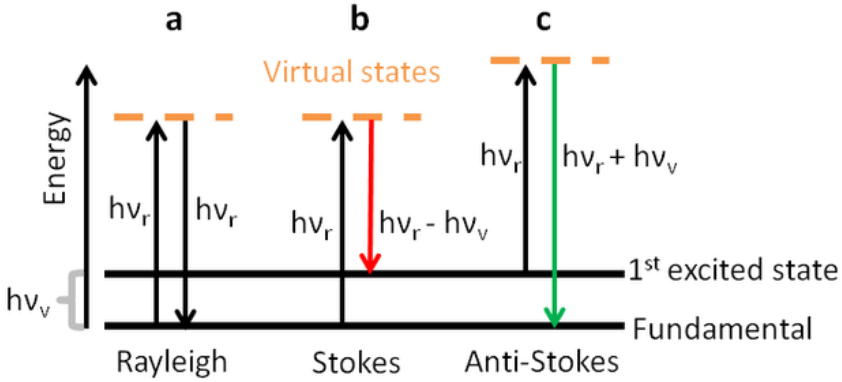

Figure 2.2. Diffusion phenomena: a) elastic scattering, namely Rayleigh scattering; b) and c) anelastic scattering, Stocks and Anti-Stokes [3]

In the context of Raman spectroscopy, a spectrum is generally presented as a function of a quantity called Raman Shift ($\Delta\tilde{\nu}$) which allows the position of the peaks to be in principle independent from the laser frequency and which allows, with attention, to compare spectra obtained with different excitations (the frequency however plays a role in the aspect of the spectrum as the wavelength varies, the intensity of diffusion varies, there may be fluorescence phenomena, etc. [4–6]). The Raman shift expression is reported in equation 2.1.

$$\Delta\tilde{\nu} = \tilde{\nu}_L - \tilde{\nu}_S = \frac{1}{\lambda_L} - \frac{1}{\lambda_S} \qquad (2.1)$$

where $\tilde{\nu}$ = wave number; λ=wavelength; subscript stays for L=laser, S=scattered

In practice the position of Raman peaks are a fingerprint of a certain material.

Going into much detail for the material characterized in this thesis one should stressed out that for carbonaceous material this characterization is not straightforward, since very broad and overlapped signal are recorded. In practice the information that could be obtained are about graphitization/crystallinity of graphitic domain.

Carbonaceous materials are generally characterized by a mixture of sp^3, sp^2 and sp^1 carbon and the physical properties of that depend on the ratio between those. Diamond has a structure with sp^3 carbons, but there are many forms of sp^2 carbon with varying degrees of graphitic order, from nanocrystalline graphite to glassy carbon. In general, an amorphous carbon has a mixture of sp^3, sp^2 and even sp^1 sites. For example, diamond-like carbon (DLC) has an intermediate fraction of sp^3 carbon; hydrogenated amorphous carbon (a-C: H) has a rather low content of sp^3 and tetrahedral

amorphous carbon (ta-C) has a high content of sp^3 carbon. The ternary diagram shown in Figure 2.3 shows the various phases of the carbonaceous materials also as a function of the hydrogen content, one passes from carbonaceous materials to polymers going from left to right.

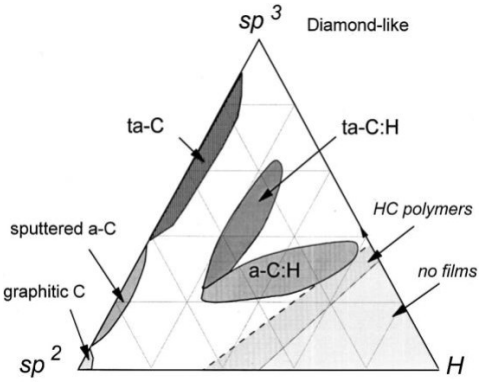

Figure 2.3. Phase diagram of carbon as a function of sp^2, sp^3 and hydrogen content [5]

The diagram shown (Figure 2.3) above does not give a complete description of the carbonaceous material, especially in the catalytic field, it is in fact useful to consider the degree of clustering of the sp^2 phase, the amorphous carbonaceous materials with the same content of sp^3 and H show, in fact, different electronic optical properties and mechanics as a function of the clustering of the sp^2 phase. The spectrum of a Raman analysis, which provides for the excitation of the π states of the atoms and therefore of sites in sp^2 configuration, is therefore influenced by the degree of order and aggregation of these sites, and only indirectly by the sp^3 sites. These parameters are obtained by analysing the position, intensity, and width of the predominant bands G and D1 (D in Figure 2.4), generate from the vibrational mode of graphite. The G band of graphite is located in the range 1580–1600 cm^{-1} and is due to the vibrational mode of stretching in the plane of the pairs of carbon atoms with sp^2 hybridization. Band D1 is instead located at 1350 cm^{-1} and competes with the vibrational breathing mode of the aromatic ring, this is visible only in the presence of defects, or in materials with sp^3 carbon atoms or heteroatoms in the graphitic plane (Figure 2.4 on the left).

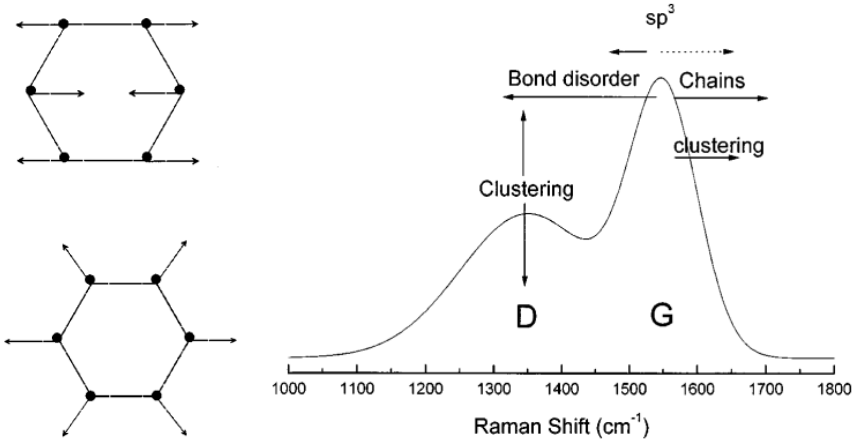

Figure 2.4. Vibration modes of the D and G bands and relative position in Raman shift [5,6]

There are also other minor bands that make up the spectrum in the 1100-1700 cm^{-1} region and which are necessary for a good deconvolution of the spectrum, Table 2.1 summarizes the bands and their vibrational mode as reported by Sadezky et al. and which are used in all the deconvolutions that will be shown [8,9,10,11].

Table 2.1. Vibrational mode of carbonaceous material used for deconvolution

Band	Raman shift (cm^{-1})			Vibrational mode
	Soot	Disordered graphite	Highly oriented graphite	
G	~1580 cm^{-1}	~1580 cm^{-1}	~1580 cm^{-1}	Graphite ideal lattice (E_{2g})
D1	~1350 cm^{-1}	~1350 cm^{-1}	-	Disordered lattice (A_{1g}) : edge
D2	~1620 cm^{-1}	~1620 cm^{-1}	-	Disordered lattice (E_{2g}) : surface
D3	~1500 cm^{-1}	-	-	Amorphous carbon
D4	~1200 cm^{-1}	-	-	Disordered lattice (A_{1g}) : polyenes and ionic impurities

In addition to the position of the band, also the intensity or the area are useful for gain more information. Ferrari et al. [5] have proposed a model to evaluate the degree of graphitization using three parameters:

- The radio between D1 and G band: I_{D1}/I_G;
- The Raman shift value of D1 e G;
- The full width at half maximum of G band (FWHM).

The model defines an amorphization trajectory which is described in Figure 2.5 and is divided into three stages. In the first stage, the introduction of grain boundaries into the defect-free graphite can be translated as the appearance of graphite nanocrystallites, and the vibrational mode D1 begins to be observed. The I_{D1} / I_G ratio increases as the G-band position shifts to higher Raman shifts, from 1581 cm^{-1} to 1600 cm^{-1}. In this first stage, the size of the nanocrystallites follows the equation identified by Tuinstra and Koenig (T-K). The two researchers observed the inverse proportionality between the ratio of the intensities of the two I_{D1} / I_G bands with the size of the graphite crystallites along the crystallographic axis (L_a). In the second stage we pass from graphite nanocrystallites to amorphous carbon, the sp^3 hybrid carbon content increases. The greatest effects on the Raman spectrum are the position of the G band which returns again towards 1580 cm^{-1} and then moves up to 1510 cm^{-1}. The width of the G band increases, and the I_{D1} / I_G ratio decreases in response to the decrease in the number of aromatic rings. In this case, for graphite nanocrystallites with a diameter of less than 2nm, the T-K equation follows a new quadratic trend as shown in Figure 2.5. At the third stage the carbon content with sp^3 hybridization increases from 20% to 85% while the aromatic rings are replaced by olefin chains. Peak G translates from 1510 cm^{-1} to 1570 cm^{-1} and the I_{D1} / I_G ratio is low or zero.

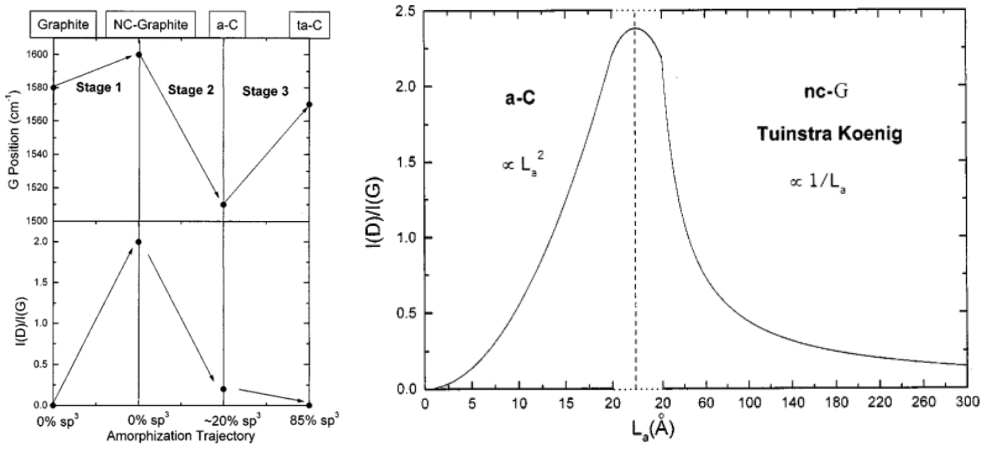

Figure 2.5. Stages of amorphization and crystallite size as a function of the I_{D1}/I_G ratio [5,6]

In the Raman spectra of carbonaceous materials, a series of bands are then observed in the region 2300-3300 cm^{-1}, according to Cuesta at al. [8] are due to overtones and combinations of the vibrational modes of graphite. The two peaks at 2700 cm^{-1} and 2900 cm^{-1} are assignable to the overtone of the D1 (2D) band and to the combination G + D1 or as other groups affirm to the combination D1 + D2 [8–10]. Additional shoulders at 3100 cm^{-1} and 2400 cm^{-1} can be assigned to the overtones of bands D2 and D4, respectively, and are difficult to identify for materials with little graphitization. Generally, for materials such as carbon blacks, two distinct bands similar to those of graphene oxide are observed, for this reason they are often called graphene oxide bands. The proposed structural model for oxidized graphite consists of graphene oxide sheets characterized by two types of regions: aromatic regions with non-oxidized benzene rings and regions containing C-OH, epoxide and double bonds, the relative size of the two regions depends on the degree of oxidation. It is therefore these defects, also present in carbon blacks, that determine a similarity of the spectrum [11]. In addition to what Ferrari has shown, Santangelo et al. they also define that the degree of long-range ordering can be obtained from the intensity ratio between the 2D band and the G band and that a good parameter to evaluate graphitization is in general the intensity ratio between the 2D band and the D1 band [12]. To make comparisons, all spectra must be normalized with respect to the intensity measured at 1600 cm^{-1}, or in general with respect to the Raman shift itself. So practically in this thesis all this thing have been taking into account to gain information about the properties of carbon support and catalysts.

2.1.3. XRD

One of the most used methodologies for the study of crystalline structures is X-ray diffraction. When a radiation beam is made to affect a crystal, a vibration of the electrons is induced at the same frequency as the radiation, these act as a new source of radiation (diffusion) and there are particular directions in which the various waves produced constructive interference giving the phenomenon of diffraction. The directions of diffusion of the radiation depend on the spatial arrangement of the atoms and therefore on the crystalline structure of the material. Each atom can be imagined as a source of photons (spherical waves) and for a series of equidistant atoms it is possible that the waves are in phase (as shown in Figure 2.6).

There are two theories, the kinematic and the dynamic one, the first applies to powders and polycrystals, the second is used for single crystals and for the simulation of spectra. Since only powder analyses will be done, only the first will be briefly explained. The kinematic theory of diffraction considers only the radiation diffused in an elastic manner, that is, only the diffused radiation with a wavelength coinciding with the wavelength of the incident radiation and excludes

phenomena of absorption and inelastic diffusion. In accordance with the kinematic theory of diffraction, the constructive interference of radiation is allowed thanks to three requirements:

- the atoms are arranged according to a periodic or crystalline order.
- the wavelength of electromagnetic radiation is of the same order of magnitude as the interatomic distances (0.1 - 100 Å).
- the radiation is diffused with an angle coinciding with the angle of the incident radiation (reflection condition of the Ewald sphere).

Considering two electromagnetic waves that propagate along the parallel directions, S_0 and S_0', we have that these form an angle of incidence ϑ with the family of crystalline planes with indices (hkl) and distant d, the electromagnetic waves are therefore reflected (diffused) along the new directions S and S '. The two waves are separated by an optical path difference equal to 2d · sin (ϑ) and are in phase, therefore they generate a measurable signal, only if the optical path difference is a multiple of the wavelength. Therefore, once a certain atomic plane has been identified, a signal is observed when condition 2.2 holds:

$$2dsen\theta = n\lambda \qquad (2.2)$$

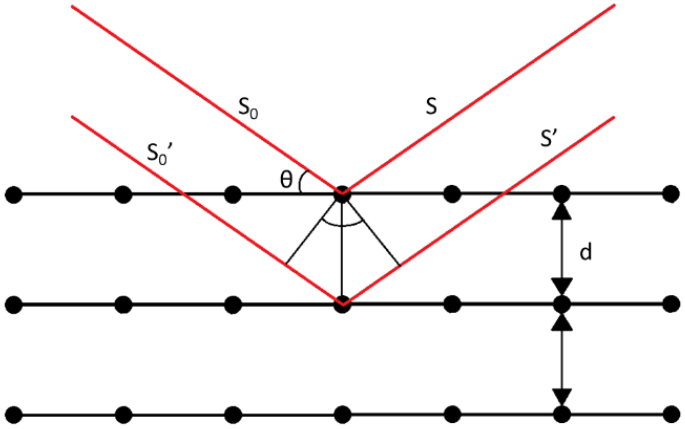

Figure 2.6. Schematization of a bidimensional crystal. In red the incident radiation and its reflection in cinematic condition

To meet the refraction conditions of the different crystallographic planes, the angle ϑ is changed and a rotation is applied on the sample to minimize any effects of preferential orientation of the crystals. From the position of the peaks, it is possible to determine the symmetry of the sample, while the analysis of the width at half height and the intensity of each individual peak provides information on the physical properties of the crystal, in particular on the size of the crystallites. The XRD analysis on powders were performed with a Bruker AXS D8 ADVANCE Plus diffractometer.
The information that could be obtained in the case of carbonaceous material are again about the degree of crystalline domain extension, linked with graphitization degree. Two characteristic band appear at around 25° and 45° respectively linked to (002) and (100) planes which became broader when crystalline domain became smaller, which generally what is observed for carbon black-like material. Another useful information, talking about Fe-N-C materials, is the residual of iron or iron carbide in the material, which gives characteristic signal Figure 2.7.

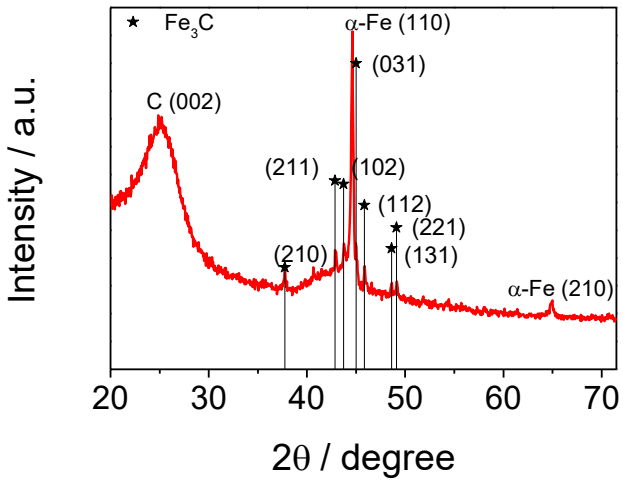

Figure 2.7. XRD of non-acid leached Fe-N-C, the inorganic residual are evident

2.1.4. N_2 physisorption

One of the fundamental characteristics for a good catalyst is to have a porous structure with a high surface area that allows an easy diffusion of the reactants towards the active sites and the removal of the products. The analysis of the surface area as well as the volume of pores and their distribution in size can be obtained from adsorption / desorption measurements of N_2 at 77 K (therefore in isothermal conditions). The measurements were carried out on ASAP 2020 Plus instrumentation (Micrometrics).

In the next paragraphs a description of the technique is given referring to the 2015 IUPAC Technical Report by Thommes et al. [13].

In general, adsorption is an enrichment of molecules or atoms in the vicinity of an interface, the material that is adsorbed is called adsorbate, while the material itself in the vapor phase is called adsorbent. Adsorption can be divided into physisorption, in which the molecules interact by intermolecular forces, and chemisorption in which chemical bonds are formed. The reverse process is instead called desorption and does not always occur in a similar and opposite way to adsorption, so the measured curves (Figure 2.9) may have hysteresis (Figure 2.10).

The surface of a material is not easily definable. At the atomic scale we speak of the Van der Waals surface, or the area formed by the outer part of the van der Waals spheres of the surface atoms (1). The second surface (2), the one evaluated by physisorption, does not coincide with the van der Waals surface. This surface is known as the Connolly surface (3) and is defined as the surface drawn from the bottom of a spherical probe molecule rolling on the van der Waals surface. The surface 'r' is located at the distance r from the Connolly surface (Figure 2.8).

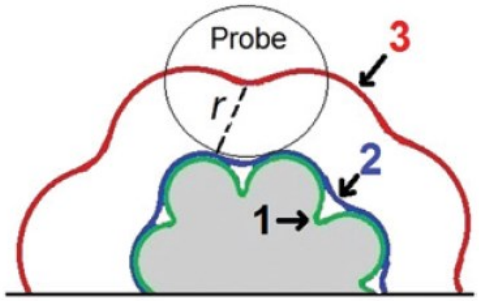

Figure 2.8. Material surfaces: 1) Van der Waals surface, 2) Connolly surface and 3) 'r' surface

In the case of porous adsorbents, i.e., for most of the materials that are analysed with this technique, the surface can be further divided into external and internal surface, but with two different meanings: in the general case the external surface is defined as the surface outside from pores, while the inner surface is the surface of all pore walls; in the presence of microporosity, on the other hand, the external surface is defined as a non-microporous surface. By convention, pores are divided by size:

- Micropore: dim < 2 nm
- Mesopore: 2 nm < dim < 50 nm
- Macropore: dim >50 nm

In practice, the quantity of adsorbed gas is measured (preferably in mol g^{-1}) and the isotherm is plotted with respect to the relative equilibrium pressure (p / p^0), where p^0 is the saturation pressure of the pure adsorbent at the operating temperature, and p is the system pressure.
Before determining an adsorption isotherm, it is necessary to remove all physiosorbed species on the surface of the adsorbent, avoiding irreversible damage to the surface or solid structure. This is achieved by degassing that is a procedure that involves exposing the material to a high vacuum (for microporous materials, pressures < 1 Pa are preferable) at high temperatures (200-300 °C), considering the temperatures of degradation of the samples, for a time up to 24 hours, especially if the temperature cannot be too high. This operation is done after weighing and transferring the material to be analysed into a glass vial equipped with a cap with a membrane that allows to create a vacuum and insert gas. The cruet itself will then be used to make the actual measurement.

Adsorption / desorption isotherms
As anticipated, the adsorption and desorption curves do not always coincide, plus there are different forms of isotherm classified by the IUPAC [13] as follows and as shown in Figure 2.9:

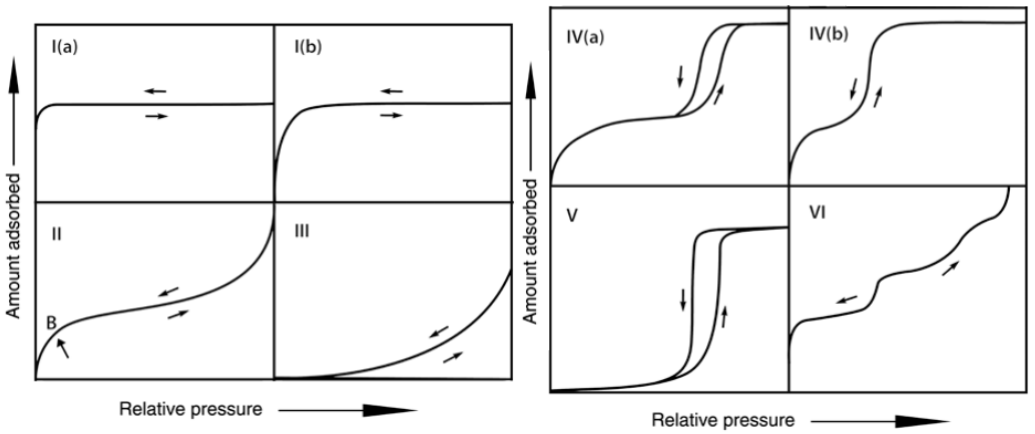

Figure 2.9. Physisorption isotherm as classified by IUPAC [13]

Type I reversible isotherms are given by microporous solids having relatively small external surfaces (e.g., some activated carbons, zeolites, and some porous oxides). A Type I isotherm is concave with respect to the p / p^0 axis, and the adsorbed quantity approaches a limit value. Type I (a) isotherms are given by microporous materials having mostly narrow micropores (width <1 nm), while Type I (b) isotherms are obtained from materials with wider pore size distribution, including larger micropores and / or small mesopores (<2.5 nm). Type II reversible isotherms are given by the physisorption of most of the gases on non-porous or macroporous adsorbents. The shape is the result of a

monolayer-multilayer adsorption up to a high p / p^0. If the shoulder is well defined at point B, the near-linear centre section usually corresponds to the completion of a monolayer, while a more gradual curvature is an indication of monolayer overlap and the formation of multilayer adsorption.
In the case of a Type III isotherm there is no Point B and the formation of the monolayer is not identifiable; adsorbent-adsorbent interactions are relatively weak and the adsorbed molecules are clustered around the most favourable sites on the surface of non-porous or macroporous solids.
Type IV isotherms are given by mesoporous adsorbents (for example gels and mesoporous molecular sieves), in this case the monolayer-multilayer adsorption begins on the mesopore walls, as in the Type II isotherm, which is followed by capillary condensation or the phenomenon whereby a gas condenses into a liquid phase in a pore at a pressure lower than the saturation pressure p^0 of the liquid. A typical feature of Type IV isotherms is a final saturation plateau of varying length. In the case of a Type IV (a) isotherm, capillary condensation is accompanied by hysteresis, and this occurs when the pore width exceeds a certain critical width that depends on the adsorption system and the temperature (for example, for the adsorption of nitrogen and argon in cylindrical pores at 77 K and 87 K, respectively, hysteresis starts to occur for pores larger than 4 nm). On the other hand, with adsorbents having mesopores of smaller width, completely reversible Type IV (b) isotherms are observed.
Type V isotherms are very similar to Type III at low p / p^0, while at higher p / p^0 molecular clustering is followed by pore filling. For example, Type V isotherms are observed for the adsorption of water on micro and mesoporous hydrophobic adsorbents.
Type VI reversible isotherm is representative of layer-by-layer adsorption on a highly uniform non-porous surface. The step height represents the capacity for each adsorbed layer, while the step sharpness depends on the system and the temperature. Among the best examples of Type VI isotherms are those obtained from highly graphitized carbon-black.

Hysteresis
As anticipated, isotherms can have hysteresis resulting from metastable adsorption or from effects due to the distribution of pores in the matrix. Figure 2.10 shows the main forms that can be observed.

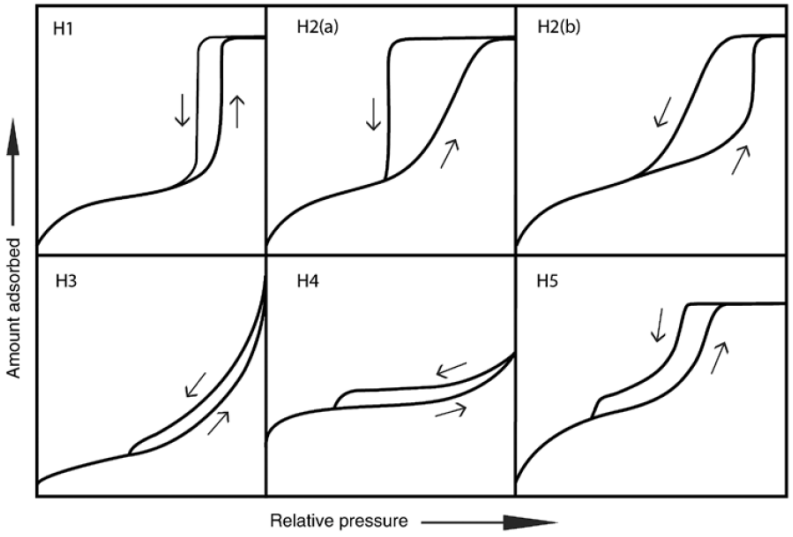

Figure 2.10. Possible hysteresis cycle in the physisorption isotherm as classified by IUPAC [13]

The Type H1 cycle (Figure 2.10) is found in materials that have uniform mesopores, such as in silicas obtained from hard templates (MCM-41, MCM-48, SBA-15), from some glass with controlled pores and mesoporous carbons sorted. Type H2 hysteresis loops are given by more complex pore structures: H2 (a) is observed in many silica gels, some porous glasses (e.g. vycor) as well as some ordered mesoporous materials (e.g. SBA silicas -16 and KIT-5), while the H2 type cycle (b) is observed for some mesocellular silica foams; both cycles are due to pore blocking or percolation phenomena.
Type H3 cycles are given by non-rigid aggregates of lamellar particles (for example certain clays) but also by materials in which the network of pores consists of macropores that are not completely filled. Similar is the H4 cycle, but the adsorption branch is now a hybrid of Types I and II, the more pronounced adsorption at low p / p^0 is associated with the filling of micropores. H4 cycles are often found with aggregate crystals of zeolites, some mesoporous zeolites, and mesoporous carbons.
Although the Type H5 cycle is unusual, it is observed with certain structures containing both open and partially blocked mesopores (e.g., capped hexagonal silica).

Brunauer-Emmett-Teller Method (BET)

To evaluate the surface of porous materials, the BET method continues to be the most used procedure despite the weakness of its theoretical foundations. In fact, under certain carefully controlled conditions, the BET area of a non-porous, macroporous or mesoporous solid (i.e., a Type II or Type IV(a) isotherm), can be considered as an "area accessible by the probe" ((i.e., the effective area available for adsorption). It is customary to apply the BET equation 2.3 in the linear form to determine n_m (first step of the method):

$$\frac{p/p^\circ}{n(1-p/p^\circ)} = \frac{1}{n_m C} + \frac{C-1}{n_m C}(p/p^\circ) \qquad (2.3)$$

Where n is the specific quantity of adsorbent at the relative pressure p / p^0 and n_m and the specific capacity of a monolayer. According to BET theory, the parameter C is exponentially related to the adsorption energy of the monolayer, but it is now generally accepted that the value of C rather gives a useful indication of the shape of the isotherm in the BET interval. Therefore, if the value of C is at least 80, the shoulder of the isotherm is easily identifiable, and Point B (Figure 2.9 II) is quite defined. If C is low (<50) Point B cannot be well identified and therefore there is an overlap of single-layer and multi-layer adsorption, and the interpretation of n_m is not precise. When C < 2, the isotherm is Type III or Type V and the BET method is not applicable. A high C value> 150 is finally associated with adsorption in narrow micropores.
The linearity range of the BET diagram is always limited to a part of the isotherm, generally in the range p / p^0 from 0.05 to 0.30 for the Type II and Type IV (a) isotherms, which are also those observed for the materials analysed in this project for carbon black and mesoporous carbons respectively. The linear BET range is shifted at low pressures when the adsorption energy is high, especially if the surface is energetically homogeneous or crystalline (for example, for adsorption of nitrogen or argon on graphitized carbon or xenon on clean metal films).
The second step in applying the BET method is the calculation of the BET area (a_s) from the capacity of the monolayer (2.4). This requires a knowledge of the mean area, σ_m (molecular cross-sectional area), occupied by the adsorbate molecule in the complete monolayer.

$$a_s(\mathrm{BET}) = n_m \cdot L \cdot \sigma_m / m \qquad (2.4)$$

The BET method can be applied to many Type II and IV isotherms, but extreme caution is required in the presence of micropores (i.e., with Type I isotherms and combinations of types I and II or types I and IV isotherms). It may be impossible to separate the single-layer-multilayer adsorption and micropore filling processes, in fact with microporous adsorbents, the linear range of the BET plot can be very difficult to locate.
It is therefore good to emphasize that in the presence of a high percentage of micropores, the surface area value obtained is subject to a greater error due to the difficulty of identifying the linear region. For that reason, recently DFT method are coupled with BET method to evaluate surface area, those method will be presented later in the text (Pore size distribution section).
The pore volume (V_p) is derived from the quantity of adsorbed vapor at a relative pressure close to unity (for example at $p / p^0 = 0.95$), assuming that the pores are filled with the adsorbate in the liquid state, i.e., applying the rule by Gurvich. During the data processing of this project, it was decided to take the total volume at a relative pressure of 0.98.

Pore size distribution
The isotherm shape itself certainly gives information about the nature of material in term of pore dimension, but it is not indicative on the actual pore size distribution. DFT calculation are wildly used and allow also to calculate theoretical isotherm giving a material with a certain dimension of pore. By convolution of those it possible to fit the experimental data, therefore the weight of various theoretical isotherm used gives the pore size distribution. There are two methods that are used, based on different assumptions:

- The Non Local Density Functional Theory (NLDFT) uses a classical fluid density functional theory to construct the adsorption isotherms in ideal pore geometries (e.g., N_2 adsorption in the slit-pore model at 77 K)
- The Quenched Solid Density Functional Theory (QSDFT) which is based on similar approach but taking into account the morphological specifics.

For carbonaceous material, the second one is more indicated. With those methods also an evaluation of surface area (micropore and mesopore) could obtain as an alternative to BET.

2.1.5. XPS
XPS analysis where carried out on an ultra-high vacuum (UHV) chamber at a pressure of 5×10^{-10} mbar in the Department of Chemical Science of the University of Padova and at the university of Brescia by Dr. Tomasz Kosmala and Prof. Luca Gavioli respectively.
The XPS (X-Ray photoelectron spectroscopy) technique is a surface characterization technique (from a few nanometres to a few tens depending on the energy of the beam) in UHV based on the photoelectric effect. The electrons generated by the photoelectric effect are endowed with a kinetic energy (2.5) which according to the principle of energy conservation is:

$$E_k = hv - E_b - \phi_{spect} \qquad (2.5)$$

where E_k is the kinetic energy of the photoemitted electron following irradiation with photons of energy hv minus the E_b value of the binding energy of the electron in the atom, the energy term of the spectrometer derives from the experimental set-up. The sample and the spectrometer are grounded and consequently will have the same Fermi level:

$$E_k = hv - E_b - \phi_{sample} - (\phi_{spect} - \phi_{sample}) = hv - E_b - \phi_{spect}$$

The advantage of this setup is that the term ϕ_{spect} is more stable than the sample one. This energetic scheme is reported in Figure 2.11

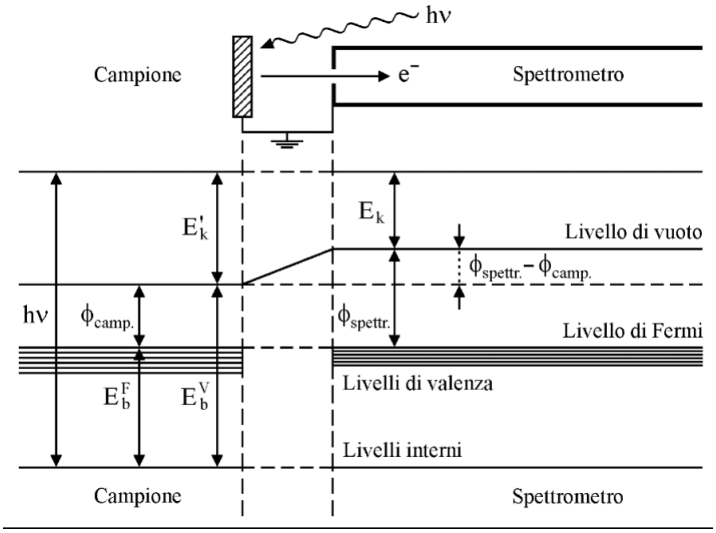

Figure 2.11. Energetic level scheme for a sample in a XPS device [14]

The X-ray sources used are metal anodes, typically Al and/or Mg, which are bombarded with high-energy electrons (~ 15 keV). The emission spectrum of the source consists of a characteristic line Kα, a background given by inelastic interactions (Bremsstrahlung radiation) and by other characteristic lines of lower intensity. For this reason, monochromators are used, such as Rowland's circle ones. The emission lines exploited are for Al the $K\alpha_1$ = 1486.6eV and for the Mg the $K\alpha_2$ = 1253.6eV. The use of two sources is generally due to the fact that electrons can also be emitted by the Auger effect, since this phenomenon does not depend on the intensity of the beam, the use of two sources allows to discriminate the peaks due to the photoelectric effect and those due to the Auger effect.
The electrons emitted after the interaction between radiation and matter are collected and collimated by means of electromagnetic lenses inside a hemispherical concentric hemispheric analyser (Figure 2.12) or concentric cylinders to determine the kinetic energy. Rearranging equation 5 we then go back to the binding energy and therefore to the information on the atom that emitted these electrons.

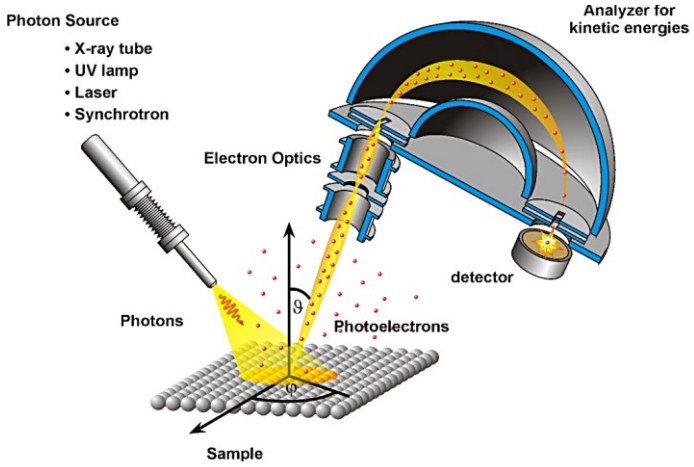

Figure 2.12. Scheme of XPS instrument (www.rowbo.info)

The spectrum obtained (an example is given in chapter 4), expressed as a function of the E_b binding energy, is characterized by:

- a series of elastic peaks, due to the photoelectrons emitted which reached the detector without exchanging energy with the system.
- a growing background towards major Eb, caused by inelastic processes.

For this thesis project we are interested in deriving the signals of O (1s), C (1s), S (2p), Fe ($2p^{3/2}$) and N (1s) to get an idea of the surface composition and deconvolution of the nitrogen peak to get information on the type of functional groups Fe-N and C-N that have formed.
For Nitrogen (Figure 2.13a) different component could be used to deconvolute the raw experimental data:

- Peak at 397.8 eV could be ascribed to Iminic N
- Peak at 388.8 eV could be ascribed to Pyridinic N
- Peak at 399.9 eV could be ascribed to N_x-Fe/amine
- Peak at 400.7 eV could be ascribed to Pyrrolic N
- Peak at 401.7 eV could be ascribed to Graphitic N
- Peak at 401.7 eV could be ascribed to Graphitic N

Even if is not easy to gain certain information, since the deconvolution with multiple peaks is tricky, this technique gives at least a qualitative information on surface functionalization. Also for carbon and Fe a deconvolution could be made (Figure 2.13b, c); information about sp^3, sp^2 content and on oxygen group could be obtain, while for iron the presence of metallic or oxidised iron centre could be discriminate.

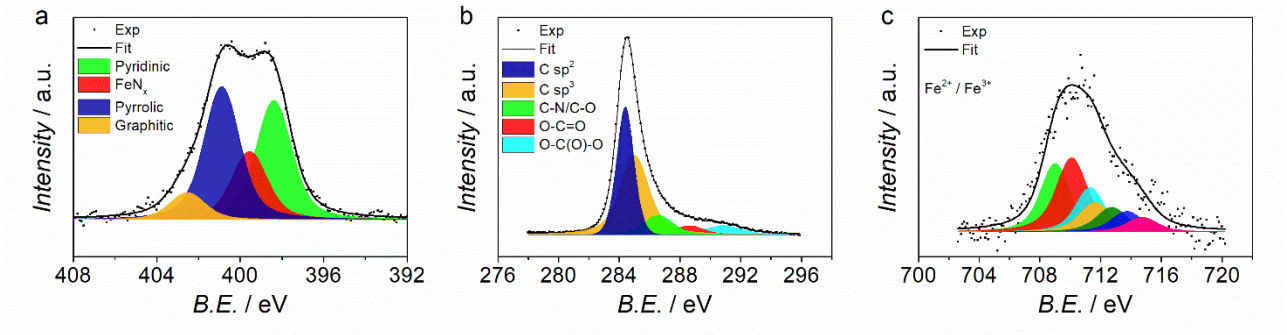

Figure 2.13. Deconvolution of a) N1s, b) C 1s and c) Fe 2p peaks

2.1.6. UV-Vis

UV-Vis spectroscopy is a widely used characterization technique for organic or metalorganic molecules that exhibit absorptions in the visible region (for example dyes), in UV and sometimes in the near IR (NIR). It is a useful technique when synthesizing metal complexes characterized by metal-ligand transitions that allow them to be discriminated from the species used for the synthesis, i.e., the reactants.
In UV-Vis measurements the electronic transitions of molecules are studied, the ultraviolet or visible radiation incident on the material is absorbed by a molecule that passes from its fundamental electronic state to an excited electronic state.

In practice, the intensity of the radiation transmitted by the sample (I_{sample}) is measured and compared to that transmitted (I_{ref}) by a solution containing only the solvent (reference) to calculate the transmittance (2.6) from which it is then possible to obtain the absorbance (2.7).

$$T = \frac{I_{sample}}{I_{ref}} \qquad (2.6)$$

Absorbance is preferable to transmittance since, as stated by the Lambert-Beer law, it is directly proportional to the concentration of the species in solution, therefore, known the molar extinction coefficient, the concentration of the analyte can be obtained or vice versa:

$$A(\lambda) = -logT = \log\left(\frac{I_{ref}}{I_{sample}}\right) = \varepsilon(\lambda)[C]l \qquad (2.7)$$

Where ε it is the molar extinction coefficient, l is the optical path and *[C]* the concentration

The instruments can be single beam or double beam, in the first case the spectrum of the reference (also used as baseline) and then that of the sample must be recorded, while in the double beam instruments the intensities are recorded simultaneously. Also in this case it is necessary to carry out a baseline using measuring the spectrum of the solvent alone (generally using an empty cuvette as a reference). The general scheme of a double beam tool is shown in Figure 2.14.

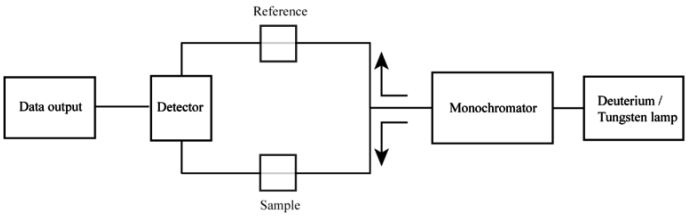

Figure 2.14. Diagram of a two beam instrument for Uv-Vis measurements

In a typical UV-visible spectrum the wavelength is reported in the abscissa and the absorbance in the ordinate. If the material is not completely transparent to the radiation, a series of peaks of varying height will be observed for each transition in relation to the intensity of the absorption itself (value of ε). Before each measurement, as mentioned, it will be necessary to create a baseline by making a spectrum of the solvent alone, in this way if the solvent is absorbent in the measurement range, subtracting the baseline will eliminate these contributions. An example spectrum is shown in Figure 2.15.

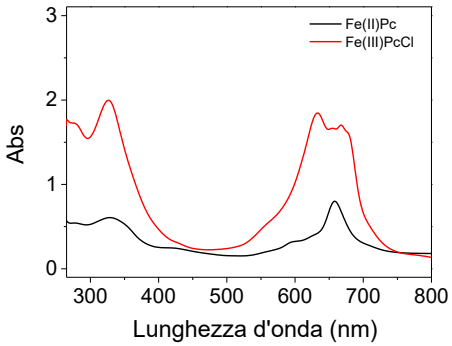

Figure 2.15. Example of a UV-Vis for phthalocyanine of Fe(II) and Fe(III) in DMF

The measurements were carried out using a UV-Vis-NIR Cary 5000 (Agilent) instrument like the one shown in Figure 2.16 at the laboratory where the thesis project was carried out using 1cm quartz

cuvettes. This technique was mainly used for two reasons, for complex synthesis successful checking and to evaluate the amount of hydrogen peroxide production in electrolysis experiment. For the latter a brief explanation is given below.

Figure 2.16. Instrument used for Uv-Vis measurement

The amount of produced H_2O_2 was evaluated by a spectrophotometric method involving the complexation of the peroxide with potassium titanium oxide sulphate ($TiOSO_4$ xH_2O) and its detection at 410 nm. A 0.02 M Ti(IV) standard solution was prepared in a 100 mL round bottom flask through dissolution of the proper amount of the salt in 30 mL of MilliQ H_2O and 27.2 mL of H_2SO_4 and further addition of MilliQ H_2O to a final volume of 100 mL. The calibration solutions were prepared in 2 mL graduated flasks containing Ti(IV) reagent (0.02 M) and a proper amount of H_2O_2 added as pure reagent or diluted solution. In Figure 2.17 the spectra and calibration curve are reported. The obtained equation was A = 0.81381 [H_2O_2 / mM] + 0.00601

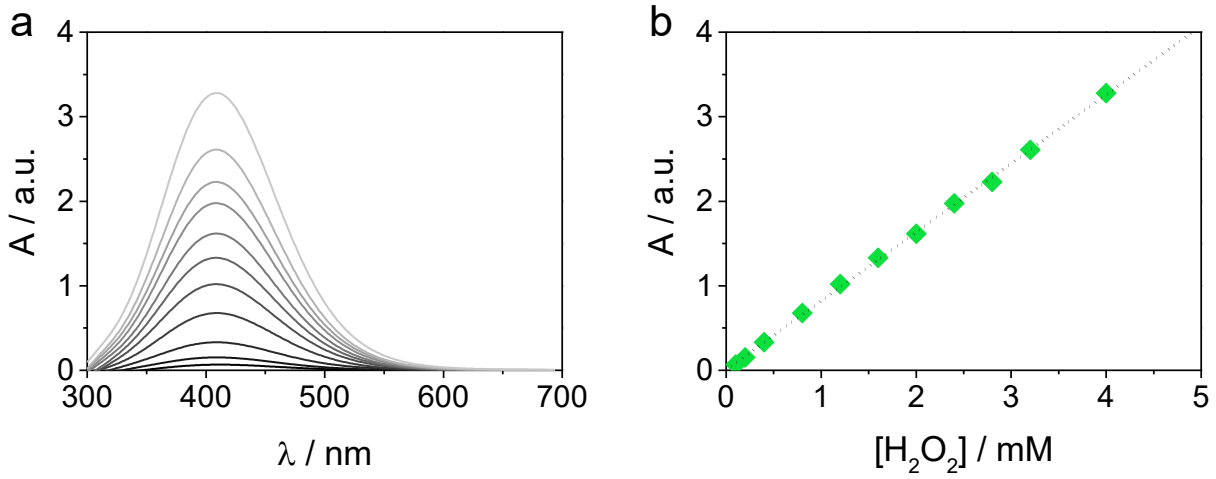

Figure 2.17. a) Uv-Vis spectra at different concentration of hydrogen peroxide and b) calibration curve

2.1.7. XAS

X-ray Absorption Spectroscopy (XAS) is a synchrotron technique wildly used to evaluate the local geometric and/or electronic structure of matter. The X-ray absorption near-edge structure (XANES) is linked to core transitions to quasi bound states (multiple scattering resonances). This allow to gain information of geometry and oxidation state. In the high kinetic energy range the absorption spectra are dominated by EXAFS (extended X-ray absorption fine structure), which is a single scattering event. This part of the spectra allow to obtain information on coordination numbers, interatomic distances, and degree of disorder. The experimental date are fitted to gain this information. In this thesis Fe K-edge X-ray absorption spectroscopy (XAS) spectra were measured at the SAMBA beamline (Synchrotron SOLEIL), at room temperature in fluorescence mode, using a Ge 33-pixel detector. The beamline is equipped with a sagittally focusing Si 220 monochromator

and two Pd-coated mirrors that were used to remove X-rays harmonics. The catalysts were pelletized as disks of 10 mm diameter using boron nitride as a binder. The EXAFS data analysis was performed with the GNXAS code, which is based on the decomposition of the EXAFS χ(k) signal into a summation over n-body distribution functions γ(n) calculated by means of the multiple-scattering (MS) theory. Details of the theoretical framework of the GNXAS approach are described in refs [15,16]. The Fe coordination shells have been modelled with Γ-like distribution functions which depend on four parameters, namely, the coordination number N, the average distance R, the mean-square variation σ^2, and the skewness β. Note that β is related to the third cumulant C_3 through the relation $C_3=\sigma^3\beta$.

2.1.8. SEM

The scanning electron microscope (SEM) uses a focused high energy electron beam to evaluate the morphology and/or chemical composition (using the produced x-ray, EDX). The SEM system is based on the interaction of an electronic beams with the matter which generate a secondary electron which are focused on a CCD camera. Secondary electrons show the morphology and the topography on samples and the backscattered electrons are most valuable for illustrating contrasts in composition in multiphase samples. The energy of electrons is included in the range 100 eV and 30 keV, they are, generally, generated by a tungsten filament a high temperature.

In the contest of this thesis, this technique was used to performed morphological studies and compositional, in particular to evaluate iron content in Fe-N-C as an alternative determination of ICP or XPS. Figure 2.18 shows an example of SEM for a sample with Sn nanoparticles, as confirmed by EDX analysis.

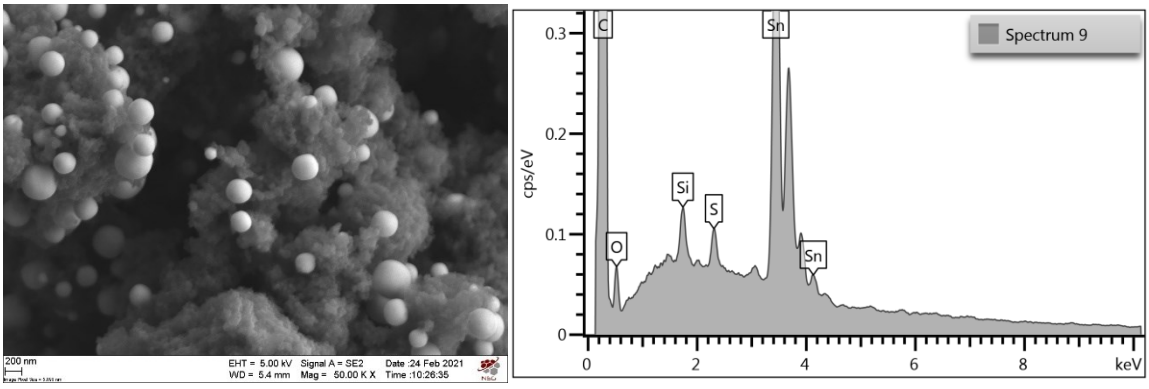

Figure 2.18. Example of SEM image, the bright spot are metal nanoparticles on carbon support, on the right example of EDX response

2.1.9. TEM

Transmission electron microscopy (TEM) is a microscopy technique that gives information about micro-structure of the samples through high-resolution and high magnification imaging. It is based on the irradiation of the sample with an electron beam within a high vacuum. The beam is generated via thermionic effect due to the heating of a tungsten filament. The beam is thus manipulated using electromagnetic lenses to collimate and focalize it on the sample. The recorded image (on fluorescence screen) depends on electron dispersion by sample and is formed of alternating dark and light zones. Generally metal nanoparticle appear as black spot on grey agglomerate of carbon particles. Transmission electron microscopy (TEM) images (Figure 2.19) were recorded using FEI Tecnai G12.

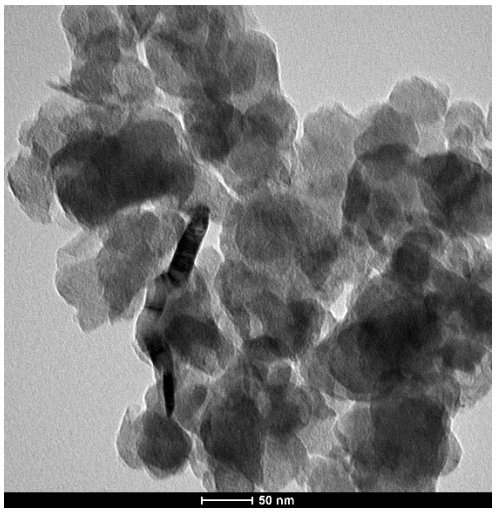

Figure 2.19. Example of a TEM image of Fe-N-C, some iron NPs are visible

2.1.10. ICP-MS

Inductively coupled plasma mass spectrometry (ICP-MS) is an elemental analysis technology used for detecting most elements of the periodic table down to nanogram levels. The Inductively Coupled Plasma (ICP) is an ionization source that fully decomposes a sample into ions. ICP-MS was used to quantify the metallic components of the samples, mainly Fe and Sn.

2.2. Electrochemical

This section describes the electrochemical investigation techniques used to evaluate the properties and processes that occur at the electrode interface of the catalysts. Some theoretical backgrounds are given in Appendix (10.1). The techniques used were linear scanning voltammetry (LSV), cyclic voltammetry (CV), chronoamperometry (AC) and impedance measurements. The instrumentation used in this thesis project for the electrochemical characterization was an Autolab Model PGstat 101N bipotentiostat/galvanostat equipped with an impedance FRA and RRDE electrodes from MetrOhm AG Italiana Srl.

2.2.1. Example of characterization for M-N-C materials

The first phase of each electrochemical measurement for analysis of the catalytic properties towards the ORR is the recording of the background in an argon atmosphere, this allows to characterize the capacitive component of the current, the anodic and cathodic discharge limit and allows to observe any unrelated phenomena from the reduction of oxygen, (an electrode activation phase is always carried out in which cyclic voltammetries are carried out at 200 mV s^{-1} for 20-30 cycles). As can be seen in Figure 2.21, where the CVs in Ar are reported at different scanning speeds, the electrochemical signal is characterized by a pair of peaks between 0.5 and 0.7 V. vs RHE. The presence of these peaks is common in carbons with an amorphous component and is often linked to the active redox quinone-hydroquinone pair present in the carbon matrix, which consists of two electron transfers and two consecutive or concerted proton transfers (Figure 2.20).

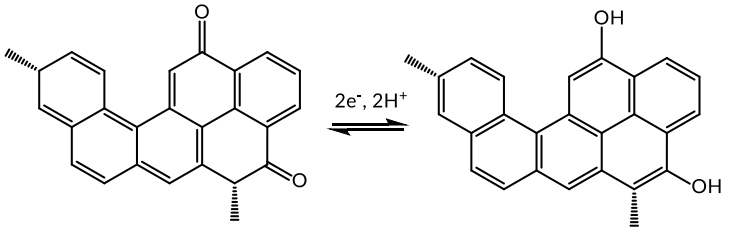

Figure 2.20. Electrochemical reaction of quinone-hydroquinone conversion

However, it is possible that at these potentials, the Fe^{3+} / Fe^{2+} oxidation reaction of the metal component present also takes place [17]. The reduction to Fe^{2+}, by some research groups, is reported as essential to start the reduction process, or to have oxygen adsorption [18,19]. All voltammetric measurements in Ar are carried out in a potential window such as to avoid hydrogen and oxygen evolution processes that are not of interest and could damage the deposited film.

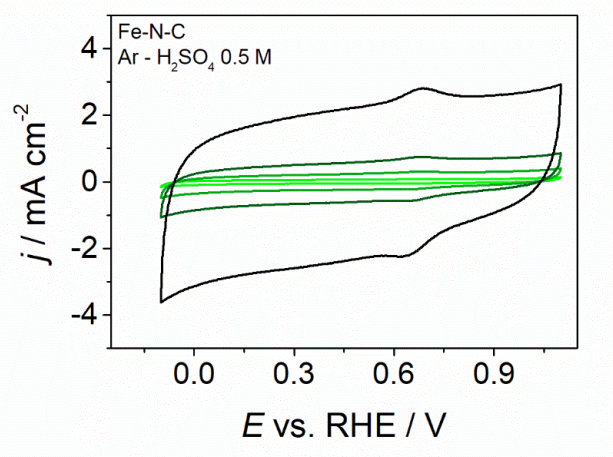

Figure 2.21. Cyclic voltammetries in Ar (H_2SO_4 0.5 M) at different scanning rates for FePhenCB

After the activation and recording of background, the electrolyte is saturated with oxygen, then the CVs and LSVs are recorded. Figure 2.22 shows the CVs in oxygen at different scanning speeds from which two characteristics can be observed:

- the absence of the oxidation return peak
- the shift of the reduction peak with the scanning speed.

The first characteristic is due to the fact that the material effectively adsorbs oxygen and then reduces it to water or hydrogen peroxide, while it is not able to catalyse the inverse reaction in this window of potential (however, a peak would not be observed, but an anodic discharge). The second characteristic indicates an irreversible reaction, the linear relationship between the peak potential and the logarithm of the root of the scanning speed (or from the speed considering the property of the log a^n = n log a) is in fact typical of irreversible reactions (Figure 2.22). These characteristics are typical of the oxygen reduction reaction, consequently the observed trend of the peak potential is in accordance with what was expected and is a first confirmation that the process that we are interested in catalysing is taking place.

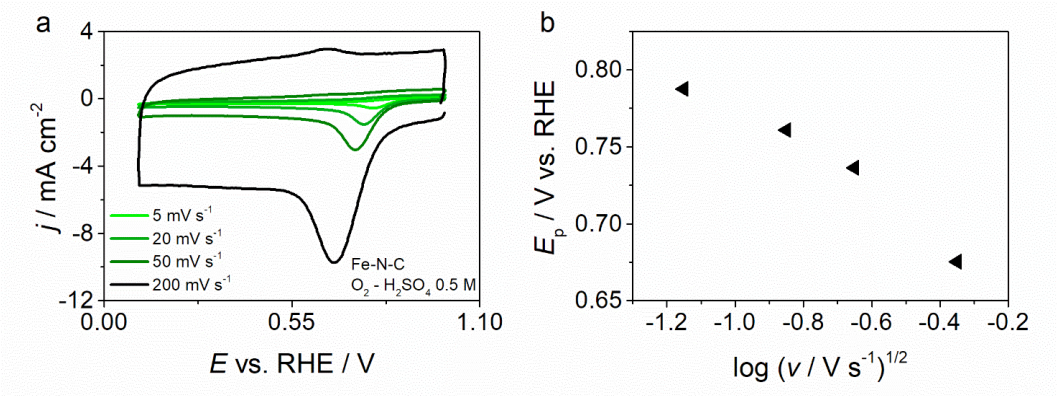

Figure 2.22. a) Cyclic voltammetry In Oxygen at different scan rate, and b) shift of peak potential with the scan rate

The following figures show the analyzes from which it is possible to derive the electrochemical parameters useful for evaluating the activity. Figure 2.23a shows the difference between the voltammetry in Ar and in oxygen, the reduction peak around 0.7 V is evident. Figure 2.23b shows the LSV obtained at 1600 rpm, below the disc current due to the reduction is shown oxygen, while the current recorded by the ring due to the electrochemical oxidation of hydrogen peroxide is shown at the top; from the ratio of the currents, it will be possible to calculate the number of electrons exchanged and the quantity of hydrogen peroxide produced.

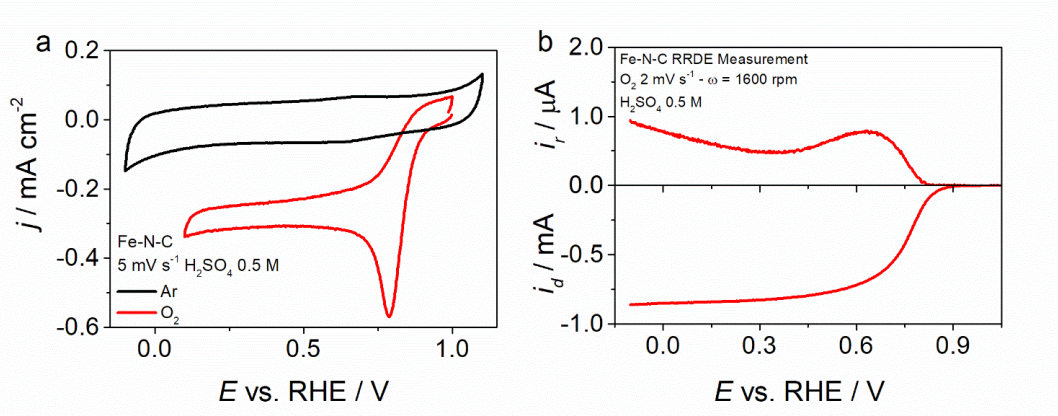

Figure 2.23. a) Cyclic voltammetry in Ar and O_2 saturated solution and b) RRDE response in O_2 saturated electrolyte

Figure 2.24a shows the LSVs at different rotation speeds and the related Koutecky-Levich (K-L) analysis considering the current density at 0.0 V (even in the absence of a current plateau). It is observed how the linear trend (Figure 2.24b) describes the experimental data well, confirming the validity of the K-L, furthermore the slope is comparable with that obtained for an ideal 4-electron process. In fact, remember that the limiting current does not depend on the potential but only on the number of exchanged electrons and other hydrodynamic parameters, including the rotation speed. This type of analysis together with the RRDE technique therefore provide a good estimate of the number of electrons exchanged and therefore of the tendency of the material to reduce oxygen to water rather than to hydrogen peroxide.

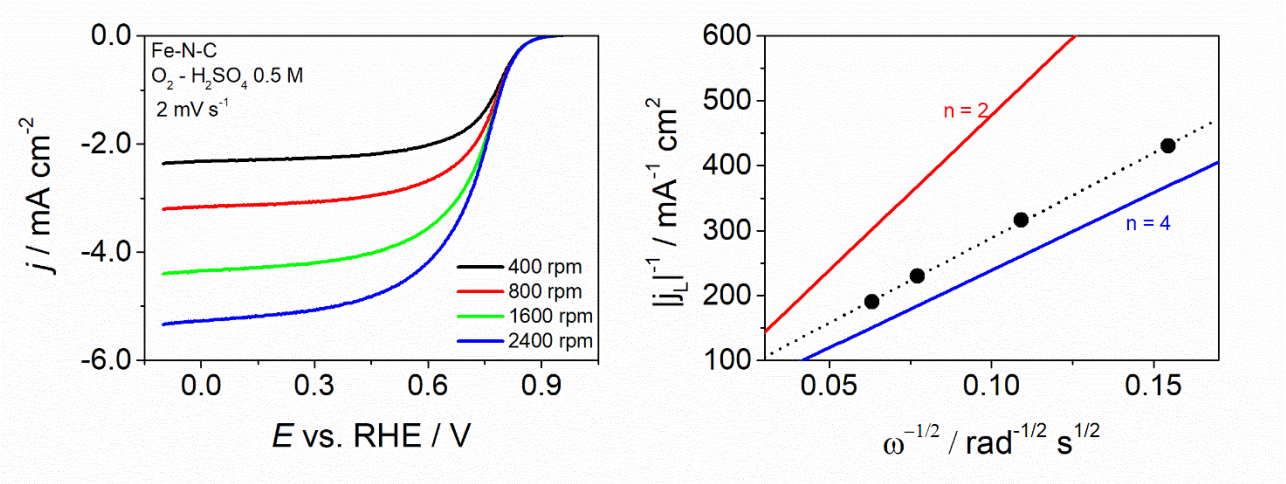

Figure 2.24. a) K-L analysis for the determination of exchange electron

2.2.2. Electrochemical technique for the evaluation of active site: Nitrite Stripping

The high catalytic activity towards ORR by the Fe-N-C materials has been widely demonstrated, but the same cannot be said about the nature of the active sites involved in the reaction. Techniques such as Mössbauer and X-ray absorption spectroscopy (XAS) have been widely used but provide only bulk and non-surface information, while surface techniques such as XPS are unable to determine the actual number of electrochemically accessible sites with respect to the total present on the surface.

The intrinsic activity of an electrocatalyst is given by:

$$i[A\ g^{-1}] = F[A\ s\ mol^{-1}] \times TOF[siti\ elettronici^{-1}\ s^{-1}] \times MSD[mol\ g^{-1}] \qquad (2.8)$$

where *i* is the current normalized to loading at a certain potential, the TOF is the turnover frequency in electronic sites per second and the MSD is the density of active sites.

In general, it is not easy to divide the two contributions, a greater amount of iron is linked to a greater number of active sites and therefore to a greater density which has the effect of increasing the activity, on the other hand, other parameters such as morphology, can affect the MSD. It has also been shown that increasing the amount of iron favours the formation of inactive species that can obstruct access to the sites. In the same way, high currents can be due to high TOF, i.e., in the presence of sites capable of reducing more oxygen molecules per unit of time, even on materials with a low density of sites. The attempt is therefore to be able to separate the two contributions and by combining other investigation techniques understand what are the synthesis parameters that allow you to increase one contribution rather than the other.

The strong interaction of FeN_x metal centres with nitrites has recently been studied in a reversible electrochemical process that allows materials to be poisoned and restored by applying different potentials to the material. The objective of these measurements is therefore to determine the MSD and therefore the TOF of the FeN_x sites.

The measurements were carried out by the research team of Professor Anthony Kucernak at "The Imperial College of Science, Technology and Medicine" in London by Dr. Asad Mehmood. The same group is the author of the article in which this procedure is presented [20,21].

Experimentally, various RDE procedures are followed with a 3-electrode configuration as summarized in Figure 2.25. An acetate-buffered pH electrolyte (pH 5.2) with 0.2 / 0.3 mg cm^{-2} loading is used, the reference electrode is calomel (SCE).

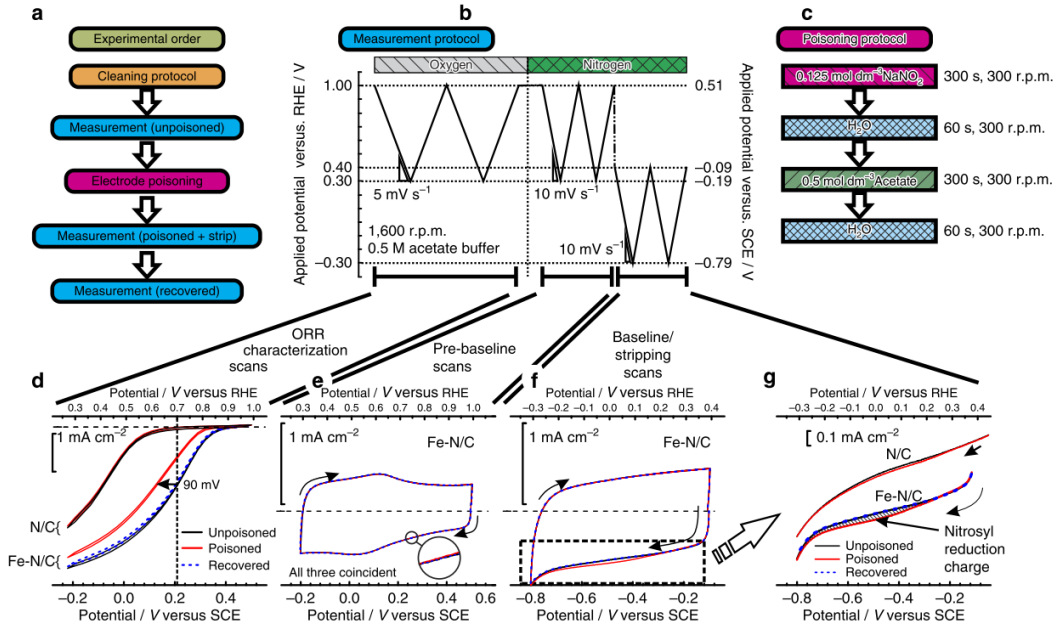

Figure 2.25: Protocol Nitrite poisoning. (a) flow chart showing the steps for evaluating the performance of a catalyst and determining the density of the catalyst sites; (b) protocol used to measure the electrochemical performance of the ORR and evaluate the charge associated with the reductive stripping of the adsorbed nitrites; (c) protocol used to poison the electrode using a solution containing nitrites; (d) ORR performance of the catalyst before, during and after adsorption of nitrites; (e) baseline (avoiding the nitrite reduction area) for the catalyst before, during and after adsorption of the nitrite; (f) baseline scanning in the nitrite reductive stripping region before, during and after nitrite adsorption; (g) detail in the nitrite stripping region [20].

The reactions that take place during these steps in the metal centres can be summarized as follows:

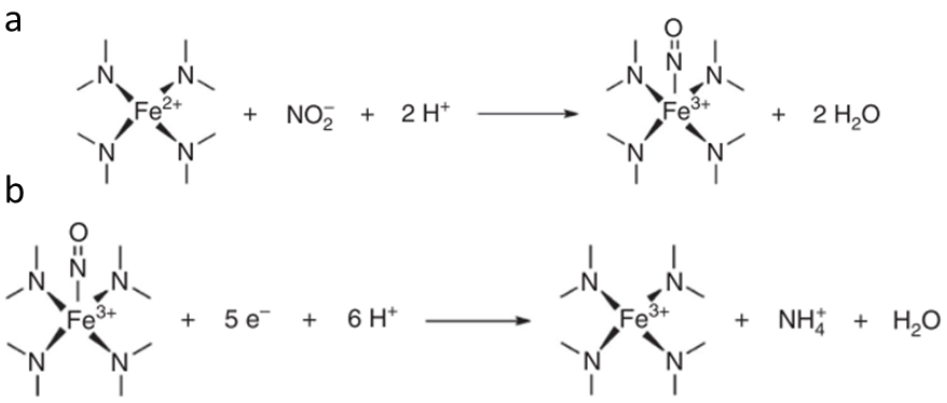

Figure 2.26 a) Poisoning and b) nitrite stripping on FeN_x centres

The density of MSD active sites is then determined by the charge associated with stripping:

$$MSD[mol\ sites\ g^{-1}] = \frac{Q_{strip}[C\ g^{-1}]}{n_{strip}\ F[C\ mol^{-1}]} \qquad (2.9)$$

Where Q_{strip} is the charge determined by voltammetric measurements in nitrogen in the stripping region before and after poisoning (Figure 2.25f), n_{strip} are the number of electrons exchanged in the stripping process and F is the Faraday constant.

While the turnover frequency can be determined from the difference in kinetic current at 0.8V (Δi_k) between the poisoned and non-poisoned material and from the previously calculated density of the sites:

$$TOF\ (0.8\ V)[s^{-1}] = \frac{\Delta i_k[A\ g^{-1}]}{F[A\ s\ mol^{-1}] \cdot MSD[mol\ g^{-1}]} \qquad (2.10)$$

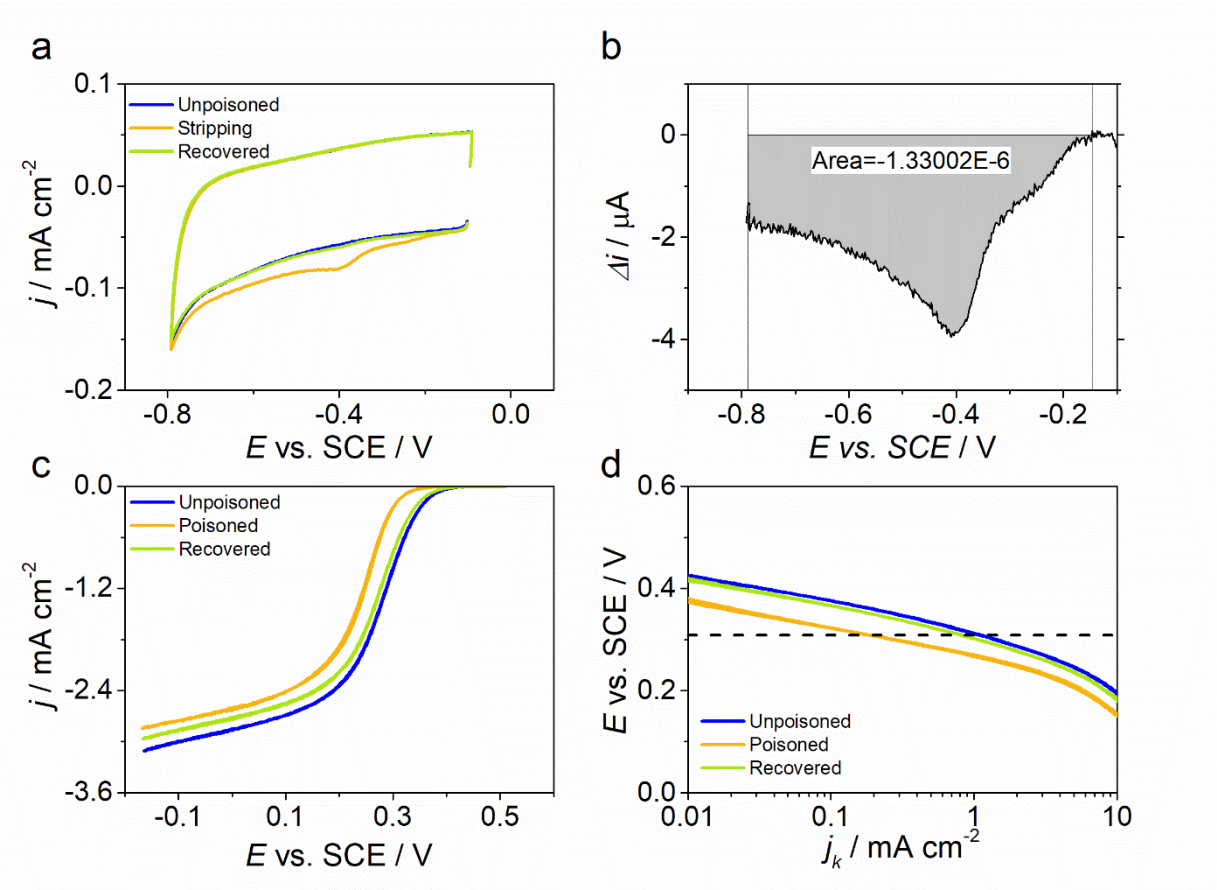

Figure 2.27. Voltametric response during a typical stripping analysis recorded in acetate buffer: a) CV in the stripping region before, during and after stripping in argon purged electrolyte, b) stripping charge area extrapolated from the CV showed in 'a', c) LSV at 1600 rpm and d) Tafel plot in O_2 saturated electrolyte.

2.2.3. GDE: Arenz Cell

Setup different from RRDE are needed to better understand the working of catalyst under more realistic condition, as for example a setup where the catalyst is separated from the electrocyte has been proposed and commercialized. Indeed, the setup was bought from Gustav Sievers [22] (gde-cell.com, Figure 2.28) and consist of a steel body that serve also as a contact for applying the potential to the working electrode which consist of a carbon paper with the catalyst deposit on the surface. Also the same is possible with a PEEK body with metal contact as proposed in other work [23]. Contrary to the original setup a carbon felt under the carbon paper was used to improve the electrical contact between the electrode and the cell body, since it does not interfere with the actual electrochemical measurement, this could be needed because carbon paper and Nafion membrane are sold with different thickness and a certain height is necessary to obtain a good contact between catalyst and membrane. As anticipated, a Nafion membrane was placed between the catalyst and the upper body (made of Teflon) of the cell. Also application in alkaline media with the suitable membrane have been proposed and tested here [24,25]. The advantage of this setup is that is easy to prepare, in the simple case the membrane rests on the carbon paper and the pressure induce by the clamp use to assemble the cell is sufficient to have a good adherence. Generally using 0.5 M H_2SO_4 as electrolyte bring to resistance of the other of 20 Ω which, depending on the potentiostat could be problematic to compensate with very high current, therefore, on some occasion higher acid concentration could be needed, for example Arenz and co-worker use 4M $HClO_4$ to reduce ohmic drop. The type of measurements that could be carried out with this setup are essentially two, cyclic voltammetry under Ar or O_2 flux and chronoamperometry at given potential (or chronopotentiometry). The first were used to characterize material behaviour in this setup, the second to verify the stability/durability. Clearly also impedance spectroscopy analysis can be carried out to evaluate the ohmic drop.

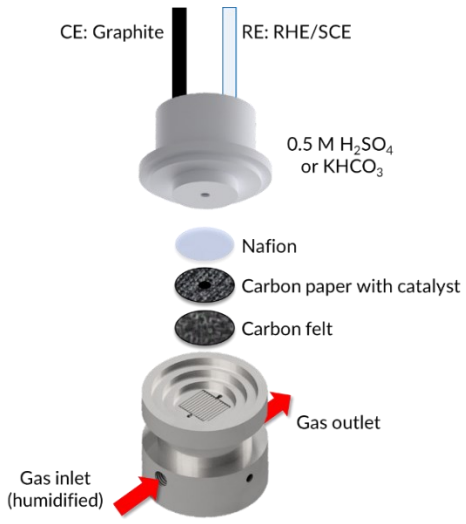

Figure 2.28. Scheme of the cell in all its component

2.2.4. GDE: Electrolyzer

For electrolysis measurement a commercial setup (Figure 2.29a) was bought from Gaskatel GmbH. It consist of a primary cell made of polypropylene (PP), an optional secondary compartment (Figure 2.29b) that could be put between the gas feed chamber, which is the cell part that allow to feed the gas from behind the catalyst layer which face the electrolytic solution in the primary cell on in the secondary. Working with the secondary cell compartment and a cation/anion conductive

membrane allow to work in divided cell and therefore permit a quantification of electrolysis product could be made, in practice the primary cell that contain the counter electrode is separated from the compartment with the working and the reference electrode. In this configuration the working electrode is the gas diffusion electrode, the counter electrode is a Pt wire and the reference electrode a RHE which thanks to some capillaries work in a Lugging-like configuration.

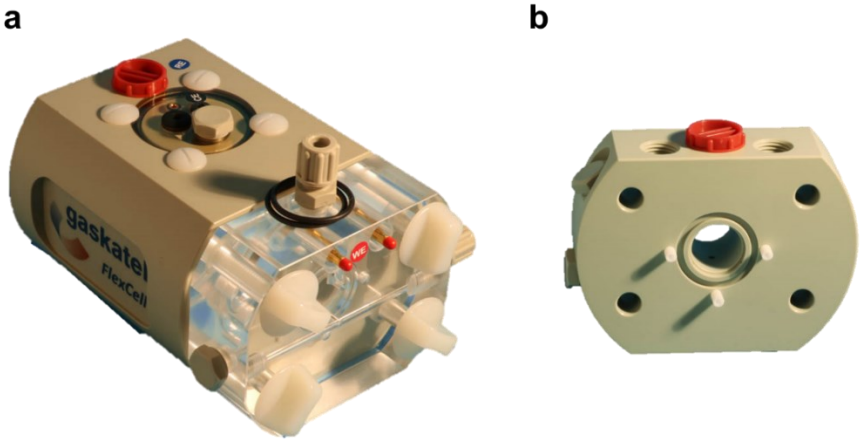

Figure 2.29. Scheme of the cell in for electrolysis a) main chamber and the gas compartment for undivided measurements, and b) additional chamber to perform measurements in divided cell

2.3. Bibliography

[1] E.M. Thompson, CHN analysis, R. Soc. Chem. 30 (1999) 25–29. https://doi.org/10.1260/0957456991496844.

[2] T.F. Scientific, https://www.brechbuehler.ch/fileadmin/redacteur/pdf/oea/FLASHSmart/app-notes/AN42213_Flash_2000_CHNS_Analyzer_Stability-LInearity-Repeatability_and_Accuracy.pdf (accessed August 24, 2019).

[3] M.G.F. Nataf, New approaches to understand conductive and polar domain walls by Raman spectroscopy and low energy electron microscopy, (2016) 143.

[4] P. Zhou, Choosing the Most Suitable Laser Wavelength For Your Raman Application, 1 (2015) 6. http://bwtek.com/wp-content/uploads/2015/07/raman-laser-selection-application-note.pdf.

[5] A.C. Ferrari, J. Robertson, Interpretation of Raman spectra of disordered and amorphous carbon, Phys. Rev. B. 61 (2000) 14095–14107. https://doi.org/10.1103/PhysRevB.61.14095.

[6] A.C. Ferrari, Determination of bonding in diamond-like carbon by Raman spectroscopy, Diam. Relat. Mater. 11 (2002) 1053–1061. https://doi.org/10.1016/S0925-9635(01)00730-0.

[7] M. Pawlyta, J.N. Rouzaud, S. Duber, Raman microspectroscopy characterization of carbon blacks: Spectral analysis and structural information, Carbon. 84 (2015) 479–490. https://doi.org/10.1016/j.carbon.2014.12.030.

[8] A. Sadezky, H. Muckenhuber, H. Grothe, R. Niessner, U. Pöschl, Raman microspectroscopy of soot and related carbonaceous materials: Spectral analysis and structural information, Carbon. 43 (2005) 1731–1742. https://doi.org/10.1016/j.carbon.2005.02.018.

[9] B.S. Elman, M.S. Dresselhaus, G. Dresselhaus, E.W. Maby, H. Mazurek, Raman scattering from ion-implanted graphite, Phys. Rev. B. 24 (1981) 1027–1034. https://doi.org/10.1103/PhysRevB.24.1027.

[10] Y. Wang, D.C. Alsmeyer, R.L. McCreery, Raman spectroscopy of carbon materials: structural basis of observed spectra, Chem. Mater. 2 (1990) 557–563. https://doi.org/10.1021/cm00011a018.

[11] L. Bokobza, J.-L. Bruneel, M. Couzi, Raman Spectra of Carbon-Based Materials (from Graphite to Carbon Black) and of Some Silicone Composites, C. 1 (2015) 77–94. https://doi.org/10.3390/c1010077.

[12] S. Santangelo, G. Messina, G. Faggio, M. Lanza, C. Milone, Evaluation of crystalline perfection degree of multi-walled carbon nanotubes: Correlations between thermal kinetic analysis and micro-Raman spectroscopy, J. Raman Spectrosc. 42 (2011) 593–602. https://doi.org/10.1002/jrs.2766.

[13] M. Thommes, K. Kaneko, A. V. Neimark, J.P. Olivier, F. Rodriguez-Reinoso, J. Rouquerol, K.S.W. Sing, Physisorption of gases, with special reference to the evaluation of surface area and pore size distribution (IUPAC Technical Report), Pure Appl. Chem. 87 (2015) 1051–1069. https://doi.org/10.1515/pac-2014-1117.

[14] G.A. Rizzi, Schema XPS, (n.d.). http://wwwdisc.chimica.unipd.it/gianandrea.rizzi/privata/documentazione/insegnamenti/Laboratorio di Preparazione e Caratterizzazione dei Materiali II/XPS_intro.pdf.

[15] A. Filipponi, A. Di Cicco, C.R. Natoli, X-ray-absorption spectroscopy and n-body distribution functions in condensed matter. I. Theory, Phys. Rev. B. 52 (1995) 15122–15134. https://doi.org/10.1103/PhysRevB.52.15122.

[16] A. Filipponi, A. Di Cicco, X-ray-absorption spectroscopy and n-body distribution functions in condensed matter. II. Data analysis and applications, Phys. Rev. B. 52 (1995) 15135–15149. https://doi.org/10.1103/PhysRevB.52.15135.

[17] A. Zitolo, V. Goellner, V. Armel, M.T. Sougrati, T. Mineva, L. Stievano, E. Fonda, F. Jaouen, Identification of catalytic sites for oxygen reduction in iron- and nitrogen-doped graphene materials, Nat. Mater. 14 (2015) 937–942. https://doi.org/10.1038/nmat4367.

[18] U. Tylus, Q. Jia, K. Strickland, N. Ramaswamy, A. Serov, P. Atanassov, S. Mukerjee, Elucidating oxygen reduction active sites in pyrolyzed metal-nitrogen coordinated non-precious-metal electrocatalyst systems, J. Phys. Chem. C. 118 (2014) 8999–9008. https://doi.org/10.1021/jp500781v.
[19] Q. Jia, N. Ramaswamy, U. Tylus, K. Strickland, J. Li, A. Serov, K. Artyushkova, P. Atanassov, J. Anibal, C. Gumeci, S.C. Barton, M.T. Sougrati, F. Jaouen, B. Halevi, S. Mukerjee, Spectroscopic insights into the nature of active sites in iron–nitrogen–carbon electrocatalysts for oxygen reduction in acid, Nano Energy. 29 (2016) 65–82. https://doi.org/10.1016/j.nanoen.2016.03.025.
[20] D. Malko, A. Kucernak, T. Lopes, In situ electrochemical quantification of active sites in Fe-N/C non-precious metal catalysts, Nat. Commun. 7 (2016) 13285. https://doi.org/10.1038/ncomms13285.
[21] D. Malko, A. Kucernak, T. Lopes, In situ electrochemical quantification of active sites in Fe–N/C non-precious metal catalysts, Nat. Commun. 7 (2016) 13285–13292. https://doi.org/10.1038/ncomms13285.
[22] M. Inaba, A.W. Jensen, G.W. Sievers, M. Escudero-Escribano, A. Zana, M. Arenz, Benchmarking high surface area electrocatalysts in a gas diffusion electrode: measurement of oxygen reduction activities under realistic conditions, Energy Environ. Sci. 11 (2018) 988–994. https://doi.org/10.1039/C8EE00019K.
[23] J. Schröder, V.A. Mints, A. Bornet, E. Berner, M. Fathi Tovini, J. Quinson, G.K.H. Wiberg, F. Bizzotto, H.A. El-Sayed, M. Arenz, The Gas Diffusion Electrode Setup as Straightforward Testing Device for Proton Exchange Membrane Water Electrolyzer Catalysts, JACS Au. 1 (2021) 247–251. https://doi.org/10.1021/jacsau.1c00015.
[24] S. Alinejad, J. Quinson, J. Schröder, J.J.K. Kirkensgaard, M. Arenz, Carbon-Supported Platinum Electrocatalysts Probed in a Gas Diffusion Setup with Alkaline Environment: How Particle Size and Mesoscopic Environment Influence the Degradation Mechanism, ACS Catal. 10 (2020) 13040–13049. https://doi.org/10.1021/acscatal.0c03184.
[25] M. De Jesus Gálvez-Vázquez, P. Moreno-García, H. Xu, Y. Hou, H. Hu, I.Z. Montiel, A. V. Rudnev, S. Alinejad, V. Grozovski, B.J. Wiley, M. Arenz, P. Broekmann, P. Moreno-García, Environment Matters: CO2RR Electrocatalyst Performance Testing in a Gas-Fed Zero-Gap Electrolyzer, ACS Catal. 10 (2020) 13096–13108. https://doi.org/10.1021/acscatal.0c03609.

3. Synthesis, from support to catalyst preparation

In the field of carbon based material as a catalyst or as building block for more complex catalytic system, are crucial to have tool to prepared them in a controlled and reproducible way. During the PhD project several aspects have been considered. First of all, different method were used to modify the carbon matrix by acting on its morphology or composition, namely activation of commercial carbon black was done to enhance the surface area and pore network, doping with nitrogen, sulphur and metal were achieved to tune the activity toward the oxygen reduction reaction and also a surface modification was done to evaluate the role of single nitrogen site on ORR. In the following paragraph a detail explanation of those synthesis is reported.

3.1. Activation of carbon

Commercial carbon black present a wildly range of surface area and pore size distribution, passing from low surface area (around 50 m^2 g^{-1}), like for example the here used CB SuperP , to medium porous carbon, like the inflated Vulcan XC72 and finishing to high surface are carbon like EC300J or PBX51. Despite that to achieve a more accurate control, activation treatment with several agent could be performed. Pore in material are conventionally divided in three class depending on their dimension, micropore (d < 2nm), mesopore (2 nm < d < 50 nm) and macropore (d > 50 nm). The first two are of interest in the field of catalysis and generally could be controlled with those activation treatment.

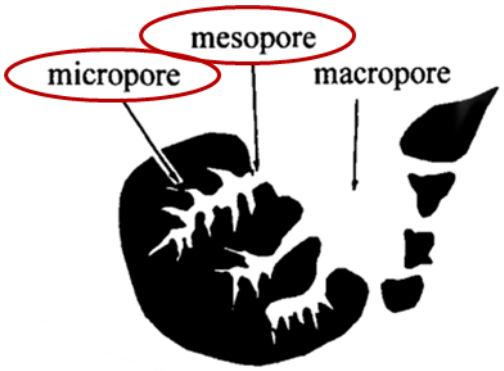

Figure 3.1. Pictorial representation of pore inside carbonaceous material

Typically, the carbon matrix react opening new pore or by widening the existing ones, these reactions occur at high temperature that span, depending on reagent from 600 to 1200 °C. Generally, when a gas (H_2O, CO_2, NH_3) is used for the scope the procedure is called physical activation, while when solid/liquid (KOH, $MgCl_2$, $ZnCl_2$, H_3PO_4) are used the procedure is called chemical activation [1–6]. In this thesis two types of gases were used to enhance the pore structure, namely water and carbon dioxide, in the following paragraph a brief explanation on pore opening process is given.

3.1.1. H_2O activation treatment

The treatment with steam should favour the widening of pore, therefore an evolution of mesopore linked to the degradation of amorphous carbon. The reaction involved are the following [7]:

$$C + H_2O \rightleftharpoons H_2 + CO \quad (3.1)$$
$$C + 2H_2O \rightleftharpoons 2H_2 + CO_2 \quad (3.2)$$
$$C + CO_2 \rightleftharpoons 2CO \quad (3.1)$$
$$CO + H_2O \rightleftharpoons CO_2 + H_2 \quad (3.3)$$

The existence of multiple reaction leads in general to a growing of porosity in all dimensional range. Since water is introduce as liquid and then vaporized by the high temperature of treatment, a flow of inert gas is needed. This also allow to remove H_2 that it's a reaction inhibitor [8].

3.1.2. CO_2 activation treatment

The CO_2 treatment brings to a general evolution of porosity favouring the opening of new micropore [2,18,19], according to the reaction

$$C + CO_2 \rightleftharpoons 2CO \quad (3.4)$$

where the CO_2 act as oxidating agent over the carbon matrix.
Several mechanisms have been proposed, and some of that highlight the role of oxygen functional group in the reactivity [8], following the reaction:

$$CO_2 \rightleftharpoons CO + (O) \quad (3.5)$$
$$C + (O) \rightleftharpoons CO \quad (3.6)$$

where the second reaction (3.6) suggest the possible role of oxygen in carbon gasification made by CO_2. A key parameter to control is the CO_2 flux that could influence the final effect, too low flux does not allow to remove the produce CO and therefore inhibiting the reaction C/CO_2 [8], while too high flux could cause a non-controlled evolution of porosity [10].

3.1.3. Experimental procedure

In the practice the setup for the activation treatments consisted of a tubular furnace (Carbolite, with a quartz tube Ø =55 mm) flanged at both sides to control the inner atmosphere. The outlet flange was connected to the purging line directed to a scrubber, whereas the inlet flange was connected to the N_2 mass flow control. For water treatment, the inlet flange also lodged a stainless steel needle, which was connected to a syringe pump (SKE Research Equipment) and positioned so that the needle tip laid at the entrance of the oven. The syringe pump was actioned after purging the tubular furnace with N_2 and once the temperature reached the targeted temperature (950 °C). The syringe pump injected milli-Q water at 1 mL min^{-1}, achieving the almost instantaneous water evaporation. A certain amount of carbon black (CB, Super P®) was placed in the furnace with a 100 sccm N_2 flow (controlled by a PR4000B mass-flow, mks instrument) at 25 °C for 90 min and then heated up to 100 °C for 1 h to remove moisture and oxygen. The temperature was then raised to the final temperature with a rate of 5 °C min^{-1}. Once the set temperature was reached, the nitrogen flow was reduced to 50 sccm. The starting CB (hereafter referred to as CBSt-X where X =

treatment time in min.) was treated for a period in the range 10–60 minutes, and then cooled down to ambient temperature within a 50 sccm N_2 flow.
Carbon dioxide activation was carried out with the same procedure with the only difference that, once the targeted temperature of 950 °C was reached, the nitrogen flow was replaced by a flow of CO_2 of 100 sccm. The pristine CB was treated for a period in the range 1–9 h (hereafter referred as $CBCO_2$-W where W = treatment time in hour), and then cooled down to ambient temperature with a 50 sccm N_2 flow. To evaluate the role of temperature, other treatments have been carried out at 850 °C and 1050 °C maintaining a constant exposure time of 5 h. These last samples were named as $CBCO_2$-5-Y (where Y is the temperature in °C).
All the obtained samples were vibro-milled (Retsch MM 400, 10 mL, and 5 mL steel jars with steel balls) obtaining a micrometric powder to facilitate further treatments or characterization.

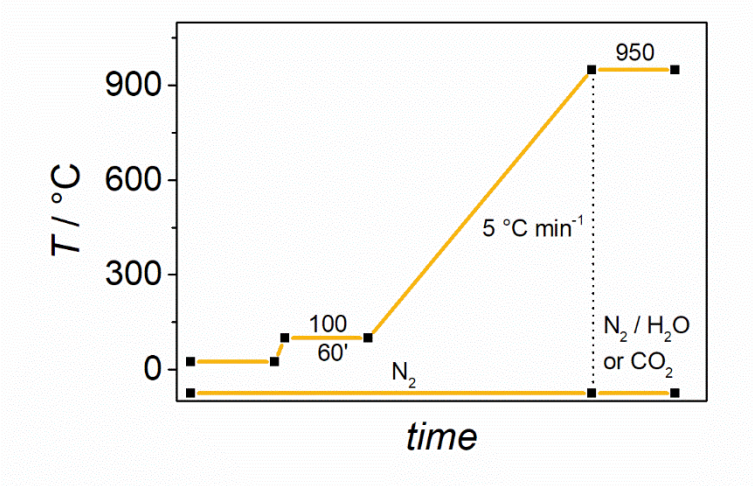

Figure 3.2. Temperature profile vs. time for activation treatments

3.1.4. Example of activation effect on Vulcan XC72

Compositional analysis

Elemental analysis was carried out in order to evaluate variation on carbon, hydrogen, and sulphur content, and by reflect, of oxygen.
The result are reported in Table 3.1, the percentage of all elements remain almost constant, so we can conclude that the steam activation treatment does not affect the composition in a significant way.

Table 3.1: Composition of carbon and activated carbon by elemental analysis

%C wt.%	%H wt.%	%S wt.%	%O[a] wt.%
97.10	0.07	0.63	2.20
97.34	0.16	0.43	2.07
96.78	0.19	0.42	2.61
96.66	0.22	0.42	2.70
96.64	0.23	0.41	2.72

[a] %O = 100 – (%C + %S + %H)

Physisorption analysis

The effect of activation treatment was also evaluated by adsorption/desorption analysis carried out with N_2 at 77.3 K. The recorded isotherm was analysed by QSDFT model using a slit/cylindrical pore model which gives the lowest error on fitting of the experimental isotherm.

Table 3.2. Weight loss, BET surface area, parameter derived from QSDFT analysis and total pore volume for all carbon materials

	t min.	m_i g	m_f g	%$_{lost}$	*BET* $m^2\ g^{-1}$	$S_{0.5\text{-}35nm}$ $m^2\ g^{-1}$	S_{μ}^{QSDFT} $m^2\ g^{-1}$	S_{meso}^{QSDFT} $m^2\ g^{-1}$	V_{μ}^{QSDFT} $cm^3\ g^{-1}$	V_{meso}^{QSDFT} $cm^3\ g^{-1}$	V_{tot} $cm^3\ g^{-1}$
XC72	**0**	-	-	100	223	225	132	93	0.050	0.308	0.724
XC72St20	**20**	3.365	2.605	77	457	426	244	182	0.100	0.370	0.883
XC72St40	**40**	3.933	2.062	52	622	579	261	318	0.108	0.597	1.325
XC72St60	**60**	4.046	1.591	39	772	717	272	445	0.112	0.867	1.585
XC72St120	**120**	6.668	1.045	16	924	889	294	595	0.118	1.310	2.202

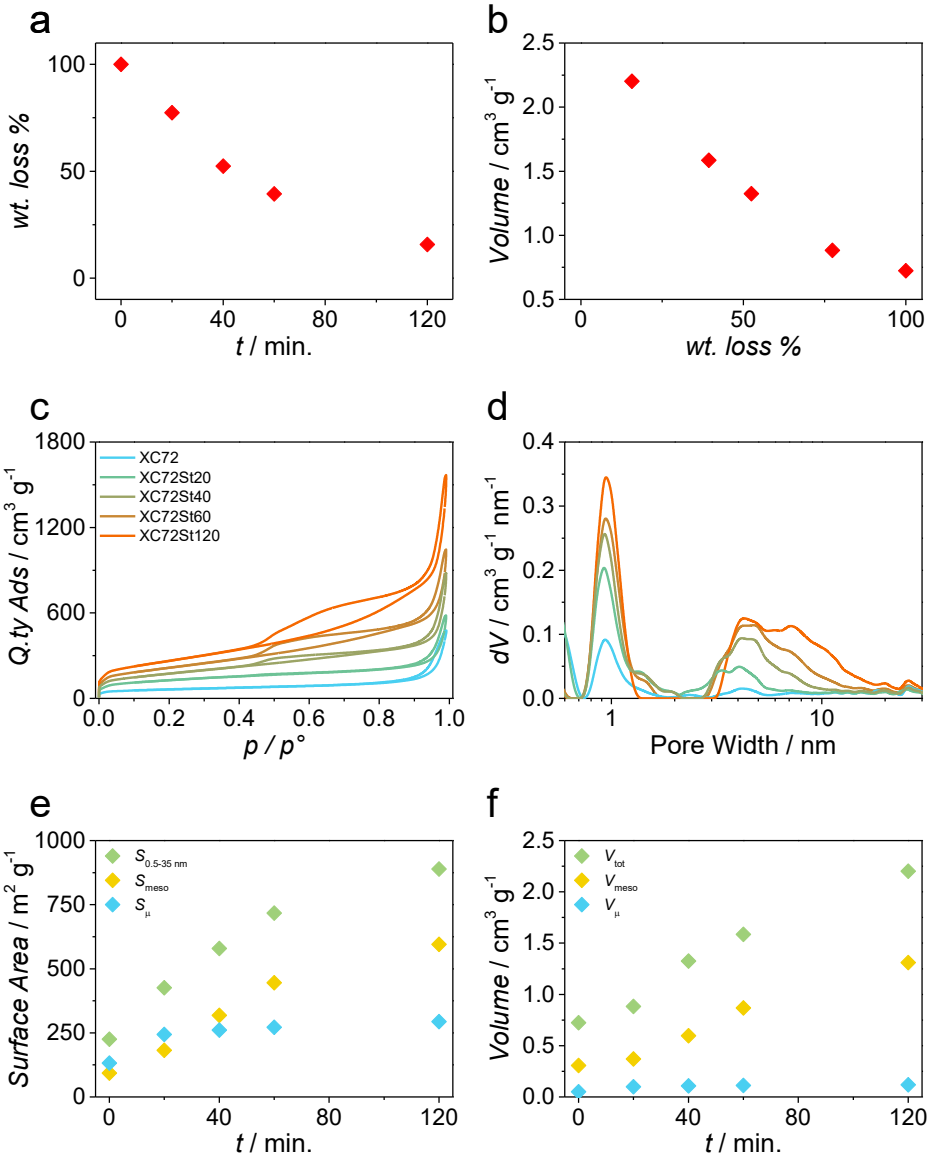

Figure 3.3. a) wt. loss as a function of treatment duration, b) total pore volume as a function of wt. loss, c) experimental isotherm and d) pore size distribution, e) evolution of microporous, mesoporous surface area and e) volume as a function of time

The first confirmation of a reaction of the carbon was done by a simple analysis of the weight of carbon before and after treatment, after 20 min. a percentage of 23% is already lost and after two hours only the 16% of initial mass is preserved, confirming a high reactivity of carbon with water at 950 °C (Table 3.2). This parameter well correlate with time and total volume of pore (Figure 3.3a,b)
A first analysis derived from the isotherms (Figure 3.3c) was done by BET analysis (Table 3.3), by this method we observe a growing from 223 $m^2 g^{-1}$ to 924 $m^2 g^{-1}$. QSDFT analysis allow to obtain the surface area (in a range of 0.5-35 nm of pore width), pore volume and pore size distribution (Figure 3.3d). From all this parameter an increment of micropore and mesopore was observed, also applying Gurvitsch law the total pore volume shows an increment. In detail micropore double in volume after the first 20 min. to then remain stable at around 0.1-0.12 $cm^3 g^{-1}$; mesopore grows more than micropore and the dimension distribution also became wider, the pristine carbon (XC72) has a small peak centred at 3/4 nm, while in the sample treated 120 min. (XC72St120) the distribution span from 3 to 11 nm (Figure 3.3d).
The general increment of surface area and pore volume in function of time are showed in Figure 3.3e,f and they are in perfect agreement with the observed wight loss.

3.2. Heteroatoms doped carbon synthesis

Heteroatoms doped carbon could be prepared in several ways, but generally the treatment at high temperature in inert atmosphere (pyrolysis) is generally used. In addition to control porosity, hard [11,12] or soft [13–17] template approach are sometimes used. The hard template synthesis is robust and reproducible, but requires the downstream removal of the template, usually silica or alumina, which poses the problem of their complete removal even by using hazardous acid such as HF that react well with SiO_2. The soft template method represents an easier alternative being based on the use of amphiphilic block copolymers as structure-orienting agents and templates, which completely decompose during the pyrolysis step leaving a network of pores. This method is a typical ‘‘bottom-up’’ synthesis, whereby mesoporous structures are generated from a carbon-yielding source thanks to the self-assembly of amphiphilic molecules. One example is the pyrolysis of a resorcinol-formaldehyde resin using a PEO-b-PS (polyethylene oxide-block-polystyrene) copolymer as a sacrificial templating agent [18,19]. The doping could be introduced in the precursor or after using precursor as melamine [19].

3.3. Metal-Nitrogen-Carbon synthesis, a general approach to characterize M-N-C based materials

In this paragraph a fast overview of some methodologies of synthesis of M-N-C are reported (mainly with M = Fe) including the synthesis used in this thesis.
The general approach is to mix together a source of carbon, nitrogen and metal and heating that at high temperature (> 600 °C) to achieve the formation of N-doped graphitic domain with M-N coordinating centre, which are as explained before the actual catalytic site in those material.
The pictorial representation of the resulting material is represented in Figure 3.4.

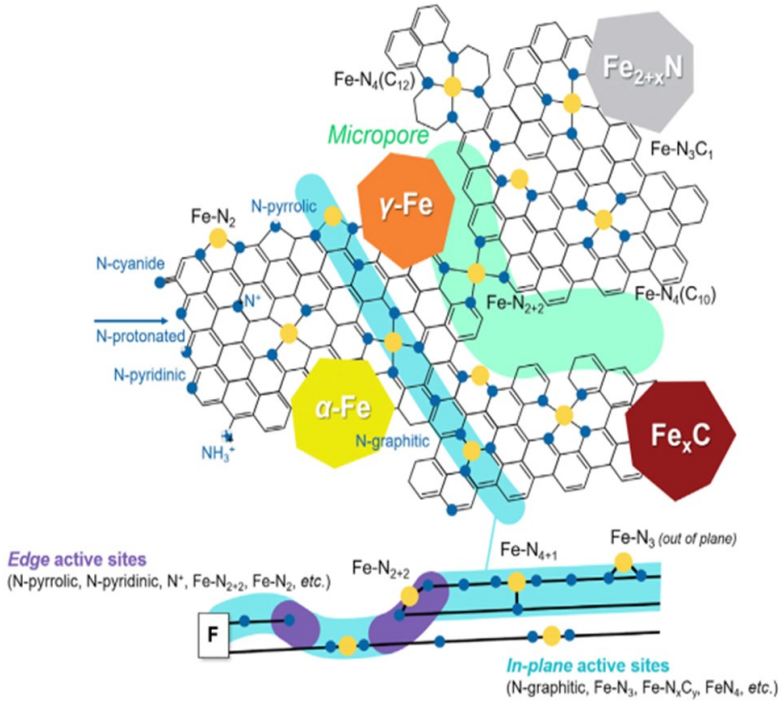

Figure 3.4. The Plurality of Active Sites Observed in Fe-N-C Electrocatalysts

3.3.1. Pyrolysis of metal porphyrins

Kramm et al. prepared catalysts from FeTMPPCl and iron-oxalate dihydrate. These precursors were used for the preparation of the standard catalysts and the catalysts with intermediate acid leaching [20]. The main strategy of this synthesis is to use a precursor in which the site of interest, namely FeN_4 is performed in the precursor [21]. Even this procedure have been overtaken by other method both in terms of cheapness and activity reached, represent the first successful effort to synthesize an attractive material as PGM-free catalysts for ORR.

3.3.2. Pyrolysis of metal salts, nitrogen precursor and carbon

Another common strategy is to use metal salt, like iron acetate, iron chloride or iron acetylacetonate mixed with nitrogen containing molecules, mainly 1,10-phenathroline and a carbon precursor or support, which could be also already doped with nitrogen. For example, Atanassov et al. [22] used iron salt and carbendazim to synthetise Fe-N-C catalysts. Similarly in this thesis preformed metal-nitrogen complexes where used with commercial carbon black showing that aromatic nitrogen containing molecule, like phenanthroline, are the best choice as nitrogen precursor [23].
This methodology take the advantage of being very easy and use cheap precursor, while the main disadvantage is the partial lack of control on final functionalization of surface compared to other methods. Common in this synthetic route is to use an acid leaching step to eliminate all inorganic species that are not useful for ORR catalysis and could hinder the accessibility to actual active site, a scheme is given in Figure 3.5 and refer to all the synthesis of M-N-C catalyst in this thesis.
This consist in 4 passages:

- Mechanical mixing of precursor in a mortar or via ball-milling
- Heating treatment in inert atmosphere (N and/or H_2) → Formation of active site, nitrogen doping
- Acid washing step → removal of Fe, FeO_x and similar species

- Heating treatment → removal of adsorbed species from acid washing, growing of graphitization degree

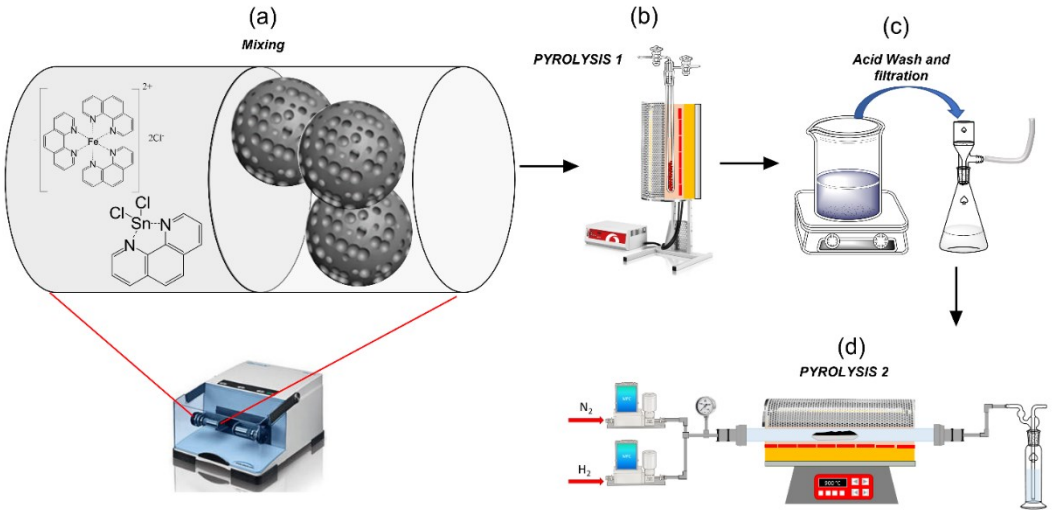

Figure 3.5. a) Mixing of precursors via ball-milling, b) first heating treatment, c) acid washing and d) final hating treatment

3.3.3. Use of ZIF-8

A milestone of Fe-N-C catalysts synthesis was reached whit the idea to use Zinc-Imidazole frameworks (ZIF-8) as carbon-nitrogen precursor and "sacrificial agent" since they contain a preformed ZnN_4 sites (Figure 3.6). Two approaches have been developed, the pyrolysis of $Fe(ac)_2$, 1,10-phenanthroline and ZIF-8 at 1050 °C [24], namely over the Zn fusion temperature or the pyrolysis of ZIF-8 just below the melting point of Zn to form a Zn-N-C which could give an ionic exchange [25] with Fe promoting the formation of sole FeN_4 sites [26]. The latter poi4nt is the main advantage of using ZIF-8 since the formation of FeN_4 has proven to be favoured [27].

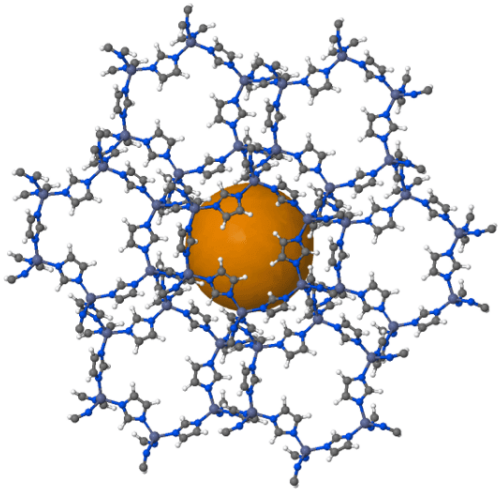

Figure 3.6. ZIF structure, in orange the porosity of the structure

3.3.4. Use of aniline or naphthalene polymer

Polymer derived from aniline or 1,5-diaminonaphthalene have been wildly used for synthetizing Fe-N-C materials, sometimes coupled with a hard template approach to control also the morphology of the final catalyst [28–30]. The synthesis was proposed by Zelenay et al. [31] and summarized in Figure 3.7 and take the advantage of polymer to deposit on carbon nanoparticle surface an on the ability of iron to coordinate nitrogen, giving a great functionalization with Fe, N on the surface of

conductive carbon nanoparticles. This still represents to date one of the most promising routes with the ZIF-8 approach.

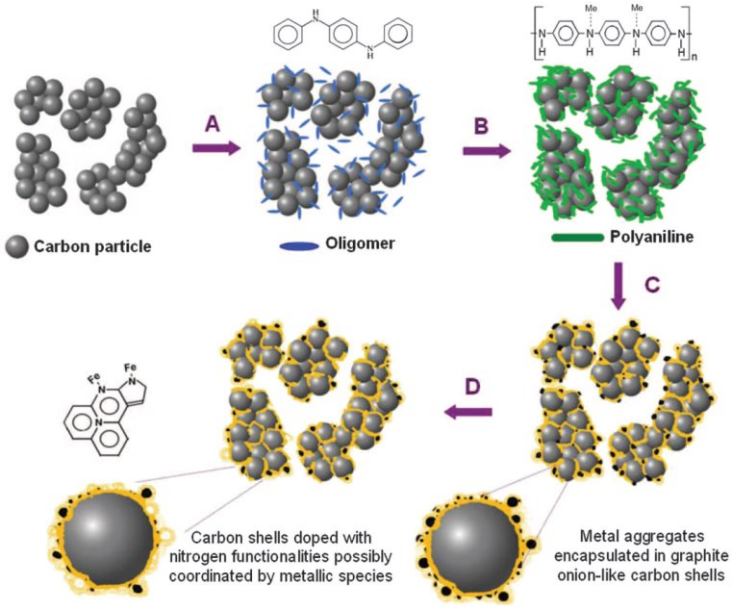

Figure 3.7. Schematic diagram of the synthesis of PANI-M-C catalysts. (A) Mixing of high–surface area carbon with aniline oligomers and transition-metal precursor (M: Fe and/or Co). (B) Oxidative polymerization of aniline by addition of APS. (C) First heat treatment in N2 atmosphere. (D) Acid leaching. The second heat treatment after acid leach is not shown [31].

3.3.5. Use of NH_3 as nitrogen source

Also, ammonia has been proposed as nitrogen source, and at the same time as etching agent to achieve both site formation and nitrogen doping. One example is an early work of Jaouen in 2006 [32].

3.3.6. Synthesis via CVD

Similar to the approach of Menga et al. [26] is the route proposed by Li Jiao et al. [33] in which a pre-synthetise Zn-N-C is used to prepared Fe-N-C using $FeCl_3$ vapour as to achieve the exchange with Zn.

3.3.7. Fe-N-C catalysts preparation in this project

Iron(II)-phenanthroline chloride [hereafter referred to as $Fe(Phen)_3Cl_2$ or Fephen], was synthesized from anhydrous $Fe^{II}Cl_2$ and 1,10-phenantroline in ethanol according to literature [17]. The synthesis of Fe-N-C catalysts were carried out as follow: 200 mg of CB or the activated carbon and 222 mg of $Fe(Phen)_3Cl_2$ (equivalent to the 2 $\%_{molar}$ of iron compared to the molar amount of carbon) was vibro-milled at 18, 20 and 25 Hz for 1 h (20 min. for each frequency in ascending order), then heated at 900 °C in a tubular furnace (Carbolite, with a quartz tube Ø =25 mm) for 2 h under nitrogen-hydrogen atmosphere (9% H2 in the mixture, HG 2400 Claind) and eventually cool down to ambient temperature under pure nitrogen flow. The resulting powder was vibro-milled and then washed at reflux in 100 mL 1 M solution of H_2SO_4 for 3 h at 100 °C under continuous stirring and then filtered and rinsed with at least 0.5 L of milli-Q water and finally dried in oven at 40 ◦C overnight. After the acid leaching, the powder was vibro-milled a second time and then heated again at 900 °C as described before. The resulting powder, labelled as FNCBSt-X, $FNCBCO_2$-W or $FNCBCO_2$-5-Y (where X and W are the treatment time in min. and hours, respectively and Y is the temperature treatment) are the final catalyst. The sample obtained from the non-treated CB was

labelled as FNCB. This procedure allows to obtain more or less 200 mg of catalyst. The catalysts were vibro-milled another time before electrochemical test with the same settings listed above. Other iron molar percentage were also prepared, i.e., 1% and 4%, which however resulted in less active ORR catalysts with respect to the 2 %molar one (see 4.1.4).

3.4. Surface functionalization: Grafting

The synthesis through the grafting procedure is basically the introduction of specifical functional group on a carbon support. Grafting means that a molecule is bonded on the surface via covalent bond onto a certain surface, a carbon in this case.
The foundations of this reaction are explainable with a Tour-like reaction (Figure 3.8) in which an in-situ generated aryldiazonium cation or introduced as salt react spontaneously with a conjugated system, as the carbon surface:

- an electron of π-system reduce the cation leaving an unpaired electron on conjugated system
- with a second electron, coming from the breaking of the bond between the diazonium group and the aromatic ring an aryl radical is formed
- the aryl radical binds to the p-system through the unpaired electron

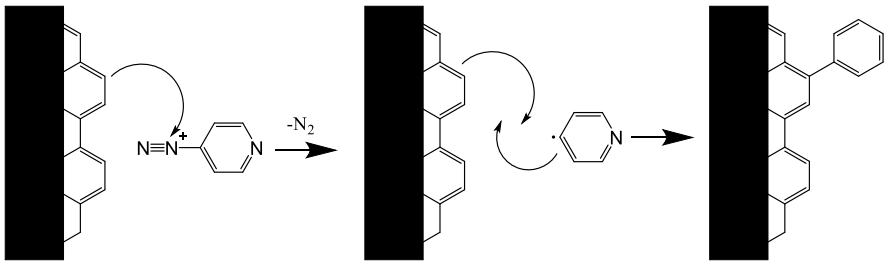

Figure 3.8. Dediazotation by Nucleophilic Attack of the Carbon Surface on the Benzene-diazonium Cation Followed by the Heterolytic Formation of a Covalent C-C Bond Between the Surface and the Aryl Group

The great advantages of this synthesis are that could be conducted in water, are occurring spontaneously and are in principle controllable with the time and temperature of grafting. Despite that one key point is the possibly of introducing single type of site in the carbon surface that could be studied separately, this condition is hardly achievable with pyrolysis route. Some notable examples are from the author that gave the name to Tour reaction, which study the functionalization of nanotube in ionic liquid [34] and in water [35].
In the field of oxygen reduction reaction, Tuci et al. published two study of carbon nanotube functionalization with several nitrogen containing molecule, in particular pyridinic and pyrrolic groups onto nanotubes to study the effect of the introduction of these functional groups on ORR, pyridinic nitrogen seems to favour a tetra-electronic pathway, while pyrrolic groups seems to promote the 2-electron reduction [36,37].
On carbon black the reaction was successfully carried out by Toupin et al. [38,39] by generating in situ diazonium salt that consequently generate the aryl radical, as already explained in Figure 3.8.
The functionalization could be checked via XPS since the nitrogen group is located on the surface and therefore a quantitative analysis could be carried out (Figure 3.9). Generally, the coverage seems to not overshoot couple of monolayers, but with more complex molecule, like 5-

AminoIndole, polymerization could occur giving more complex surface. This was observed by electrochemical studies [40], but in principle could append also spontaneously if the aryl radical react with attached molecule instead of carbon surface. The behaviour of poly-indole was also observed by Xu et. al [41] since several redox reaction could occur in the polymeric chain.

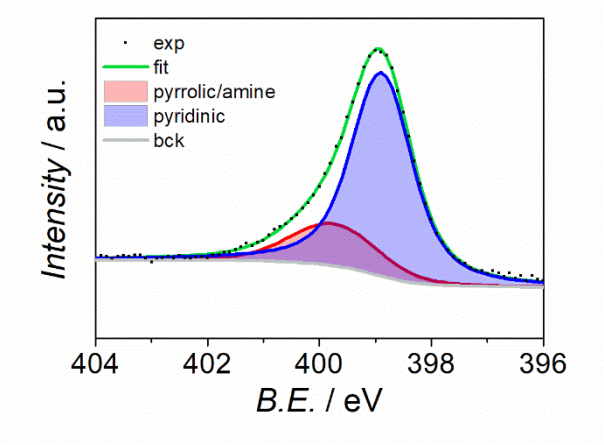

Figure 3.9. XPS N1s peak deconvolution

Another effect generated by the anchoring of molecules is the occlusion of the micropores (smaller than 10 Å), a result confirmed by surface analysis (Figure 3.10).

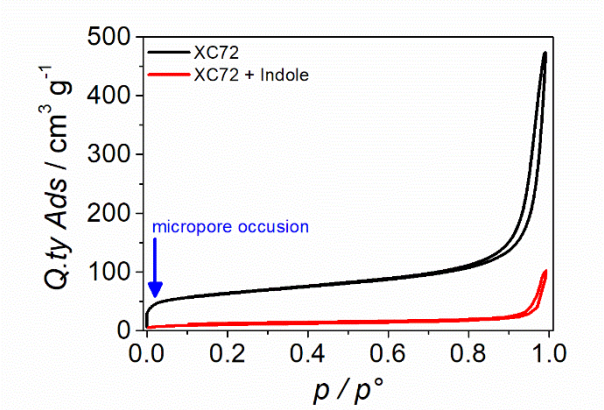

Figure 3.10. Evolution of N_2 physisorption isotherm after grafting of 5-Aminoindole

3.5. Bibliography

[1] M. Molina-Sabio, M.T. González, F. Rodriguez-Reinoso, A. Sepúlveda-Escribano, Effect of steam and carbon dioxide activation in the micropore size distribution of activated carbon, Carbon. 34 (1996) 505–509. https://doi.org/10.1016/0008-6223(96)00006-1.

[2] F. Rodríguez-Reinoso, M. Molina-Sabio, M.T. González, The use of steam and CO2 as activating agents in the preparation of activated carbons, Carbon. 33 (1995) 15–23. https://doi.org/10.1016/0008-6223(94)00100-E.

[3] F. Rodriguez Reinoso, M. Molina-Sabio, Activated carbons from lignocellulosic materials by chemical and/or physical activation: an overview | Francisco Rodriguez-Reinoso - Academia.edu, Carbon. 30 (1992) 1111–1118. http://www.academia.edu/4303771/Activated_carbons_from_lignocellulosic_materials_by_chemical_and_or_physical_activation_an_overview.

[4] A. Tyagi, S. Banerjee, S. Singh, K.K. Kar, Biowaste derived activated carbon electrocatalyst for oxygen reduction reaction: Effect of chemical activation, Int. J. Hydrogen Energy. 45 (2020) 16930–16943. https://doi.org/10.1016/j.ijhydene.2019.06.195.

[5] W. Shenggao, H. Wen, Z. Mingchen, G. Yuan, D. Quanrong, M. Yangwu, X. Qinfang, W. Geming, Synergistic effects of microstructures and active nitrogen content on the oxygen reduction reaction performance of nitrogen-doped carbon nanofibers via KOH activation heat treatment, J. Mater. Sci. 55 (2020) 10725–10739. https://doi.org/10.1007/s10853-020-04673-9.

[6] M. Mazzucato, G. Daniel, A. Mehmood, T. Kosmala, G. Granozzi, A. Kucernak, C. Durante, Effects of the induced micro- and meso-porosity on the single site density and turn over frequency of Fe-N-C carbon electrodes for the oxygen reduction reaction, Appl. Catal. B Environ. 291 (2021) 120068. https://doi.org/10.1016/j.apcatb.2021.120068.

[7] G. Tobias, L. Shao, C.G. Salzmann, Y. Huh, M.L.H. Green, Purification and Opening of Carbon Nanotubes Using Steam, J. Phys. Chem. B. 110 (2006) 22318–22322. https://doi.org/10.1021/jp0631883.

[8] J. Blackwood, A. Ingeme, The Reaction of Carbon with Carbon Dioxide at High Pressure, Aust. J. Chem. 13 (1960) 194. https://doi.org/10.1071/CH9600194.

[9] M. Thommes, K. Kaneko, A. V. Neimark, J.P. Olivier, F. Rodriguez-Reinoso, J. Rouquerol, K.S.W. Sing, Physisorption of gases, with special reference to the evaluation of surface area and pore size distribution (IUPAC Technical Report), Pure Appl. Chem. 87 (2015) 1051–1069. https://doi.org/10.1515/pac-2014-1117.

[10] A.C. Lua, J. Guo, Activated carbon prepared from oil palm stone by one-step CO2activation for gaseous pollutant removal, Carbon. 38 (2000) 1089–1097. https://doi.org/10.1016/S0008-6223(99)00231-6.

[11] R. Brandiele, L. Picelli, R. Pilot, V. Causin, A. Martucci, G.A. Rizzi, A.A. Isse, C. Durante, A. Gennaro, Nitrogen and Sulfur Doped Mesoporous Carbons, Prepared from Templating Silica, as Interesting Material for Supercapacitors, ChemistrySelect. 2 (2017) 7082–7090. https://doi.org/10.1002/slct.201701404.

[12] V. Perazzolo, C. Durante, R. Pilot, A. Paduano, J. Zheng, G.A. Rizzi, A. Martucci, G. Granozzi, A. Gennaro, Nitrogen and sulfur doped mesoporous carbon as metal-free electrocatalysts for the in situ production of hydrogen peroxide, Carbon. 95 (2015) 949–963. https://doi.org/10.1016/j.carbon.2015.09.002.

[13] E. Trevisanello, F. De Bon, G. Daniel, F. Lorandi, C. Durante, A.A. Isse, A. Gennaro, Electrochemically mediated atom transfer radical polymerization of acrylonitrile and poly(acrylonitrile-b-butyl acrylate) copolymer as a precursor for N-doped mesoporous carbons, Electrochim. Acta. 285 (2018) 344–354. https://doi.org/10.1016/j.electacta.2018.07.209.

[14] S. Lu, W. Xu, Y. Chen, Y. Jiang, Q. Yao, F. Luo, Y. Wang, X. Chen, Soft template synthesis of honeycomb-like ratiometric oxygen sensitive polystyrene nanospheres and their application in anti-counterfeit authentication and food packaging dynamic indication, Sensors Actuators

B Chem. 232 (2016) 585–594. https://doi.org/10.1016/j.snb.2016.04.007.
[15] M. Kopeć, M. Lamson, R. Yuan, C. Tang, M. Kruk, M. Zhong, K. Matyjaszewski, T. Kowalewski, Polyacrylonitrile-derived nanostructured carbon materials, Prog. Polym. Sci. 92 (2019) 89–134. https://doi.org/10.1016/j.progpolymsci.2019.02.003.
[16] V. Tkachenko, C. Matei Ghimbeu, C. Vaulot, L. Josien, L. Vidal, J. Poly, A. Chemtob, Diblock Copolymer Core-Shell Nanoparticles as Template for Mesoporous Carbons: Independent Tuning of Pore Size and Pore Wall Thickness, Langmuir. 35 (2019) 16324–16334. https://doi.org/10.1021/acs.langmuir.9b02994.
[17] Y. Zou, X. Zhou, J. Ma, X. Yang, Y. Deng, Recent advances in amphiphilic block copolymer templated mesoporous metal-based materials: assembly engineering and applications, Chem. Soc. Rev. 49 (2020) 1173–1208. https://doi.org/10.1039/C9CS00334G.
[18] M. Mazzucato, G. Daniel, V. Perazzolo, R. Brandiele, G.A. Rizzi, A.A. Isse, A. Gennaro, C. Durante, Mesoporosity and nitrogen doping: The leading effect in oxygen reduction reaction activity and selectivity at nitrogen-doped carbons prepared by using polyethylene oxide-block-polystyrene as a sacrificial template, Electrochem. Sci. Adv. (2022) 1–18. https://doi.org/10.1002/elsa.202100203.
[19] V. Perazzolo, G. Daniel, R. Brandiele, L. Picelli, G.A. Rizzi, A.A. Isse, C. Durante, PEO-b-PS Block Copolymer Templated Mesoporous Carbons: A Comparative Study of Nitrogen and Sulfur Doping in the Oxygen Reduction Reaction to Hydrogen Peroxide, Chem. - A Eur. J. 27 (2021) 1002–1014. https://doi.org/10.1002/chem.202003355.
[20] U.I. Kramm, I. Herrmann-Geppert, S. Fiechter, G. Zehl, I. Zizak, I. Dorbandt, D. Schmeißer, P. Bogdanoff, Effect of iron-carbide formation on the number of active sites in Fe-N-C catalysts for the oxygen reduction reaction in acidic media, J. Mater. Chem. A. 2 (2014) 2663–2670. https://doi.org/10.1039/c3ta13821f.
[21] S. Pylypenko, S. Mukherjee, T.S. Olson, P. Atanassov, Non-platinum oxygen reduction electrocatalysts based on pyrolyzed transition metal macrocycles, Electrochim. Acta. 53 (2008) 7875–7883. https://doi.org/10.1016/j.electacta.2008.05.047.
[22] A. Serov, K. Artyushkova, P. Atanassov, Fe-N-C oxygen reduction fuel cell catalyst derived from carbendazim: Synthesis, structure, and reactivity, Adv. Energy Mater. 4 (2014) 1–7. https://doi.org/10.1002/aenm.201301735.
[23] M. Mazzucato, C. Durante, How determinant is the iron precursor ligand in Fe-N-C single-site formation and activity for oxygen reduction reaction?, Electrochim. Acta. 394 (2021) 139105. https://doi.org/10.1016/j.electacta.2021.139105.
[24] F. Luo, C.H. Choi, M.J.M. Primbs, W. Ju, S. Li, N.D. Leonard, A. Thomas, F. Jaouen, P. Strasser, Accurate evaluation of active-site density (SD) and turnover frequency (TOF) of PGM-free metal-nitrogen-doped carbon (MNC) electrocatalysts using CO cryo adsorption, ACS Catal. (2019) 4841–4852. https://doi.org/10.1021/acscatal.9b00588.
[25] J. Tian, A. Morozan, M.T. Sougrati, M. Lefèvre, R. Chenitz, J.-P.P. Dodelet, D. Jones, F. Jaouen, Optimized synthesis of Fe/N/C cathode catalysts for PEM fuel cells: A matter of iron-ligand coordination strength, Angew. Chemie - Int. Ed. 52 (2013) 6867–6870. https://doi.org/10.1002/anie.201303025.
[26] D. Menga, J.L. Low, Y.S. Li, I. Arčon, B. Koyutürk, F. Wagner, F. Ruiz-Zepeda, M. Gaberšček, B. Paulus, T.P. Fellinger, Resolving the Dilemma of Fe-N-C Catalysts by the Selective Synthesis of Tetrapyrrolic Active Sites via an Imprinting Strategy, J. Am. Chem. Soc. 143 (2021) 18010–18019. https://doi.org/10.1021/jacs.1c04884.
[27] A. Zitolo, V. Goellner, V. Armel, M.T. Sougrati, T. Mineva, L. Stievano, E. Fonda, F. Jaouen, Identification of catalytic sites for oxygen reduction in iron- and nitrogen-doped graphene materials, Nat. Mater. 14 (2015) 937–942. https://doi.org/10.1038/nmat4367.
[28] D. Malko, A. Kucernak, T. Lopes, Performance of Fe–N/C Oxygen Reduction Electrocatalysts toward NO_2^-, NO, and NH_2OH Electroreduction: From Fundamental Insights into the Active Center to a New Method for Environmental Nitrite Destruction, J. Am. Chem. Soc. 138 (2016) 16056–16068. https://doi.org/10.1021/jacs.6b09622.
[29] D. Malko, T. Lopes, E. Symianakis, A.R. Kucernak, The intriguing poison tolerance of non-

precious metal oxygen reduction reaction (ORR) catalysts, J. Mater. Chem. A. 4 (2015) 142–152. https://doi.org/10.1039/c5ta05794a.
[30] F. Luo, A. Roy, L. Silvioli, D.A. Cullen, A. Zitolo, M.T. Sougrati, I.C. Oguz, T. Mineva, D. Teschner, S. Wagner, J. Wen, F. Dionigi, U.I. Kramm, J. Rossmeisl, F. Jaouen, P. Strasser, P-block single-metal-site tin/nitrogen-doped carbon fuel cell cathode catalyst for oxygen reduction reaction, Nat. Mater. (2020) 1–9. https://doi.org/10.1038/s41563-020-0717-5.
[31] G. Wu, K.L. More, C.M. Johnston, P. Zelenay, High-performance electrocatalysts for oxygen reduction derived from polyaniline, iron, and cobalt, Science. 332 (2011) 443–447. https://doi.org/10.1126/science.1200832.
[32] F. Jaouen, M. Lefèvre, J.P. Dodelet, M. Cai, Heat-treated Fe/N/C catalysts for O2 electroreduction: Are active sites hosted in micropores?, J. Phys. Chem. B. 110 (2006) 5553–5558. https://doi.org/10.1021/jp057135h.
[33] L. Jiao, J. Li, L.L.R. Richard, Q. Sun, T. Stracensky, E. Liu, M.T. Sougrati, Z. Zhao, F. Yang, S. Zhong, H. Xu, S. Mukerjee, Y. Huang, D.A. Cullen, D.J. Myers, F. Jaouen, Q. Jia, Chemical vapor deposition of Fe-N-C oxygen reduction catalysts with full utilization of dense Fe-N4 sites, ChemRxiv. (2020). https://doi.org/10.26434/chemrxiv.12918983.v1.
[34] B.K. Price, J.L. Hudson, J.M. Tour, Green chemical functionalization of single-walled carbon nanotubes in ionic liquids, J. Am. Chem. Soc. 127 (2005) 14867–14870. https://doi.org/10.1021/ja053998c.
[35] B.K. Price, J.M. Tour, Functionalization of single-walled carbon nanotubes “on water,” J. Am. Chem. Soc. 128 (2006) 12899–12904. https://doi.org/10.1021/ja063609u.
[36] G. Tuci, C. Zafferoni, A. Rossin, A. Milella, L. Luconi, M. Innocenti, L. Truong Phuoc, C. Duong-Viet, C. Pham-Huu, G. Giambastiani, Chemically Functionalized Carbon Nanotubes with Pyridine Groups as Easily Tunable N-Decorated Nanomaterials for the Oxygen Reduction Reaction in Alkaline Medium, Chem. Mater. 26 (2014) 3460–3470. https://doi.org/10.1021/cm500805c.
[37] X. Zhang, L. Truong-Phuoc, X. Liao, G. Tuci, E. Fonda, V. Papaefthymiou, S. Zafeiratos, G. Giambastiani, S. Pronkin, C. Pham-Huu, An Open Gate for High-Density Metal Ions in N-Doped Carbon Networks: Powering Fe-N-C Catalyst Efficiency in the Oxygen Reduction Reaction, ACS Catal. 11 (2021) 8915–8928. https://doi.org/10.1021/acscatal.1c01638.
[38] M. Toupin, D. Bélanger, Thermal stability study of aryl modified carbon black by in situ generated diazonium salt, J. Phys. Chem. C. 111 (2007) 5394–5401. https://doi.org/10.1021/jp066868e.
[39] M. Toupin, D. Bélanger, Spontaneous functionalization of carbon black by reaction with 4-nitrophenyldiazonium cations, Langmuir. 24 (2008) 1910–1917. https://doi.org/10.1021/la702556n.
[40] H. Talbi, D. Billaud, Electrochemical properties of polyindole and poly(5-cyanoindole) in LiClO4-acetonitrile and in HCl and HClO4 solutions, Synth. Met. 93 (1998) 105–110. https://doi.org/10.1016/s0379-6779(97)04098-8.
[41] L. Xu, D. Li, W. Zhou, Y. Ding, Y. Wu, J. Xu, X. Duan, High-efficiency electrodeposition of polyindole nanocomposite using MoS2 nanosheets as electrolytes and their capacitive performance, Arab. J. Chem. 13 (2020) 6061–6071. https://doi.org/10.1016/j.arabjc.2020.05.006.

4. Effects of the induced micro-and meso-porosity on the single site density and turn over frequency of Fe-NC carbon electrodes for the oxygen reduction reaction

Fe-N-C have emerged as one of the best non-PGM alternatives to Pt/C catalysts for the electrochemical reduction of O_2 in fuel cells. In this chapter, the effect of steam and CO_2 treatments at high temperatures on the nanometric porous structure of a commercial carbon black is studied. Using those support materials, different Fe-N-C catalysts have been prepared to achieve a better understanding on the role of micro- and mesopores of the support towards catalytic site formation and site activity. Different time and temperature of treatments result in an almost linear increment of surface area and microporous volume, which allows better nitrogen functionalization. Site density evaluation, performed using a recently described NO-stripping technique, showed an increase in site density and TOF which correlates well with the morphology variation. The percentage of active iron increases from 2.65% to 14.74% in activated catalysts confirming a better access of electrolyte to the iron sites.

4.1. Results

4.1.1. Carbon supports activation and characterization

4.1.1.1.Physisorption analysis

The carbon black used here, namely Super P® Conductive CB was chosen as starting carbon material because of the relatively low surface area (66 $m^2\ g^{-1}$) and a comparable micropore and mesopore area (Table 4.1). The first parameter evaluable to follow to confirm the activation success is the calculation of burn-off, namely the mass loss percentage [1,2]. CO_2 treatment is weaker in term of reactivity compared to steam, indeed 1 h of treatment at 950 °C in carbon dioxide result in a burn-off of only 3% while with steam at the same temperature the % of weight loss is 64%.

The second analysis that could be made is the physisorption of N_2 at 77.3 K. For samples treated with CO_2 at different exposure the isotherms change from a hybrid I-II type with a very small hysteresis for the pristine CB sample, indicating a starting material made of macropore with a small amount of micro and mesopore, to isotherms with H3/H4 type hysteresis for the activated CBs (Figure 4.1a). The same is true for different temperature of treatment (Figure 4.1b), the isotherm of sample treated at 1050°C shows a more pronounced H3/H4 type hysteresis. This result is in line with the endothermic nature of the reaction, which is actually one of the reasons why steam and CO_2 are preferred for activation instead of air [1].

In general, the growing of initial uptake at low relative pressure indicates an evolution of micro and mesopore (Figure 4.1a, b, d, and e), whereas the steep uptake at high relative pressure indicates that also macropores are evolving, or large mesopore are widen. The appearance of this type of hysteresis is also related to slit-shaped pores, supporting the choice of the DFT model. The characteristic hysteresis closure at relative pressure of about 0.45 is generally due to cavitation [3,4]. As said, the effect of carbon dioxide activation is generally described as an opening of narrow micropores followed by widening due to the reaction $C + CO_2 \rightarrow 2CO$ enhanced by the oxidizing behaviour of CO_2 in the 800-1000 °C range of temperature [5–7]. The actual mechanism is not well understood, and the phenomenon could occur in different steps and furthermore the surface chemistry of the CB (oxygen and hydrogen content) can impact on the reactivity.

In our case it was possible to observe a general evolution of the surface area initially due to the evolution of micropore that for longer treatment is also accompanied by the development of mesoporosity and macroporosity. Increasing CO_2 treatment time produces a linear evolution of surface area (~ 260 m^2 g^{-1} for 9 h) with a slightly preferential evolution of micropore accompanied by an evolution of mesopore due to a widening effect (Figure 4.1g). Figure 4.1d report the evolution of pore dimensions and it is evident that the CO_2 treatment mostly increases the pore volume while keeping the pore diameter almost unchanged. This can be explained considering either the opening of new pores or the elongation of those already existing. The same is true for temperature variation (Figure 4.1e, g). It is possible to conclude that an increment of 100 °C in the set temperature from 950 °C to 1050 °C is more effective than the increment of 4h at 950 °C (from 5h to 9h). The histogram in Figure 4.1l resumes the effect of time and temperature on the increment of the surface area, and it is well evident that the increment of temperature is more effective.

The adsorption isotherm for the sample activated with steam gas, are shown in Figure 4.1c. As observed for carbon dioxide activation, the isotherms evolve from a hybrid I-II type with no or negligible hysteresis to a pronounced H3/H4 hysteresis loop of CBSt-60, which indicates an evolution of micro and to a more extent of mesopore as observed also for the CO_2 treatments. The action seems slightly different, in fact, a preferential widening of mesopore of various dimension, in particular for the longer treatment (60 min) and a consistent gain in volume. Nevertheless, a peak around 4-5 nm arises, probably due to the opening of existing pore of 2-3 nm in the pristine CB, as visible in the histogram in Figure 4.1f. This confirms that both opening and widening/elongation effects are present.

From Figure 4.1i, it is evident that the surface area in all dimensional range increase almost linearly with the time of exposure. It is important to stress out that the steam treatment is much more effective at 950 °C than at 800 °C as evidenced in Figure 4.1m, where the effect of time exposure is also reported. Furthermore, steam treatment is much more effective than the CO_2 one, since almost the same textural values are obtained with a 20 min steam treatment compared to a 9 h CO_2 treatment at the very same temperature. Summarizing we were able to prepare different CB supports starting from a low surface area one, where a significant and fast improvement in pore volume is achieved with steam, while with CO_2 a more controlled evolution is possible.

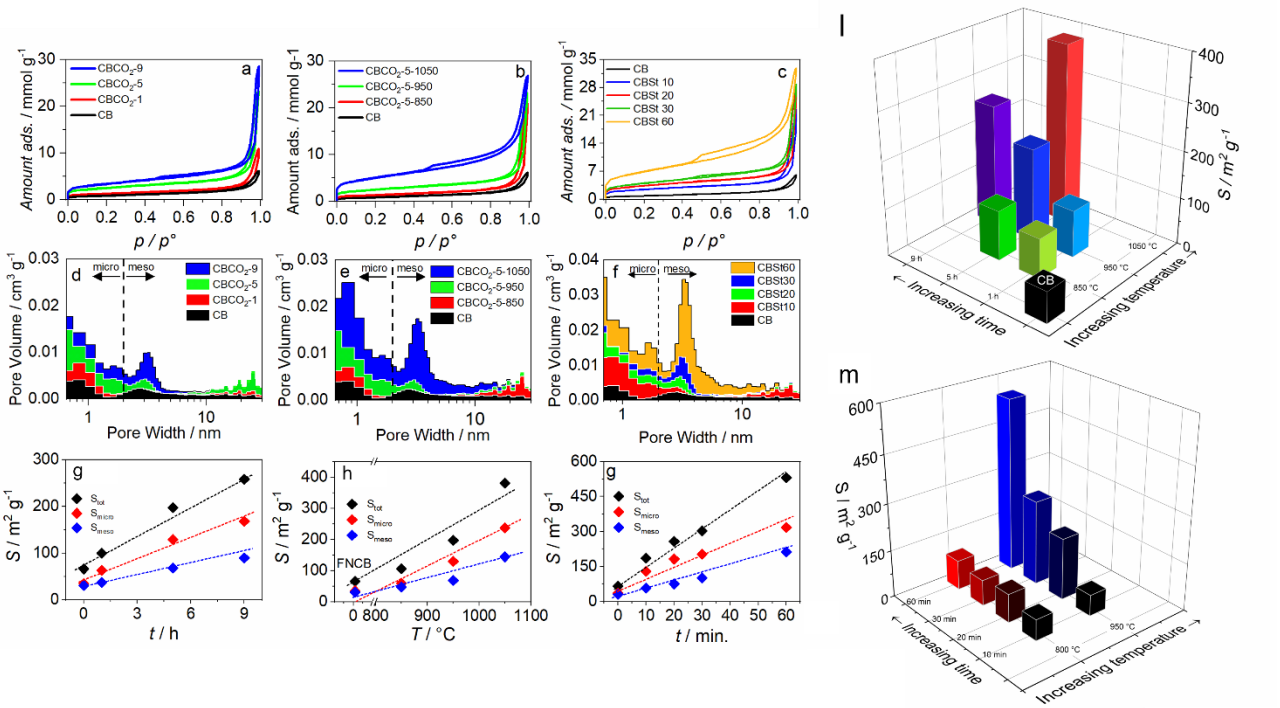

Figure 4.1. (a-c) N_2 adsorption isotherms and (d-f) pore size distribution for CO_2 treatment at (a, d) fixed temperature varying the exposure time and (b, e) fixed exposure time of 5 h and different temperature and (c, f) steam treatment at different exposure time; (g-i) surface area and surface of macropore and micropore with respect to time and temperature of activation treatment; Combined effect of time and temperature in (l) CO_2 treatment and (m) steam treatment

Table 4.1. Textural properties and elemental analysis of activated CB supports

	EA[a]		S [b]	S_μ [c]	S_{meso}	V_μ [c]	V_{meso}	V_{tot} [d]
	%C	%H	$m^2\ g^{-1}$	$m^2\ g^{-1}$	$m^2\ g^{-1}$	$cm^3\ g^{-1}$	$cm^3\ g^{-1}$	$cm^3\ g^{-1}$
CBSt-0	98.75	0.17	66	35	31	0.015	0.137	0.204
CBSt-10	85.86	0.12	186	129	57	0.058	0.365	0.767
CBSt-20	98.81	0.12	257	182	75	0.081	0.432	0.923
CBSt-30	97.29	0.17	303	202	101	0.092	0.485	0.982
CBSt-60	97.29	0.17	531	318	213	0.146	0.742	1.108
$CBCO_2$-1	98.87	0.06	100	63	37	0.027	0.200	0.368
$CBCO_2$-5	98.23	0.24	197	129	68	0.055	0.457	0.791
$CBCO_2$-9	98.08	0.08	258	168	90	0.076	0.456	0.969
$CBCO_2$-5-850	96.79	0.10	106	59	47	0.024	0.355	0.719
$CBCO_2$-5-950	98.23	0.24	197	129	68	0.055	0.457	0.791
$CBCO_2$-5-1050	97.33	0.10	381	237	144	0.108	0.580	0.903

[a]elemental analysis by CHNS elemental analyser, [b]QSDFT slit method 0.5-40nm, [c]pore width < 2 nm, [d]obtained by applying Gurvitsch law at $p/p^0 \sim 0.98$

4.1.1.2.Raman characterization

The activation treatment could in principle also affect the degree of graphitization, for that reason Raman characterization was performed on all samples (Figure 4.2a). Up to 5 bands (Figure 4.2b, Table 10.1) in the region between 1100 and 1700 cm^{-1} [8–11] are used for the deconvolution, after a normalization relative to the G band peak (namely to the Raman shift around 1600 cm^{-1} for which the maximum intensity is recorded [12]). The region between 2200 and 3200 cm^{-1} is generally called the graphene/graphene oxide region because at least two distinct bands similar to those of graphene oxide are observed in materials such as CB (Figure 4.2a). The similarity comes from the

aromatic region with non-oxidized benzene rings and the regions containing C-OH, epoxide, and double bonds. [10,13–15]. No particular changes were neither observed in I_G/I_{D1} ratio or in G band position upon steam treatment (Figure 4.2c and f), only a slight change in graphene/graphene oxide band in the region 2400 ÷ 3000 cm^{-1} was observed when comparing CBSt-60 with the pristine CB. More evident changes were observed for carbon dioxide treatment (Figure 4.2d,e), in particular the I_G/I_{D1} ratio and the G band position slightly changed (Table 10.2), though without a clear trend, and the evident the decreasing of the D1 band intensity for sample treated at 950 and 1050 °C. This behaviour agrees with the raising of graphitization degree in the material [8,16]. These properties is also evaluable by calculating the R2 parameter, where R2 = D1/(G + D1 + D2) is the ratio between the area of D1 peak and the sum of G, D1 and D2 areas. For poorly organized carbon materials R2 > 0.5, while a R2 < 0.5 is indicative of highly graphitized carbons. In the present case the R2 parameter slightly decreases after prolonged CO_2 or steam treatment or increasing the temperature (Table 10.2 and Figure 4.2f), confirming a reasonable increase of graphitization [17].

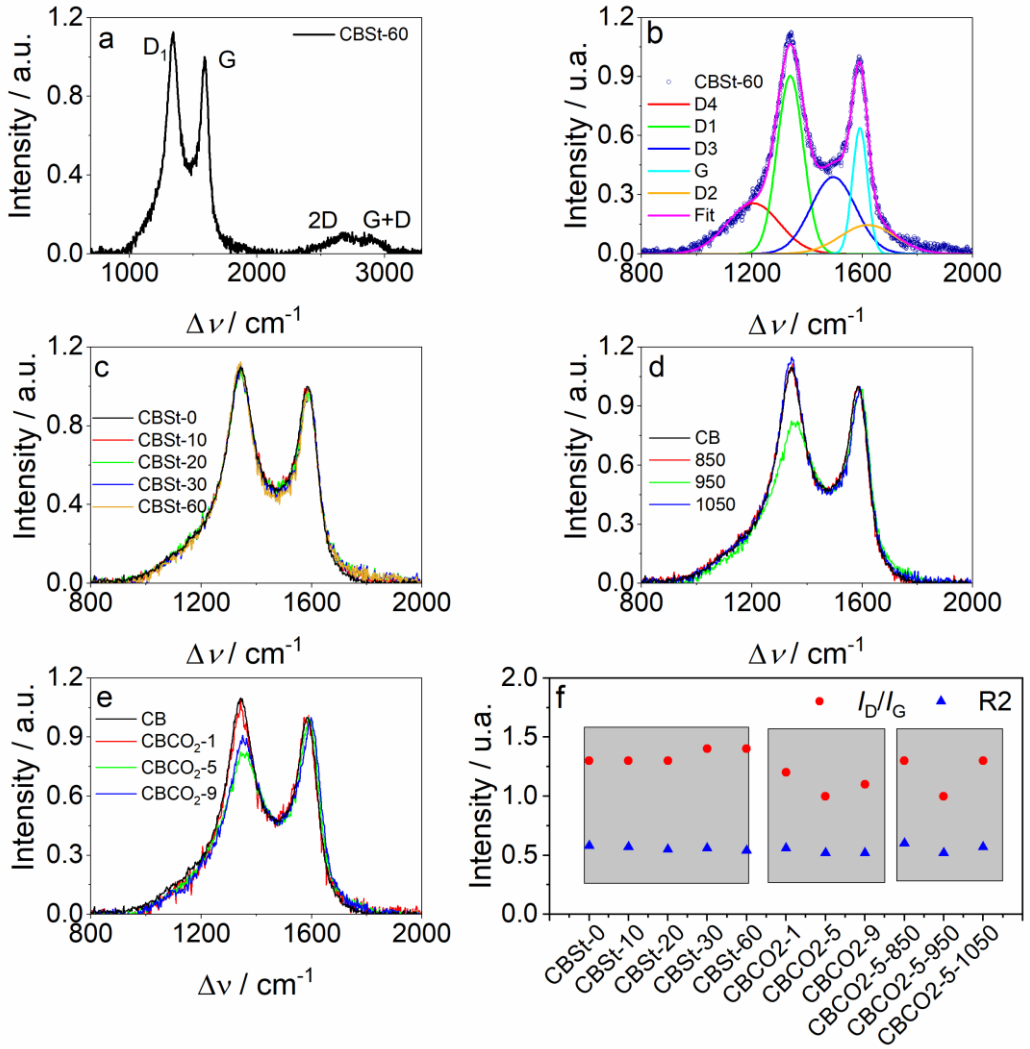

Figure 4.2. a) full range Raman spectrum for CBSt-60; b) example of Raman spectrum deconvolution; Overlay of spectra acquired in different activation condition c) steam; d) CO_2 treatment at different temperature for 5 h; e) CO_2 treatment at different exposure time; f) I_d/I_g ratio variation within single set of activated carbons and R2 values

4.1.1.3.Other characterization

All the Fe-N-C catalysts where prepared by thermal treatment of activated CBs and $Fe(Phen)_3Cl_2$ at 900 °C according to a procedure described in the experimental section.

The optimal amount of iron-phenanthroline used for the formation of $Fe\text{-}N_x$ active sites in the final catalyst was defined by evaluating the effect of different initial amounts on the resultant catalyst ORR activity. The selection was made by adopting $CBCO_2$-5 and four different $Fe(Phen)_3Cl_2$ molar concentrations i.e., 0, 1, 2 and 4 $\%_{mol}$. According to the elemental analysis reported in Table 10.3, the maximum amount of nitrogen was obtained for the 2% sample. More details are given in one of the following paragraphs.

Elemental analysis confirms that the nitrogen fixation on all catalyst. Interestingly, the weight percentage concentration grows by one order of magnitude on going from 0.1 % in FNCB to 1.06 % in FNCBSt-30 and to 0.9 % for $FNCBCO_2$-5. However, it is bizarre to see that the most porous sample of each set shows a small decrement in nitrogen content. This might suggest that the percentage around 1% of nitrogen is the maximum obtainable with these support materials under the adopted synthetic conditions, and also that the higher micro/mesopore content are beneficial in Fe/N fixation.

A further characterization that could reveal the morphology and the presence of inorganic phases is TEM. In principle an ideal Fe-N-C must contain only isolated FeN_4 sites because they lead to the production of water (4e-ORR), while other phases like FeO_x or FeC_x are less or inactive and could also hinder the accessibility toward the active site. Figure 4.3 shows TEM images of the investigated catalysts obtained from different activated supports. Sorting through the images of the steam activated catalysts, there are no evident changes in CBs particle size, which remains in the range of 40-80 nm as for the pristine CB particles. This is not surprisingly since the activation treatment act consuming carbon on the surface, but it does not lead to particle breaking, which it has to append is more probable during the milling phase. More evident is the morphology variation, since the activated CBs becomes progressively more porous and less dense on passing from zero to 60 min of steam treatment (Figure 4.3a-e). Isolated iron NPs enveloped in a carbon shell are visible since the leaching of protect NPs is more demanding. The CO_2 activated Fe-N-C samples are reported in Figure 4.3f-j. Also in this case, there is no evident change in the particles dimension, while some shell-like nanoparticles and some nanotube like structure containing Fe NPs could be observed. In general, these samples do not show a large quantity of Fe NPs, in good agreement with the low content of surface iron derived from the XPS analysis (vide infra).

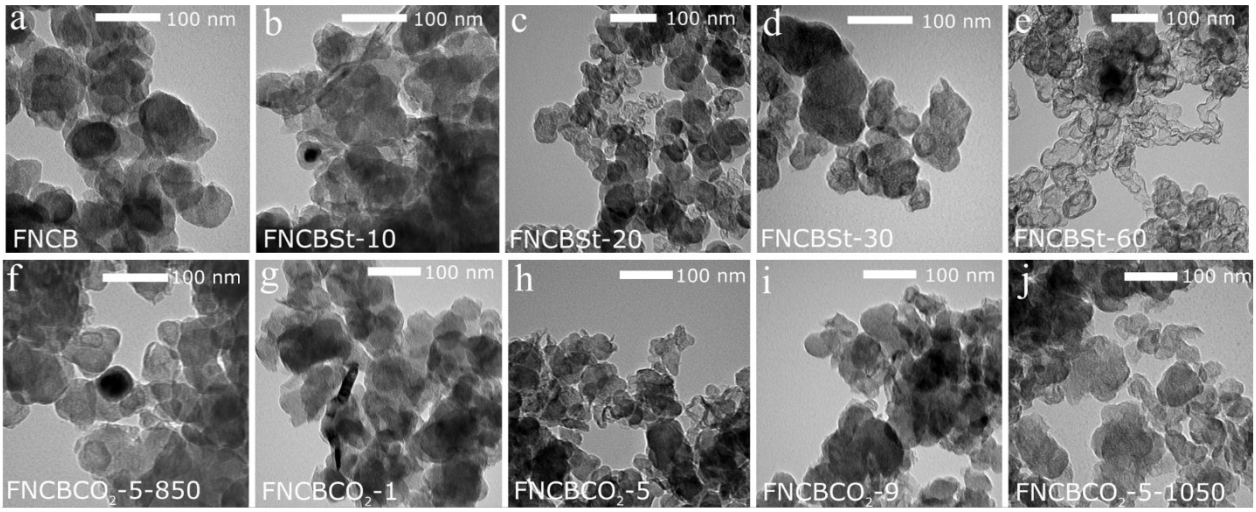

Figure 4.3. a-e) TEM images of steam treated samples and f-j) TEM images of CO_2 treated ones

Elemental analysis gives the bulk composition of catalysts, and it is limited to C, H, N and S, therefore, to evaluate the surface composition, which is the part of material that act in the catalytic process, XPS analysis was used, which evidenced the surface presence of iron, oxygen, carbon, and nitrogen. The maximum nitrogen surface content is limited to ca. 1 % (in FNCBCO$_2$-9 and FNCBCO$_2$-5-850, see Table 4.2), as already evidenced from the bulk elemental analysis.

Table 4.2. Elemental analysis and XPS data deconvolution

	EA [a]			XPS [b]			
	%C	%N	%H	C 1s	O 1s	N 1s	Fe 2p
FNCBSt-0	95.91	95.91	95.91	91.52	7.04	1.03	0.41
FNCBSt-10	88.18	88.18	88.18	90.54	8.25	0.80	0.41
FNCBSt-20	91.46	91.46	91.46	92.37	6.26	0.91	0.46
FNCBSt-30	91.23	91.23	91.23	92.58	6.01	0.91	0.50
FNCBSt-60	92.11	92.11	92.11	93.58	5.51	0.64	0.27
FNCBCO$_2$-1	87.32	87.32	87.32	90.45	8.40	0.78	0.36
FNCBCO$_2$-5	95.75	95.75	95.75	92.34	6.79	0.59	0.27
FNCBCO$_2$-9	92.28	92.28	92.28	87.74	10.51	1.12	0.63
FNCBCO$_2$-5-850	91.53	91.53	91.53	86.14	11.78	1.23	0.85
FNCBCO$_2$-5-950	95.75	95.75	95.75	92.34	6.79	0.59	0.27
FNCBCO$_2$-5-1050	95.07	95.07	95.07	91.73	7.38	0.71	0.18
	N 1s deconvolution [c]						
	N$_{Iminic}$	**N**$_{Pyridinic}$	**N**$_{Fe\text{-}Nx}$	**N**$_{Pyrrolic}$	**N**$_{Graphitic}$	**N**$_{N\text{-}O}$	
FNCBSt-0	95.91	95.91	95.91	91.52	7.04	1.03	
FNCBSt-10	88.18	88.18	88.18	90.54	8.25	0.80	
FNCBSt-20	91.46	91.46	91.46	92.37	6.26	0.91	
FNCBSt-30	91.23	91.23	91.23	92.58	6.01	0.91	
FNCBSt-60	92.11	92.11	92.11	93.58	5.51	0.64	
FNCBCO$_2$-1	87.32	87.32	87.32	90.45	8.40	0.78	
FNCBCO$_2$-5	95.75	95.75	95.75	92.34	6.79	0.59	
FNCBCO$_2$-9	92.28	92.28	92.28	87.74	10.51	1.12	
FNCBCO$_2$-5-850	91.53	91.53	91.53	86.14	11.78	1.23	
FNCBCO$_2$-5-950	95.75	95.75	95.75	92.34	6.79	0.59	
FNCBCO$_2$-5-1050	95.07	95.07	95.07	91.73	7.38	0.71	

[a] elemental analysis by CHNS elemental analyser, [b] surface chemical composition from XPS measurements expressed in weight percentage, [c] speciation of the nitrogen according to the deconvolution of high-resolution N 1s core-level XPS spectra

Up to 6 components (Figure 4.4a and Figure 10.10) i.e., imine N (397.8 eV), pyridinic N (398.8 eV), Fe-N$_x$ (399.9 eV), pyrrolic N (400.7 eV), graphitic N (401.7 eV) and N-O group (402.7 eV) [18,19] were used to fit the spectra. The low N content (< 1%, close to the XPS detection limit) suggests taking with caution the deconvoluted data. Actually, the data show an apparent increment of pyridinic and pyrrolic nitrogen, but a diminution of Fe-N$_x$ (apart from the FNCBCO$_2$-9 sample, see Figure 4.4d-f and Table 4.2). This last finding was unexpected considering that several works in literature claim the fundamental role of microporosity for the iron-nitrogen centre formation and therefore Fe-N$_x$ were expected to increase moving from pristine to activated carbons showing a significant higher content of micropores [20,21]. That with other anomalies [22] bring to the conclusion that XPS measurements are helpful to characterize different nitrogen sites in non-porous samples, while it has some limits to determine bulk N sites in highly porous samples, in

particular when the nitrogen content is too low. Regarding this last aspect other considerations are done later when showing the electrocatalytic results. The C 1s peak was also examined (Figure 4b and Figure 10.11) to evaluate the sp^2/sp^3 ratio and the superficial graphitization degree. The main carbon components at BE between 284.2-284.4 eV is attributed to C-sp^2. At higher BE (285.4 eV), the peak represents the sp^3 C-C bond. There is also a substantial amount of carbon bound to nitrogen or/and to oxygen: peaks at BEs higher than 286.4 eV are due to carbon species bound to oxygen (C=O, O-C=O, O-C(O)-O or oxygen and nitrogen (C-N=O, N-C=O). The peak at 291.1 eV is due to shakeup satellite (π-π*) [23–26]. No evident changes have been observed from the C 1s high-resolution core-level XPS spectra of different samples activated in steam or CO_2, but a slight increment of sp^2 accompanied by a decrement of sp^3 is clearly visible (Figure 4.4c) when the CBs were activated in CO_2 at different temperatures.

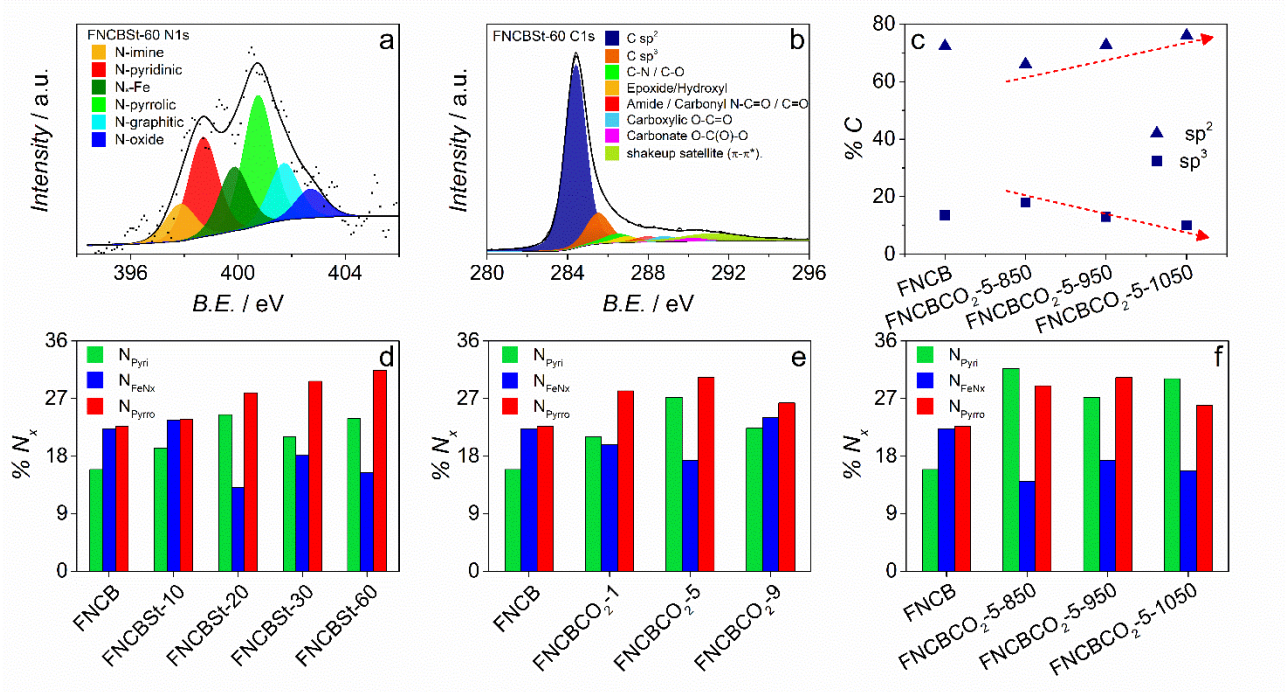

Figure 4.4. High-resolution core-level XPS spectra of N 1s (a) and C 1s (b) regions and deconvolution into single chemical components, c) sp^2 and sp^3 content variation in CO_2 treated catalysts as function of temperature, d-f) nitrogen functional groups speciation derived from the deconvolution of the N 1s spectra (data resumed in Table 4.2).

4.1.2. Electrochemical characterization of Fe-N-C catalysts

4.1.2.1. Oxygen reduction reaction via RRDE analysis

An example of voltammetric response for those material is shown in Chapter 2/10, where FNCBSt-30 and FNCBCO₂-5 were chosen as example. The other catalysts show very similar behaviour. In all cases, the voltammetric background shows a couple of peaks between 0.5 V ad 0.7 V vs. RHE, which could be attributed to the reversible Fe^{3+}/Fe^{2+} and/or to a quinone/hydroquinone redox couple [19,27]. The samples obtained from activated CBs are also characterized by a higher capacitive current with respect to the pristine one, ascribable to the increased active surface area. In oxygen-saturated electrolyte, a very intense and narrow peak appears at around 0.75 V vs. RHE (scan rate at 5 mV s^{-1}) which is not present in the background and is assigned to the ORR process (Figure 2.21/2.22). The peak potential shifts, as expected, with the variation of the scan rate, pointing out the irreversibility of the ORR reaction.

Fe-N-C catalysts obtained from steam activated carbon black, were characterized by RRDE measurement (Figure 4.5a). Half-wave potential clearly shifts toward positive potential passing from

FNCB to FNCBSt-60, while there is a diminution of the limiting current (j_L). The first effect can be attributed to an increase of the site density or simply an increase of the accessible sites, that allows ORR at lower overpotential. If we rely on the fact that passing from FNCB to FNCBSt-60, pyridinic and pyrrolic functional groups increase as pointed out by XPS analysis, the ORR mechanism probably follows a 2x2 e^- pathway. This would explain also why the limiting current density is lower with respect to that expected for a 4e^- pathway, and this is even more evident for the activated Fe-N-Cs.

The selectivity is also influenced by the loading on the electrode indeed the relatively higher loadings used for the RRDE analysis (0.6 mg cm^{-2}) result in the formation of thicker catalyst layer which might hinder the H_2O_2 release [28]. In following paragraph this effect was studied (4.1.3) for FNCBCO$_2$-5. It is evident that for RRDE measurements, the quantity of hydrogen peroxide produced (Figure 4.10) are proportional to the loading meaning that the reduction pathway is not a pure 4e^- and for higher loading some hydrogen peroxide is trapped in the material and could be further reduced to water. Therefore, when a highly porous carbon is used, H_2O_2 is not further reduced to H_2O, but it is released from the electrode layer.

The histograms in Figure 4.5b show two other important parameters for evaluating the ORR performance, namely kinetic current j_k and $E_{1/2}$ half-wave potential. The latter increases from 0.6 V vs. RHE to 0.654 V vs. RHE and j_k from 0.16 to 0.50 A g^{-1} (3 times higher) passing from the FNCB to the activated FNCBSt-60. Figure 5c shows that the Tafel slope (around −100 mV dec^{-1}) does not significantly change within this set of materials and the right-shift is caused by the increment of kinetic current. The number of transferred electron and peroxide yield is comparable for all sample (Figure 4.5d), averaging around 3.90 and 5% at 0 V vs. RHE, respectively.

The explanation of this improvement in activity must be searched in variation of morphology and chemistry of the samples. As reported in Figure 4.5e and f, the almost linear correlation between both $E_{1/2}$ as well as j_k with the microporous surface (that grows linearly with treatment time as reported in Figure 4.1) is rather clear. In the first instance, this should be attributed to a higher percentage of the sole Fe-N_x (not necessarily the density per unit of area) that are preferentially formed in the micropores, but from our XPS analysis this correlation is not straightforward at all.

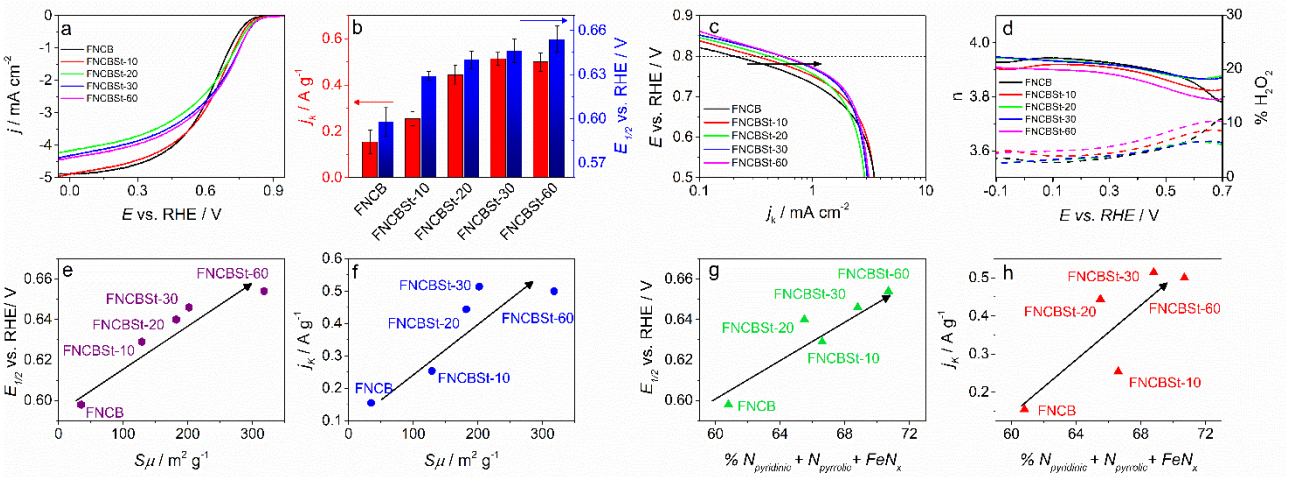

Figure 4.5 a) LSV recorded in oxygen-saturated electrolyte. The scan rate was 2 mV s^{-1} and rotation speed was 1600 rpm. b) kinetic current and half-wave potential for FNCBSt-X, c) Tafel plot and d) transferred electron number and hydrogen peroxide yield derived from RRDE measurements for FNCBSt-X; e) $E_{1/2}$ and f) j_k correlations with surface area of micropores; g) $E_{1/2}$ and h) j_k correlation with pyridinic, pyrrolic and Fe-N_x group percentage (see Table 4.2).

If we rely on the XPS deconvolution, the reported improvement is only explainable by considering the overall increase of the pyridinic, pyrrolic and Fe-N_x centres. All the sites are able to catalyse the ORR to water via either the 4e^- pathway or the 2x2 electron pathway. In the latter case, reducing

hydrogen peroxide before leaving the catalyst layer. In other word, the highest surface area, and in particular the higher micropore surface area, brings a preferential nitrogen functionalization to create C-N (pyridinic, pyrrolic) and Fe-N_x instead of graphitic and iminic groups, so the improvement in activity is related to a higher percentage content of groups that effectively catalyse ORR (Figure 4.5g and h).

Similarly, to what observed with steam activated sample, is seen for CO_2 activated carbon (Figure 4.6). The LSV recorded from CB samples, treated at different CO_2 exposure times, exhibit a well-defined plateau, with the sole exclusion of FNCBCO_2-9. It is evident that $E_{1/2}$ becomes more positive passing from FNCB to FNCBCO_2-5 (Figure 4.6a), so that it results even more positive than the steam activated samples. It is possible that CO_2 treatment leads to a wider network of interconnected pores allowing a better diffusion of reactants and products toward active sites, in particular near the surface of carbon. Similarly, the effect of temperature in CO_2 treatment leads to better catalytic performances with the exclusion of FNCBCO_2-5-1050. The diminution of activity observed for both FNCBCO_2-9 and FNCBCO_2-5-1050, which however showed the highest surface area among their respective sets (see Table 4.1), is not easy to understand also considering that for steam treatment this was not observed. Our presumption is that a too long exposure or too high temperature could promote some secondary porogenic effect of phenanthroline that block interconnected pores and hindered the diffusion during Fe/N doping.

Also for the CO_2 activated Fe-N-C catalysts, $E_{1/2}$ or j_k correlate with the superficial nitrogen content (Figure 4.6c and f).

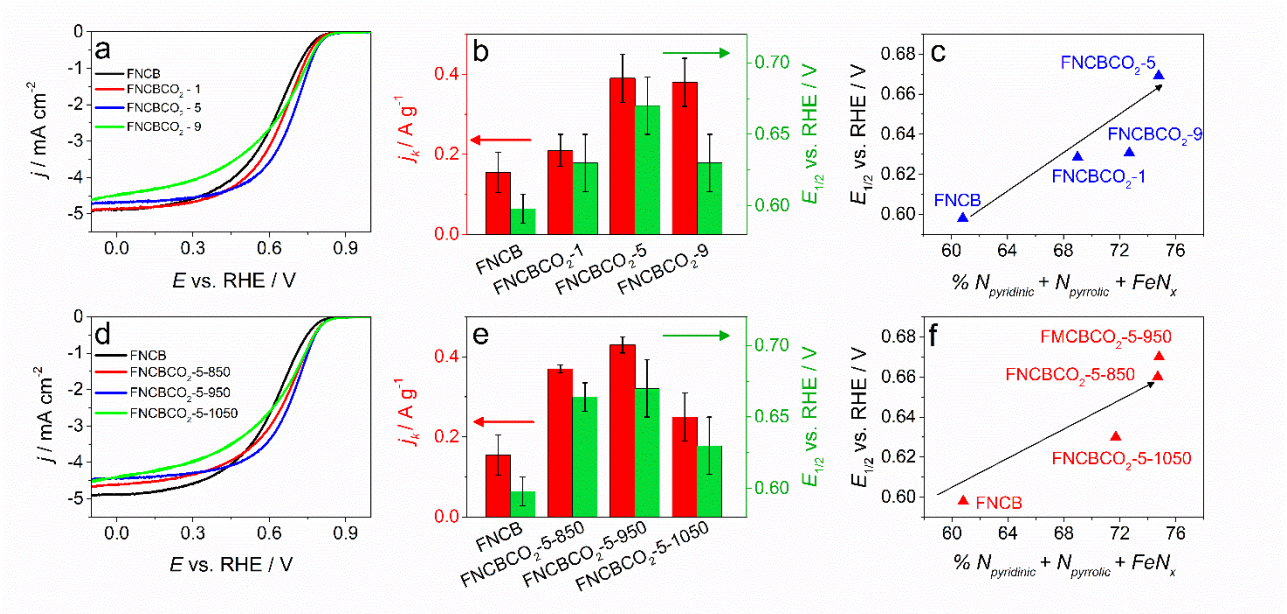

Figure 4.6. LSV recorded in oxygen-saturated electrolyte for CO_2 series of samples for time effect (a) and temperature effect (d). The scan rate was 2 mV s^{-1} and rotation speed was 1600 rpm. kinetic current and half-wave potential for (b) FNCBCO_2-X and (e) FNCBCO_2-5-Y; $E_{1/2}$ correlations with pyridinic, pyrrolic and Fe-N_x group percentage for (c) FNCBCO_2-X and (f) FNCBCO_2-5-Y; (see Table 4.2).

4.1.2.2.Quantification of Active sites

If on one hand XPS is able to identify surface functionalization on the other the low amount of nitrogen and iron coupled with the great variety of different sites makes this technique not fully reliable. In addition, even if it's a surface probing method, it does not fully probe the real electrochemical accessible surface.
Another option to quantify the number of Fe-N_x sites relies on the electrochemical nitrite stripping developed by Malko et al. This method is based on the selective interaction of Fe-N_x sites with probe molecule NO_2^-, NO or NH_2OH [see reference above] which reversibly binds to the Fe centre as nitrosyl at mildly acidic pH value of 5.2 [29–31]. When the catalyst layer is poisoned, there is an excess of cathodic charge, Q_{strip}, which can be related to the gravimetric site density according to the formula:

$$\mathrm{MSD}\ [\mathrm{mol\ sites\ g^{-1}}] = \frac{Q_{strip}[\mathrm{C\ g^{-1}}]}{\mathrm{n}_{strip}F[\mathrm{C\ mol^{-1}}]} \quad (4.1)$$

where n_{strip} is the number of electrons associated with the reduction of one adsorbed nitrosyl per site to NH_3 (NH_4^+ in this reaction media).
The MSD is strictly related to the activity of catalysts with the intrinsic activity of the active sites, namely the turnover frequency (TOF). The activity in terms of kinetic current is indeed given by the expression:

$$j_K = F \cdot TOF \cdot MSD \quad (4.2)$$

where *F* is the Faraday constant, TOF is the turnover frequency of Fe-N_x sites and MSD the gravimetric active sites density. Therefore, an active catalyst could be obtained either from a high turnover frequency or a high accessibility to sites.
A summary of electrochemical result is reported in Figure 4.7. A clear reductive current is evident in Figure 4.7a due to nitrite stripping, as highlighted by the difference between the two curves (Figure 4.7b). The diminution in activity at 0.8 V vs. RHE (0.309 vs. SCE) is clear from LSV and Tafel plots (Figure 4.7c and d). The recovered LSV, i.e., the LSV recorded after the NO stripping, shows that most of the activity is recovered but there is a diminution in current at higher overpotential. This could be caused by some sites that are permanently poisoned or more probable due to a time-dependent catalyst degradation. It is worth noting that the shape of LSV is stretched compared with LSV in Figure 4.6 probably due to the effect of electrolyte or lower catalyst loading (0.2 mg cm^{-2}) used for the nitrite stripping versus 0.6 mg cm^{-2} employed for all the other electrochemical measurements. Other results are reported in Figure 10.12 and Figure 10.13.

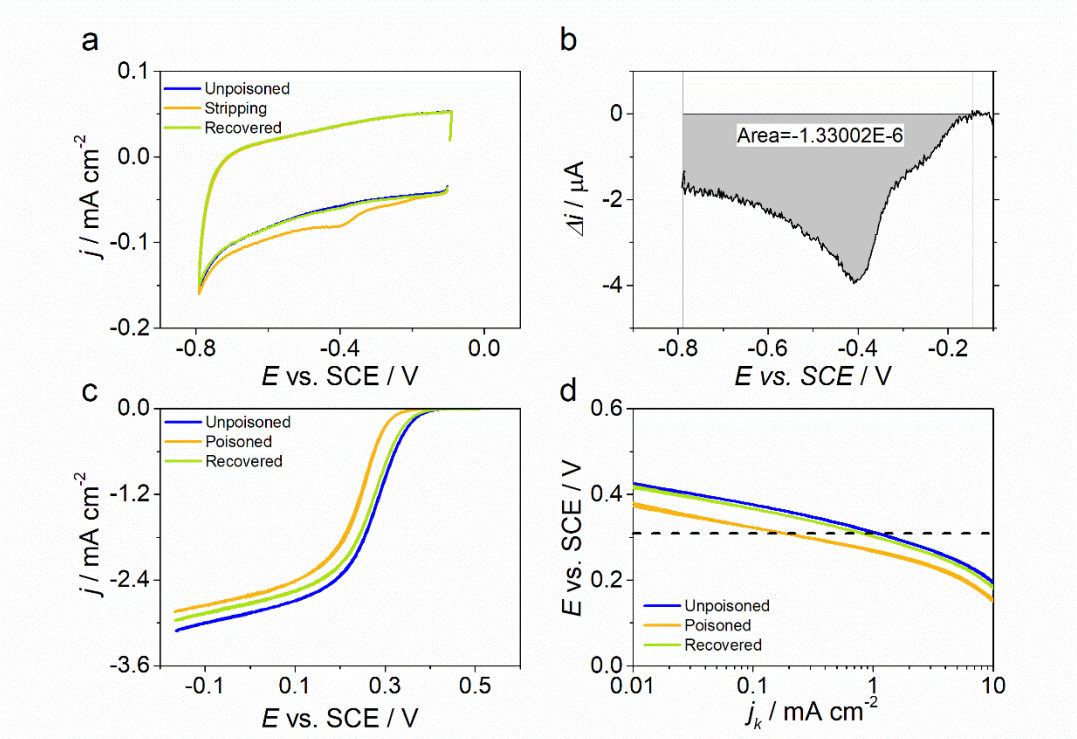

Figure 4.7. a) nitrite stripping and recovered CVs of FNCBCO$_2$-5 recorded in Ar-saturated electrolyte at 10 mV s^{-1}, b) magnification of the stripping area integrated for the site density determination, c) LSV recorded before, during and after poisoning at 1600 rpm and 5 mV s^{-1} in O$_2$-saturated electrolyte, and d) Tafel plots for the poisoned and recovered catalyst.

The aim of this study was to verify the role of controlled porosity of the support on the activity, and therefore on site formation. It is hence interesting to observe that according to NO-stripping findings, the site density increases almost linearly both with respect to micropore surface area and volume (but also for mesopores). This outcome is in disagreement with the XPS findings but support the thesis of poor reliability. The consequence is that increasing both the activation treatment time and temperature the formation of Fe-N$_x$ sites is favoured.

Even with some outliner points, it is evident that a more porous network allows higher functionalization, whereas a more open structure entails a higher accessibility to sites and as a consequence, a global higher site density (Figure 4.8a).

Carbon dioxide is evidently more effective than steam in increasing site density which means that not only micropore, higher in steam activated carbon, are involved in site formation. The SD and TOF is also in good correlation with activity parameter such as kinetic current, mainly for steam activated sample. In general, these two correlations combined together are in perfect agreement with the increment of kinetic current at 0.8V (as well as onset potential) with increasing time treatment.

As and end note, a map plotting TOF vs. SD is proposed in order to show that higher activity could be achieved both increasing sites density and the turnover frequency, as by definition of the kinetic current (here indicated with gray hyperbola). For the steam-activated samples is clear that both SD and TOF contribute to the increasing of activity.

It is interesting to observe that the percentage of “effective iron” i.e., the percentage of iron active for ORR that can be counted by nitrite poisoning with respect the total amount of iron determined by XPS increases from 2.65 in FNCB to 11.01 % in FNCBSt60 (Table 4.8). Therefore, it would be in principle possible to further increase the kinetic current to a certain extent just by extending the steam treatment. Clearly, this last reasoning does not consider that the subsequent

functionalization with Fe-N_x sites is in any case limited by the capability of fixing Fe-N_x while not changing the textural properties. For the CO_2 sets, it appears that the activated samples move along a single isocurve, indeed these sample are in general more active but some for a higher SD and others for higher TOFs.
Figure 4.8d compares our catalyst with some benchmark samples used in Primbs at al. work, which represent the state of the art Fe-N-C materials for ORR and include also commercial catalyst (PAJ).[12]
It is clear that the carbon activation with CO_2 and steam leads to a more open structure, which in the end resemble preferentially to the behaviour of UNM or Pajarito powder (PAJ), i.e., the catalysts with specific textural properties induced by the hard template synthesis. This apparently means that increasing the micro and mesopore surface and volume helps preferentially the enhancement of TOF than the SD, but this must be link to a change in site activity. To increase the SD as in CNRS and ICL catalysts, it is necessary to change the type of Fe-N_x precursor that must be able to efficiently pin the active sites avoiding the clogging of micro and mesopores.
Regarding the increase of TOF we can make more insightful consideration by taking into account the sole steam sets. If we plot the change in kinetic activity with stripping charge (or site density), we see that there is good straight-line dependence, but with non-zero intercept (Figure 4.8e). This hold strongly with steam sets material although this effect is not as evident for the CO_2 treated material possibly because of the interaction of NO_2 with other iron species (like oxide or carbide). This appears to suggest that there are a given number of sites that are "inactive" for the ORR, or alternatively we overestimate the stripping charge by a constant amount for all catalysts (that amount is 0.667 C g^{-1} based on the intercept) and we should ignore those sites – i.e., we should subtract the "inactive" sites from the total sites:

$$Q_{strip,corr} = Q_{strip} - 0.667\ C\ g^{-1} \tag{4.3}$$

The corrected data gives a new scenario (4.3), the increment in activity is mainly due to SD increment and the TOF is oscillating around an average value of 3.11 $\pm$ 0.39 electron $sites^{-1}$ s^{-1} (Figure 4.8f,g). Looking at the slope ($8.11 \cdot 10^{15}$ sites m^{-2}) of red fitting in Figure 4.8b, it is possible to estimate the average distance of sites, using the expression:

$$d = \frac{1}{\sqrt{slope}} \tag{4.4}$$

Which gives about 11 nm of average distance between two sites. The same effect, as said, is not evident on CO_2 set, we do not have particular clue on why this append, but it could be the case of an underestimation of sites or some difference on sites, but in absence of concrete evidence we do not do speculation.

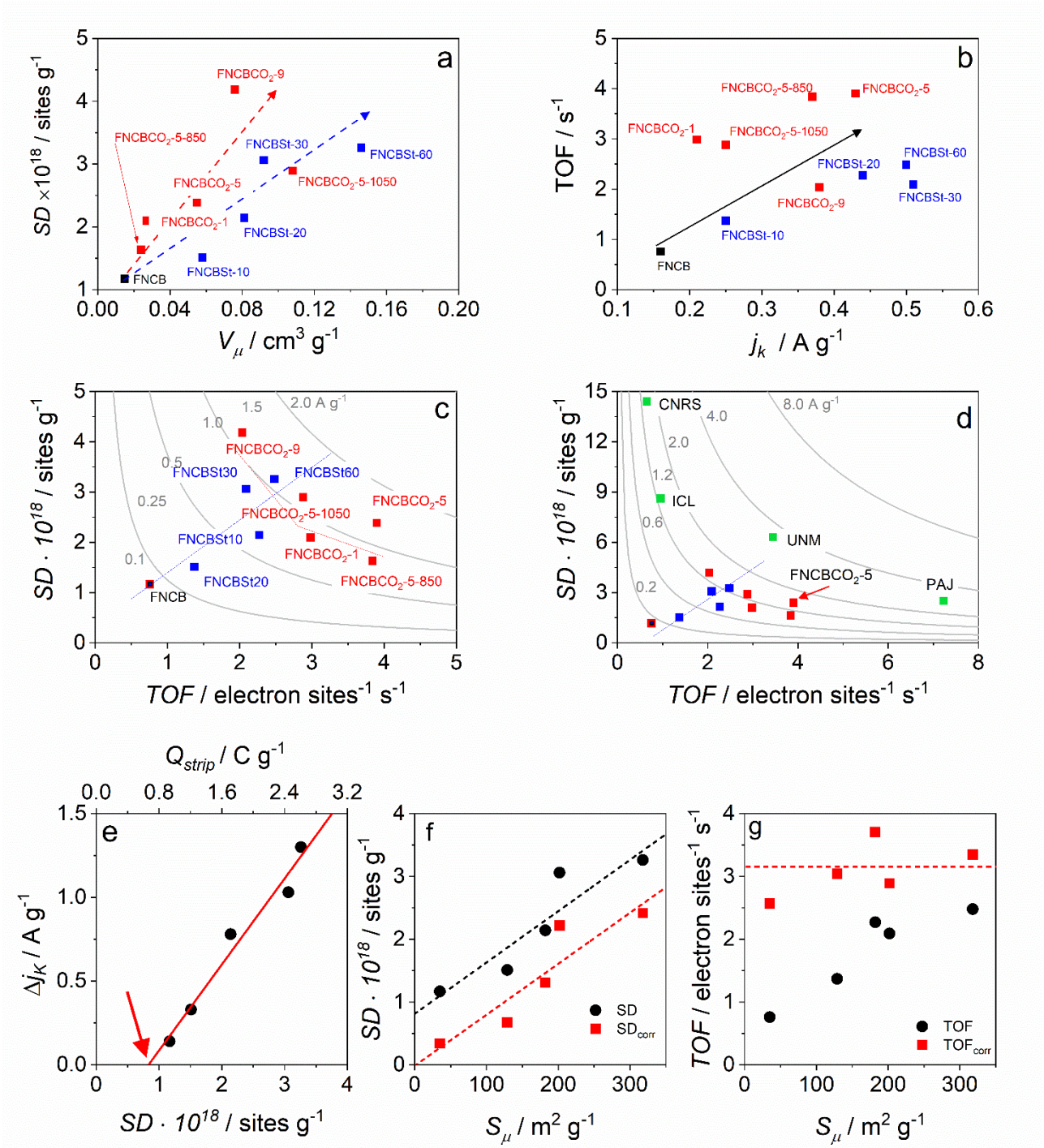

Figure 4.8. a) SD correlation with microporous volume; b) correlation between TOF and kinetic current at 0.8 V vs RHE; c) Activity map of all catalysts, in blue the steam sets and in red the CO_2 sets, grey lines represent the iso-current line which are hyperbole according to eq. 9 while blue dotted line are intended for guiding the eye from low to high catalytic activity; d) comparison with benchmark catalysts described by Primbs et al. e) SD vs. difference in kinetic current due to poisoning, f) SD and g) TOF before and after correction against microporous surface area

4.1.2.3.Stability test

Stability test, here done as chronoamperometries studies (9h), were carried out on three representative catalysts, i.e., FNCB, FNCBSt60 and $FNCBCO_2$-5 for gauging any variation in perforce due to degradation issues. Chronoamperometry was performed in O_2-saturated 0.5 M H_2SO_4 electrolyte at a rotation speed of 200 rpm and controlled temperature of 25 °C. Control

LSVs were recorded at the beginning of each experiment and then every 3 h (Figure 4.10). The aim was to understand if there was any evident change in stability related to the different treatment done on the carbon. Tests were conducted at 0.15 V vs. RHE and in general a current drop was observed in the range of 8-20 % with FNCBSt60 being apparently the less affected by performance loss. Furthermore, we observed a variation of the half-wave potential that decreases for each sample: 8 % ($\Delta E_{1/2}$ = 39 mV), 3% ($\Delta E_{1/2}$ = 21 mV) and 12 % ($\Delta E_{1/2}$ = 80 mV) for FNCB, FNCBSt60 and FNCBCO_2-5, respectively ((Figure 4.10d-f). More in general is not easy to compare result with other works because different potential, rotation speed, loading and electrolyte condition are used, but we could anyway point out that a decreasing of 20 % after 9 h are in line with other Fe-N-C catalysts [32]. In conclusion we can assert that the steam or CO_2 thermal treatments does not bring further severe stability issues with respect to the pristine catalyst material.

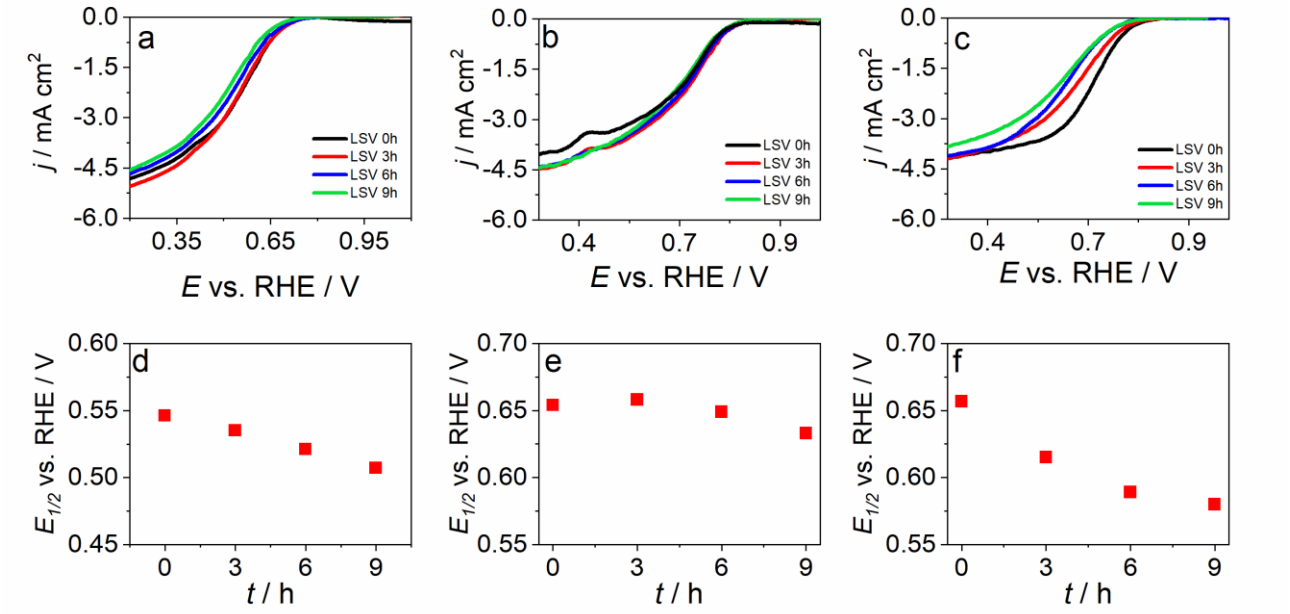

Figure 4.9. (a-c) LSV and (d-f) half wave potential variation recorded every 3h during the chronoamperometry stability test at RDE (ω = 200 rpm) in O_2-saturated 0.5 M H_2SO_4 electrolyte at (a, d) FNCB, (b, e) FNCBSt60 and (c, f) FNCBCO_2-5

4.1.3. Effect of loading on RRDE

In 2008 a nice work of Dodelet, Dahn et al. [28] pointed out the importance of correlation between loading and hydrogen peroxide production since, in particular in mild acidic electrolyte, passing from 800 µg cm^{-2} to 80 µg cm^{-2} result in an increment of H_2O_2 production from 10% to 70% at around 0.6 V vs. RHE. This depend, as said, on the actual pathway that occur, if a 4 electron or an efficient 2x2 electron pathway are predominant, loading effect will be less evident, while, if a 2 electron pathway is predominant this effect will be more evident, like in the cited paper [28], since for thinner layer H_2O_2 easily escape the surface and cannot be further reduce. It is also clear that this dependency will be also linked to the pore network of material and different variation will be observed for different pore distribution inside the catalysts.
For the benchmark catalyst that we selected, FNCBCO_2-5 the result are shown in Figure 4.10, for these catalysts appear evident that in 0.5 M H_2SO_4 even at loading of 0.2 mg cm^{-2} the amount of peroxide is low (Figure 4.10c) which suggest that this catalysts in this environment tends to produce water rather than peroxide. Clearly the lower amount of catalyst result in lower current (Figure 4.10a, b), but if the activity is calculated as kinetic current (or current normalize for the loading) it result even higher at low loading. The trend of peroxide is valid at different potential range (Figure 4.10c).

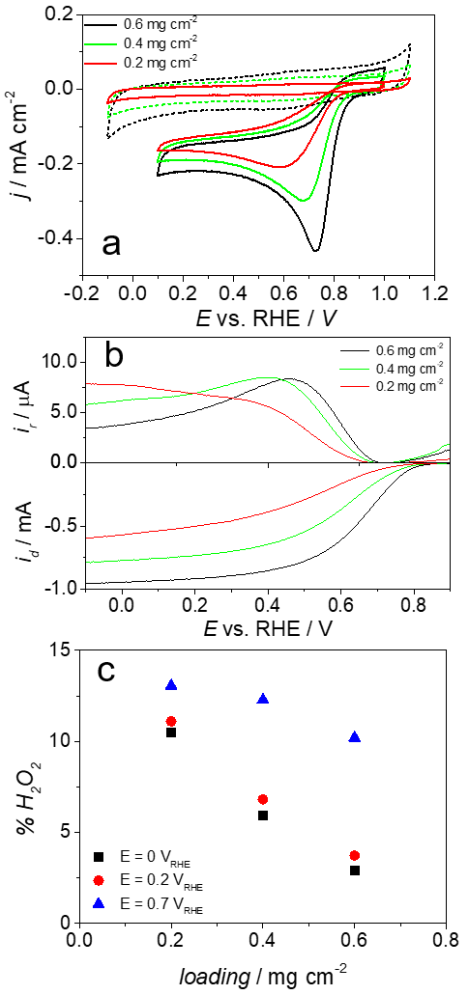

Figure 4.10. a) CVs and b) LSVs at RRDE of FNCBCO_2-5 at different catalyst loading in O_2 saturated 0.5 M H_2SO_4 c) hydrogen peroxide production at different loading and potential

4.1.4. Effect of initial molar % on Iron

In order to determine the ideal initial quantity of iron (balance between activity and quantity of iron precursor) a pristine carbon and catalyst made with 1,2 and 4 $\%_{mol}$ of iron was prepared. Also, a sample with 1% of Fe and an additional amount of phenanthroline to reach the quantity added within the 2% sample was prepared (marked as 1*). The sample with the 2% of iron shows the best compromise between activity and precursor quantity, indeed the sample prepared with 4% was slightly better in term of activity but considering that a similar activity is obtained with half of the iron the 2% represents an excellent choice. Also, the sample with the additional phen reach good activity just below the 2% one. Nitrite stripping confirm that the SD does not growth significantly after the 2% and this is in line with the amount of H_2O_2 produced and the activity in term of half-wave potential.
In Table 4.3 and Figure 4.11 data and correlation are reported.

Table 4.3. ORR and Stripping data

	$E_{j=0.1}$ V vs. RHE	$E_{1/2}$ V vs. RHE	$j_{L,0V}$ mA cm^{-2}	$j_{0.8V}$ mA cm^{-2}	j_K A g^{-1}	n -	H_2O_2 %	SD sites g^{-1}	TOF s^{-1}	Δj_k A g^{-1}
C	0.380	0.17	1.81	-	-	3.48	26.0	0	0	0
Fe_1CBCO_2-5	0.743	0.471	3.09	0.03	0.04	3.70	14.9	1.11E+18	0.24	0.04
Fe_1*$CBCO_2$-5	0.812	0.640	4.13	0.15	0.26	3.95	2.7	2.23E+18	1.83	0.65
Fe_2CBCO_2-5	0.822	0.669	4.63	0.23	0.41	3.95	2.7	2.38E+18	3.90	1.49
Fe_4CBCO_2-5	0.842	0.666	4.28	0.37	0.68	3.92	4.2	2.27E+18	2.21	0.80

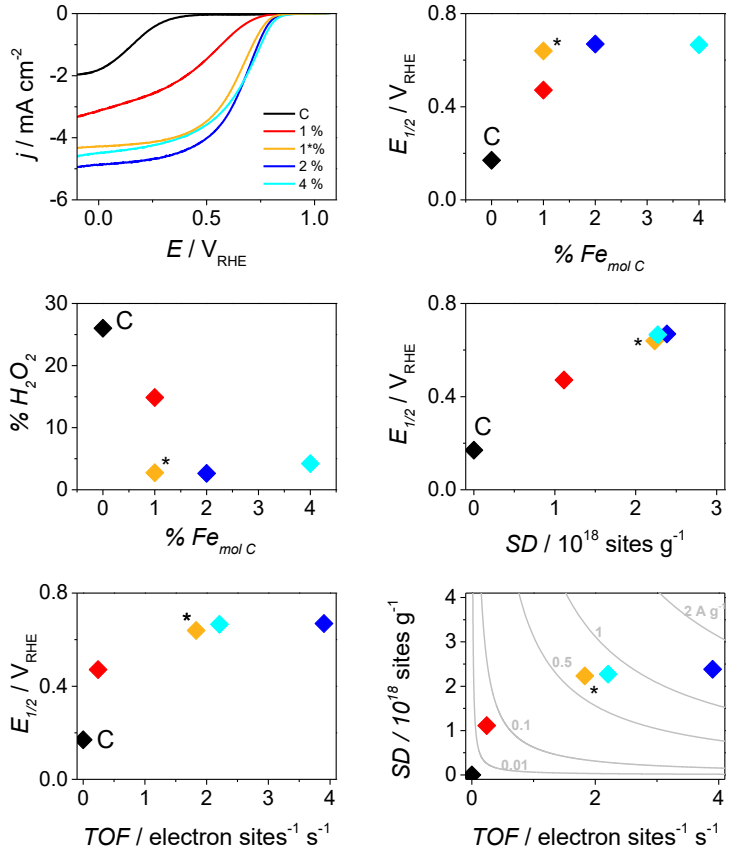

Figure 4.11. LSV and correlation

4.2. Conclusion

This chapter covers the effect of activation, namely a controlled evolution of micro and mesopores content of a commercial carbon black. Fe-N-C catalysts prepared by thermal treatment of activated carbons with $Fe(Phen)_3Cl_2$ were used as indicator of the effect of morphology variation on final catalysts. All the activated supports give higher activity if compared with the pristine one, where the steam treatment allows to obtain a faster evolution of pore and a good improvement in activity. It was established that standard XPS analysis leads to not fully precise interpretation of N 1s spectrum since it is difficult to single out the contribution of the $Fe\text{-}N_x$ components with respect to the pyridinic and pyrrolic one especially when the nitrogen content is low (< 1), and due to the proximity in term of binding energy. Site density of $Fe\text{-}N_x$ centres was successfully characterize by nitrite stripping showing that the improvement in activity is both caused by an increment in site density and turnover frequency. This is in good agreement with evolution of micro and mesopore in the support indicating the importance pore structure in carbon precursor, in particular the role of micro and meso pore is important either in site formation and/or site accessibility.

4.3. Bibliography

[1] Y. Zhu, J. Gao, Y. Li, F. Sun, J. Gao, S. Wu, Y. Qin, Preparation of activated carbons for SO 2 adsorption by CO 2 and steam activation, J. Taiwan Inst. Chem. Eng. 43 (2012) 112–119. https://doi.org/10.1016/j.jtice.2011.06.009.

[2] S. Román, J.F. González, C.M. González-García, F. Zamora, Control of pore development during CO2 and steam activation of olive stones, Fuel Process. Technol. 89 (2008) 715–720. https://doi.org/10.1016/j.fuproc.2007.12.015.

[3] C.F. Chang, C.Y. Chang, W.T. Tsai, Effects of burn-off and activation temperature on preparation of activated carbon from corn cob agrowaste by CO2 and steam, J. Colloid Interface Sci. 232 (2000) 45–49. https://doi.org/10.1006/jcis.2000.7171.

[4] M. Thommes, K. Kaneko, A. V. Neimark, J.P. Olivier, F. Rodriguez-Reinoso, J. Rouquerol, K.S.W. Sing, Physisorption of gases, with special reference to the evaluation of surface area and pore size distribution (IUPAC Technical Report), Pure Appl. Chem. 87 (2015) 1051–1069. https://doi.org/10.1515/pac-2014-1117.

[5] M. Molina-Sabio, M.T. González, F. Rodriguez-Reinoso, A. Sepúlveda-Escribano, Effect of steam and carbon dioxide activation in the micropore size distribution of activated carbon, Carbon. 34 (1996) 505–509. https://doi.org/10.1016/0008-6223(96)00006-1.

[6] F. Rodríguez-Reinoso, M. Molina-Sabio, M.T. González, The use of steam and CO2 as activating agents in the preparation of activated carbons, Carbon. 33 (1995) 15–23. https://doi.org/10.1016/0008-6223(94)00100-E.

[7] F. Rodriguez Reinoso, M. Molina-Sabio, Activated carbons from lignocellulosic materials by chemical and/or physical activation: an overview | Francisco Rodriguez-Reinoso - Academia.edu, Carbon. 30 (1992) 1111–1118. http://www.academia.edu/4303771/Activated_carbons_from_lignocellulosic_materials_by_chemical_and_or_physical_activation_an_overview.

[8] A.C. Ferrari, Determination of bonding in diamond-like carbon by Raman spectroscopy, Diam. Relat. Mater. 11 (2002) 1053–1061. https://doi.org/10.1016/S0925-9635(01)00730-0.

[9] M. Pawlyta, J.N. Rouzaud, S. Duber, Raman microspectroscopy characterization of carbon blacks: Spectral analysis and structural information, Carbon. 84 (2015) 479–490. https://doi.org/10.1016/j.carbon.2014.12.030.

[10] A. Sadezky, H. Muckenhuber, H. Grothe, R. Niessner, U. Pöschl, Raman microspectroscopy of soot and related carbonaceous materials: Spectral analysis and structural information, Carbon. 43 (2005) 1731–1742. https://doi.org/10.1016/j.carbon.2005.02.018.

[11] V. Perazzolo, C. Durante, R. Pilot, A. Paduano, J. Zheng, G.A. Rizzi, A. Martucci, G. Granozzi, A. Gennaro, Nitrogen and sulfur doped mesoporous carbon as metal-free electrocatalysts for the in situ production of hydrogen peroxide, Carbon. 95 (2015) 949–963. https://doi.org/10.1016/j.carbon.2015.09.002.

[12] V. Palomares, A. Goñi, I.G. De Muro, I. De Meatza, M. Bengoechea, I. Cantero, T. Rojo, Conductive additive content balance in Li-ion battery cathodes: Commercial carbon blacks vs. in situ carbon from LiFePO4/C composites, J. Power Sources. 195 (2010) 7661–7668. https://doi.org/10.1016/j.jpowsour.2010.05.048.

[13] B.S. Elman, M.S. Dresselhaus, G. Dresselhaus, E.W. Maby, H. Mazurek, Raman scattering from ion-implanted graphite, Phys. Rev. B. 24 (1981) 1027–1034. https://doi.org/10.1103/PhysRevB.24.1027.

[14] Y. Wang, D.C. Alsmeyer, R.L. McCreery, Raman spectroscopy of carbon materials: structural basis of observed spectra, Chem. Mater. 2 (1990) 557–563. https://doi.org/10.1021/cm00011a018.

[15] L. Bokobza, J.-L. Bruneel, M. Couzi, Raman Spectra of Carbon-Based Materials (from Graphite to Carbon Black) and of Some Silicone Composites, C. 1 (2015) 77–94. https://doi.org/10.3390/c1010077.

[16] A.C. Ferrari, J. Robertson, Interpretation of Raman spectra of disordered and amorphous carbon, Phys. Rev. B. 61 (2000) 14095–14107.

https://doi.org/10.1103/PhysRevB.61.14095.
[17] R. Sparkes, N. Hovius, A. Galy, R.V. Kumar, J.T. Liu, Automated Analysis of Carbon in Powdered Geological and Environmental Samples by Raman Spectroscopy, Appl. Spectrosc. 67 (2013) 779–788. https://doi.org/10.1366/12-06826.
[18] M. Primbs, Y. Sun, A. Roy, D. Malko, A. Mehmood, M.-T. Sougrati, P.-Y. Blanchard, G. Granozzi, T. Kosmala, G. Daniel, P. Atanassov, J. Sharman, C. Durante, A. Kucernak, D. Jones, F. Jaouen, P. Strasser, Establishing reactivity descriptors for platinum group metal (PGM)-free Fe–N–C catalysts for PEM fuel cells, Energy Environ. Sci. 13 (2020) 2480–2500. https://doi.org/10.1039/D0EE01013H.
[19] F. Jaouen, J. Herranz, M. Lefévre, J.P. Dodelet, U.I. Kramm, I. Herrmann, P. Bogdanoff, J. Maruyama, T. Nagaoka, A. Garsuch, J.R. Dahn, T. Olson, S. Pylypenko, P. Atanassov, E.A. Ustinov, Cross-laboratory experimental study of non-noble-metal electrocatalysts for the oxygen reduction reaction, ACS Appl. Mater. Interfaces. 1 (2009) 1623–1639. https://doi.org/10.1021/am900219g.
[20] R. Chenitz, U.I. Kramm, M. Lefèvre, V. Glibin, G. Zhang, S. Sun, J.P. Dodelet, A specific demetalation of Fe-N4 catalytic sites in the micropores of NC-Ar + NH3 is at the origin of the initial activity loss of the highly active Fe/N/C catalyst used for the reduction of oxygen in PEM fuel cells, Energy Environ. Sci. 11 (2018) 365–382. https://doi.org/10.1039/c7ee02302b.
[21] F. Jaouen, M. Lefèvre, J.P. Dodelet, M. Cai, Heat-treated Fe/N/C catalysts for O2 electroreduction: Are active sites hosted in micropores?, J. Phys. Chem. B. 110 (2006) 5553–5558. https://doi.org/10.1021/jp057135h.
[22] M. Mazzucato, G. Daniel, A. Mehmood, T. Kosmala, G. Granozzi, A. Kucernak, C. Durante, Effects of the induced micro- and meso-porosity on the single site density and turn over frequency of Fe-N-C carbon electrodes for the oxygen reduction reaction, Appl. Catal. B Environ. 291 (2021) 120068. https://doi.org/10.1016/j.apcatb.2021.120068.
[23] M. Blanco, D. Mosconi, M. Otyepka, M. Medveď, A. Bakandritsos, S. Agnoli, G. Granozzi, Combined high degree of carboxylation and electronic conduction in graphene acid sets new limits for metal free catalysis in alcohol oxidation, Chem. Sci. 10 (2019) 9438–9445. https://doi.org/10.1039/C9SC02954K.
[24] D. Mosconi, M. Blanco, T. Gatti, L. Calvillo, M. Otyepka, A. Bakandritsos, E. Menna, S. Agnoli, G. Granozzi, Arene C–H insertion catalyzed by ferrocene covalently heterogenized on graphene acid, Carbon. (2019). https://doi.org/10.1016/j.carbon.2018.11.010.
[25] G. Levi, O. Senneca, M. Causà, P. Salatino, P. Lacovig, S. Lizzit, Probing the chemical nature of surface oxides during coal char oxidation by high-resolution XPS, Carbon. (2015). https://doi.org/10.1016/j.carbon.2015.04.003.
[26] S. Pylypenko, S. Mukherjee, T.S. Olson, P. Atanassov, Non-platinum oxygen reduction electrocatalysts based on pyrolyzed transition metal macrocycles, Electrochim. Acta. 53 (2008) 7875–7883. https://doi.org/10.1016/j.electacta.2008.05.047.
[27] V. Perazzolo, E. Grądzka, C. Durante, R. Pilot, N. Vicentini, G.A. Rizzi, G. Granozzi, A. Gennaro, Chemical and Electrochemical Stability of Nitrogen and Sulphur Doped Mesoporous Carbons, Electrochim. Acta. 197 (2016) 251–262. https://doi.org/10.1016/j.electacta.2016.02.025.
[28] A. Bonakdarpour, M. Lefevre, R. Yang, F. Jaouen, T. Dahn, J.P. Dodelet, J.R. Dahn, Impact of loading in RRDE experiments on Fe-N-C catalysts: Two- or four-electron oxygen reduction?, Electrochem. Solid-State Lett. 11 (2008) 105–108. https://doi.org/10.1149/1.2904768.
[29] D. Malko, A. Kucernak, T. Lopes, In situ electrochemical quantification of active sites in Fe–N/C non-precious metal catalysts, Nat. Commun. 7 (2016) 13285–13292. https://doi.org/10.1038/ncomms13285.
[30] D. Malko, A. Kucernak, T. Lopes, Performance of Fe–N/C Oxygen Reduction Electrocatalysts toward NO_2^- , NO, and NH_2OH Electroreduction: From Fundamental Insights into the Active Center to a New Method for Environmental Nitrite Destruction, J. Am. Chem. Soc. 138 (2016) 16056–16068. https://doi.org/10.1021/jacs.6b09622.

[31] S. Specchia, P. Atanassov, J.H. Zagal, Mapping transition metal–nitrogen–carbon catalyst performance on the critical descriptor diagram, Curr. Opin. Electrochem. 27 (2021). https://doi.org/10.1016/j.coelec.2021.100687.
[32] S.H. Liu, J.R. Wu, F.S. Zheng, J.M. Guo, Impact of iron precursors on the properties and activities of carbon-supported Fe-N oxygen reduction catalysts, J. Solid State Electrochem. 19 (2015) 1381–1391. https://doi.org/10.1007/s10008-015-2759-1.

5. How determinant is the iron precursor ligand in Fe-NC single-site formation and activity for oxygen reduction reaction?

This chapter of the thesis is focused on the iron precursor ligand effect on the Fe-N_x site formation when mixed with a commercial carbon black. Iron complexes coordinating different nitrogen ligands such as phthalocyanine, 1,10-Phenanthroline, 2,2'-Bipyridyl, imidazole, EDTA, etc., were tested. Twelve different complexes were used to achieve a better understanding on the role of ligands on site formation and activity, i.e., the site density (SD) and the turn-over frequency (TOF), respectively. The observation made bring to the conclusion that Fe-N_x active sites can be effectively formed only when ligands containing aromatic nitrogen rings are used. Another finding was that the ligand decomposition could lead to substantial changes in the carbon morphology developing an increased micropore volume, while mesopore surface area is reduced. Several electrochemical characterisations were carried out in both acidic and alkaline electrolyte by RRDE technique showing that the catalytic activity deeply depends on the type of iron complex, even if such difference is much less important when KOH was used as electrolyte. This bring to the attention to the fact that in alkaline media Fe has a less central role.
Site density was determined with NO electrochemical stripping method showing a good correlation with the activity ($E_{1/2}$) in acid media, while no correlation was observed in alkaline media. $Fe(phen)_3Cl_2$ shows the higher SD probably due to a combined action of precursor ability on fixing Fe-N_x site but also on the ability to open new microporosity, which are also linked to site formation. Parallel to that, phenomena of mesopore occlusion bring to the conclusion that there is a limit on the ability to increase catalytic activity simply by playing on the initial content of complex, this is also corroborated to the fact that when try to increase the SD by increasing the complex loading at the same time the textural properties worsen and no better activity was observed. Stability test and post-stress test site density analysis on the best catalysts show a higher stability in alkaline electrolyte. In acid electrolyte, the kinetic current decreases by 60% after 7000 cycles and this was proven to depends by the decreasing of the SD, attesting the labile nature of Fe-N_x sites when used in demanding conditions.

5.1. Result

5.1.1. Synthesis of Fe-N complexes

The complexes were purchased or synthetized according to procedures reported in the experimental section using different ligands (Figure 5.1) with pyridinic ring, pyrrolic or diazole structure. The complex formation was checked via elemental analysis and the result are reported in Table 10.1. The different ligands were selected considering the cheapness and availability. Therefore, we limited the use of very expensive ligands, such as porphyrins or phthalocyanines, to the sole Fe(III)-Phthalocyanine-Chloride (FePHTA), which is commercially available at a reasonable price. The complexes were labelled as FeX_y (where X is the ligand used and y the ligand to metal ratio). Iron complexes of 1,10-Phenantroline and 2,2'-Bipyridyl ($FeBPY_3$) were synthetized with different metal/ligand stoichiometry ($FePHEN_n$, n = 1-3 and $FeBPY_n$, n = 1-3). In this case not all the complexes have the same counterion, which is Cl^- for the mono and three coordinated ($FePHEN_1$ and $FePHEN_3$, respectively), whereas the bi-coordinated has thiocyanate [42]. Some doubts are raised in literature about the major form of the monocoordinated complex $FePHEN_1$ sustaining that the complex isn't in complexed form, while the complexed form is a minor product [43]. On the other hand, other works reported that when the synthesis is done in MeOH from $FeCl_3$ and 1,10-

Phenantrholine the major product is indeed $Fe(phen)Cl_3$ [44]. On regard elemental analysis supported the formation of $Fe(phen)Cl_3$. The effect of iron oxidation state was not considered. For procedure see appendix (10.2.3)

5.1.2. Synthesis of Fe-N-C Materials

Various Fe-N-C catalysts were synthetised similarly to the catalysts described on the previous chapter by mixing an iron complex and Vulcan XC72, then heated to 900 °C in a tubular furnace, washed at reflux in H_2SO_4, and then heated again at 900 °C. The resulting powders labelled as FX_y (where X is the ligand used in precursor and y the ligand to metal ratio for PHEN and BPY) are the final catalysts. A control metal-free catalyst for was synthetize with the same procedure using only phenanthroline as nitrogen precursor. Furthermore, the direct pyrolysis of $FPHEN_3$ without the use of Vulcan XC72 support was done (10.3.1).

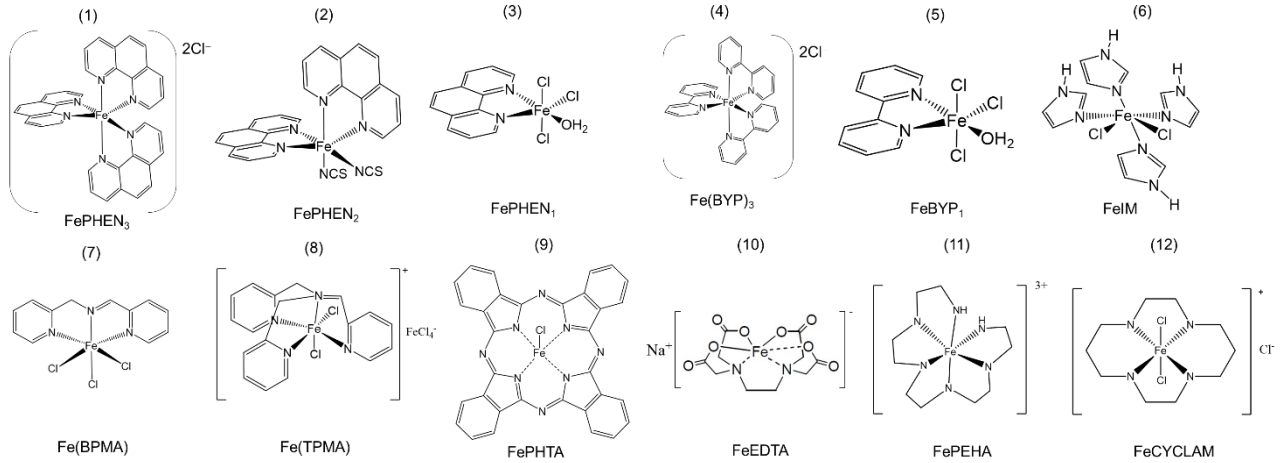

Figure 5.1. Different iron complexes synthetized (1-8, 10-12) or purchased (9) for the synthesis of Fe-N-C catalysts. The ligand of interest are PHEN = 1,10–Phenanthroline (1-3); BPY = 2,2'-Bipyridyl (4,5); Imidazole (6), BPMA = bis(2-pyridylmethyl)amine (7); TPMA = Tris(2-pyridylmethyl)amine (8) and PHTA = Phthalocyanine (9), EDTA = Ethylenediaminetetraacetate (10), PEHA = Pentaethylenehexamine (11), CYCLAM =1,4,8,11-Tetraazacyclotetradecane (12).

5.1.3. Fe-N-C synthesis and characterization

All synthesis were carried out as explained before. The presence of a carbon support is fundamental to have a pre-formed network of pore that allow catalytic sites to form. Just as a confirmation we prepared a catalyst by pyrolyzing only an iron complex, the obtained powder were shiny indicating the presence of graphite and or of iron species. The ORR catalytic behaviour of Fe-N-C catalysts prepared with $FePHEN_3$ ($FPHEN_3$) and without Vulcan XC72 ($FPHEN_3py$) is reported in Figure 10.15 and the main electrochemical parameters are reported in Table 10.4. This behaviour find confirmation in literature also for other metal complexes as observed by Onodera et al. for a cobalt/phenanthroline/phenol resin precursor [1].
Table 5.1 summarize the composition of catalysts detected via elemental analysis and EDX, it is clear that phenanthroline complexes and phthalocyanine are more able to fix iron on the catalyst, but the same is not true for nitrogen, showing the different behaviour of various complexes. Bases only on this information $FPHEN_3$ and $FPHEN_1$ seem the most promising ones.
The catalysts with the lower content of nitrogen are those prepared from $FePHEN_2$, FeIM and $FeBPY_3$ complexes. For the first one, we assume that the different counterion, namely SCN^-, have an impact on complex stability. It is interestingly also to note that no sulphur was observed in $FPHEN_2$ catalyst suggesting that the decomposition mechanism involve firstly the loss of phenanthroline ligands leaving an iron thiocyanate complex that can decompose without fixing nitrogen or sulphur in the carbon matrix. This hypothesis is supported by the thermal evolution of similar complexes studied by Ellingsworth et al.[2] and by Bagabas et al. [3].

Table 5.1. Elemental analysis of the Fe-N-C catalysts determined from CHNS and EDX analysis.[a]

		C	N	H	S	C	O	S	Fe
		CHNS analysis				EDX			
0	**XC72**	97.10	-	0.07	0.63	-	-	-	-
1	**$FPHEN_3$**	90.68	0.82	0.40	0.32	95.72	3.24	0.40	0.64
2	**$FPHEN_2$**	97.07	0.22	0.14	-	98.51	1.13	0.04	0.16
3	**$FPHEN_1$**	96.45	0.49	0.24	0.32	97.97	1.84	0.01	0.16
4	**$FBPY_3$**	97.62	0.24	0.15	0.09	98.46	1.16	0.27	0.10
5	**$FBPY_1$**	97.25	0.49	0.12	0.36	98.46	0.87	0.24	0.04
6	**FIM**	96.28	0.24	0.12	0.14	98.84	0.87	0.24	0.03
7	**FTPMA**	97.09	0.45	0.16	0.20	98.61	1.07	0.27	0.06
8	**FBPMA**	96.89	0.32	0.17	0.28	98.58	1.18	0.19	0.05
9	**FPHTA**	88.17	0.39	1.37	0.17	93.34	5.11	-	0.82

[a] all the reported values are in weight percentage.

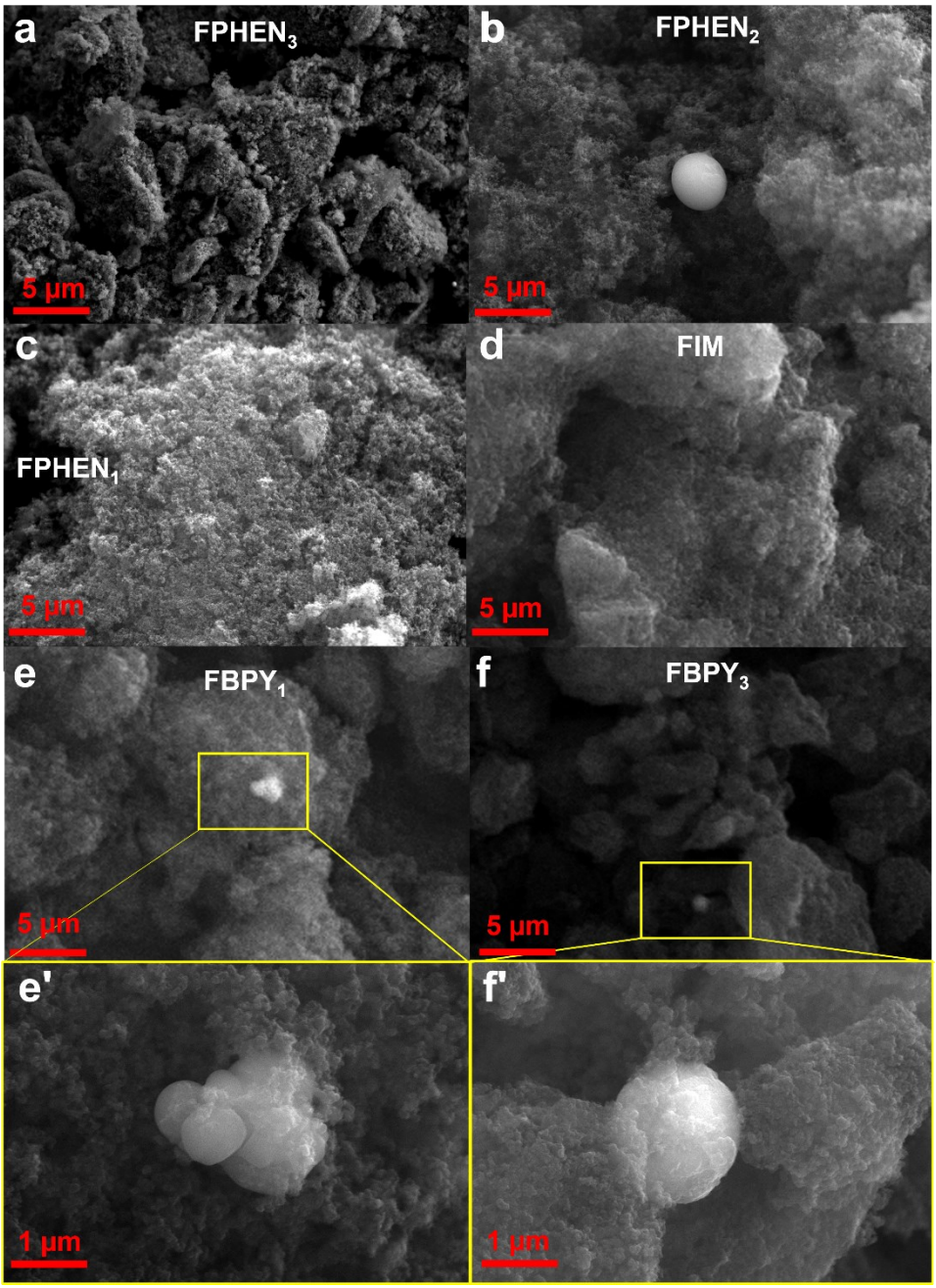

Figure 5.2. Representative SEM images of a selection of Fe-N-C catalysts. Carbon particle agglomerates are visible (c, d), that are of the order of 50-100 nm as in the pristine carbon [4,5]. Some metallic particles are visible as brighter object (a, b, e, f, e' and f').

SEM-EDX analysis were carried out to have information on composition and morphology. The composition from EDX has been already shown in Table 5.1, while selected image are reported in Figure 5.2 and Figure 10.16. In the SEM resolution scale, some iron particles are visible, furthermore the carbon nanoparticles (50-100 nm) are similar in morphology, size, and shape than in pristine Vulcan XC72 [4,5].

Table 5.2. Physisorption parameter derived from ads/des. isotherms at 77.3 K with BET, QSDFT and Gurvitsch methods.

		S_{BET} $m^2\ g^{-1}$	$S_{0.5\text{-}40nm}$ $m^2\ g^{-1}$	S_{μ}^{QSDFT} $m^2\ g^{-1}$	S_{meso}^{QSDFT} $m^2\ g^{-1}$	V_{μ}^{QSDFT} $cm^3\ g^{-1}$	V_{meso}^{QSDFT} $cm^3\ g^{-1}$	V_{tot} $cm^3\ g^{-1}$
0	**XC72**	223	225	132	93	0.050	0.308	0.724
1	**$FPHEN_3$**	213	280	246	34	0.083	0.092	0.283
2	**$FPHEN_2$**	97	94	46	48	0.018	0.111	0.225
3	**$FPHEN_1$**	311	329	228	101	0.086	0.165	0.440
4	**$FBPY_3$**	200	187	106	81	0.043	0.223	0.456
5	**$FBPY_1$**	270	284	212	72	0.075	0.177	0.459
6	**FIM**	229	232	150	82	0.059	0.244	0.458
7	**FTPMA**	207	220	164	56	0.059	0.179	0.400
8	**FBPMA**	170	193	142	51	0.050	0.140	0.368
9	**FPHTA**	211	212	131	81	0.050	0.118	0.194

Due to the different nature of ligand, we expect a different effect on carbon support during the heating treatment. For that reason, we performed N_2 physisorption analysis for all the prepared Fe-N-C catalysts (Table 5.2 and Figure 5.3). It is expected that two effects can be in play, i.e., from one side the pyrolysis of the organic ligand can induce a reduction of the micro and mesopore surface and volume, on the other side the generation of small etching molecule such as NO, NO_2, CO, CO_2 and NH_3 can induce an increase of the textural properties.

All catalysts show a Type I(b) isotherm [6] typical of microporous solid having relatively small external surfaces as is the case of a carbon Vulcan XC72 (Figure 5.3d). Type I(b) isotherms are also found within materials having pore size distributions over a broader range including narrow mesopores. This is expectable due to the nature of precursor and the absence of a control on pore size. In addition, all the isotherms are characterized by a type H4 hysteresis loop typical of micro-mesoporous carbons.

Focusing on the catalysts prepare with phenanthroline complexes, we observed a continuous decrease of mesoporous volume and of the total volume consequently (Figure 5.3c). For micropore instead an increment is observed. It is possible that the diminution of mesopore surface and volume is linked to a mesopore occlusion act by phenanthroline while, the increase of microporous surface area volume could be linked to the etching caused by small molecules generated during the pyrolysis of the complex ligands [7]. $PHEN_2$ seems an exception in the set of phen-based catalysts, indeed a low surface area, a low nitrogen fixation and a modest activity (see later) were observed, suggesting a different degradation mechanism of $FePHEN_2$. Similar conclusions can be drawn also for the catalysts $FBPY_3$ and $FBPY_1$, even if to a different extend. In fact, it is interesting to observe how $FeBPY_1$ (the same is for $FePHEN_1$) has a higher effect on micropore formation and mesopore occlusion. The pore size distribution in Figure 5.3e shows a distribution in a wide range; the undulated shape is probably an artefact due to the chosen model on isotherm interpretation, however what is important here to note is not the distribution itself but the average profile that diminishes where a higher mesopore occlusion had occurred. Imidazole iron complex does not affect greatly the surface area probably due to a lower carbon deposition on the support, which, by the way, results also in a poor nitrogen fixation. In the case of FeBPMA and FeTPMA the two have very similar behaviour as Fe/N source, that leads to a catalyst with an evident decrement in wide mesopore and macropore and an increment of micropore surface area and volume (Table 5.2 and Figure 5.3e), which remarks the similar behaviour of FBPMA and FTPMA

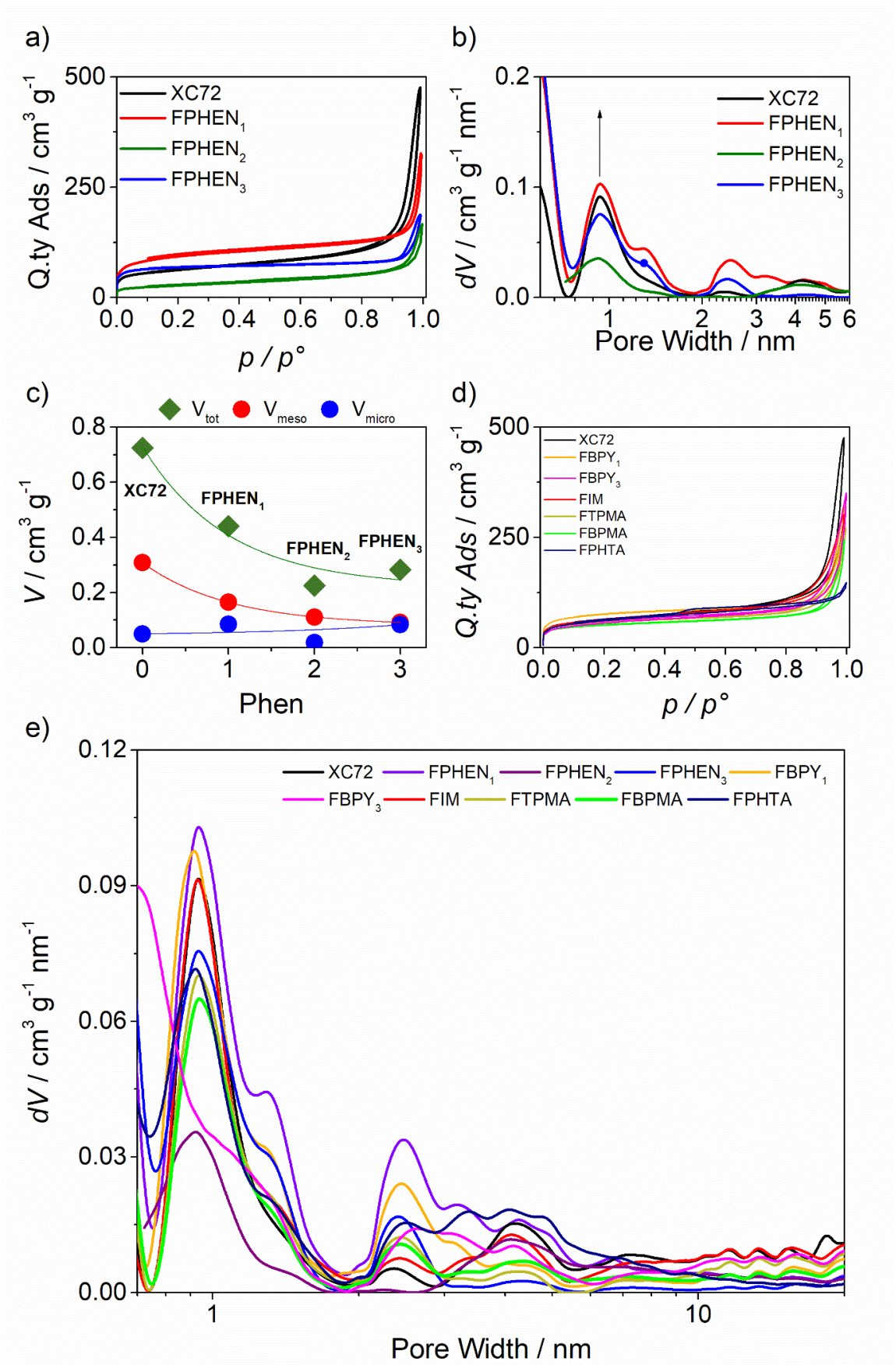

Figure 5.3. a) Isotherms and b) narrow range pore size distribution comparison of $FPHEN_x$ catalysts compared to the sole support; Evolution of c) pore volume for $FPHEN_x$ catalysts compare to sole support; d) Isotherms of other materials and e) pore size distribution comparison of catalysts.

ORR activity of catalysts in acidic media

The activity of each catalyst was tested in acidic media (0.5 M H_2SO_4) using rotating ring disk electrode (RRDE). A summary of obtained results is shown in Figure 5.4 and Table 5.3. It is interesting to note that the catalysts prepared by using the Fe-Phthalocyanine complex, which contains a preformed Fe-N_4 site, is active but not the most active. The best activity was observed for $FPHEN_3$ by judging the half-wave potential and the kinetic current at 0.8 V vs. RHE. The phenanthroline like structure seem to be beneficial for activity/site formation, indeed $FPHEN_1$ and $FBPY_1$ show good performances. This is unexpectedly not confirmed by the result for $FBPY_3$, which is obtained with $FeBPY_3$ complex, even after repeating the synthesis multiple times (both complex and catalysts were re-prepared). Also, the higher activity of $FBPY_1$ if compared with $FPHEN_1$ is quite strange and do not explain why the use of $FeBPY_3$ as precursor lead to mediocre activity. Kim et al. demonstrated that a high stability of the iron ligand complex affects the atomic state of both Fe and N in the pyrolyzed electrocatalyst, because during the pyrolysis, larger amounts of N dopants were preserved as pyridinic sites rather than converted to graphitic sites [8]. Therefore, one possible observation is that $FeBPY_3$ has a lower stability so that the preservation of N-pyridinic site is less efficient than in $FPHEN_3$.

For the abovementioned reason, the catalysts prepared with non-aromatic ligands, such as EDTA, PEHA and CYCLAM cannot have a reactivity comparable with that of the catalysts shown in Figure 5.4. The formers are not comparable in terms of $E_{1/2}$ and j_k with $FPHEN_3$ and this is due to the poor ability to fix nitrogen in the carbonaceous matrix and to create Fe-N_x active sites. The latter assumption is confirmed by elemental analyses of corresponding catalysts that show little or negligible nitrogen and iron content (Table 10.9).

FTPMA and FBPMA behave in similar way, as observed for the data of nitrogen fixation, and this is probably due to the similar structure of the ligand. The catalysts made from FeIM and $FePHEN_2$ are the worst of series, this is probably due to different reasons. The former has a different cyclic structure (no pyridine cycle) that is less efficient in doping with nitrogen, probably due to a lower stability or due to the five-fold nature of the cycle.

The selectivity toward the four electron pathway, namely from O_2 to H_2O, is very high for all the catalysts, with $FPHEN_3$. Conversely the catalysts prepared by FeEDTA, FePEHA and FeCYCLAM show a much lower selectivity versus the four electron O_2 reduction, and that is probably due to the lack of nitrogen functional groups able at the reduction, in particular the step from H_2O_2 to water [9] (Table 10.9 and Figure 10.17). It is worth to stress that in general a low hydrogen peroxide production could be linked to a loading effect (see previous chapter), which is known to produce a dummy 4 electron determination in presence of a 2+2 electron pathway.

It is also interesting to observe that in acid electrolyte, the catalytic activity expressed as $E_{1/2}$ scales with the nitrogen content determined by elemental analysis, that confirm the fundamental role of the ligand precursor in the ability to generate the active sites in the resulting Fe-N-C catalyst (Figure 5.4d).

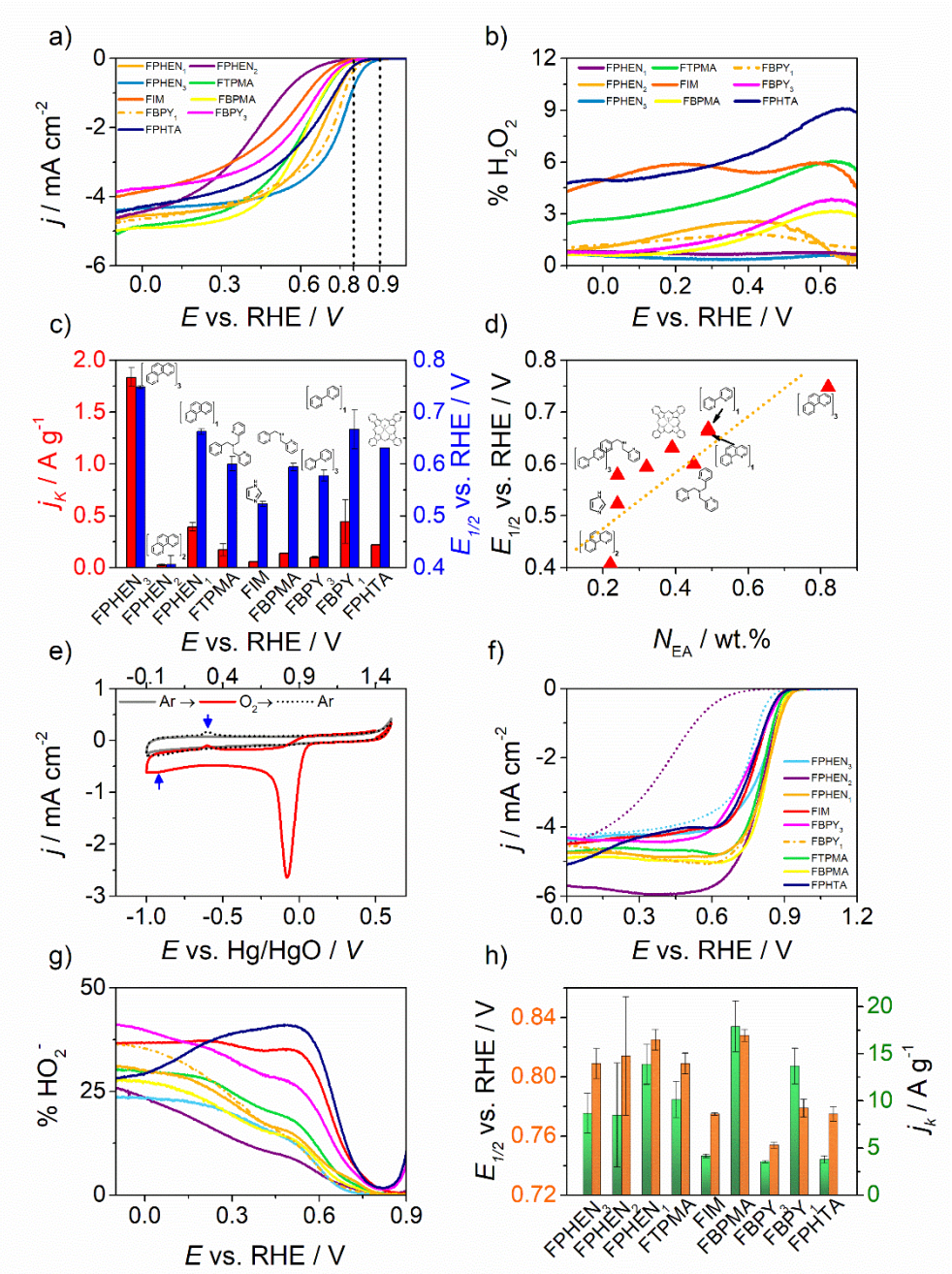

Figure 5.4. Electrochemical data of different Fe-N-C catalysts in O_2 saturated 0.5 M H_2SO_4: a) LSV at 1600 rpm, 2 mV s^{-1}, b) H_2O_2 yield, c) summary of activity in term of half-wave potential and kinetic current at 0.8V vs. RHE and finally d) variation of half-wave potential as a function of nitrogen content determined from elemental analysis. Electrochemical data of different Fe-N-C catalysts in O_2 saturated 0.1 KOH: e) cyclic voltammetry in Ar and O_2 for $FPHEN_3$ at 5 mV s^{-1}, f) LSV at 1600 rpm, 2 mV s^{-1}, g) HO_2^- yield, h) summary of kinetic current and half-wave potential.

Table 5.3. Electrochemical data for Fe-N-C catalysts in O_2 saturated 0.5 M H_2SO_4 electrolyte

		$E_{j=0.1}$ V vs. RHE	$E_{1/2}$ V vs. RHE	j_L mA cm^{-2}	$j_{0.8\,V}$ mA cm^{-2}	$j_{k,\,0.8\,V}$ A g^{-1}	n -	%H_2O_2 at 0.7 V
1	**FPHEN$_3$**	0.871	0.748 ± 0.003	4.29	0.88	1.84 ± 0.09	3.99	0.6
2	**FPHEN$_2$**	0.714	0.41 ± 0.02	4.48	0.02	0.03 ± 0.01	3.98	-
3	**FPHEN$_1$**	0.825	0.663 ± 0.005	4.65	0.23	0.39 ± 0.04	3.99	0.8
4	**FBPY$_3$**	0.781	0.58 ± 0.01	3.85	0.06	0.10 ± 0.01	3.98	4.2
5	**FBPY$_1$**	0.824	0.67 ± 0.04	4.37	0.25	0.4 ± 0.2	3.97	1.5
6	**FIM**	0.762	0.523 ± 0.005	3.64	0.04	0.059 ± 0.003	3.87	4.2
7	**FTPMA**	0.799	0.60 ± 0.01	4.60	0.10	0.17 ± 0.06	3.96	5.1
8	**FBPMA**	0.793	0.594 ± 0.007	4.88	0.08	0.141 ± 0.002	3.99	2.1
9	**FPHTA**	0.824	0.631 ± 0.005	4.30	0.22	0.390 ± 0.002	3.90	8.9

ORR activity of catalysts in alkaline media

To expand our analysis, we also performed analysis in alkaline media. Figure 5.4e reports as an example, the CV of ORR process compared to the same response in Ar saturated electrolyte. The ORR process is evidenced by a well-defined reduction peak at 0.795 V vs. RHE. Furthermore, upon saturation with oxygen a new redox couple, with a peak-peak separation of almost 300 mV, appears at more cathodic potentials (blue arrows in the picture). This electrodic process can be linked to Fe^{3+}/Fe^{2+} oxidation reaction of iron oxide or iron hydroxide species formed during the potential scan after O_2 saturation. To confirmation this, Fe_3O_4 was purposely added to the catalyst ink (10 wt.% in the ink with respect to the carbon catalyst) and the cyclic voltammetry recorded at the modified electrode shows a more intense peak in the same position which can be linked to Fe oxidation (Figure 10.22) [10,11].

Figure 5.4f,g shows the LSV and peroxide yield in this media and it is clear that the activity recorded in KOH is very different from the acid scenario. As expected, the activity in alkaline environment is higher than in acidic electrolyte, but it is curious to note how catalysts which were not very active in acid electrolyte are very active in alkaline electrolyte such as FPHEN$_2$ (Table 10.11).

Figure 5.4f shows that in general the activity is high and comparable for all catalysts, and some shows even higher activity compared to FPHEN$_3$ that had the higher activity in acid media (FTPMA and FBPMA). As already observed, the catalytic activity does not correlate with the same parameter observed in acid, and this is due to the different mechanisms and sties involved in the reduction process. One explanation is the fact that some functional group like graphitic and pyridinic [12–14] nitrogen are less active in acid electrolyte due to protonation, while Fe-N_4 could be blocked in alkaline environment by OH^- adsorption, and at the same time the presence of FeC_x NPs under carbon layer could enhance the activity in alkaline media even without the direct exposure of metal [15].

Figure 5.4g shows that a mixed 2/4 electron pathway is more favourable in alkaline environment. A variation of the number of exchange electron can be observed on some LSV where a curvature is present paired by a variation of the H_2O_2 yield derived from the ring current (reported as HO_2^-% yield in Figure 5.4g). This is particularly evident in FPHEN$_3$ where O_2 appears to follow a mixed 2+2/4 electron process, where O_2 can be reduced to both H_2O and H_2O_2 the latter being further reduced at more negative potential.

NO_2 stripping: SD and TOF determination

As showed in previous work and in this thesis [16–21] site density (SD) and turn over frequency (TOF) allow to understand if the increment in activity is a consequence of higher SD or of change of intrinsic activity of the sites. The idea in this case was to understand whether different iron nitrogen complex can induce a more efficient formation of Fe-N_x active sites or the formation of active sites with different intrinsic reactivity, namely in SD or TOF. Typical voltammetric response are shown in Figure 5.5a, c which report the CV in Ar-purged electrolyte after poisoning and stripping of -NO, and the LSV recorded at 1600 rpm 5 mV s^{-1} in O_2 saturated electrolyte before and after the poisoning of Fe-N_x sites with nitrosyl groups and after the recovery of catalytic activity obtained after the removal of NO groups by electrochemical stripping.
Figure 5.5c also shows the deactivation of catalysts, almost fully recovered after stripping. It is however worth to mention that the catalytic activity is not completely suppressed upon NO-poisoning, and this attests that other active sites than Fe-N_x are present in the catalysts.
Figure 5.5d, reports the Tafel plots for $FPHEN_3$ in O_2 saturated electrolyte of the three steps: unpoisoned, poisoned and recovered. The Tafel slope does not change in the three different conditions attesting the mechanism is not affected by the switch off of Fe-N_x active site, but what sensitively changes is the kinetic current, which decrease of almost an order of magnitude between the unpoisoned and poisoned sample. In conclusion this methodology certainly gives a powerful tool to compare different material, even if certainly does not probe all the active sites in those catalysts.

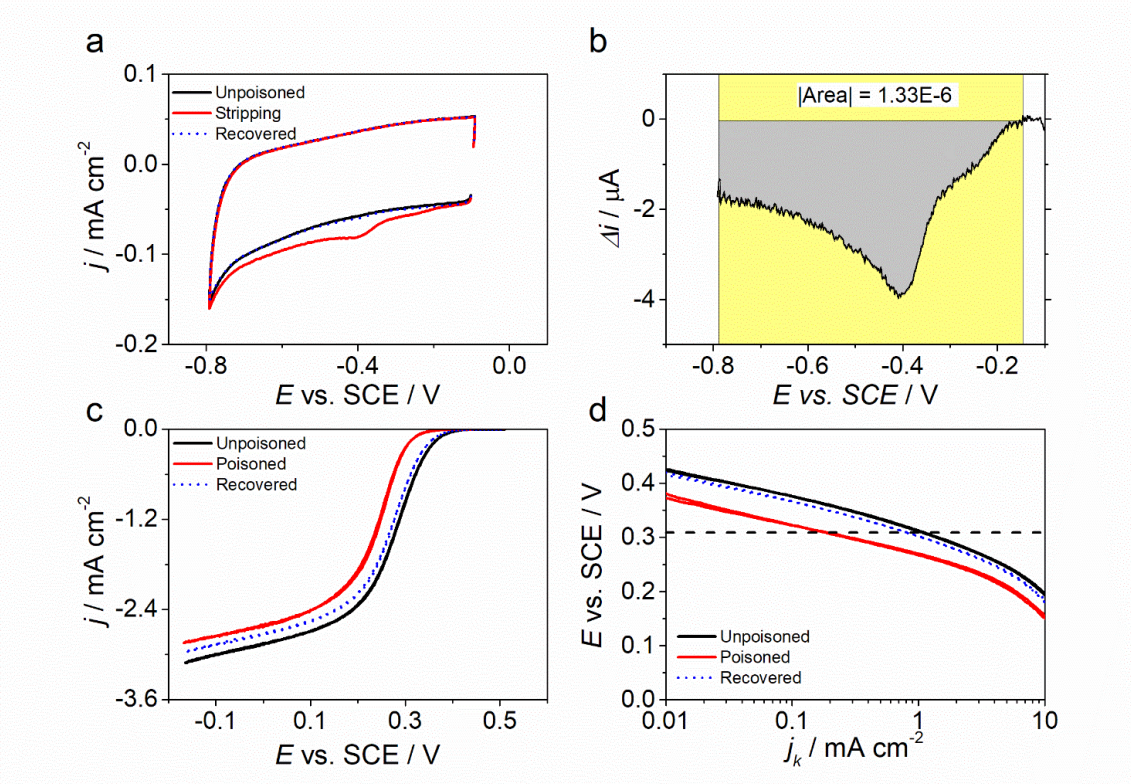

Figure 5.5. Voltametric response during a typical stripping analysis recorded in acetate buffer: a) CV in the stripping region before, during and after stripping in argon purged electrolyte, b) stripping charge area extrapolated from the CV showed in 'a', c) LSV at 1600 rpm and d) Tafel plot in O_2 saturated electrolyte.

Table 5.4 and Figure 5.6 show that in the catalysts prepared from different Fe-N complexes, the activity is incremented both due to the site density and TOF growth (Figure 5.6a and b, respectively).
The trend with SD points out a clear structure-activity relationship. It is worth to mention that the NO-stripping was also carried out as a control measure on a sample of nitrogen doped carbon free of any metallic contamination. Looking at the trend of the points in Figure 5.6a and observing the intercept for SD tending to zero, it is clear that this point does not coincide with the point obtained for the nitrogen doped carbon, which confirm that the addition of metal, even in small quantities, hugely improve the activity. This correlation seems to be a log-type with a steep initial increment to reach an almost linear trend (dotted blue line Figure 5.6a).
These two dependencies are summarized in Figure 5.6c, it is evident that the climbing of iso-current curve is done diagonally meaning that both SD and TOF are growing. From this it is possible to conclude that $FePHEN_3$ as precursor seems to be able to create more and more active sites compare to other precursors.
The half-wave potential and therefore the SD show an apparent dependence on the hierarchical factor HF (Figure 5.6d), which is a descriptor of how much interconnected are micropores and mesopores. HF is expressed by the equation:

$$HF = (V_{\mu} \times S_m)/ (V_{TOT} \times S_{QSDFT}) \quad (5.1)$$

where V_{μ} and V_{TOT} are the volume of micropore and the total volume pore respectively, whereas S_m and S_{QSDFT} are the surface area of mesopore, and the total surface area (from 0.5 to 35 nm of pore width) determined by the quenched-solid density-functional-theory model [22].
A maximized HF is beneficial since a good amount of mesopore and micropore are present. We already proved that the iron complexes have at different extend the capability to increase the micropore volume by the action of small molecules such as CO, CO_2, NO, NO_2, etc. but at the same time to decrease the area of mesopores because of the pyrolysis of the ligand itself. The result is that the best catalysts in term of $E_{1/2}$ and SD are those showing high HF value even if the catalyst with better HF ($FPHEN_1$) is not the best catalyst ever ($FPHEN_3$) (Figure 5.6d). This is a clear indication that the catalyst precursor is not only able to fix Fe-N_x and other nitrogen active sites into the carbon matrix, but it has also an effect on the textural properties, and the two effects can oppose each other. This clearly places a limit on the ability to increase the catalytic activity simply by playing on the initial content of complex, since while we try to increase the SD by increasing the complex loading at the same time, we are going to worsen the textural properties (HF) by modifying the micro/mesopore ratio. This was also previously described in another chapter by playing with the initial amount of $FePHEN_3$. Again, this summarized in the fact that the iron-nitrogen precursor complex plays a dual role in determining the overall catalytic activity in terms of both the number of active sites available and the usability of the active sites themselves, i.e., textural properties.
Parallel to that we also evaluate a utilization factor (Φ in Table 5.4), calculated as a ration between the SD found and the theoretical maximum amount of Fe-N_x based on Fe in these samples. This suggests that $FePHEN_3$ is efficient to fix iron but probably most of iron is not spent to form Fe-N_x sites, or at least to form sites that are detected by nitrite stripping, i.e., accessible by the reagents and electrolyte. On the contrary other complex like FeBPMA allows to fix less iron but a larger amount of it is used to form active sites, that can be reached by reagents.

Table 5.4. Nitrite stripping data and utilization factor

		Q_{STRIP} C g^{-1}	Δj_k [a] A g^{-1}	SD 10^{18} sites g^{-1}	MSD 10^{-6} mol sites g^{-1}	TOF [a] e^- sites^{-1} s^{-1}	Φ %
1	**$FPHEN_3$**	3.39	4.52	4.24	7.03	6.66	6.11
2	**$FPHEN_2$**	0.77	0.15	0.96	1.59	0.96	5.56
3	**$FPHEN_1$**	2.09	0.90	2.61	4.33	2.16	14.92
4	**$FBPY_3$**	1.29	0.40	1.61	2.68	1.54	34.45
5	**$FBPY_1$**	1.76	1.11	2.19	3.64	3.16	20.73
6	**FIM**	0.71	0.05	0.88	1.46	0.34	31.41
7	**FTPMA**	1.34	0.12	1.68	2.79	0.48	26.74
8	**FBPMA**	2.00	0.38	2.50	4.15	0.95	45.28
9	**FPTHA**	2.31	0.06	2.88	4.78	0.13	3.26
	Metal free	0.16	0.00[b]	0.20	0.32	0.00[b]	-

[a] 0.309 V vs. SCE ≈ 0.8 V vs. RHE, [b] no faradic current at this potential

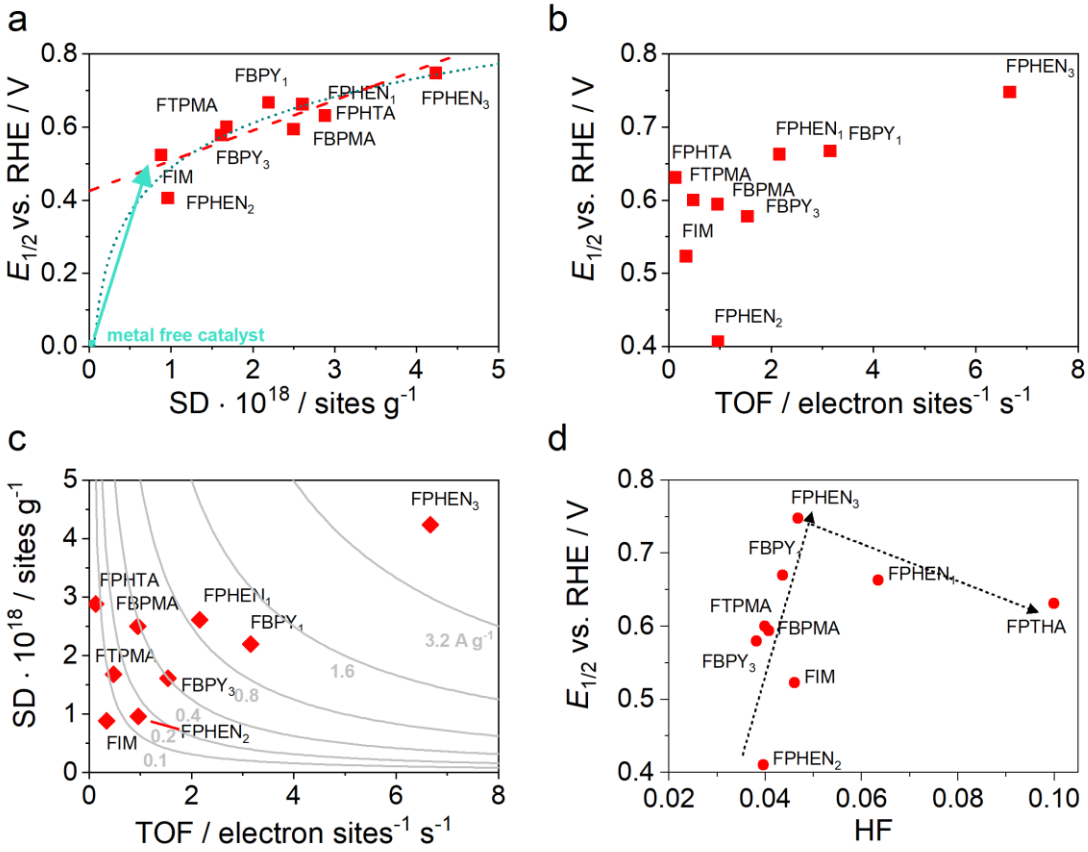

Figure 5.6. a, b) Correlation of activity ($E_{1/2}$) and SD/TOF, c) current map by plotting SD vs. TOF and d) Correlation between $E_{1/2}$ and the hierarchical factor HF determined by Equation 6, dotted lines are only intended for guiding the eye.

Accelerated *stress-test (AST) / Stability Test*

It is well known that stability is the Achilles heel of Fe-N-C catalysts [23–25] and for this reason we performed durability/stability test on the best performing catalyst, namely $FPHEN_3$. Intensive cycling (7000 cycles) was performed between 0.55 and 1.05 V vs. RHE for both electrolytes.

Figure 5.7a shows the LSV profile variation in O_2-saturated 0.5 M H_2SO_4, and it is clear that $E_{1/2}$ shift to more negative potential as well as the kinetic current decay of about 60% after 7000 cycles (Figure 5.7b,c). It is also interesting to observe, and not easily explainable, that the hydrogen peroxide yield progressively decreases as shown in Figure 7c passing from 3% to 1% at 0.7 V vs. RHE.

Similar behaviour is observed in O_2-saturated 0.1 M KOH the behaviour is similar Figure 5.7d), but a greater stability is observed, after the same number of cycles the activity at 0.8 V vs. RHE decay of only 10%, the same is true for half-wave potential. In fact, in acid electrolyte the decrement is of about 60 mV (Figure 5.7c) while in KOH is less than 10 mV. In this case also a slightly reactivation is present (first 400 cycle), and the amount of peroxide production slightly increase to became constant (Figure 5.7f).

Stripping on the same electrode performed after AST reveal that a SD decrement (from 4.19×10^{18} to 2.83×10^{18} sites g^{-1}) is responsible of activity decay in acid media, while in KOH the SD remains almost unchanged (from 4.19×10^{18} to 4.72×10^{18} sites g^{-1}). For degradation reason the data before the AST was take on a different electrode with the same loading (0.6 mg cm^{-2}). To summarise, the lower stability in acid electrolytes appears to be determined by the extinction of active sites either by chemical modification of the active site itself or by changes in the structure of the substrate and thus its accessibility.

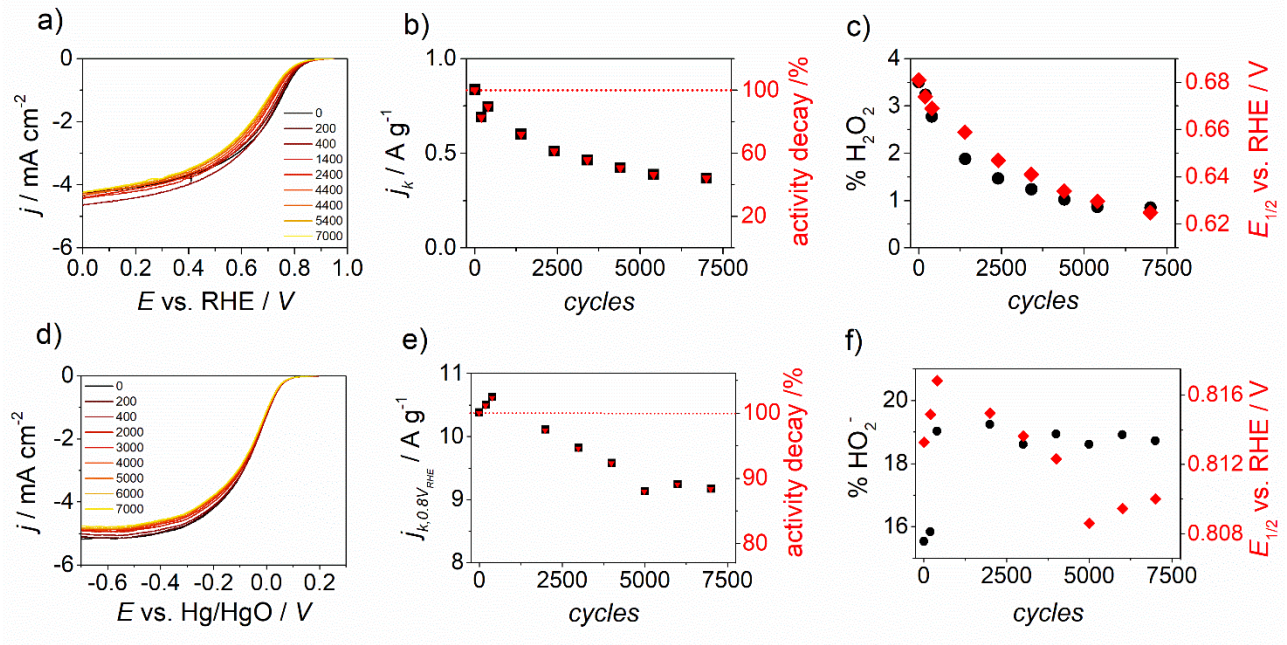

Figure 5.7. AST result in (a-c) O_2-saturated 0.5 M H_2SO_4 and (d-e) O_2-saturated 0.1 M KOH: a, d) LSV at 5 mV s^{-1} 1600 rpm, b, e) kinetic current variation c, f) H_2O_2 yield and $E_{1/2}$ variation.

5.2. Conclusion

This chapter cover the effect of different iron complex on the formation of FeN_x sites and therefore on the activity toward the ORR. Twelve complexes were considered to synthesize as many Fe-N-C catalysts with Vulcan XC72 as carbon support. The absence of aromatic section on the ligand, like for EDTA or CYCLAM lead to poor iron and nitrogen fixation and thus to poor activity towards the ORR.

The study of catalysts prepared from 1,10-Phenanthroline, 2,2'-Bipyridyl, Phthalocyanine, TPMA and BPMA complexes revealed a dual role for the complex. On the one hand, the ability to form Fe-N_x sites depends on the type of complex, but on the other hand, the pyrolysis of the complex leads to a modification of the textural properties of the final catalyst with a decrease of the mesopores surface and an increase of the micropores volume. The best catalyst was the one prepared with $Fe(phen)_3Cl_2$.

It was proved that there is a limit on the capability to increase catalytic activity simply by playing on the initial content of complex, since increasing the complex loading does not increase the SD or TOF, but it is even detrimental since textural properties worsen. This aspect is confirmed by the utilization factor Φ, which suggests that $FePHEN_3$ is efficient to fix iron but probably most the Fe-N_x sites, remains not accessible by the reagents and electrolyte. Conversely, other complex like FeBPMA allows to fix less Fe-N_x sites, which are however better accessible.

5.3. Bibliography

[1] T. Onodera, S. Suzuki, T. Mizukami, H. Kanzaki, Enhancement of oxygen reduction activity with addition of carbon support for non-precious metal nitrogen doped carbon catalyst, J. Power Sources. 196 (2011) 7994–7999. https://doi.org/10.1016/j.jpowsour.2011.05.041.

[2] E.C. Ellingsworth, B.T. Ab, G. Szulczewski, Thermal conversion of [Fe(phen) 3](SCN) 2 thin films into the spin crossover complex Fe(phen) 2 (NCS) 2 3, 3 (2013) 3745. https://doi.org/10.1039/c3ra22534h.

[3] A.A. Bagabas, M. Alsawalha, M. Sohail, S. Alhoshan, R. Arasheed, Synthesis, crystal structure, and characterization of cyclohexylammonium tetraisothiocyanatocobaltate(II): A single-source precursor for cobalt sulfide and oxide nanostructures, Heliyon. 5 (2019) e01139. https://doi.org/10.1016/j.heliyon.2019.e01139.

[4] M. Williams, L. Khotseng, Q. Naidoo, L. Petrik, A. Nechaev, V. Linkov, Applicability of analytical protocols for the characterisation of carbon-supported platinum group metal fuel cell electrocatalysts, S. Afr. J. Sci. 105 (2009) 285–289. https://doi.org/10.4102/sajs.v105i7/8.76.

[5] B. Paczosa-Bator, Effects of type of nanosized carbon black on the performance of an all-solid-state potentiometric electrode for nitrate, Microchim. Acta. 181 (2014) 1093–1099. https://doi.org/10.1007/s00604-014-1216-7.

[6] M. Thommes, K. Kaneko, A. V. Neimark, J.P. Olivier, F. Rodriguez-Reinoso, J. Rouquerol, K.S.W. Sing, Physisorption of gases, with special reference to the evaluation of surface area and pore size distribution (IUPAC Technical Report), Pure Appl. Chem. 87 (2015) 1051–1069. https://doi.org/10.1515/pac-2014-1117.

[7] T. Onodera, T. Mizukami, S. Suzuki, J. Kawaji, K. Yamaga, T. Yamamoto, Analysis of forming process of nitrogen-doped carbon catalyst derived from Fe 1,10-phenanthroline compound and its oxygen reduction reaction activity, Catal. Commun. 43 (2014) 66–71. https://doi.org/10.1016/j.catcom.2013.09.011.

[8] M. Kim, J.M. Yoo, C.Y. Ahn, J.H. Jang, Y.J. Son, H. Shin, J. Kang, Y.S. Kang, S.J. Yoo, K.S. Lee, Y.E. Sung, Rational Generation of Fe−Nx Active Sites in Fe−N−C Electrocatalysts Facilitated by Fe−N Coordinated Precursors for the Oxygen Reduction Reaction, ChemCatChem. 11 (2019) 5982–5988. https://doi.org/10.1002/cctc.201901242.

[9] U. Tylus, Q. Jia, K. Strickland, N. Ramaswamy, A. Serov, P. Atanassov, S. Mukerjee, Elucidating oxygen reduction active sites in pyrolyzed metal-nitrogen coordinated non-precious-metal electrocatalyst systems, J. Phys. Chem. C. 118 (2014) 8999–9008. https://doi.org/10.1021/jp500781v.

[10] H. Wang, Z. Xu, H. Yi, H. Wei, Z. Guo, X. Wang, One-step preparation of single-crystalline Fe2O3 particles/graphene composite hydrogels as high performance anode materials for supercapacitors, Nano Energy. (2014). https://doi.org/10.1016/j.nanoen.2014.04.009.

[11] K. Duschek, M. Uhlemann, H. Schlörb, K. Nielsch, K. Leistner, Electrochemical and in situ magnetic study of iron/iron oxide films oxidized and reduced in KOH solution for magneto-ionic switching, Electrochem. Commun. (2016). https://doi.org/10.1016/j.elecom.2016.09.018.

[12] W. Zhong, Z. Wang, S. Han, L. Deng, J. Yu, Y. Lin, X. Long, M. Gu, S. Yang, Identifying the Active Sites of a Single Atom Catalyst with pH-Universal Oxygen Reduction Reaction Activity, Cell Reports Phys. Sci. 1 (2020) 100115. https://doi.org/10.1016/j.xcrp.2020.100115.

[13] M. Rauf, Y. Di Zhao, Y.C. Wang, Y.P. Zheng, C. Chen, X.D. Yang, Z.Y. Zhou, S.G. Sun, Insight into the different ORR catalytic activity of Fe/N/C between acidic and alkaline media: Protonation of pyridinic nitrogen, Electrochem. Commun. 73 (2016) 71–74. https://doi.org/10.1016/j.elecom.2016.10.016.

[14] P.G. Santori, F.D. Speck, J. Li, A. Zitolo, Q. Jia, S. Mukerjee, S. Cherevko, F. Jaouen, Effect of Pyrolysis Atmosphere and Electrolyte pH on the Oxygen Reduction Activity, Stability and Spectroscopic Signature of FeN x Moieties in Fe-N-C Catalysts, J. Electrochem. Soc. 166

(2019) F3311–F3320. https://doi.org/10.1149/2.0371907jes.
[15] R. Sgarbi, K. Kumar, F. Jaouen, A. Zitolo, E.A. Ticianelli, F. Maillard, Oxygen reduction reaction mechanism and kinetics on M-NxCy and M@N-C active sites present in model M-N-C catalysts under alkaline and acidic conditions, J. Solid State Electrochem. 25 (2021) 45–56. https://doi.org/10.1007/s10008-019-04436-w.
[16] M. Mazzucato, G. Daniel, A. Mehmood, T. Kosmala, G. Granozzi, A. Kucernak, C. Durante, Effects of the induced micro- and meso-porosity on the single site density and turn over frequency of Fe-N-C carbon electrodes for the oxygen reduction reaction, Appl. Catal. B Environ. 291 (2021) 120068. https://doi.org/10.1016/j.apcatb.2021.120068.
[17] G. Daniel, Y. Zhang, S. Lanzalaco, F. Brombin, T. Kosmala, G. Granozzi, A. Wang, E. Brillas, I. Sirés, C. Durante, Chitosan-Derived Nitrogen-Doped Carbon Electrocatalyst for a Sustainable Upgrade of Oxygen Reduction to Hydrogen Peroxide in UV-Assisted Electro-Fenton Water Treatment, ACS Sustain. Chem. Eng. 8 (2020) 14425–14440. https://doi.org/10.1021/acssuschemeng.0c04294.
[18] D. Malko, A. Kucernak, T. Lopes, In situ electrochemical quantification of active sites in Fe-N/C non-precious metal catalysts, Nat. Commun. 7 (2016) 13285. https://doi.org/10.1038/ncomms13285.
[19] D. Malko, A. Kucernak, T. Lopes, Performance of Fe–N/C Oxygen Reduction Electrocatalysts toward NO_2^- , NO, and NH_2OH Electroreduction: From Fundamental Insights into the Active Center to a New Method for Environmental Nitrite Destruction, J. Am. Chem. Soc. 138 (2016) 16056–16068. https://doi.org/10.1021/jacs.6b09622.
[20] M. Primbs, Y. Sun, A. Roy, D. Malko, A. Mehmood, M.-T. Sougrati, P.-Y. Blanchard, G. Granozzi, T. Kosmala, G. Daniel, P. Atanassov, J. Sharman, C. Durante, A. Kucernak, D. Jones, F. Jaouen, P. Strasser, Establishing reactivity descriptors for platinum group metal (PGM)-free Fe–N–C catalysts for PEM fuel cells, Energy Environ. Sci. 13 (2020) 2480–2500. https://doi.org/10.1039/D0EE01013H.
[21] F. Luo, C.H. Choi, M.J.M. Primbs, W. Ju, S. Li, N.D. Leonard, A. Thomas, F. Jaouen, P. Strasser, Accurate evaluation of active-site density (SD) and turnover frequency (TOF) of PGM-free metal-nitrogen-doped carbon (MNC) electrocatalysts using CO cryo adsorption, ACS Catal. (2019) 4841–4852. https://doi.org/10.1021/acscatal.9b00588.
[22] G. Daniel, T. Kosmala, F. Brombin, M. Mazzucato, A. Facchin, M.C. Dalconi, D. Badocco, P. Pastore, G. Granozzi, C. Durante, Highly Graphitized Fe-N-C Electrocatalysts Prepared from Chitosan Hydrogel Frameworks, Catalysts. 11 (2021) 390. https://doi.org/10.3390/catal11030390.
[23] X. Xie, C. He, B. Li, Y. He, D.A. Cullen, E.C. Wegener, A.J. Kropf, U. Martinez, Y. Cheng, M.H. Engelhard, M.E. Bowden, M. Song, T. Lemmon, X.S. Li, Z. Nie, J. Liu, D.J. Myers, P. Zelenay, G. Wang, G. Wu, V. Ramani, Y. Shao, Performance enhancement and degradation mechanism identification of a single-atom Co–N–C catalyst for proton exchange membrane fuel cells, Nat. Catal. 3 (2020) 1044–1054. https://doi.org/10.1038/s41929-020-00546-1.
[24] U. Martinez, S. Komini Babu, E.F. Holby, P. Zelenay, Durability challenges and perspective in the development of PGM-free electrocatalysts for the oxygen reduction reaction, Curr. Opin. Electrochem. 9 (2018) 224–232. https://doi.org/10.1016/j.coelec.2018.04.010.
[25] Y. Shao, J. Dodelet, G. Wu, P. Zelenay, PGM-Free Cathode Catalysts for PEM Fuel Cells: A Mini-Review on Stability Challenges, Adv. Mater. 31 (2019) 1807615. https://doi.org/10.1002/adma.201807615.

6. Synergistic Effect of Sn and Fe in Fe-N_x site formation and activity in Fe-N-C Catalyst for ORR

This chapter covers the experiment performed by introducing a secondary metal centre. Here classical Fe-N-C materials were co-doped with Sn as a secondary metal centre.

The addition of a second metal, generally to Fe-N-C catalysts, could have an impact of site formation [1], final activity [2], or stability [3]. For example, the addition of Ni to the precursor mixture results in a lower number of sites, due to competition mechanisms during the pyrolysis [1], while the addition of Mn shows an activity improvement in alkaline environment [2], and the use of copper seems to be beneficial to activity [2]. Recently also Zr was used to improve the activity of Fe-N-C. In this case the effect was induced by a synergistic effect between Fe-N_x site and ZrO_x present on the carbon surface [4]. *d*-group metals (4^{th} period) are generally the only used to fabricate M-N-C catalysts, because of their better performances. Indeed, other metal are less interesting due to the inability to form nitrogen coordinating single sites materials (in pyrolytic condition) or to the tendency of forming NPs instead of isolated metal-nitrogen sites [5,6]. Other metals are too pricy or are more prone to catalyse other reactions, such as the homogeneous CO_2 reduction [7–11]. In a recent paper, Strasser et Co. showed the possible role of Sn in oxygen reduction reaction (ORR) in real fuel cell system [3]. Sn is a *p*-block element that was substantially [12] never studied in the single sites catalyst shape, conversely to other transition metals such as Fe or Co [13,14]. In fact, Sn is typically used as catalyst in nanoparticle form [15,16]. For this reason, the present work aims to study the effect of Sn on an already consolidated material made from iron-phenanthroline and carbon black support [17] to see how its addition impacts the physico-chemical and catalytical properties of the resulting material.

Sn-N-C according to literature shows excellent activity, in particular in fuel cell setup, here the same catalyst shows a non-negligible activity in 0.5 M H_2SO_4 electrolyte, but not as high as expected, meaning the different and uncertain nature of active sites. On the other hand, in mixed Fe,Sn-N-C catalysts, the presence of Sn improves the catalytic activity probably because of a higher Fe-N_4 site density, whereas the possible synergistic co-presence of Fe-N_4 and Sn-N_x was not proved, but not excluded, while the role of Sn nanoparticles was excluded in acid, but not in alkaline media.

At the same time, it is important to develop and improve methodology to test the catalysts under realistic conditions, which is one of the problems of rotating (ring) disk electrode (R(R)DE) analysis. Indeed, rotating techniques do not always reflect the performance on Membrane electrode assembly (MEA); floating electrode and gas diffusion electrode (GDE) cells are two of the possible alternatives, whose results can be directly compared to flowing tests, levelling the problem of scaling promising materials as characterized by RRDE but showing sloppy performance in full device tests [18–21]. As a result of this, the measured mass activity with GDE electrode technique will be a more reliable screening metric to down select materials for scale up. Therefore here, for the first time up to our knowledge, Pt-free material are tested for ORR in GDE electrode setup in both performance and durability tests. The comparison between the two setups has then been extensively study on a benchmark Fe-N-C and discussed in chapter 8.

6.1. Result and discussion

6.1.1. Synthesis of Sn_xFe_y-N-C Materials

The two complexes were used to synthesize of Fe-N-C catalysts as follow: 200 mg of Vulcan XC72 or $CBCO_2$-5 (Vulcan XC72 treated at 950 °C in CO_2 gas flow [22]) and a suitable ratio of Sn-phen/Fe-phen complexes (different molar percentage of metal compared to the molar amount of carbon support were chosen) were vibro-milled at 18, 20 and 25 Hz for a total of 1 hour (20 min. for each frequency in ascending order). Then the mixture was heated at 900 °C in a tubular furnace (Carbolite, with a quartz tube ∅ = 25 mm) for 2 hours under reductive nitrogen-hydrogen atmosphere (9% H_2 in the mixture, HG 2400 Claind) and eventually cool down to ambient temperature under pure nitrogen flow. $Fe(phen)_3Cl_2$ was chosen as precursor since it gives the best activity among several Fe/N complexes [17]. The resulting powder was vibro-milled and then washed at reflux in 100 mL 1 M solution of H_2SO_4 for 3h at 100°C under continuous stirring. The suspension was then filtered and rinsed with at least 0.5 L of milli-Q water and finally dried in oven at 40 °C overnight. Three reference samples prepared by utilizing only Sn-phen were prepared and washed, for the reason later explained (see also Appendix, paragraph 10.3.1.3), also in 4 M HCl, 2 M H_2SO_4 or 2 M HNO_3 at 90 °C for 6 h in Ar atmosphere according to Luo et al. SI [3]. After the acid leaching, the powder was vibro-milled or pounded in a mortar and then heated again at 900 °C as described before. The resulting powders are labelled as Sn_xFe_yC (where x and y are the initial percentage of tin and iron, respectively and C is the name of carbon support). The catalysts were vibro-milled a final time before electrochemical test with the same settings listed above.

A control metal-free catalyst was synthetized adopting the same procedure but using only phenanthroline as nitrogen precursor but reaching the same molar amount as it would be with $2\%_{mol}$ of $Fe(phen)_3Cl_2$. This sample is named as N-C along the text.

6.1.2. Carbon support selection and catalyst preparation

The first step was to select a proper carbon support for evaluating the Sn effect on the Fe-N_x sites formation and activity. On this regard, four different carbons were considered i.e., Vulcan XC72, EC-300J, MC and $CBCO_2$-5, which are all commercially available with the exception of $CBCO_2$-5. The latter is a commercial carbon (CB, Super P) activated with CO_2 at 950 °C for 5 h (see also previous chapter) in a tubular furnace [22]. These four supports were chosen for the different pore structure: medium-low micro/mesoporous carbon ($CBCO_2$-5 and Vulcan XC72), highly porous (EC-300J) and highly mesoporous (MC) as shown in Figure 6.1a,b. Initially, four catalysts with equal molar content of Sn and Fe complexes in the synthetic mixture (Sn_1Fe_1) but with a different carbon support were synthetized. The 1/1 composition was chosen as a preliminary composition test. The four supports were characterized by elemental analysis (EA) to detect the nitrogen content and the possible traces of sulphur (which could have an impact on the final activity [23]). N_2 physisorption analysis was also performed for guiding the selection of the four carbon supports, among several others, on the base of the surface area and of pore size distribution that are generally not made explicit from the commercial seller (Table 10.13). The final choice of the carbon support was made by evaluating the one that once functionalized with Sn-phen and Fe-phen showed the best compromise between nitrogen content, according to EA, and ORR activity in term of $E_{1/2}$ and j_k determined by RRDE measurements at 1600 rpm (2 mV s^{-1}) in O_2-saturated 0.5 M H_2SO_4. According to the $E_{1/2}$ and j_k (at 0.8 V vs. RHE) parameters reported in Table 6.5 and Figure 6.1c,d, Sn_1Fe_1XC72 was the catalyst with better catalytic performance ($E_{1/2}$= 0.719 V vs. RHE, j_k = 1.16 A g^{-1}), even if similar performances were achieved with EC300J, which represent therefore a good alternative ($E_{1/2}$= 0.722 V vs. RHE, j_k = 1.08 A g^{-1}). On the base of these findings, Vulcan XC72 was selected as support to carry out all the other Sn/Fe combinations. Specifically, five different catalysts with different Sn-phen/Fe-phen ratio were prepared (Sn_xFe_yXC72), along with two samples with only Sn (Sn_xXC72 with x = 2, 4) and one sample with only iron (Fe_2XC72, [17] and chapter 7).

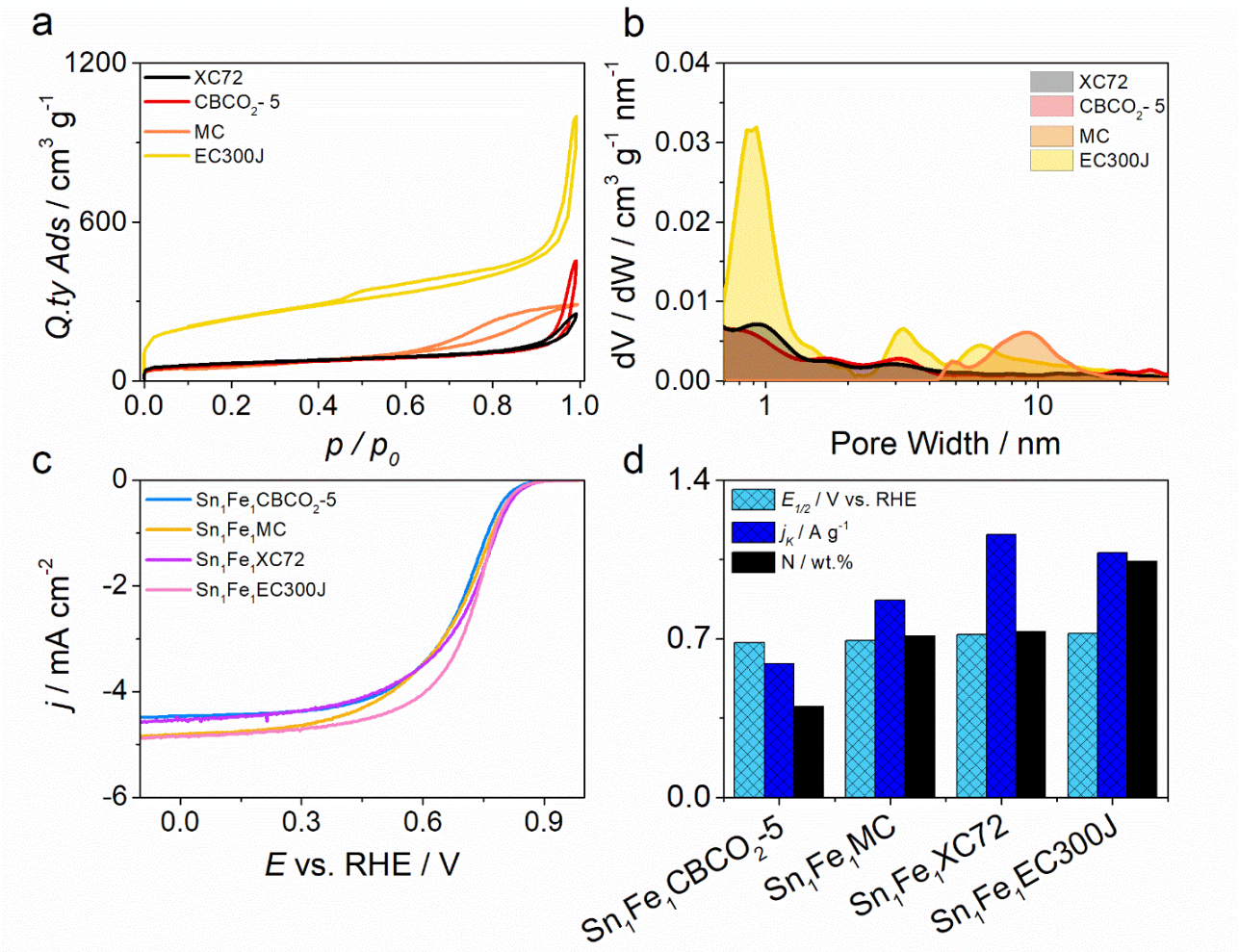

Figure 6.1. a) N_2 adsorption/desorption isotherms and b) pore size distribution for the 4 carbon supports. c) LSVs at RDE of Sn_1Fe_1X recorded at 1600 rpm, 2 mV s^{-1} in O_2 saturated 0.5 M H_2SO_4 and d) summary of N content ad activity in term of half-wave potential and kinetic current for the four Sn_1Fe_1X.

6.1.3. Physico-Chemical characterization of Sn_xFe_yXC72 catalysts

The morphological/compositional aspect of Sn_xFe_yXC72 catalysts were defined by SEM-EDX analysis (a selection of images is reported in Figure 6.3, other are shown in Figure 10.21), EA and ICP-MS (Table 6.1). Samples with Fe or Fe and Sn apparently show only agglomerations of carbon nanoparticles, which have dimension in the order of 100 nm, in line with literature findings on XC72 carbon [24,25]. Interestingly, when only Sn-phen is used as metal precursor, a dispersion of bright metallic Sn nanoparticles (NPs) spanning from 100 to 1000 nm was observed (see later XRD analysis), which make sense considering the reductive atmosphere (high temperature and hydrogen gas). This unexpected result justify the lower carbon content recorded by elemental analysis (Table 6.1) for the two samples Sn_2XC72 and Sn_4XC72 where Sn wt.% over 4 % was detected (Table 6.1). This result might suggest two things: (i) the acid leaching is not effective in removing Sn NPs possibly formed during the first pyrolysis step (or alternatively during the second pyrolysis step, during which an insoluble salt can form during the acidic treatment) and/or (ii) when Fe is present, some competition, that we do not fully understand, which does not allow Sn NPs to form, or in a more general way hinder the fixation of Sn in the matrix. This last hypothesis would find confirmation by both ICP-MS and SEM-EDX that in the case of Sn give wt.% lower than 0.2 % in Sn_xFe_yXC72 catalysts. It is interesting to note that the synthesis temperature (900 °C) is over the

melting point of tin, therefore the carbon morphology helps to form NP dispersion instead of bigger agglomerate since tin should be in liquid form at this temperature.
The formation of Sn NPs only in certain conditions prompted us to study more in depth the effect of the acid leaching on Sn_4XC72 by employing different acid solutions i.e., HCl, HNO_3 and more concentrated H_2SO_4 (see 10.4.1.3 in Appendix for nomenclature and Table 10.15). It was observed that nitric acid is quite ineffective since the percentage of tin in the Sn_4N2T sample remains high (4.89 %). HCl brings some improvements in removing Sn NPs in Sn_4C2T (1.17 %), but H_2SO_4 actually remains the best choice, even if the condition, 3h at 100 °C in 1 M H_2SO_4, successfully adopted for the Fe_xXC72 are not sufficiently effective for Sn_xXC72, probably the main issue was the high Sn content and a not enough time of treatment, coupled with a slow reaction in diluted acid. In fact, only doubling the H_2SO_4 concentration as well as the washing duration (6 h at 90 °C under N_2 in 2 M H_2SO_4 similarly to Luo et al. [3]) allows to lower the Sn concentration (0.90 %) of one order of magnitude and the NPs dispersion become less evident (Figure 10.21). The electrochemical behaviour of Sn_4XC72 after the different acid washing was tested in both O_2 saturated 0.5 M H_2SO_4 and 0.1 M KOH (Figure 10.22). A more in-depth discussion on this point can be found in supporting information. It is however worth to say that the catalytic performances remain similar for the Sn_xXC72 treated in different acidic condition (Table 10.16 and Table 10.17), perhaps some improvements can be claimed especially for the sample treated in nitric acid but overall, the activity are lower that Fe_2XC72 sample taken as reference. Similar findings were observed in alkaline environment, where the selectivity versus H_2O_2 increases to almost 50 % (Figure 10.22). This seems to suggest that in acidic conditions Sn NPs have not a central role in ORR activity. The same is not true in alkaline environment, where at least at negative potential (below 0.3 V vs. RHE) a secondary mechanism seems to be present, indeed for higher amount of Sn NPs on the surface the amount of peroxide is lower, suggesting some role of Sn in ORR catalysis (Figure 10.22c-e). Even if not the central point of this work, the study of Sn NPs for ORR was not founded in literature, that is why we spent some time in studying that.
The nature of nanoparticles was further investigated by means of XRD analysis that shows that only metallic Sn phases are evident, while no clear peaks from SnO or SnO_2 were detected (see XRD analysis, 10.4.1.5 and Figure 10.23). This is reasonable considering the reductive atmosphere during synthesis, but we cannot exclude that a low crystalline layer of oxide (not even Sn-N_x) is present on the surface, since EDX also detected oxygen when NP are analysed.
If we now look at the metal composition derived from ICP and EDX in Sn_xFe_yXC72 catalysts (Table 6.1), it can be observed that iron concentration scales in good agreement with the amount of phenanthroline added in the precursor mixture with the two complexes (Fe-phen and Sn-phen), suggesting that the additional phenanthroline from Sn-phen helps fixing both nitrogen and iron. This also well correlate with SD that will be discuss later in the text. This leads to the conclusion that it does not matter how phenanthroline is added in the mixture, since an increment in iron and Fe-N_x is observed (Figure 10.24) regardless of whether the nitrogen source is Fe-phen, Sn-phen, or additional phenanthroline (see also 10.4.1.7 in Appendix, in particular the sample marked as 1* in Figure 10.30). This is understandable since the amount of Fe initially added is at least one order of magnitude higher than the final amount in the catalysts, in other words it is more a matter of being able to fix iron instead of having it available in the initial precursor mixture. In any case we already saw that the 2 molar percentage is optimal for this type of synthesis [17]. This do not belittle the role of Sn-phen, in particular to obtain Sn-N_x formation, but we want to stress out the role of phenanthroline to achieve Fe-N fixation.

XPS performed on selected samples (Fe_2XC72, Sn_1Fe_2XC72, Sn_2Fe_2XC72 and Sn_4XC72) shows the signals of both N, Fe and Sn. All sample shows a characteristic N1s peak with multiple component assignable to pyridinic, pyrrolic, graphitic and M-N_x. For Sn_4XC72 the component relative to M-N_x could be linked to some SnN_x. Fe 2p deconvolution shows the presence of Fe^{2+} and Fe^{3+} which is in line with the finding for Fe-N-C material [22]. Finally, Sn 3d peak shows that Sn is present as Sn^{4+} in all sample, in line with the finding of Luo et al. [3], for Sn_4XC72 this shows that, as expectable, the surface of metallic NPs is oxidized, but not in crystalline form, a small shoulder of peak (Figure 10.25) could be linked to metallic tin signal. In general, the signal from metallic species, confirm that Sn is not present as metal phase, that uphold the presence of FeN_x sites and the possible co-presence of some SnN_x sites. Quantitative analysis was not elaborated since the amount is close to detection limit.

Table 6.1. Composition of the catalysts derived from EA (C, N, H, S), EDX (C, O, S, Fe, Sn) and ICP-MS (Fe, Sn)

	C_{EA} wt.%	N_{EA} wt.%	H_{EA} wt.%	S_{EA} wt.%	C_{EDX} wt.%	O_{EDX} wt.%	S_{EDX} wt.%	Fe_{EDX} wt.%	Sn_{EDX} wt.%	Fe_{ICP} wt.%	Sn_{ICP} wt.%
Sn_1Fe_1XC72	91.03	0.73	0.32	0.33	97.02	2.34	0.28	0.36	0.05	0.20	0.04
Sn_2Fe_2XC72	89.54	1.28	0.46	0.26	94.71	4.20	0.24	0.69	0.17	0.45	0.11
Sn_2Fe_1XC72	95.43	0.87	0.24	-	96.98	2.47	0.02	0.39	0.15	0.27	0.12
Sn_3Fe_1XC72	93.51	1.44	0.26	0.26	96.06	3.12	0.21	0.46	0.15	0.37	0.09
Sn_1Fe_2XC72	92.87	0.94	0.34	0.16	96.99	2.34	0.17	0.51	0.00	0.29	0.04
Sn_4XC72	85.94	0.83	0.30	0.23	85.20	2.77	0.20	-	11.83	-	7.20
Sn_2XC72	92.16	0.27	0.18	-	93.13	1.45	-	-	5.43	-	4.60
Fe_2XC72	90.68	0.82	0.40	0.32	95.72	3.24	0.40	0.64	-	0.34	-
N-C	98.55	0.23	0.17	-	-	-	-	-	-	-	-

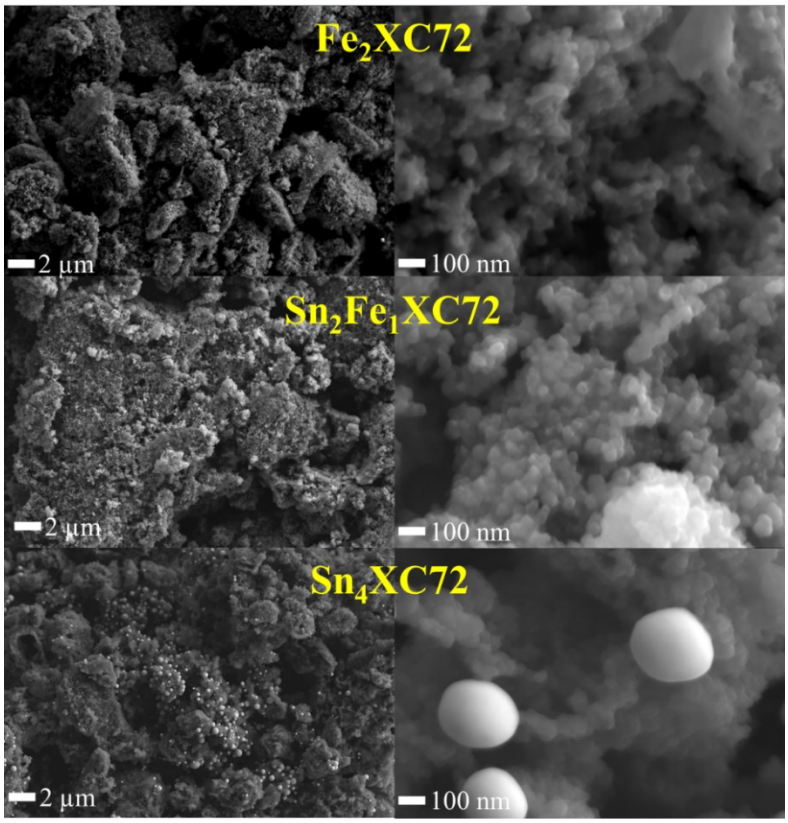

Figure 6.3. SEM images for Fe_2XC72, Sn_2Fe_1XC72 and Sn_2XC72 as a reference, only in the latter NP are present as white spot.

To further identify the structure of Fe-N_x moieties, XAS measurements were performed at the Fe K-edge on three selected catalysts, namely Fe_2XC72, Sn_1Fe_2XC72 and Sn_2Fe_2XC72. A detailed extended X-rays absorption fine structure (EXAFS) analysis show that the Fe atoms are atomically dispersed on the carbon matrix in all the samples (10.4.1.6, Figure 6.4, Figure 10.26, and Figure 10.27), with the Fourier transform (FT) of the EXAFS signal characterized by a first peak at ca 1.5 Å assigned to the Fe-N first coordination shell, and a minor peak at 2.6 Å assigned to Fe-C backscattering from the second coordination shell. The EXAFS spectra were fitted assuming the presence of in-plane nitrogen atoms, and also oxygen atoms as axial ligands. The structural parameters obtained from the analysis are summarized in Table 10.18, and they show a Fe-N coordination number around 4 for all the catalysts, demonstrating that iron forms Fe-N_4 moieties in both the Sn-free and Sn-containing samples. Moreover, an axial signal between Fe and a light atom can be probed, suggesting that two O atoms are adsorbed on top of the Fe-N_4 moieties, as previously found in other Fe-N-C catalysts [26,27]. No Fe-Fe backscattering is detectable in all the EXAFS spectra, thus confirming the absence of metal NPs. As far as the X-ray absorption near edge structure (XANES) region of the spectrum is concerned, the Fe K-edge XANES spectra of Fe_2XC72, Sn_1Fe_2XC72 and Sn_2Fe_2XC72 are superimposed (Figure 10.27), further demonstrating that the same Fe-based active sites are present in all the catalysts.

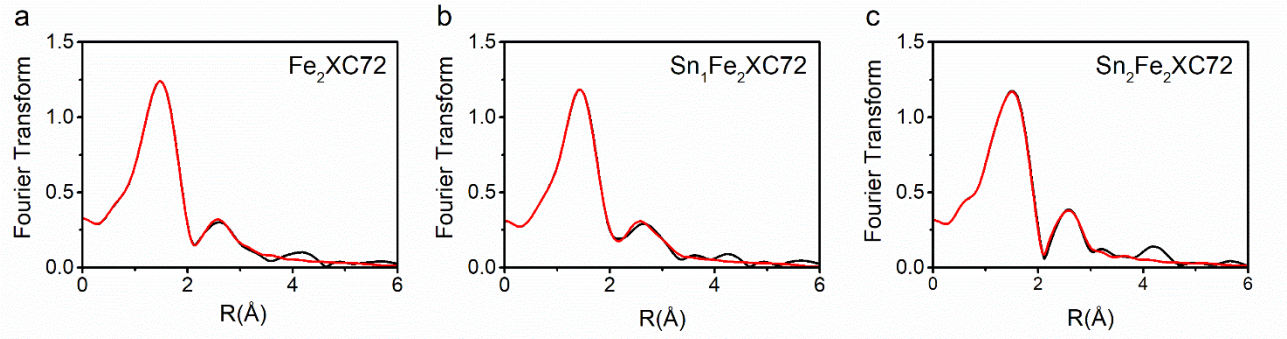

Figure 6.4. Fe K-edge EXAFS analysis in the Fourier transformed space of a) Fe_2XC72, b) Sn_1Fe_2XC72 and c) Sn_2Fe_2XC72. The black curves represent the experimental spectra while the red curves represent the calculated spectra without phase-shift correction applied.

6.1.4. Electrochemical characterization

All the samples were characterized in both acid and alkaline electrolyte and the result are listed in Table 6.2 and Figure 6.4. In H_2SO_4 the activity for the sample with only Sn is increased when more Sn-phen is added to the initial precursor mixture. In fact, the half-wave potential increase from 0.413 to 0.548 V vs. RHE and the kinetic current pass from 0.03 to 0.19 A g^{-1} (Table 6.2). We underline however that these two samples do not show a clear limiting current plateau (Figure 6.4a). If we consider that in the final catalyst the amount of Sn is proportional to the precursor mixture, we can in first instance hypothesize that Sn NPs have a role in activity, but the experiments carried out on the Sn_4X samples treated with different acid would lead to other conclusions, i.e., decreasing the Sn content and so the number of Sn NPs does not lead to a decreasing of activity. Another note is that if Sn NPs have an activity this should be very low since the weight amount of Sn is very high in these samples. As matter of fact, the activity even seems to increase as if the removal of Sn NPs could lead to a better exposure of other active sites. The only reason for such a behaviour in Sn_4X catalysts is the formation or exposition of carbon topological defects, nitrogen defects or Sn-N_x sites, even if no direct evidence can be brought for their

presence, apart from the detection of charged Sn (2+ or 4+) from XPS. These considerations together does not allow to fully understand the main role of Sn in these catalysts, what it is certain is that Sn_2XC72 and Sn_4XC72 performed better that a N-doped carbon (N-C, Figure 10.28), in particular Sn_2XC72 that has the same amount of N (around 0.3 wt.%), which could be another signal of active site differences. On the other hand, Fe_2XC72 show a very good activity ($E_{1/2}$ = 0.748 V vs. RHE and j_k = 1.83 A g^{-1}), which result comparable with bimetallic system (Figure 6.4b) [17]. The best performances are observed for Sn_1Fe_2XC72 ($E_{1/2}$ = 0.753 V vs. RHE and j_k = 2.11 A g^{-1}). In this case the larger amount of iron combined with the presence of Sn or the effect of the additional source of phenanthroline, gives a better fixation/formation of active sites that, as reported later, is in line also with the nitrite stripping results (Figure 6.5). This statement is also in line with the growing activity passing from Sn_1Fe_1XC72, Sn_2Fe_1XC72 to Sn_3Fe_1XC72 (Figure 6.4b). In fact, nitrogen, and iron fixation (Figure 6.4c and d) and also SD (Figure 6.5) increases with the increasing of the amount of Sn-phen in the initial mixture. The same is not true for the Sn as determined by ICP-MS (Table 6.1), which gives more credit to the idea that the main role in activity is due to Fe, but in any case the addition of tin is not harmful for the overall activity/site formation, as observed for other system with Ni [1]. This means that the presence of Sn complex in the mixture does not compete with Fe-N_x sites formation, but at most the opposite is true, that is that Fe do not allow Sn NPs to form.
Passing to alkaline electrolyte we observe a lower difference between samples if we look at the onset or half wave potential (Table 6.2), Sn_2Fe_1XC72 ($E_{1/2}$ = 0.848 V vs. RHE) result to be the most active followed by Sn_3Fe_1XC72 ($E_{1/2}$ = 0.801 V) and Sn_1Fe_1XC72 ($E_{1/2}$ = 0.790 V). The trend in catalytic activity apparently does not match with the nitrogen, iron, or tin content. Indeed, also Sn_4 and Sn_2 perform significantly well [17]. Interestingly, only these two samples clearly present a double step linear sweep voltammetry (Figure 10.22 and Figure 10.24a), which corresponds with a maximum trend for the % H2O2 determined at the ring (Figure 10.22 and Figure 10.24b). This current profile is present also for the Sn_xFe_yXC72 series even if in this case the second step is much less accentuated. This behaviour suggests that H_2O_2 forms at the first step and it is then further reduced in the second step. Therefore, the presence of Sn involves a preferential 2+2 reduction mechanism, which is different from what observed in iron containing ones, where H_2O_2 is produced even in not negligible amount but it is harder to be further reduced to H_2O at more negative potentials. In the case of Sn_XXC72 the presence of NPs could have a different role, at least in alkaline electrolyte, catalysing the preferential formation of H_2O_2 and also its further reduction. This is clearly seen by correlating the peroxide yield with the amount of tin detected by EDX (Figure 10.22e).
It can be observed that the activity is not strictly comparable between the two different electrolytes (Table 6.2, Figure 10.24, and Figure 6.4c-f). This finding is common for this type of material, meaning that the active site switches their activity by changing the electrolyte pH. In general, the peroxide production results higher in alkaline electrolyte (close to the 50%, Table 6.2), suggesting a mixed 4/2+2/2 electrons pathway different from what observed in acid where the highest yield was under the 5% along the whole range of potential analysed (Table 6.2). It is known from literature, that in metal porphyrin like systems, the Fe-N_4 metal centre are inactive when Fe is in the III redox state because poisoned by strongly adsorbed OH^- [28]. Similarly, pyridinic N has high ORR activity in alkaline medium than in acid one, because the protonation in acidic medium suppresses the catalytic activity [29]. This can explain on one and the low performances of Fe-N_4 containing catalysts in alkaline electrolyte and the comparable performance of tin containing catalysts. The fact that at different pH different active sites come into play is made explicit by the graph in Figure 6.4f

where no correlation is observed between a performance descriptor such as $E_{1/2}$ in the two different electrolytes.

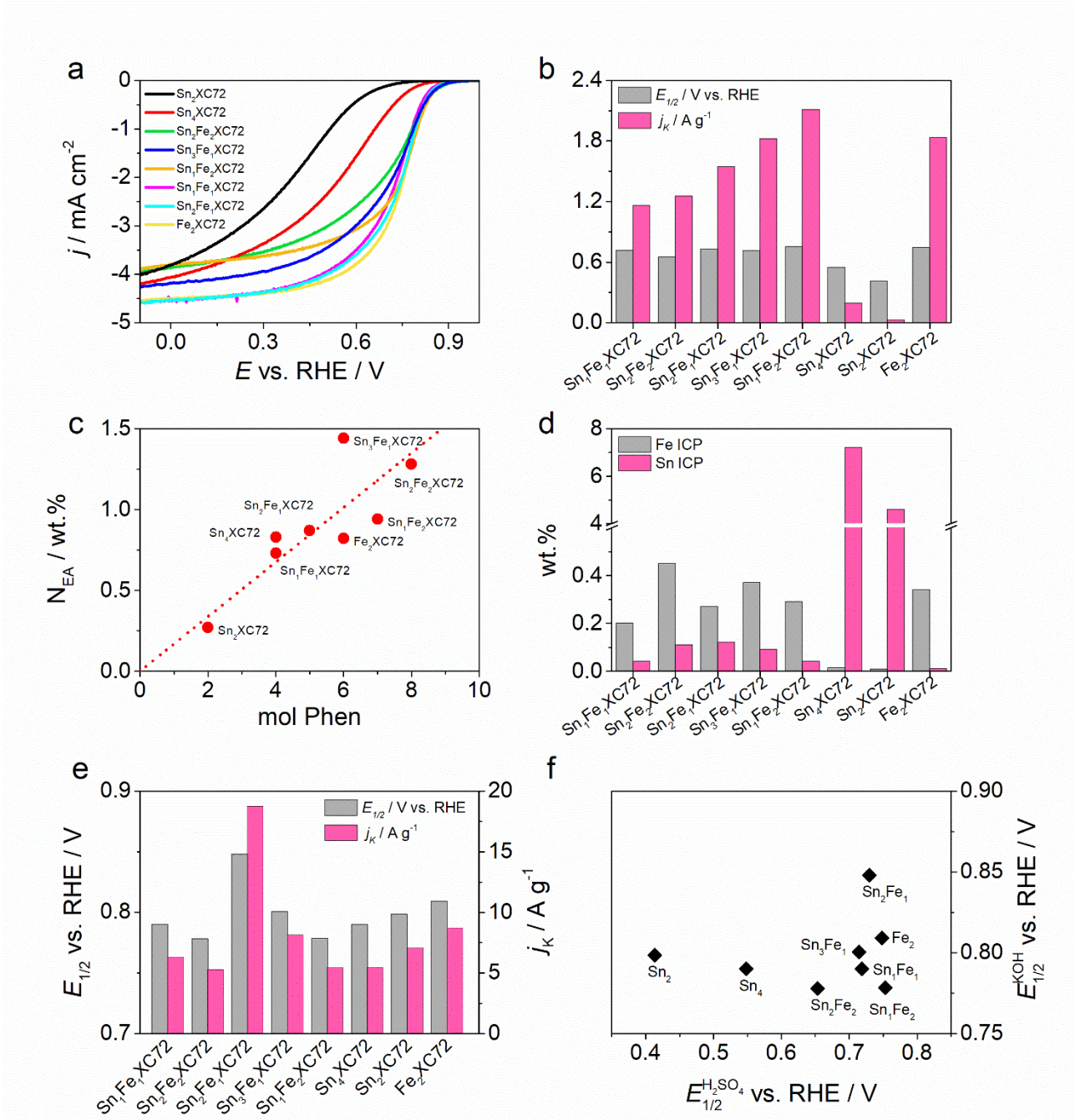

Figure 6.4. a) LSV at RDE of investigate catalysts in O_2 saturated 0.5 M H_2SO_4; b) activity comparison in term of half-wave potential and kinetic current for acid electrolyte c) correlation between phenanthroline amount in the precursor mixture and nitrogen fixation, d) metal content in the catalysts derived from ICP-MS, e) activity comparison in term of half-wave potential and kinetic current for alkaline electrolyte, and f) comparison of half-wave potential in the two electrolytes, the absence of correlation is clear.

Table 6.2. Electrochemical result for all the catalysts in O_2 saturated 0.5 M H_2SO_4 and 0.1 M KOH

	$E_{1/2}$[a] V	$j_k^{0.8V}$ A g^{-1}	n_{0V} -	$\%H_2O_2^{0.7V}$ -	$E_{1/2}$[a] V	$j_k^{0.8V}$ A g^{-1}	n_{0V} -	$\%H_2O_2^{0.7V}$ -
	0.5 M H_2SO_4				0.1 M KOH			
Sn_1Fe_1XC72	0.719	1.16	3.98	2.2	0.790	6.31	3.15	1.0
Sn_2Fe_2XC72	0.654	1.25	3.98	0.8	0.778	5.26	3.06	3.1
Sn_2Fe_1XC72	0.729	1.55	3.98	0.8	0.848	18.75	3.42	1.6
Sn_3Fe_1XC72	0.715	1.82	3.95	1.7	0.801	8.13	3.25	1.5
Sn_1Fe_2XC72	0.753	2.11	3.97	1.0	0.779	5.43	3.18	3.3
Sn_4XC72	0.548	0.19	3.97	2.2	0.790	5.44	3.65	4.8
Sn_2XC72	0.413	0.03	3.97	3.0	0.799	7.05	3.70	12.5
Fe_2XC72	0.748	1.83	3.99	0.6	0.809	8.70	3.53	1.0

[a] all the potentials are referred to RHE

Stripping analysis, which allows site density determination, returns a picture in agreement with what previously observed for activity, namely SD well correlate with the nitrogen content in the sample, the half-wave potential and kinetic current (Figure 6.5a, b, Table 10.19) and this was already observed in previous papers [17,22]. Before going into the merits of the question, it is worth observing the results, we recorded for the stripping tests on a nitrogen doped XC72 without metals and on Sn_xXC72. In theory N-C is expected to not give any stripping charge and so SD equal to zero should be considered; in the true a non-negligible SD of 1.95×10^{17} sites g^{-1} was found. In the case of N-C, even if it is questionable whether the active site could give NO adsorption, the found value can be regarded as limit of detection for the techniques or simply as a sort of background (Figure 10.30c). The SD determined for Sn_4XC72 is 1.71 x 10^{18} sites g^{-1} but as for N-C, we cannot be sure about the active site that are involved in the NO_2 adsorption and stripping (Figure 10.30d). Considering the large Sn content in the sample, it is clear that only a small fraction contributes to adsorb NO, even if it could also be argued that the NO adsorption on Sn is not strong or chemical reversible. In addition, Sn_4XC72 has almost double amount of Sn than Sn_2XC72, but has almost the same SD. Considering that, we can conclude that a stripping charge from Sn NPs are unlikely or very low, whereas a contribution from Sn-N_x can neither be confirmed nor excluded. Having say that, in the best catalysts (Sn_2Fe_1XC72, Sn_1Fe_2XC72, Fe_2XC72) the increment in activity is mainly due to an increment of Fe-N_4 SD (and/or Sn-N_x) since the TOF is similar. Concerning the TOF a clear trend with respect to N content or other kinetic parameter is not observed (Figure 6.5c), maybe caused by different site distribution (different sites with different activity). For example, Sn_2Fe_2 shows high SD (Figure 6.5b) but at the same time a lower TOF which results in a lower activity compared with the best catalysts (Figure 6.5c). In other words, despite a similar FeN_x local structure, as shown by XAS, some other parameters seems to influence the intrinsic activity. In fact, high SD density could result in too close sites, which interfere with each other with the result that they are not active at the same time and in the same way. Sn_3Fe_1 has a different combination of SD and TOF. SD correlates with activity in acid electrolyte while the recorded activity in acetate buffer (stripping condition) seems underestimated, which probably also affect the determination of TOF.

As anticipated the same trend with SD is not observed in the case of alkaline environment, suggesting the different role of Fe species in catalysing the reaction under alkaline conditions [17]. Different work indeed suggested that the absence of pyridinic nitrogen protonation, the presence

of Fe-N_x sites near pyridinic nitrogen, the deactivation by OH^- adsorption into Fe-N_4 centres and the presence of FeC_x NPs under carbon layer could be more active sites for ORR under basic condition [29–31].

The conclusion of this measurements is that catalysts were prepared starting Sn/Fe precursor shows better catalytic performance where Sn-phen improve Fe fixation, while the role of detected Sn in oxidized state was not easily understandable. It was observed that the sole employment of Sn-phen leads to the formation of Sn NPs, which do not appear to sensitively affect the ORR in acid electrolyte but certain has action in alkaline media, since a clear 2+2 ORR mechanism was observed only for Sn_xXC72 catalysts; also, this finding isn't find in literature, up to our knowledge.

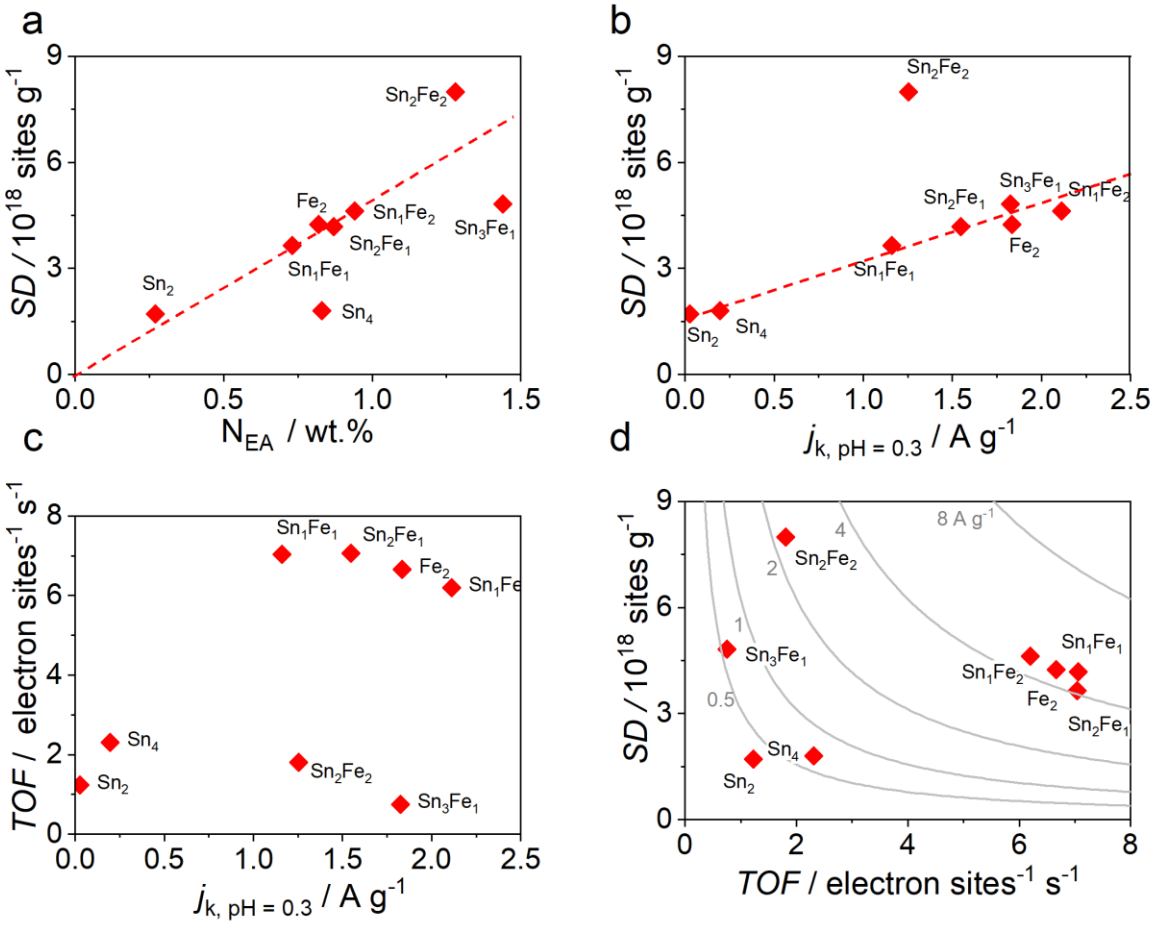

Figure 6.5. a) correlation of SD with N content, b,c) SD and TOF vs. an activity parameter (j_k). Red dotted line is intended as a guide and not as fitting of data, d) SD-TOF map with the iso-current curve.

Performing RRDE is an easy way to characterize material to obtain information on activity and selectivity, but at the same time is also known that these types of characterizations fail in predicting the real behaviour that a catalyst stumble across in a real device (fuel-cell cathode). Several approaches have been proposed in order to reach closer condition, i.e., the floating electrode [21] or the used here gas diffusion electrode setup [19].

The setup proposed by Arenz and Co. allows an easy preparation of the measurements, since only the drop-casting or spray-coating of catalyst on a carbon paper/gas diffusion layer is required and no hot-pressing or similar procedure are needed. The contact between the layer and the membrane is indeed guaranteed by the pressure generate by the upper part of the cell clamped on the bottom part. All the catalysts were then tested in this setup (Figure 6.6) showing a kinetic growing current and the absence of a limiting current as in RRDE measurements (Figure 6.4c and Figure 6.6a). It is

evident that the scale of the current density reached by GDE setup is almost 50 times higher than in RRDE setup, at least for the most active samples (Table 10.20 for extended data). The activity trend in term of kinetic current density at 0.7 V vs. RHE scales in the order Sn_1Fe_2XC72 > Sn_3Fe_1XC72 > Sn_1Fe_1XC72 > Sn_2Fe_1XC72 > Sn_2Fe_1XC72 ≈ Fe_2XC72 >> Sn_4XC72 > Sn_2XC72 and it is in good agreement with RRDE measurements with the exclusion of Fe_2XC72 (Figure 6.6b and Table 10.20). In general, Sn_xFe_yXC72 catalysts at GDE perform better than Fe_2XC72 and this can be attributed to a higher number of active Fe-N_x sites. It is worth to stress that samples that are a little out of trend could be influenced by a better dispersion on the carbon paper or to a higher "affinity" with this setup, in other word they could be the candidate out of the group for device application.

One of the key points of this measurement, and maybe the most important one in our purpose, is to show that this setup is very easily applicable to M-N-C in particular considering that, at present, only few papers adopted this method, and mainly on Pt or other metals [18,32,33]. One of possible future perspective is to close the cycle and verify how the result obtained in GDE translate to real fuel cell device in order to better understand the connection between the result obtain in laboratory condition with RDE or GDE and the actual performance under realistic condition.

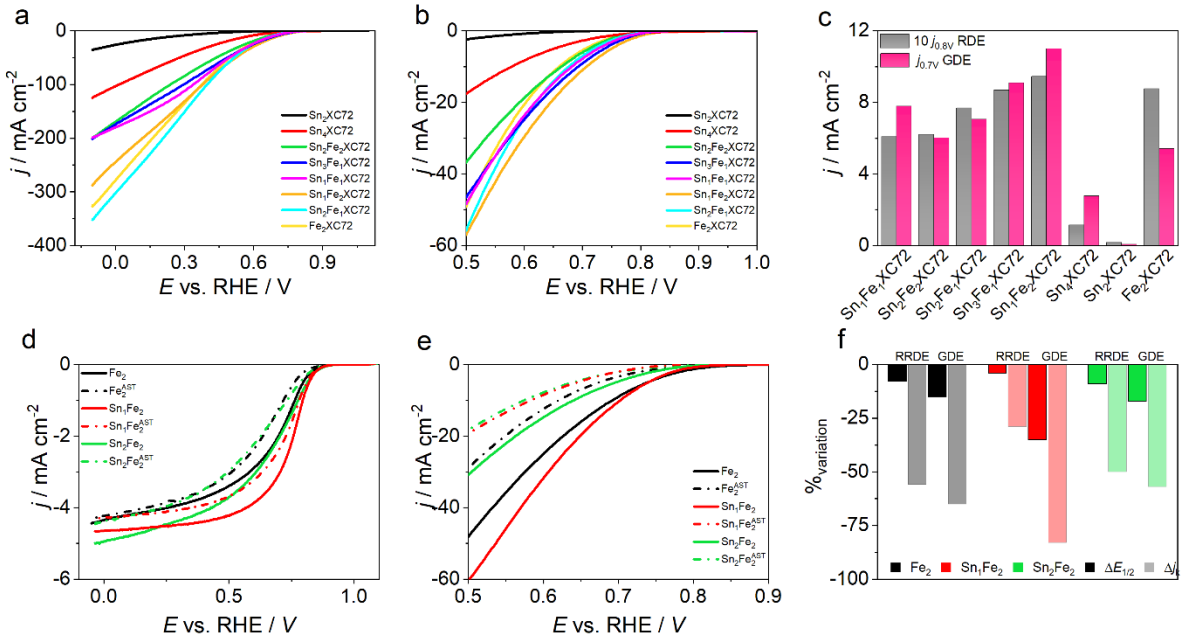

Figure 6.6. a) CVs recorded in GDE setup, only the cathodic scan is reported for clarity, b) magnified onset region of Figure 6.6a, c) current density comparison between the two setups. d) LSVs before and after (– · –) AST in d) RRDE and e) GDE setup. f) Variation (%) of current density at certain potential for the two measurements configuration.

To conclude our analysis on catalysts performance we chose to perform accelerate stress test (AST) on 3 different catalysts, i.e., Fe_2XC72, Sn_1Fe_2 XC72 and Sn_2Fe_2 XC72 (also characterize by XAS). AST are indeed fundamental, since good activity and durability are two crucial point in selecting a good catalyst candidate. The selected catalysts belong to a series where the amount on tin precursor is incremented in the mixture, keeping in mind that this led to a higher concentration of Fe, N, and active sites rather than an actual Sn fixation. Since we perform analysis on two experimental setup (RRDE and GDE) we carried out stress test on both. For the rotating electrode setup, we used a multiple cycling technique while for GDE a potentiostatic analysis [17]. Results are shown and summarized in Figure 6.6d,f and Table 6.3.

Fe_2XC72 tested at RRDE showed a higher resistance to deactivation in alkaline environment with a loss of activity of about 10% after 7000 cycle (ca. 5 mV loss in half-wave potential), while the activity loss in acid electrolyte was exceptionally pronounced (ca. −60%). On the same catalysts we also performed an AST in GDE configuration, this time comparing the activity before and after a chronoamperometry at 0.5 V vs. RHE maintained for 8 hours, by performing a cyclic voltammetry at 20 mV s^{-1}. With this setup the Ar background was also recorded and utilized for background subtraction. Figure 6.6e,f and Table 6.3 report the obtained data.

Sn_1Fe_2XC72 revealed a higher activity than the other catalysts in both setups, but the stability resulted quite different. In RRDE analysis Sn_1Fe_2XC72 resulted more stable than the other two while in GDE cell configuration it was the reverse. On one hand this shows that in GDE configuration the relation between activity and stability is inversely proportional, on the other hand shows that not always the stability recorded on glassy carbon rotating electrode is the same as in another setup. In general, the test under potentiostatic condition is more detrimental that multiple cycling, or simply the 7000 cycles are not sufficiently effective as a stress test as compared to chronoamperometry in GDE condition. In any case with the exception of Sn_1Fe_2XC72 the other two (Fe_2XC72 and Sn_2Fe_2XC72) shows similar loss in current in both setups.

This different behaviour in degradation could be linked to different aspect: firstly, the different activity recorded is probably linked to some differences in sites. This cannot apply to the Fe-N_4 sites because the EXAFS measurements found them to be the same for the three samples. It could therefore be related to the specific degradation of the Sn-based sites rather than pyridinic or pyrrolic functional groups, since these should be present in different amounts as the amount of tin complex in the synthesis mix varies. Secondly other textural properties differences could lead to different stability/activity.

Table 6.3. Result for GDE and RRDE accelerated stress test in term of variation of half-wave potential

	Δj [a] mA cm^{-2}	$\%_{var}$ -	$\Delta\%H_2O_2$ -
Fe_2XC72^{RRDE}	-0.24	-53%	-2.7
$Sn_1Fe_2XC72^{RRDE}$	-0.23	-26%	-0.9
$Sn_2Fe_2XC72^{RRDE}$	-0.32	-47%	-2.3
Fe_2XC72^{GDE}	-19	-40%	-
$Sn_1Fe_2XC72^{GDE}$	-41	-68%	-
$Sn_2Fe_2XC72^{GDE}$	-13	-41%	-

[a] 0.8 V vs. RHE for RDE and 0.5 V for GDE

6.2. Conclusion

In the present chapter the evaluation of possible cooperative effect between Sn and Fe active site in the oxygen reduction reaction was evaluated. Catalysts were prepared starting from a different Sn/Fe ratio of the respective complexes in the precursor mixture and supported on Vulcan XC72, which was proved to lead to better catalytic performance with respect to other carbon supports. XAS measurements confirmed the formation of Fe-N_4 sites, and NO nitrite stripping confirmed that the site density increases in samples where Sn-phen was increasingly added, probably for the additional source of phenanthroline, which would improve Fe fixation. Indeed, the catalytic activity versus ORR in 0.5 M H_2SO_4 grows passing from Sn_1Fe_1XC72, Sn_2Fe_1XC72 to Sn_3Fe_1XC72 and $E_{1/2}$ and j_k scales linearly with the SD, which in turn scales with the nitrogen and iron fixation in the carbon matrix. It was observed that the sole employment of Sn-phen leads to the formation of Sn NPs, which do not appear to sensitively affect the ORR in acid electrolyte. A correlation between SD and activity was not observed in the case of alkaline environment, suggesting the different role of Fe species in catalysing the reaction under alkaline conditions. Furthermore, in alkaline electrolyte Sn NPs have an effect on the selectivity rather than on activity since a clear 2+2 ORR mechanism was observed only for Sn_xXC72 catalysts.

Catalysts were tested also at GDE electrode in acid electrolyte finding s good agreement in term of activity with RRDE measurements with the exclusion of Fe_2XC72. The same setup was also used for stability tests, which evidenced a far more important loss in activity ($E_{1/2}$ and j_k) than what predicted from RRDE stress tests, pointing out the importance to implement new form of catalyst screening for possible scale-up, rather than rely on the sole rotating techniques tests.

As general remark Sn co-functionalization does not appear to bring to tangible improvements on both catalytic activity and stability of Fe-N-C. In fact, even if a certain improvement was observed, this was appointed to the general increase of N fixation that in turn leads to an increase of Fe-N_4 site formation.

6.3. Bibliography

[1] F. Luo, S. Wagner, I. Onishi, S. Selve, S. Li, W. Ju, H. Wang, J. Steinberg, A. Thomas, U.I. Kramm, P. Strasser, Surface site density and utilization of platinum group metal (PGM)-free Fe–NC and FeNi–NC electrocatalysts for the oxygen reduction reaction, Chem. Sci. 12 (2021) 384–396. https://doi.org/10.1039/D0SC03280H.

[2] N.R. Sahraie, U.I. Kramm, J. Steinberg, Y. Zhang, A. Thomas, T. Reier, J.-P. Paraknowitsch, P. Strasser, Quantifying the density and utilization of active sites in non-precious metal oxygen electroreduction catalysts, Nat. Commun. 6 (2015) 8618. https://doi.org/10.1038/ncomms9618.

[3] F. Luo, A. Roy, L. Silvioli, D.A. Cullen, A. Zitolo, M.T. Sougrati, I.C. Oguz, T. Mineva, D. Teschner, S. Wagner, J. Wen, F. Dionigi, U.I. Kramm, J. Rossmeisl, F. Jaouen, P. Strasser, P-block single-metal-site tin/nitrogen-doped carbon fuel cell cathode catalyst for oxygen reduction reaction, Nat. Mater. (2020) 1–9. https://doi.org/10.1038/s41563-020-0717-5.

[4] S. Guo, J. Hu, S. Luo, Y. Zhang, Z. Zhang, P. Dong, X. Zeng, M. Xu, L. Han, J. Yuan, C. Zhang, Y. Zhang, Zr enhanced Fe, N, S co-doped carbon-based catalyst for high-efficiency oxygen reduction reaction, Int. J. Hydrogen Energy. 47 (2022) 8348–8358. https://doi.org/10.1016/j.ijhydene.2021.12.209.

[5] H. Zhong, L. Duan, P. Ye, X. Li, A. Xu, Q. Peng, Synthesis of cobalt–nitrogen-doped mesoporous carbon from chitosan and its performance for pollutant degradation as Fenton-like catalysts, Res. Chem. Intermed. 45 (2019) 907–918. https://doi.org/10.1007/s11164-018-3655-y.

[6] A. Zitolo, N. Ranjbar-Sahraie, T. Mineva, J. Li, Q. Jia, S. Stamatin, G.F. Harrington, S.M. Lyth, P. Krtil, S. Mukerjee, E. Fonda, F. Jaouen, Identification of catalytic sites in cobalt-nitrogen-carbon materials for the oxygen reduction reaction, Nat. Commun. 8 (2017).

[7] W. Ju, A. Bagger, G.P. Hao, A.S. Varela, I. Sinev, V. Bon, B. Roldan Cuenya, S. Kaskel, J. Rossmeisl, P. Strasser, Understanding activity and selectivity of metal-nitrogen-doped carbon catalysts for electrochemical reduction of CO2, Nat. Commun. 8 (2017) 1–9. https://doi.org/10.1038/s41467-017-01035-z.

[8] X.M. Hu, S.U. Pedersen, K. Daasbjerg, Supported molecular catalysts for the heterogeneous CO2 electroreduction, Curr. Opin. Electrochem. 15 (2019) 148–154. https://doi.org/10.1016/j.coelec.2019.05.006.

[9] M.L. Pegis, B.A. McKeown, N. Kumar, K. Lang, D.J. Wasylenko, X.P. Zhang, S. Raugei, J.M. Mayer, Homogenous Electrocatalytic Oxygen Reduction Rates Correlate with Reaction Overpotential in Acidic Organic Solutions, ACS Cent. Sci. 2 (2016) 850–856. https://doi.org/10.1021/acscentsci.6b00261.

[10] S. Sinha, R. Zhang, J.J. Warren, Low Overpotential CO2Activation by a Graphite-Adsorbed Cobalt Porphyrin, ACS Catal. 10 (2020) 12284–12291. https://doi.org/10.1021/acscatal.0c01367.

[11] A. Genoni, D.N. Chirdon, M. Boniolo, A. Sartorel, S. Bernhard, M. Bonchio, Tuning Iridium Photocatalysts and Light Irradiation for Enhanced CO2 Reduction, ACS Catal. 7 (2017) 154–160. https://doi.org/10.1021/acscatal.6b03227.

[12] U.I. Kramm, I. Herrmann-Geppert, J. Behrends, K. Lips, S. Fiechter, P. Bogdanoff, On an Easy Way To Prepare Metal–Nitrogen Doped Carbon with Exclusive Presence of MeN 4 -type Sites Active for the ORR, J. Am. Chem. Soc. 138 (2016) 635–640. https://doi.org/10.1021/jacs.5b11015.

[13] S. Samad, K.S. Loh, W.Y. Wong, W. Sudarsono, T.K. Lee, W.R. Wan Daud, Effect of various Fe/Co ratios and annealing temperatures on a Fe/Co catalyst supported with nitrogen-doped reduced graphene oxide towards the oxygen reduction reaction, J. Alloys Compd. 816 (2020) 152573. https://doi.org/10.1016/j.jallcom.2019.152573.

[14] S. Yuan, L. Cui, Z. Dou, X. Ge, X. He, W. Zhang, T. Asefa, Nonprecious Bimetallic Sites Coordinated on N-Doped Carbons with Efficient and Durable Catalytic Activity for Oxygen Reduction, Small. 16 (2020) 2000742. https://doi.org/10.1002/smll.202000742.

[15] E. Negro, A. Bach Delpeuch, K. Vezzù, G. Nawn, F. Bertasi, A. Ansaldo, V. Pellegrini, B. Dembinska, S. Zoladek, K. Miecznikowski, I.A. Rutkowska, M. Skunik-Nuckowska, P.J. Kulesza, F. Bonaccorso, V. Di Noto, Toward Pt-Free Anion-Exchange Membrane Fuel Cells: Fe-Sn Carbon Nitride-Graphene Core-Shell Electrocatalysts for the Oxygen Reduction Reaction, Chem. Mater. 30 (2018) 2651–2659. https://doi.org/10.1021/acs.chemmater.7b05323.
[16] X. Zhang, J. Liu, Y. Qiao, A. Kong, R. Li, Y. Shan, Fe-boosting Sn-based dual-shell nanostructures from new covalent porphyrin frameworks as efficient electrocatalysts for oxygen reduction and zinc-air batteries, Electrochim. Acta. 320 (2019) 134593. https://doi.org/10.1016/j.electacta.2019.134593.
[17] M. Mazzucato, C. Durante, How Determinant is the Iron Precursor ligand in Fe-N-C Single-Site formation and activity for Oxygen Reduction Reaction?, Electrochim. Acta. 394 (2021) 139105. https://doi.org/10.1016/j.electacta.2021.139105.
[18] J. Schröder, V.A. Mints, A. Bornet, E. Berner, M. Fathi Tovini, J. Quinson, G.K.H. Wiberg, F. Bizzotto, H.A. El-Sayed, M. Arenz, The Gas Diffusion Electrode Setup as Straightforward Testing Device for Proton Exchange Membrane Water Electrolyzer Catalysts, JACS Au. 1 (2021) 247–251. https://doi.org/10.1021/jacsau.1c00015.
[19] M. Inaba, A.W. Jensen, G.W. Sievers, M. Escudero-Escribano, A. Zana, M. Arenz, Benchmarking high surface area electrocatalysts in a gas diffusion electrode: measurement of oxygen reduction activities under realistic conditions, Energy Environ. Sci. 11 (2018) 988–994. https://doi.org/10.1039/C8EE00019K.
[20] L. Pan, S. Ott, F. Dionigi, P. Strasser, Current challenges related to the deployment of shape-controlled Pt alloy oxygen reduction reaction nanocatalysts into low Pt-loaded cathode layers of proton exchange membrane fuel cells, Curr. Opin. Electrochem. 18 (2019) 61–71. https://doi.org/10.1016/j.coelec.2019.10.011.
[21] C.M. Zalitis, D. Kramer, A.R. Kucernak, Electrocatalytic performance of fuel cell reactions at low catalyst loading and high mass transport, Phys. Chem. Chem. Phys. 15 (2013) 4329. https://doi.org/10.1039/c3cp44431g.
[22] M. Mazzucato, G. Daniel, A. Mehmood, T. Kosmala, G. Granozzi, A. Kucernak, C. Durante, Effects of the induced micro- and meso-porosity on the single site density and turn over frequency of Fe-N-C carbon electrodes for the oxygen reduction reaction, Appl. Catal. B Environ. 291 (2021) 120068. https://doi.org/10.1016/j.apcatb.2021.120068.
[23] G. Daniel, M. Mazzucato, R. Brandiele, L. De Lazzari, D. Badocco, P. Pastore, T. Kosmala, G. Granozzi, C. Durante, Sulfur Doping versus Hierarchical Pore Structure: The Dominating Effect on the Fe–N–C Site Density, Activity, and Selectivity in Oxygen Reduction Reaction Electrocatalysis, ACS Appl. Mater. Interfaces. 13 (2021) 42693–42705. https://doi.org/10.1021/acsami.1c09659.
[24] M. Williams, L. Khotseng, Q. Naidoo, L. Petrik, A. Nechaev, V. Linkov, Applicability of analytical protocols for the characterisation of carbon-supported platinum group metal fuel cell electrocatalysts, S. Afr. J. Sci. 105 (2009) 285–289. https://doi.org/10.4102/sajs.v105i7/8.76.
[25] M. Kim, J.M. Yoo, C.Y. Ahn, J.H. Jang, Y.J. Son, H. Shin, J. Kang, Y.S. Kang, S.J. Yoo, K.S. Lee, Y.E. Sung, Rational Generation of Fe–Nx Active Sites in Fe–N–C Electrocatalysts Facilitated by Fe–N Coordinated Precursors for the Oxygen Reduction Reaction, ChemCatChem. 11 (2019) 5982–5988. https://doi.org/10.1002/cctc.201901242.
[26] J. Li, S. Ghoshal, W. Liang, M.-T. Sougrati, F. Jaouen, B. Halevi, S. McKinney, G. McCool, C. Ma, X. Yuan, Z.-F. Ma, S. Mukerjee, Q. Jia, Structural and mechanistic basis for the high activity of Fe–N–C catalysts toward oxygen reduction, Energy Environ. Sci. 9 (2016) 2418–2432. https://doi.org/10.1039/C6EE01160H.
[27] A. Zitolo, V. Goellner, V. Armel, M.T. Sougrati, T. Mineva, L. Stievano, E. Fonda, F. Jaouen, Identification of catalytic sites for oxygen reduction in iron- and nitrogen-doped graphene materials, Nat. Mater. 14 (2015) 937–942. https://doi.org/10.1038/nmat4367.
[28] J.H. Zagal, M.T.M. Koper, Reactivity Descriptors for the Activity of Molecular MN4 Catalysts

for the Oxygen Reduction Reaction, Angew. Chemie - Int. Ed. 55 (2016) 14510–14521. https://doi.org/10.1002/anie.201604311.
[29] M. Rauf, Y.-D. Di Zhao, Y.-C.C. Wang, Y.-P.P. Zheng, C. Chen, X.-D.D. Yang, Z.-Y.Y. Zhou, S.-G.G. Sun, Insight into the different ORR catalytic activity of Fe/N/C between acidic and alkaline media: Protonation of pyridinic nitrogen, Electrochem. Commun. 73 (2016) 71–74. https://doi.org/10.1016/j.elecom.2016.10.016.
[30] W. Zhong, Z. Wang, S. Han, L. Deng, J. Yu, Y. Lin, X. Long, M. Gu, S. Yang, Identifying the Active Sites of a Single Atom Catalyst with pH-Universal Oxygen Reduction Reaction Activity, Cell Reports Phys. Sci. 1 (2020) 100115. https://doi.org/10.1016/j.xcrp.2020.100115.
[31] R. Sgarbi, K. Kumar, F. Jaouen, A. Zitolo, E.A. Ticianelli, F. Maillard, Oxygen reduction reaction mechanism and kinetics on M-NxCy and M@N-C active sites present in model M-N-C catalysts under alkaline and acidic conditions, J. Solid State Electrochem. 25 (2021) 45–56. https://doi.org/10.1007/s10008-019-04436-w.
[32] G.W. Sievers, A.W. Jensen, V. Brüser, M. Arenz, M. Escudero-Escribano, Sputtered Platinum Thin-films for Oxygen Reduction in Gas Diffusion Electrodes: A Model System for Studies under Realistic Reaction Conditions, Surfaces. 2 (2019) 336–348. https://doi.org/10.3390/surfaces2020025.
[33] M. De Jesus Gálvez-Vázquez, P. Moreno-García, H. Xu, Y. Hou, H. Hu, I.Z. Montiel, A. V. Rudnev, S. Alinejad, V. Grozovski, B.J. Wiley, M. Arenz, P. Broekmann, P. Moreno-García, Environment Matters: CO2RR Electrocatalyst Performance Testing in a Gas-Fed Zero-Gap Electrolyzer, ACS Catal. 10 (2020) 13096–13108. https://doi.org/10.1021/acscatal.0c03609.
[34] V. V. Avdeeva, A. V. Vologzhanina, L. V. Goeva, E.A. Malinina, N.T. Kuznetsov, Boron Cluster Anions [BnHn] 2-(n = 10, 12) in Reactions of Iron(II) and Iron(III) Complexation with 2,2′-Bipyridyl and 1,10-Phenanthroline, Zeitschrift Für Anorg. Und Allg. Chemie. 640 (2014) 2149–2160. https://doi.org/10.1002/zaac.201400137.
[35] C. Owens, A.K. Filo, J.M. Woods, L.L. Pytlewski, A.N. Speca, N.M. Karayannis, Labile 1,10-phenanthroline N-oxide complexes with tin(II) and (IV) halides, Inorganica Chim. Acta. 45 (1980) L27–L30. https://doi.org/10.1016/S0020-1693(00)80081-X.
[36] A. Facchin, M. Zerbetto, A. Gennaro, A. Vittadini, D. Forrer, C. Durante, Oxygen Reduction Reaction at Single-Site Catalysts: A Combined Electrochemical Scanning Tunnelling Microscopy and DFT Investigation on Iron Octaethylporphyrin Chloride on HOPG**, ChemElectroChem. 8 (2021) 2825–2835. https://doi.org/10.1002/celc.202100543.
[37] D. Malko, A. Kucernak, T. Lopes, In situ electrochemical quantification of active sites in Fe–N/C non-precious metal catalysts, Nat. Commun. 7 (2016) 13285–13292. https://doi.org/10.1038/ncomms13285.
[38] D. Malko, A. Kucernak, T. Lopes, Performance of Fe–N/C Oxygen Reduction Electrocatalysts toward NO_2^- , NO, and NH_2OH Electroreduction: From Fundamental Insights into the Active Center to a New Method for Environmental Nitrite Destruction, J. Am. Chem. Soc. 138 (2016) 16056–16068. https://doi.org/10.1021/jacs.6b09622.
[39] X. Xie, C. He, B. Li, Y. He, D.A. Cullen, E.C. Wegener, A.J. Kropf, U. Martinez, Y. Cheng, M.H. Engelhard, M.E. Bowden, M. Song, T. Lemmon, X.S. Li, Z. Nie, J. Liu, D.J. Myers, P. Zelenay, G. Wang, G. Wu, V. Ramani, Y. Shao, Performance enhancement and degradation mechanism identification of a single-atom Co–N–C catalyst for proton exchange membrane fuel cells, Nat. Catal. 3 (2020) 1044–1054. https://doi.org/10.1038/s41929-020-00546-1.
[40] A. Ohma, K. Shinohara, A. Iiyama, T. Yoshida, A. Daimaru, Membrane and Catalyst Performance Targets for Automotive Fuel Cells by FCCJ Membrane, Catalyst, MEA WG, ECS Trans. 41 (2019) 775–784. https://doi.org/10.1149/1.3635611.
[41] A. Filipponi, A. Di Cicco, C.R. Natoli, X-ray-absorption spectroscopy and n-body distribution functions in condensed matter. I. Theory, Phys. Rev. B. 52 (1995) 15122–15134. https://doi.org/10.1103/PhysRevB.52.15122.
[42] A. Filipponi, A. Di Cicco, X-ray-absorption spectroscopy and n-body distribution functions in

condensed matter. II. Data analysis and applications, Phys. Rev. B. 52 (1995) 15135–15149. https://doi.org/10.1103/PhysRevB.52.15135.
[43] M. Inaba, A.W. Jensen, G.W. Sievers, M. Escudero-Escribano, A. Zana, M. Arenz, Benchmarking high surface area electrocatalysts in a gas diffusion electrode: measurement of oxygen reduction activities under realistic conditions, Energy Environ. Sci. 11 (2018) 988–994. https://doi.org/10.1039/C8EE00019K.
[44] G.W. Sievers, GDE-cell online shop, (n.d.). https://gde-cell.com/ (accessed November 2, 2021).

7. Grafting of amino-nitrogen aromatic cycle

Nitrogen-carbon based materials (N-CM) are nowadays widely studied for hydrogen peroxide production and applications in wastewater treatment because of their low cost and precursor availability [1]. Pyrolysis of small molecules like phenanthroline or dibenzothiophene coupled with a hard templating agent is a quite common method used to obtain nitrogen or sulfur doped carbons. The drawback of this method is the lack of control on the type of active sites in the resulting material, namely at least four/five types of nitrogen functional groups (pyridinic, pyrrolic, graphitic and iminic or oxidated nitrogen) are formed during the pyrolysis. A more selective way for introducing active sites is the grafting of the carbon surface with molecules bearing the desired type of functionality. In light of this, two molecules were considered in this work to mimic pyridinic and pyrrolic nitrogen, namely, amino-pyridine and amino-indole. In fact, pyridinic nitrogen is claimed to be active for the reduction of peroxide to water whereas pyrrolic group was specifically identified for promoting the 2e-ORR. The grafting process was accomplished by reflux method using $NaNO_2$ as oxidating agent and HCl to help the solubilization of amine in water [2,3]. Indole was observed to give a nice degree of grafting with a linear trend of nitrogen fixation with the temperature of synthesis.

7.1. Result and discussion

7.1.1. Synthesis

Grafting was performed on Vulcan XC72 according to Toupin et al. [2,3] with 5-AminoIndole and 4-AminoPyridine, hydrochloric acid and sodium nitrite. The ratio of reagent was 10:1:1 of carbon, $NaNO_2$ and the molecule to graft. Three different temperatures were used to study the effect on grafting degree, namely 20, 40 e 60 °C.

The grafting procedure is the following (Figure 7.1)

- Around 0.2 g of Vulcan are dispersed in 10 mL of water in a round bottom flask
- Then 0.1 equivalent of 5-AminoIndole or 4-AminoPyridine was added, and the solution was stirred for 20 min.
- 0.1 equivalent of $NaNO_2$ was then added.
- After dissolution of sodium nitrite, 2 mL of HCl was added, this also helps to fully solubilized the amine.
- After 24h at reflux at the selected temperature, the carbon was vacuum filtered with water and ethanol.
- Finally, the sample was dried overnight in an oven.

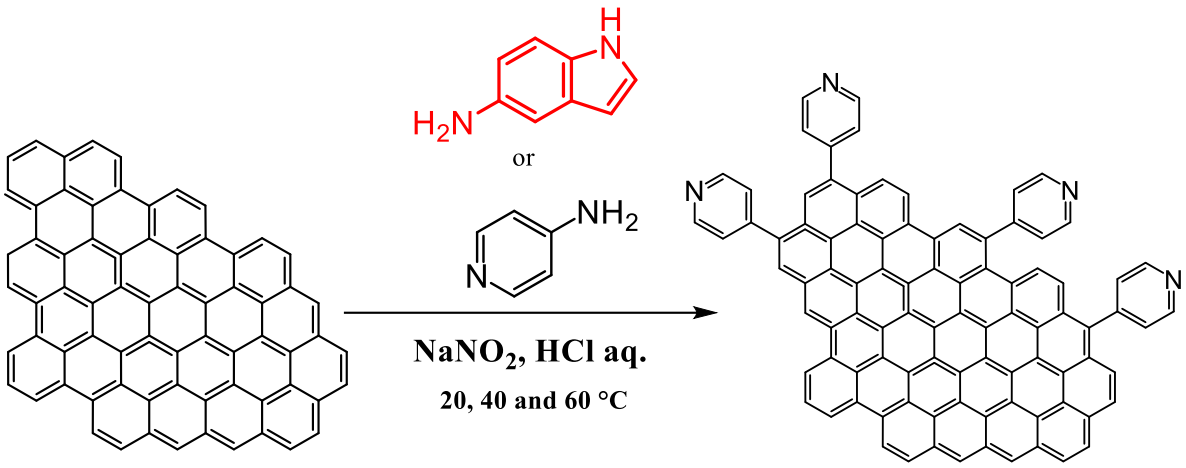

Figure 7.1. Grafting process with two molecules. VGP is for pyridine (black) and VGI for indole (red)

7.1.2. Elemental analysis

The first analysis that could be carried out is the elemental analysis which is able to give an indication of the bulk amount of nitrogen, that will be proportional to the degree of grafting. Table 7.1 shows the obtained results, for aminopyridine there is no evident trend with temperature of grafting, while for 5-aminoindole there is a nice trend passing from 2.42% to 6.56% of nitrogen.

Table 7.1. Elemental analysis of grafted samples compare to Vulcan XC72 (V)

	%C	%H	%N	%S
V	97.10	0.07	-	0.63
VGP20	95.70	0.46	0.79	0.51
VGP40	94.71	0.16	0.73	0.40
VGP60	96.62	0.34	0.47	0.51
VGI20	91.78	0.79	2.42	0.43
VGI40	88.49	1.12	3.82	0.38
VGI60	81.07	2.02	6.56	0.22
VGA60	94.82	0.27	-	0.95

According to Toupin at al. [46] during the formation of the in situ cation it is possible that it reacts directly with the conjugated system without the aryl radical being generated, thus forming a -N = N- bond. To verify the possibility of this phenomenon, a grafting synthesis was carried out with aniline at 60 °C (VGA60, Table 7.1), which if anchored through the generation of a radical should not bring nitrogen. Therefore, in the case of the formation of bonds between diazonium and carbon, the presence of nitrogen would be attributable to this bond. The result of the elemental analysis seems to exclude this possibility, also showing an increase in hydrogen linked to the grafting of aromatic rings.

7.1.3. XPS

Elemental analysis is a fast technique but does not tell anything about the speciation of nitrogen, this could be solved using XPS. From this analysis pyridinic and pyrrolic nitrogen could be distinguished since they have a different binding energy, around 398.8 eV for pyridinic nitrogen and 400.7 eV for pyrrolic; hence one could expect to observe a shift in nitrogen 1s peak for the two functionalization. Figure 7.2 shows the result for four of the six sample. For aminopyridine grafting,

the predominant peak is associated with pyridinic nitrogen, and the same is true for the pyrrolic nitrogen of aminoindole. This result is not surprising, but confirm the binding of molecule on the surface, what is less obvious is the presence of other component, suggesting that nitrogen coming from amine or nitrite is bind on the surface in other way, but at the date of writing no more information are available.

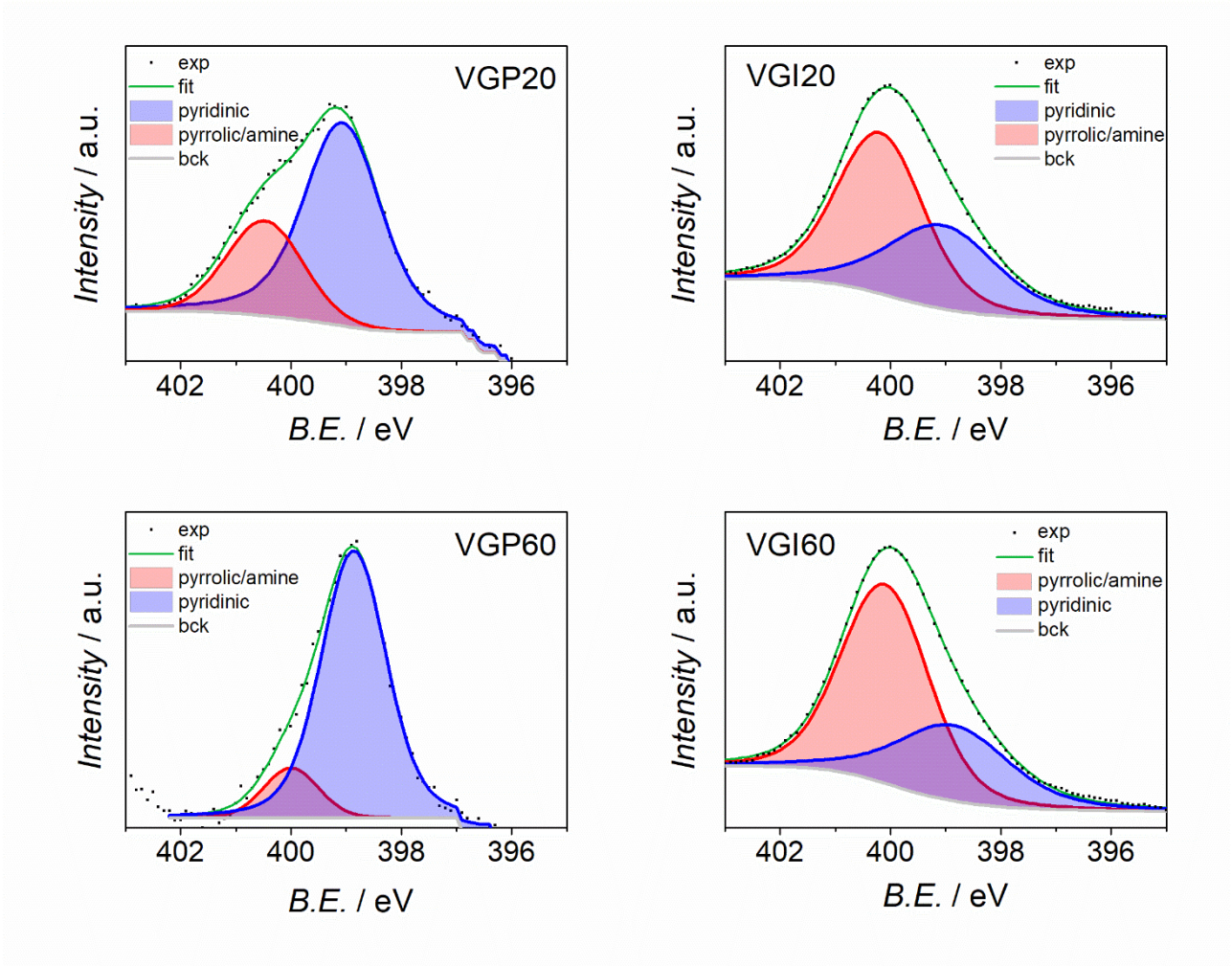

Figure 7.2. N1s deconvolution for VGI20, VGI60, VGP20 and VGP60

From the quantitative analysis, the nitrogen content (expressed as an atomic percentage) is 5.7% and 10.5% respectively for the VGI20 and VGI60 samples. These results agree with the trend described by the elementary analysis and suggest an increase in molecules anchored to the coal as the reaction temperature increases. As regards the samples grafted with pyridine, the nitrogen content is 2.5% and 1.3% respectively for the samples VGP20 and VGP60. This result is also reflected in the elementary analysis and shows how pyridine grafting does not increase with temperature but reaches a limit value.

Also, the C 1s signal were deconvoluted (Figure 7.3), there are always some components of O/N linked to carbon which could be linked to introduction of oxygen during treatment and nitrogen due to grafting. Furthermore, from the quantitative analysis it appears that the oxygen content increases from 8.1% of VGI20 to 14.3% of VGI60: this could suggest an increase in the presence of oxygen as the synthesis temperature increases and is matched by the increase in the Raman band. at 1700 cm^{-1}, associated with the presence of the functional group C=O (Figure 7.5b).

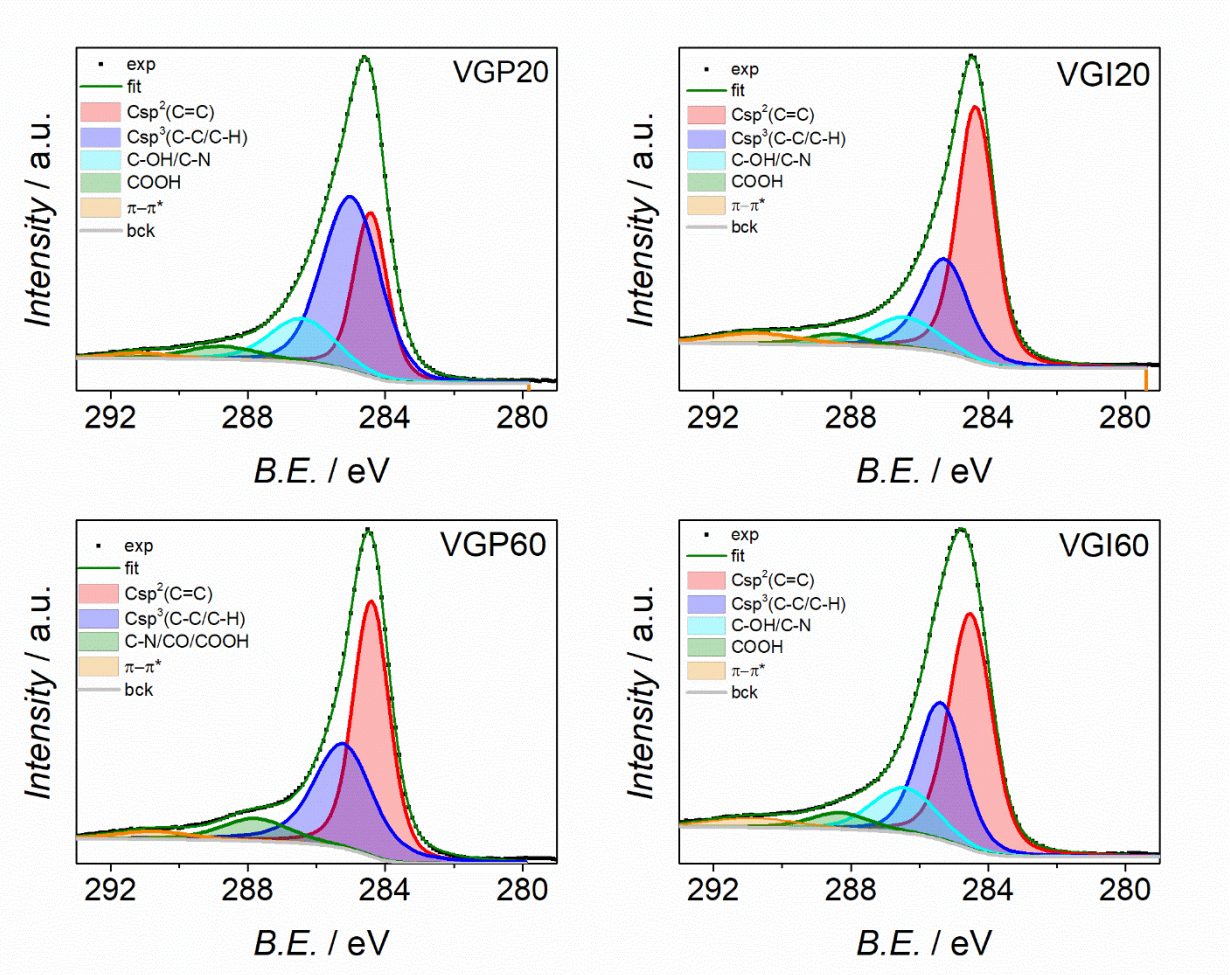

Figure 7.3. C1s deconvolution for VGI20, VGI60, VGP20 and VGP60

7.1.4. Surface Area

A final surface characterization was done to evaluate surface area change after grafting. A sample was selected as representative, namely VGI60 which shows the higher degree of grafting. Toupin et al. [2] experimentally and computationally show that small micropore (around 1 nm) are occluded by grafted molecule. Figure 7.4 clearly shows a micropore occlusion, but also, probably linked to the high grafting, a diminution of pore volume spanning through all dimensions. Just for the sake of completeness, we report that the isotherms, as expected from a commercial carbon black, have a type I/II shape and a barely visible hysteresis cycle of type H3/H4 (Figure 7.4a), typical for medium-low porous carbons with a modest content of micropores and mesopores and macropores, which perfectly fits with the properties of Vulcan XC72.

This result suggest that this catalyst could not performed ideally since the possess a poor pore network, but for the scope of the analysis this should not be too detrimental.

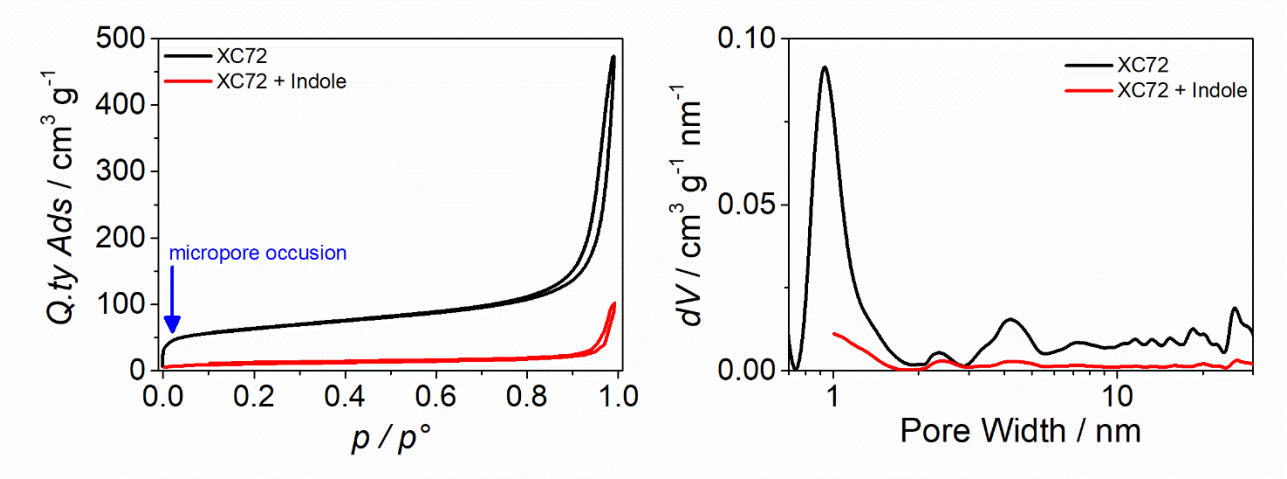

Figure 7.4. Isotherm and pore size distribution: Vulcan vs. VGI60

7.1.5. Raman

In the case of synthesis through grafting, Raman spectroscopy measurements were carried out to assess whether the introduction of molecules covalently linked to the carbon atoms of the graphitic domains produced sensitive variations of the D1 and G peaks [4–6].

Figure 7.5a shows the superimposition of VGP40 and 4-AminoPyridine spectra, no evident signal of the molecule is present on the carbon, that means that no non-grafted molecules are present, and that the eventual signal of the molecule on the surface is not detected.

Figure 7.5b shows the Raman spectra of the samples obtained through grafting of 5-Aminoindole on Vulcan-XC72. Three clear signals suggest a change in the materials, in particular the growing of a new band at around 1700 cm^{-1} is evident.

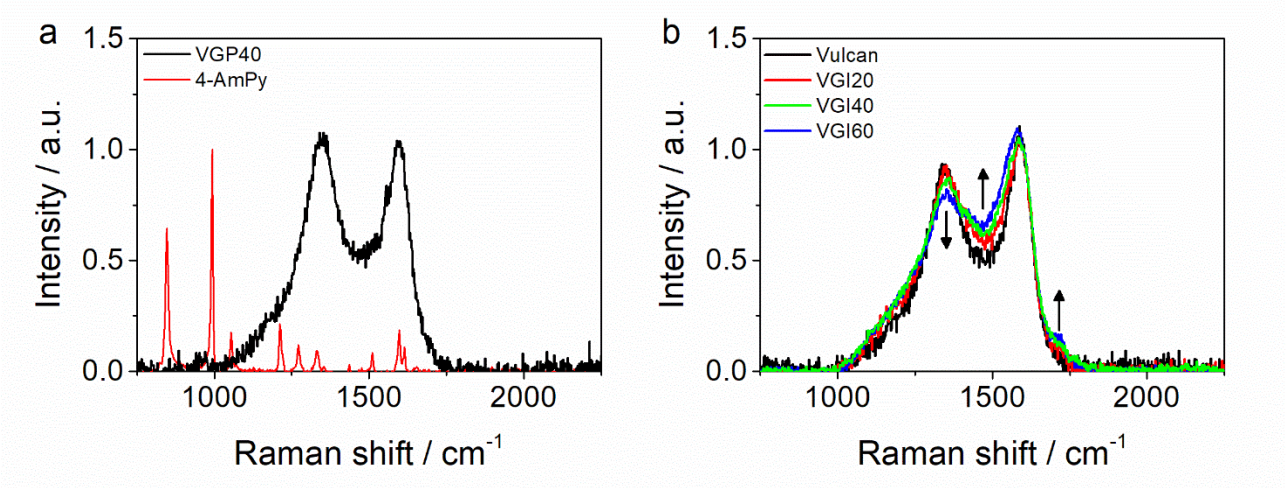

Figure 7.5. a) Comparison molecule and grafted carbon and b) comparison of indole-grafted carbon with Vulcan

In the case of grafting of pyridine molecules, a slight increase in intensity of the D1 band is observed and an equally slight lowering of the G band as the grafting temperature increases. This trend seems to be only partially confirmed by the I_{D1} / I_G ratio (Table 7.2) which suggests a saturation of the grafted molecules has been reached. In fact, even from the results of the elemental analysis, pyridine grafting does not seem to grow with increasing temperature. In all three samples, however, the increase in the I_{D1} / I_G ratio compared to the Vulcan arise. It is probable that grafting, reducing the number of C sp^2 through the formation of covalent bonds, leads to a decrease in the intensity of the G peak and breaks the symmetry of aromatic rings present in the graphite domain, increasing the D1 peak [7]. Even the increase in the A_{D3} / A_G ratio in grafted samples

compared to Vulcan XC-72 could signal an increase in the presence of molecules and functional groups [7] as a possible consequence of anchoring pyridine molecules.
Figure 10.31 shows the deconvolutions (non-linear fits) of the Raman spectra of Vulcan XC-72 and of the pyridine-functionalized samples. For all four samples it was necessary to fix the D4 band (1190 or 1200 cm^{-1}) in order to allow the fit to converge. Details are given in the Appendix (Figure 10.31 and Figure 10.32).

Table 7.2. Selected data from deconvolution of Raman spectra

	I_{D1} / IG	A_{tot}	A_{D3}/A_G	A_{D3}/A_{tot}	A_{D5}/A_{tot}	$A_?/A_{tot}$	R2
V	0.857	320	0.352	0.118	/	/	0.559
VGP20	1.012	294	0.563	0.173	/	/	0.592
VGP40	1.045	316	0.569	0.164	/	/	0.598
VGP60	1.041	327	0.513	0.149	/	/	0.602
VGI20	0.890	348	0.504	0.017	0.017	0.023	0.603
VGI40	0.846	367	0.792	0.020	0.020	0.027	0.537
VGI60	0.730	367	0.464	0.069	0.069	0.028	0.534

To what concern indole (Figure 7.5b, Figure 10.32) there is a decrease in the I_{D1} / I_G ratio (Table 7.2). A progressive increase in intensity is also observed with the temperature at a Raman shift of about 1450 cm^{-1} (called here D5) to about 1700 cm^{-1} (where a shoulder of the G peak arises, named ?).
Based on what was observed by Majumder at al. [7], Raman spectroscopy measurements on poly-indole show the presence of two bands at about 1339 and 1591 cm^{-1} attributed respectively to the stretching of the pyrrole ring and to the stretching of the phenyl ring. This result could explain the increase in intensity in correspondence of the G band with temperature, assuming that this increases the formation of radicals and induces the formation of multilayers of grafted indole molecules. On the other hand, the intensity of the D1 band decreases with increasing temperature so the contribution of the band at 1339 cm^{-1} does not seem to be present. The increase in intensity to about 1450 cm^{-1} is associated with the presence of a band (D5) whose intensity increases with temperature. Li and collaborators [8] found a signal at 1700 cm^{-1} attributable to the presence of the functional group C=O. To converge the non-linear fits of the indole grafted samples was complicated due to the new characteristics that emerged: in addition to the position of the peak of the D4 band, it was also necessary to fix the position of the D5 and D3 band. The fit results are reported in the Appendix.

7.1.6. Electrochemistry

Figure 7.6 shows the cyclic voltammetries of the samples of Vulcan grafted with pyridine. In the case of VGP40 it was necessary to cut the voltammetry as it showed too pronounced discharge. This is hardly related to the grafting itself, since there are no indication about a promotion of HER for pyridinic nitrogen, and in general we should observe the same thing for all 3 grafted sample. More probable is some type of contamination which does not seems to influence ORR, but in same way the discharge. The capacitive current of the grafted samples is in all cases greater than that of the Vulcan XC-72, confirming the presence of nitrogen atoms, therefore of a functionalization. In this case is not caused by higher surface area, but as a pseudocapacitive effect. The peak is shifted for all three sample toward more positive potential, and the same is evident from RRDE analyses (Figure 7.9a), but there is no trend with temperature of grafting that is perfectly in line with the

similar nitrogen fixation. All values are reported in Table 7.3. The cyclic voltammetries of the Vulcan series grafted with indole are shown in Figure 7.7 where graph b) is a detail of graph a). For VGI20 appear to be a slightly anticipation of oxygen reduction, but new peak are seen also in Ar saturated electrolyte peaks between 0.3 V and 0.8 V (anodic scan) and between 0.2 V and 0.7 V (cathode scan), in addition with appropriate magnification there are three peaks at 0.33, 0.55 and 0.74 V and three peaks at 0.26, 0.5 and 0.67 V. The potential of the peaks does not vary with the scanning speed, a symptom of a reversible nature of the three pairs bound to the grafted molecules. The voltametric behaviour hugely change passing from 20 to 40 °C, indeed voltammograms with further complex structures are observed. In the potential range between 0 and 1 V, the capacitive current (in Ar) is higher by about a factor of 80 compared to VGI20 and Vulcan XC-72; three peaks are also clearly visible in the anodic scan (0.37, 0.55 and 0.73 V), at the same potential observed for VGI20, showing that those are related with the film/polymer forming on surface. The increase in capacitive current is associated with a significant functionalization of the carbon, as confirmed by the elementary analysis (2.42, 3.82, 6.56%) and by XPS (5 and 10% of N for VGI20 and VGI60). In this case the analysis of oxygen reduction is complicated due to the complex shape of CVs.

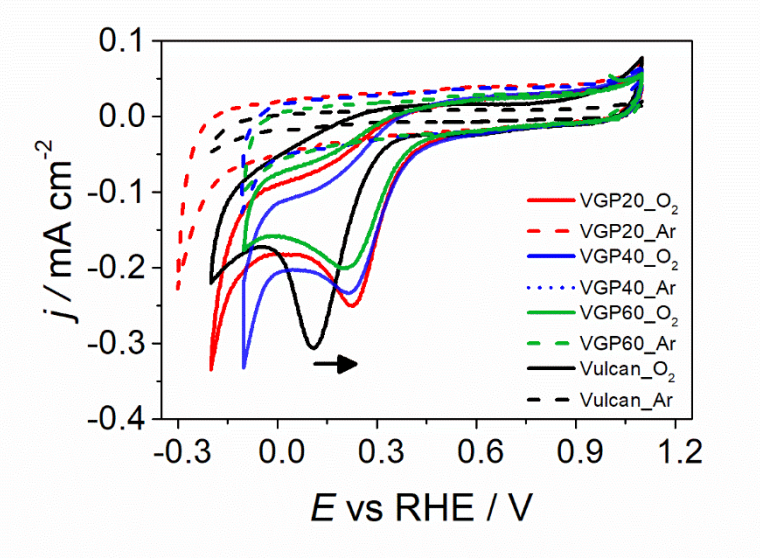

Figure 7.6. Cyclic voltammetry of pyridine-grafted Vulcan

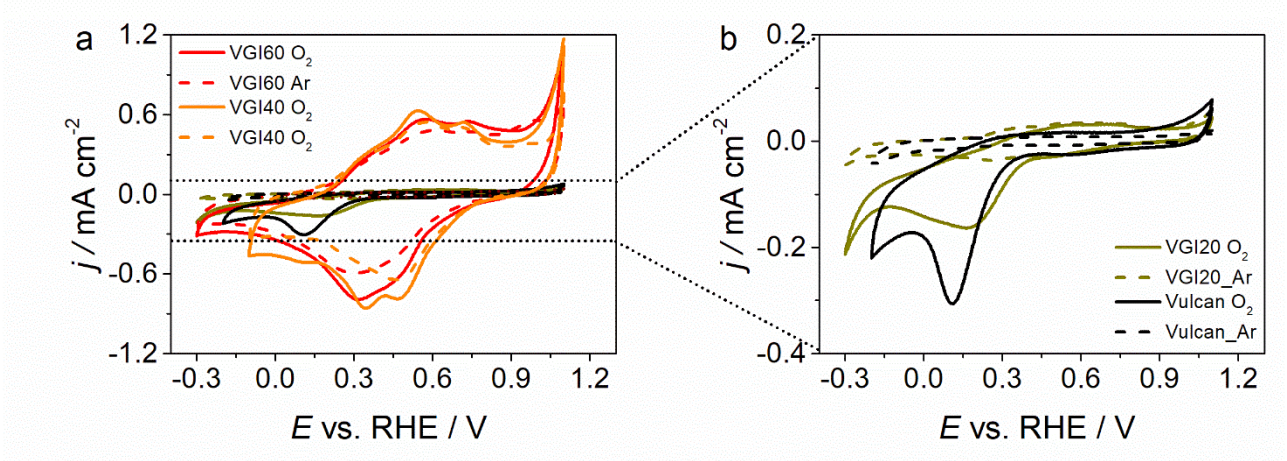

Figure 7.7. Cyclic voltammetry of indole-grafted Vulcan. b) magnification of a) for clarity reason

Tring to understand the voltammetric response of VGI samples, electrochemical study on glassy carbon with the molecule dissolved is solution where carried out. A first possible confirmation on

the nature of the redox peaks observed comes from the work of Talbi et al. [65] who studied the electro-polymerization of indole. During the synthesis and in subsequent electrochemical characterizations they observed the presence of two peaks in the anodic scan at 0.36 and 0.76 V and two peaks in the cathode scan at 0.28 and 0.62V. According to the authors, the peaks at more positive potentials would be related to the doping-dedoping processes of the polymer (transition from benzene-quinoidal form) while at less positive potentials the redox process would not involve electronic doping (IR spectroscopy measurements did not reveal the bond changes revealed for peaks at more positive potentials) [9]. This could suggest that during the syntheses at 40 and 60 °C a substantial polymerization of the indole molecules took place, presumably as a consequence of a large number of radicals formed, which is well activated above 20 °C. The presence of a multilayer of grafted molecules could explain how, despite the drastic decrease in surface area and accessible pores (Figure 7.4), the capacitive current has increased substantially (which is why poly-indole is used in nanocomposites for the development of capacitors [10]). Therefore, as said, two electro-polymerization experiments were conducted: one on Vulcan deposited in correspondence with the electroactive area of a rotating electrode (RDE) and one directly on the surface of this area (glassy carbon).

An amount of ink was deposited on an electrode to obtain 0.6 mg cm^{-2} of Vulcan. In a cell with solution (0.5 M H_2SO_4) saturated with Ar, 4-aminoindole was solubilized to obtain a 5 mM concentration. A CV was then performed at 100 mV s^{-1} for a total of 30 cycles (between 0 and 1.0 V vs. RHE). To test the catalytic activity of the modified Vulcan, the electrode was moved to a second cell with the same electrolytic solution but without 4-aminoindole and saturated with oxygen. Figure 7.8c and d show the electro-polymerization process on GC and Vulcan respectively: the first cycle has three redox pairs exactly like the VGI samples, albeit at slightly different potentials. These peaks merge into a single widened peak as the number of cycles increases, recalling in form those present in the VGI40 and VGI60 samples. The great difference is on capacitive current gives by roughness of Vulcan film.

The catalysis tests are shown in Figure 7.8a and c. The Vulcan XC-72 shows a peak for oxygen reduction as previously observed and likewise, but at more positive values, the modified Vulcan also shows a peak at 0.084 V, which however is not present in the blank or identifiable, in the CVs of VGI40 and VGI60 samples in the absence of oxygen. This test can lead to the conclusion that a multilayer of indole molecules was actually formed during the synthesis of grafting at temperatures higher than 40 °C.

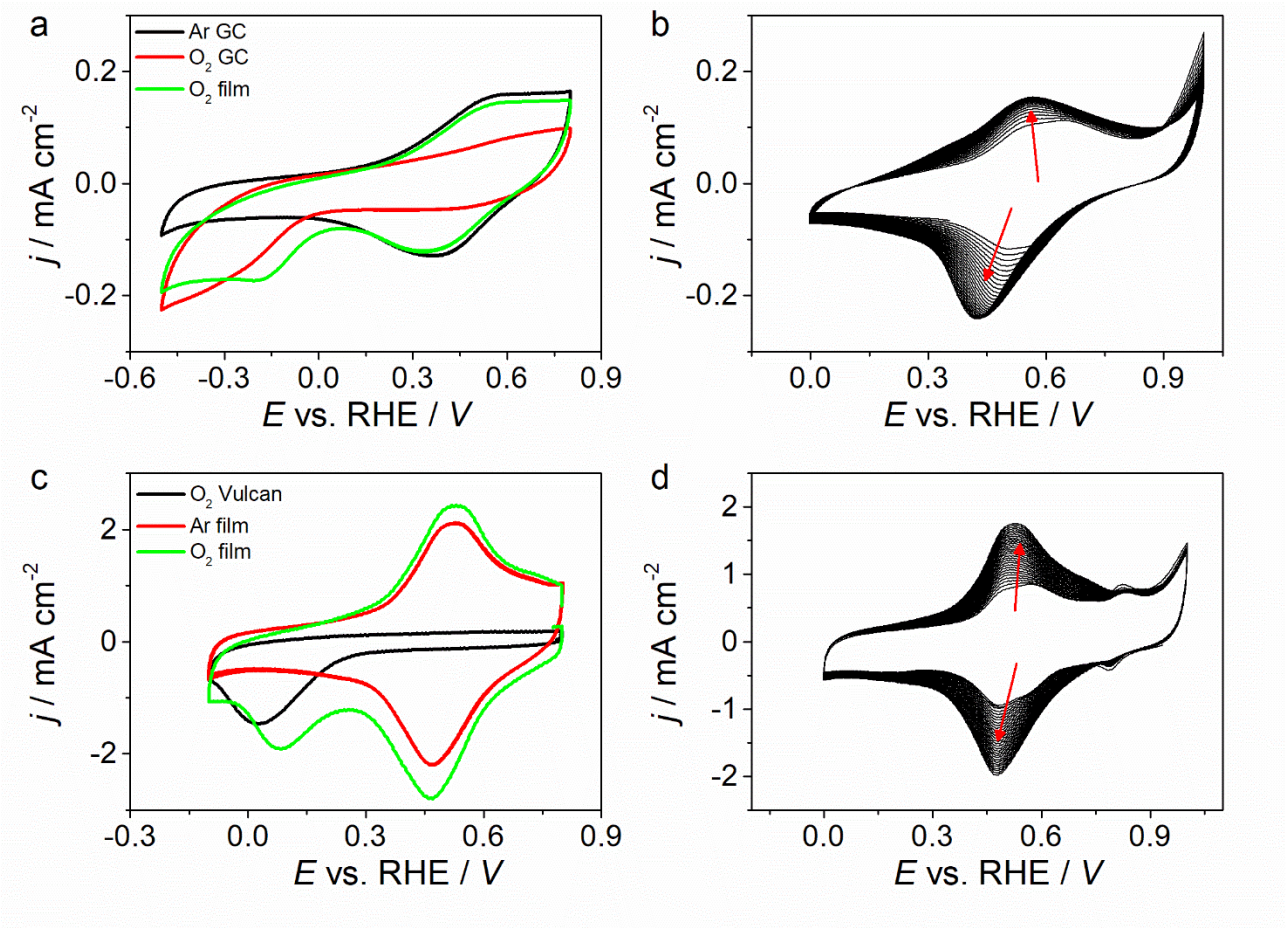

Figure 7.8. a, c) Electrochemical response of GC and Vulcan before and after electro-polymerization in Ar and O_2 saturated electrolyte. b, d) evolution of cyclic voltammetry during polymerization for GC and Vulcan.

Table 7.3. Selected electrochemical parameter derived from RRDE analysis

	$j_{0.25}$ mA cm^{-2}	$E_{0.1}$ V vs. RHE	H_2O_2 % at 0 V
V	-0.100	0.245	9.80
VGP20	-0.316	0.313	12.86
VGP40	-0.334	0.334	17.27
VGP60	-0.336	0.316	30.94
VGI20	-0.155	-	19.49
VGI40	-1.318	-	19.57
VGI60	-0.526	-	21.71

The percentage of hydrogen peroxide produced by Vulcan XC-72 (about 10% of average in the whole range of considerable potential) is much lower than that reported by Čolić and collaborators [13] who, characterizing the Vulcan in 0.1M $HClO_4$ solution, found a faradic efficiency at −0.2 V of 68% with respect to the production of hydrogen peroxide. However, it is evident that the introduction of molecules with pyridine groups has improved the performance of the material in terms of onset potential, limiting current density, half-wave potential and percentage of hydrogen peroxide produced (Figure 7.9b). In particular, the samples synthesized at 20 and 40 °C show almost the same activity and selectivity probably for the very similar amount of total nitrogen (0.79% and 0.73%). The case of VGP60 is different, which despite having less nitrogen (from the

results of AE and XPS), appears to have an activity similar to VGP20 and VGP40 but above all a selectivity towards the higher bi-electronic ORR (more than double). One explanation could lie in the fact that VGP60 has 87% nitrogen in a pyridine structure but remain hard to understand the reason for such behaviour, since other analysis did not show any hint.
For the indole the determination of H_2O_2 indicate that there are a linear increment with grafting degree (temperature) but the shape and position in potential range of LSV are difficult to explain (Figure 7.9c, d). In this case the high capacitive current linked to the not avoidable surface modification during potential scanning make exceedingly difficult to obtain a curve with no capacitive current contribution, and therefore the determination of activity parameters became complex. In conclusion, the formation of polymer chains on the surface makes it difficult to establish whether the active site is only pyrrole nitrogen.

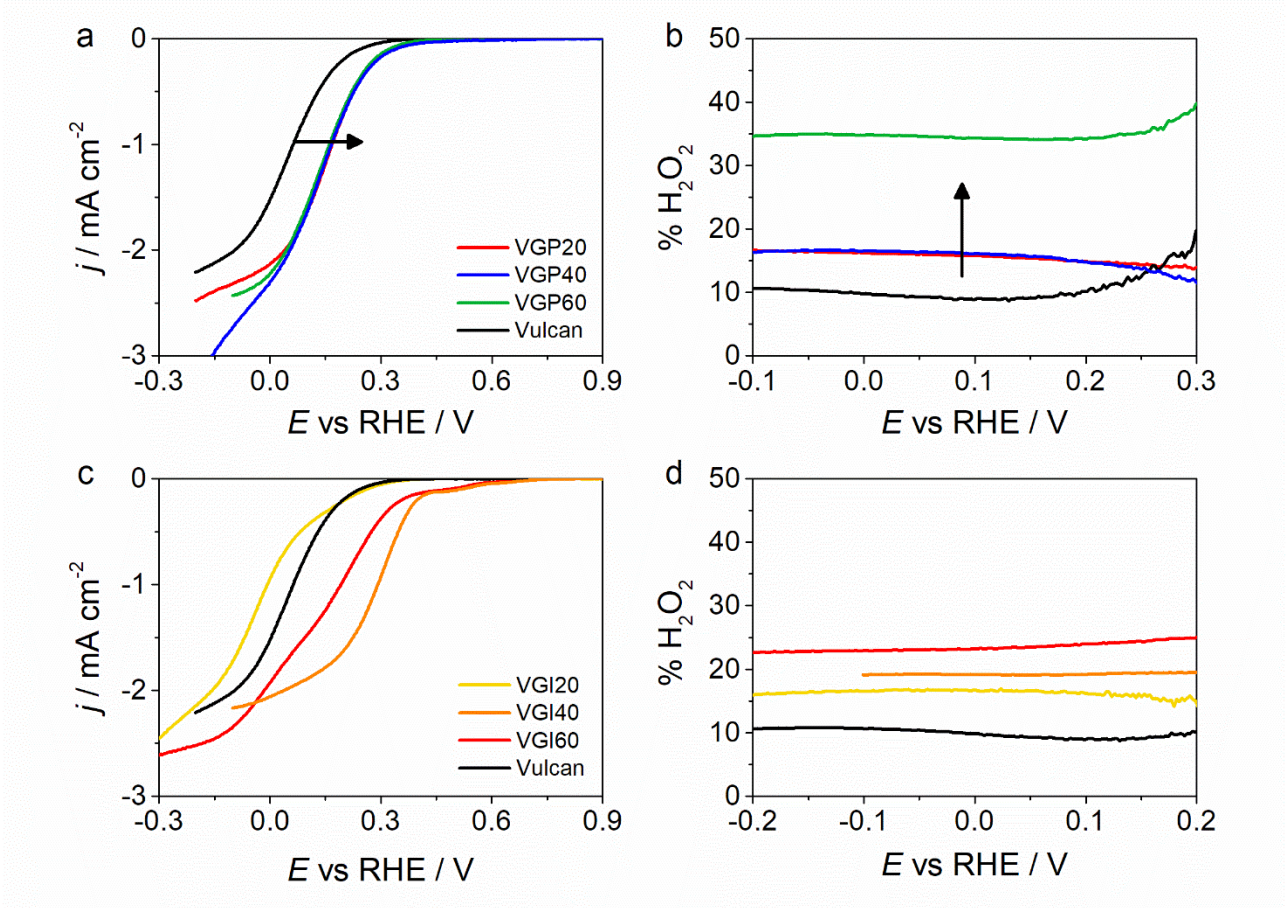

Figure 7.9. a, c) LSV in O_2 at 1600 rpm 2 mV s^{-1} and b,d) hydrogen peroxide production

The most selective sample was tested in GDE electrode configurations on a separated cell (H-cell) to quantify the amount of peroxide produced in time in a more realistic condition (Figure 7.10).
A deposit equal to 26 mg of carbon (0.87 mg cm^{-2}) was obtained. Three potentials corresponding to full regime of diffusive control and two more positive potentials of mixed regime (i.e., −0.1, 0 and 0.1 V vs. RHE) were chosen. Figure 7.11a shows the cyclic voltammetries in GDE: the CVs recorded after seven hours of electrolysis shows a probable surface modification that occurred on the catalyst given the onset of new peaks.

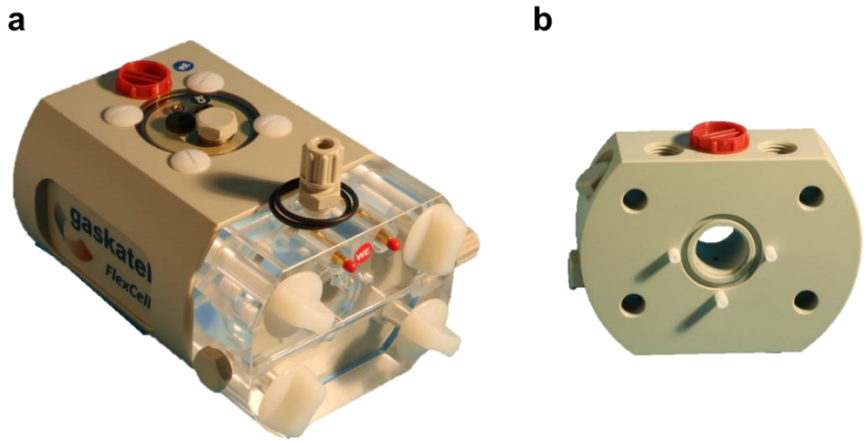

Figure 7.10. Scheme of the cell in for electrolysis a) main chamber and the gas compartment for undivided measurements, and b) additional chamber to perform measurements in divided cell

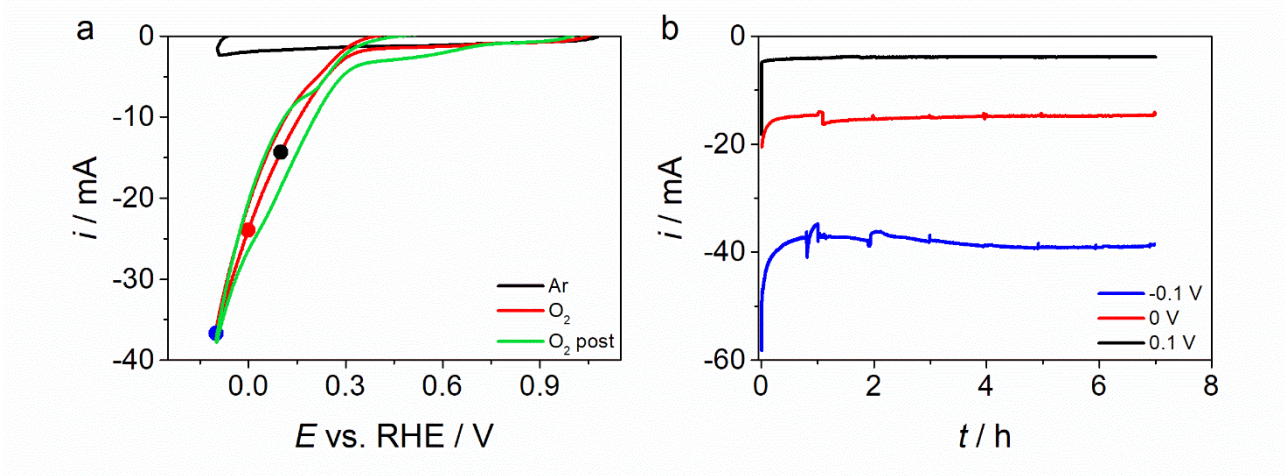

Figure 7.11. a) Cyclic voltammetry in Ar and O_2 before and after electrolysis; b) chronoamperometry at three different potentials

Figure 7.11b shows the three chronoamperometry at various potential. As far as faradic efficiency is concerned, VGP60 is confirmed as selective towards the production of hydrogen peroxide reaching up to 73% faradic efficiency in the first hour of electrolysis at a potential of −0.1 V. Selectivity remains high even at the most positive potentials (about 60% of FE for 0 and 0.1 V). A decrease in FE is observed in time since, with the accumulation of H_2O_2, the further reduction of hydrogen peroxide is inevitable; in the case of more positive potentials, a minor decrease in faradic efficiency is observed (Figure 7.12b). The concentration of hydrogen peroxide is almost constant starting from the first hour, for the potential of −0.1 V, a sign that the accumulation threshold is reached quickly. During electrolysis at 0 V this threshold is reached at the fifth hour. For the potential of 0.1 V a constant increase is observed; a linear fit performed on the data at this potential yields a production rate of hydrogen peroxide of 3.86 mM h^{-1} g^{-1} (Figure 7.12a).

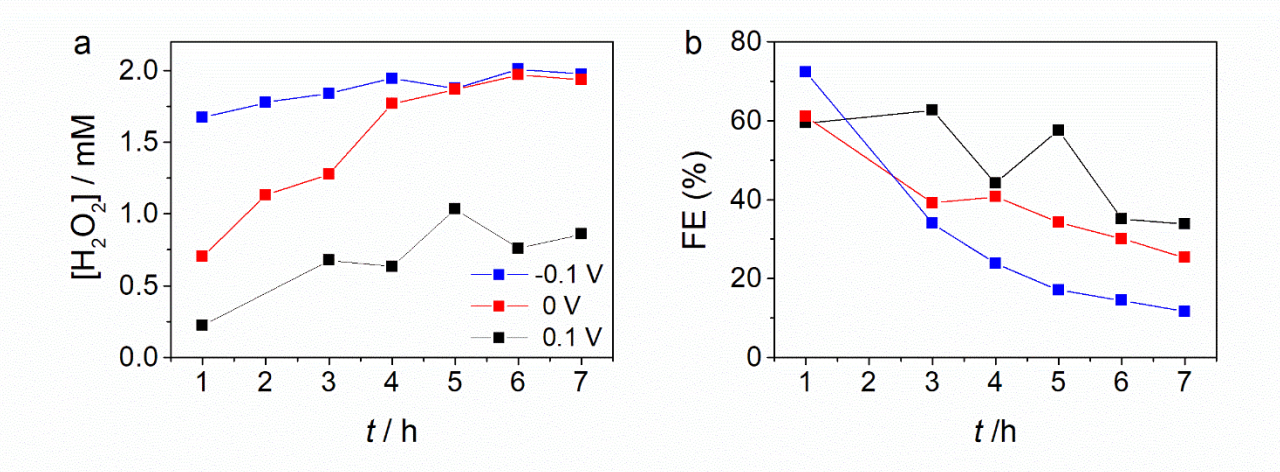

Figure 7.12. a) concentration derived from spectrophotometric analysis of electrolyte and b) faradic efficiency at three different potentials

7.2. Conclusion

Vulcan XC72 was successfully functionalized in a selective manner: the VGP60 and VGI60 samples have respectively 87% and 66% pyridine and pyrrolic nitrogen (XPS). Pyridine grafting does not appear to be temperature dependent, as confirmed by elemental analysis and XPS. The electrochemical properties are also almost identical in terms of onset potential, limit current density and half-wave potential; however, the selectivity of VGP60 towards the bi-electronic reaction is double that of the other two materials. In GDE experiment a faradic efficiency of 72% in the first hour of electrolysis at -0.1 V was observed for VGP60, reaching the accumulation limit (1.8 mM) in 3 hours. All three pyridine-graphed samples show improvements in activity and selectivity compared to Vulcan XC72, confirming when reported in the literature on the role of pyridine groups for the ORR. The extent of indole graphing increases with temperature leading to the formation, for syntheses above 20 °C, of a multilayer of molecules, the presence of which has been guessed by elementary analysis measures, XPS, Raman (with the growing of new bands) and CV and confirmed with two electro-polymerization experiments. In the literature, the role of pyrrole nitrogen is more debated than the selectivity towards bi-electronic ORR. As the indole grafted content increases, there is an increase in selectivity towards bi-electronic ORR, but the presence of an indole multilayer does not allow conclusions to be drawn regarding the actual role of pyrrole nitrogen as an active site. In conclusion, the synthesis through chemical grafting proved to be effective and without side effects in the introduction of pyridine functional groups. In this case, in fact, substantial improvements were found in the activity and selectivity of the bi-electronic ORR compared to the non-functionalized commercial Vulcan XC-72 coal.

7.3. Bibliography

[1] G. Daniel, Y. Zhang, S. Lanzalaco, F. Brombin, T. Kosmala, G. Granozzi, A. Wang, E. Brillas, I. Sirés, C. Durante, Chitosan-Derived Nitrogen-Doped Carbon Electrocatalyst for a Sustainable Upgrade of Oxygen Reduction to Hydrogen Peroxide in UV-Assisted Electro-Fenton Water Treatment, ACS Sustain. Chem. Eng. 8 (2020) 14425–14440. https://doi.org/10.1021/acssuschemeng.0c04294.

[2] M. Toupin, D. Bélanger, Spontaneous functionalization of carbon black by reaction with 4-nitrophenyldiazonium cations, Langmuir. 24 (2008) 1910–1917. https://doi.org/10.1021/la702556n.

[3] M. Toupin, D. Bélanger, Thermal stability study of aryl modified carbon black by in situ generated diazonium salt, J. Phys. Chem. C. 111 (2007) 5394–5401. https://doi.org/10.1021/jp066868e.

[4] A.C. Ferrari, Determination of bonding in diamond-like carbon by Raman spectroscopy, Diam. Relat. Mater. 11 (2002) 1053–1061. https://doi.org/10.1016/S0925-9635(01)00730-0.

[5] A.C. Ferrari, J. Robertson, Interpretation of Raman spectra of disordered and amorphous carbon, Phys. Rev. B. 61 (2000) 14095–14107. https://doi.org/10.1103/PhysRevB.61.14095.

[6] A. Sadezky, H. Muckenhuber, H. Grothe, R. Niessner, U. Pöschl, Raman microspectroscopy of soot and related carbonaceous materials: Spectral analysis and structural information, Carbon. 43 (2005) 1731–1742. https://doi.org/10.1016/j.carbon.2005.02.018.

[7] C.D. Doyle, J.M. Tour, Environmentally friendly functionalization of single walled carbon nanotubes in molten urea, Carbon. 47 (2009) 3215–3218. https://doi.org/10.1016/j.carbon.2009.07.035.

[8] N.F. Raman, S.B. Dippel, J. Heintzenberg, Soot Characterization in Atmospheric Particles From Different Sources, L. Aerosol ScL. 30 (1999) 907–908.

[9] H. Talbi, D. Billaud, Electrochemical properties of polyindole and poly(5-cyanoindole) in LiClO4-acetonitrile and in HCl and HClO4 solutions, Synth. Met. 93 (1998) 105–110. https://doi.org/10.1016/s0379-6779(97)04098-8.

[10] L. Xu, D. Li, W. Zhou, Y. Ding, Y. Wu, J. Xu, X. Duan, High-efficiency electrodeposition of polyindole nanocomposite using MoS2 nanosheets as electrolytes and their capacitive performance, Arab. J. Chem. 13 (2020) 6061–6071. https://doi.org/10.1016/j.arabjc.2020.05.006.

8. R(R)DE vs. GDE vs. H-cell: A Comparative Approach for Gauging the Activity and Stability in Fe-N-C Based Catalysts for ORR

This chapter covers the analysis made on a Fe-N-C material in order to compare the classical rotating disk analysis with the gas diffusion electrode setup. The aim of this chapter is to present a new methodology to characterize platinum free catalysts under a more realistic condition, namely in a fuel cell cathode-like configuration. A scheme with some properties is show in Figure 8.1

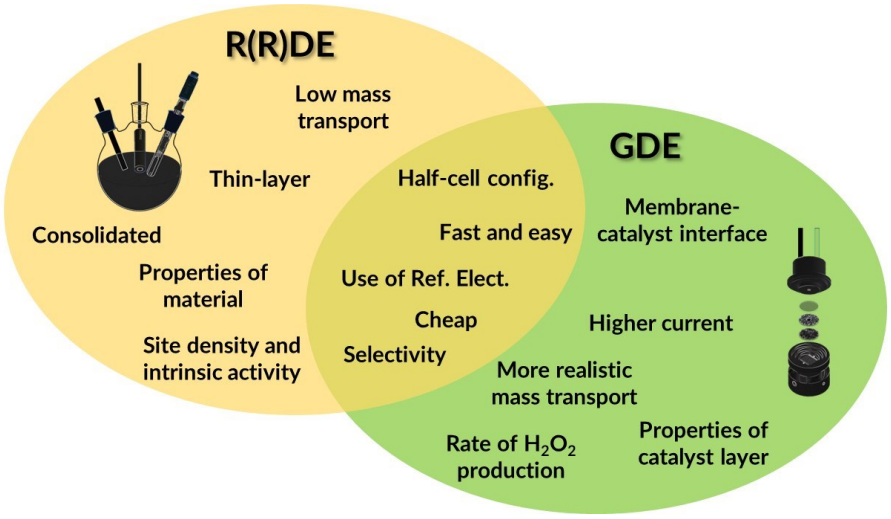

Figure 8.1. Some features of RDE and GDE setups

8.1. Experimental

8.1.1. Synthesis

The benchmark catalyst that we select to perform all the measurement was $FPHEN_3$ previously described in other chapter. Briefly is a typical 3 step synthesis (heat treatment/acid-leaching/heat treatment) with Vulcan XC72 as carbon support and $Fe(phen)_3Cl_2$ as Fe/N precursor (phen = 1,10-phenanthroline). The catalyst has 0.82 wt.% of nitrogen (EA) and 0.64 wt.% of Fe (EDX) which result in a site density of 4.24 x 10^{18} sites g^{-1} (NO_2 stripping [1]). XAS measurement confirm the single-site nature of this catalysts with absence or very low amount of nanoparticles (see 10.6.2).

8.1.2. Electrochemical test

In the following paragraph the most important aspect of electrochemical technique are reported, for more detail see chapter 4. Here we also report some advantages, disadvantages.

8.1.2.1.Stripping for Site Density (SD) and turnover frequency (TOF) determination

Determination of site density of Fe-N-C materials have been always a challenge, there are a lot of molecules that can interact with FeN_x centre which are believed to be the main active sites. For example, CN^- or SCN^- have been used to poison the site, but a quantitative determination is not possible [2,3]. The two main method that have been developed to obtain quantitative analysis are the CO pulse chemisorption/desorption [4] and the NO stripping [5–8]. The first is generally able to give a more accurate determination since the probe molecule is smaller and easily reach the metal site but suffer for the experimental condition and for the fact that compare to the second one is not

an electrochemical determination. Indeed, NO stripping is performed under more similar condition to R(R)DE analysis and in principle give a more and idea on the actual electrochemical active sites. This anyhow suffer also of some drawback, first of all the specificity of NO adsorption is not fully understand, for example has been shown that adsorption on FeO_x could occur [9], also, this determination is indicative for analysis in acid electrolyte since in alkaline environment the behaviour is generally different [10]. A last aspect to consider is that this method is time demanding since a single determination require up to 6/7 h of measurement following the published procedure and could be influenced by the goodness of drop casted layer that can impact the recorded current and of course the determination. In any case it remain one of the few methods, and possibly the only electrochemical one, that allow a reliable estimation of Fe-N_x active sites.
From the actual experimental point of view these measurements require a classical 3 electrode setup, where the electrolyte used is an acetate buffer. The choice of this media was actually made by the inventor of the procedure in other to mimic the condition of a classical acid-measurement, but at the same time to have a sufficient potential window to observe the NO stripping without hydrogen evolution interference. In practice LSVs are recorded in oxygen saturated solution before poisoning, after poisoning and after stripping. The stripping procedure is a simple cyclic voltammetry (in oxygen free solution) where a reductive peak appear linked to the reduction of NO to ammonia and clearly the stripping charge is linked to the amount of NO molecule stripped, which in principle reflect exactly the number of FeN_x sites in the material. Another clear problem appear here, since non-specific adsorption could lead to systematic error, that in any case has been shown to be negligible in most of the case [1].

8.1.2.2.R(R)DE setup and method

RDE is one if not the most established method to characterize in research laboratory catalyst for several catalytic reaction, mainly Oxygen Reduction Reaction (ORR), but also for Kinetic Modelling, calculating Equilibrium constant, Diffusion Coefficients and also in the field of corrosion [11–16].
For ORR investigation actually the RDE configuration is usually implemented with the addition of a probe (a Pt ring) to detect the possible hydrogen peroxide production, this configuration is called Rotating Ring Dick Electrode (RRDE). RRDE is in theory useful for all electrocatalytic reaction in which multiple products are possible, like H_2O_2 and H_2O for ORR or CO, H_2, CH_4, etc. in CO_2RR. In practice the selectivity of ring material, which is generally Pt, made this device almost specific for O_2 reduction. Only recently a configuration with Au as ring has been suggested for CO_2 reduction to detect CO, but the possible application for quantitative analysis is still to prove [17,18].

8.1.2.3.GDE setup and method

As said experimental setup different from RRDE are needed to better understand the working of catalyst under more realistic condition, as for example a setup where the catalyst is separated from the electrocyte has been proposed and commercialized. Indeed, the setup was bought from Gustav Sievers [19] (gde-cell.com) and consist of a steel body that serve also as a contact for applying the potential to the working electrode which consist of a carbon paper with the catalyst deposit on the surface. Also the same is possible with a PEEK body with metal contact as proposed in other work [20]. Contrary to the original setup a carbon felt under the carbon paper was used to improve the electrical contact between the electrode and the cell body, since it does not interfere with the actual electrochemical measurement, this could be needed because carbon paper and Nafion membrane are sold with different thickness and a certain height is necessary to obtain a good contact between catalyst and membrane. As anticipated, a Nafion membrane was placed between

the catalyst and the upper body (made of Teflon) of the cell. Also application in alkaline media with the suitable membrane have been proposed and tested here [21,22]. A graphite rod and a RHE (for acid electrolyte) or Hg/HgO (in alkaline media) were used as counter and reference electrode respectively. The scheme is pictured in Figure 8.2.
The advantage of this setup is that is easy to prepare, in the simple case the membrane rests on the carbon paper and the pressure induce by the clamp use to assemble the cell is sufficient to have a good adherence. Generally using 0.5 M H_2SO_4 as electrolyte bring to resistance of the other of 20 Ω which, depending on the potentiostat could be problematic to compensate with very high current, therefore, on some occasion higher acid concentration could be needed, for example Arenz and co-worker use 4M $HClO_4$ to reduce ohmic drop. This is crucial especially with Pt since higher current are reached. The type of measurements that could be carried out with this setup are essentially two, cyclic voltammetry under Ar or O_2 flux and chronoamperometry at given potential (or chronopotentiometry). The first were used to characterize material behaviour in this setup, the second to verify the stability/durability. Clearly also impedance spectroscopy analysis can be carried out to evaluate the ohmic drop.

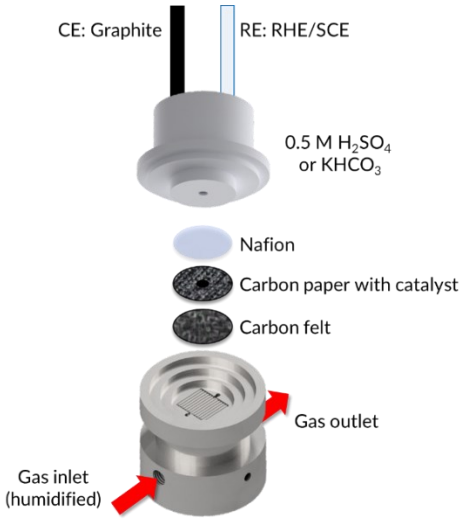

Figure 8.2. Scheme of the cell in all its component.

8.1.2.4.Electrolyzer setup and method

For electrolysis measurement a commercial setup (Figure 8.3a) was bought from Gaskatel GmbH. It consist of a primary cell made of polypropylene (PP), an optional secondary compartment (Figure 8.3b) that could be put between the gas feed chamber, which is the cell part that allow to feed the gas from behind the catalyst layer which face the electrolytic solution in the primary cell on in the secondary. Working with the secondary cell compartment and a cation/anion conductive membrane allow to work in divided cell and therefore permit a quantification of electrolysis product could be made, in practice the primary cell that contain the counter electrode is separated from the compartment with the working and the reference electrode. In this configuration the working electrode is the gas diffusion electrode, the counter electrode is a Pt wire and the reference electrode a RHE which thanks to some capillaries work in a Lugging-like configuration.

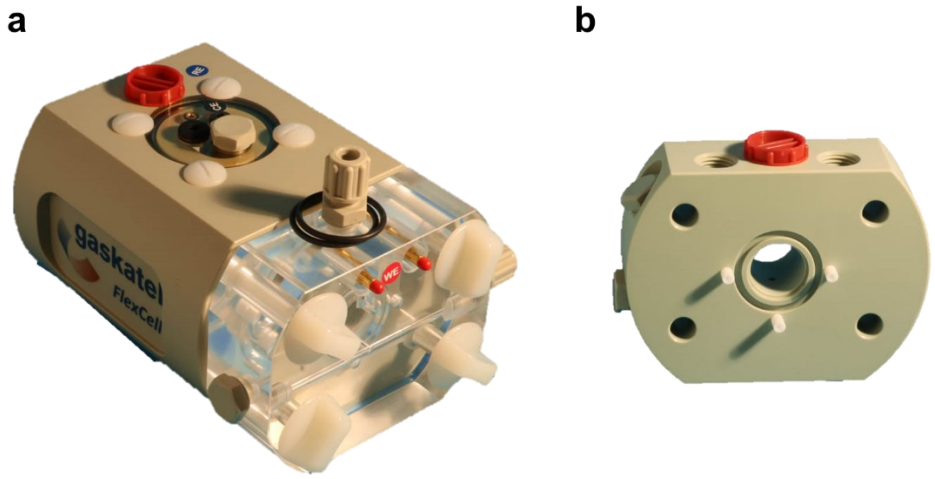

Figure 8.3. Scheme of the cell in for electrolysis a) main chamber and the gas compartment for undivided measurements, and b) additional chamber to perform measurements in divided cell.

8.1.3. Physico-chemical characterization

Fully characterization can be found in personal publication [10] ($FPHEN_3$ in that paper), but we add here a XAS analysis which reveal the single site nature of our catalyst (Appendix 10.6.2).

8.2. Result and Discussion

8.2.1. Loading Effect

Testing a catalyst in half-cell configuration (in the sense that only one compartment material are tested), is challenging since a lot of variables could impact the recorded activity that could lead to unrealistic estimation of the goodness of a certain catalyst. One major example are the good dispersion of a catalysts powder on R(R)DE surface and the strength of binding that is needed to prevent detachment from the surface. This in general leads to modification of loading of catalysts which is well known impact the result of a measurement, in particular for complex reaction such as CO_2RR and ORR, for example the selectivity towards hydrogen peroxide could be falsified when thick layer are used since if H_2O_2 remain trapped could be further reduce, and the result is an underestimation of catalysts ability. For that reason, as an introductory part, we study the effect of loading on the two system that are compared, R(R)DE and GDE, for the first one focusing on both activity and selectivity, for the second one only on activity. Since the study on RRDE was already done in other chapter, only a brief summary is reported here. For the benchmark catalyst that we selected the result are shown in Figure 8.4, for these catalysts appear evident that in 0.5 M H_2SO_4 even at loading of 0.2 mg cm^{-2} the amount of peroxide is low (Figure 8.4d) which suggest that this catalysts in this environment tends to produce water rather than peroxide. Clearly the lower amount of catalyst result in lower current (Figure 8.4e), but if the activity is calculated as kinetic current (or current normalize for the loading) it result even higher at low loading (Figure 8.4b, f). This aspect is important to a better understating of real material activity since focusing on a single loading could lead to a partial understanding of material. Clearly to add more value to R(R)DE analysis also a test in an electrolyzer with H_2O_2 quantification could be carried out (for example with potassium titanium oxide oxalate dehydrate complexation and following spectrophotometric determination of absorption at 400 nm [23]).

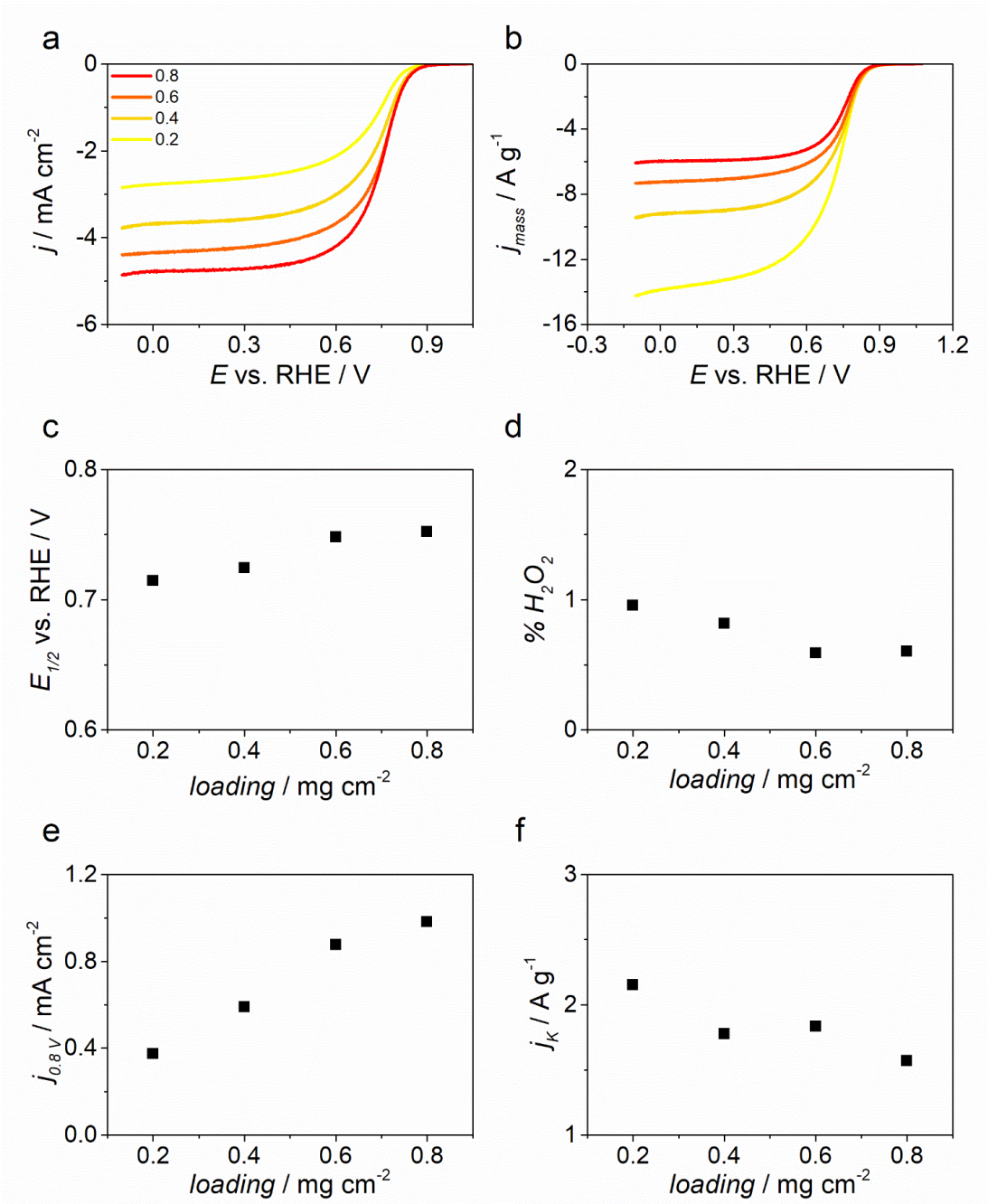

Figure 8.4. a) LSVs at 2 mV s^{-1} 1600 rpm in 0.5 M H_2SO_4, b) current normalized by loading, c) half-wave potential, d) peroxide yield, e) current density at 0.8 V vs. RHE and f) kinetic current at 0.8 V vs. RHE at 4 selected loading.

8.2.2. GDE

In a totally different setup as a gas diffusion electrode cell, we expect a different effect of the loading. In this setup the catalyst is no longer in direct contact with the electrolyte solution which serves only as a proton source (in the case of ORR) while the gas comes from the bottom the carbon paper on that the catalysts are deposited. We prepared eight different carbon paper with as many loadings starting from 0 (sole carbon paper) to 4.0 mg cm^{-2}. As it is possible to observe from Figure 8.5 even at low loading there a huge increment in activity compared to the sole carbon paper, then passing loading of around 0.5 mg cm^{-2} the increment became less evident but still detectable, reaching a limit after 3 mg cm^{-2}.

If we actually look at normalized current (Figure 8.5b, d) it possible to see that actually the activity per unit mass is lower, as already observed with RRDE (Figure 8.4). This is probably due to the layer that became too thick and the actual active material in contact with the Nafion membrane became more or less the same, also considering the assembly procedure of this configuration. In any case appear clear that variation of the order of 0.2/0.4 mg cm^{-2} for high loading does not impact the activity a lot, this method is indeed good for characterize materials even if the control on loading is not perfect.

So, in conclusion, higher loading allow to obtain higher current, but looking at mass corrected current, which is a mass normalized activity parameter, it is clear that the optimal loading is around 0.5 mg cm^{-2}.

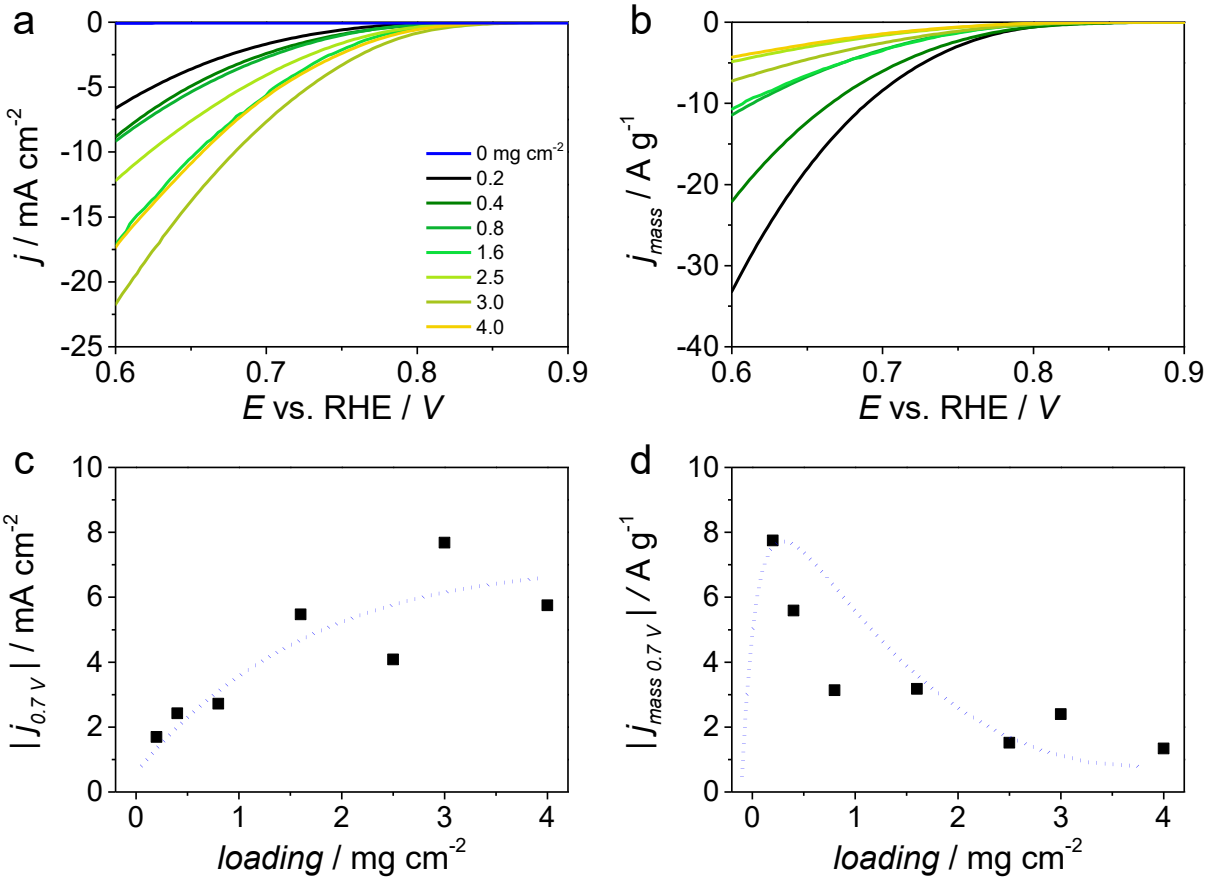

Figure 8.5. a) CV recorded at different loading (only cathodic scan is reported for clarity) on carbon paper where loading 0 is the sole carbon paper, b) current normalize for the carbon loading and c, d) the variation of current and mass current at 0.7 V vs. RHE with the various loading.

8.2.3. Effect of electrolyte

8.2.3.1.R(R)DE: Effect of pH

It is well known that changing the pH has an impact on activity, durability, and selectivity of Fe-N-C materials. Usually this is easily verifiable by using 0.5M H_2SO_4 and 0.1M KOH as solvent to perform R(R)DE analysis. As typical of metal nitrogen doped carbon materials the activity recorded in alkaline media is higher than in acidic condition (Figure 8.6**)**. Indeed, the active sites of oxygen redaction are different and seems that the role of the metal is less important, since also material that shows poor performance in acid condition perform well when passing to alkaline solution [10].

For that reason, metal-free catalyst are general more attractive to be used in alkaline condition if not meant to produce hydrogen peroxide. The different activity, which as said, is linked to different active site, leads generally to different peroxide production for example in the material show here the yield of peroxide was lower than 5% in acid and close to 50 % in KOH.

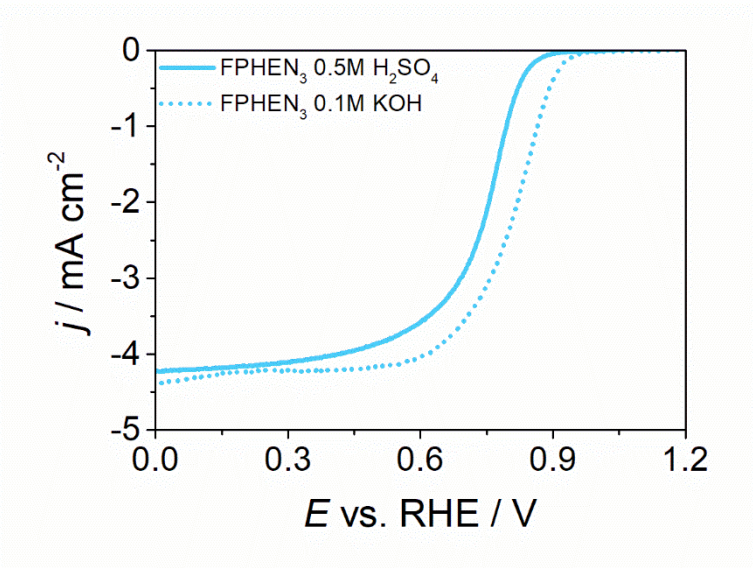

Figure 8.6. LSVs recorded in the two opposite pH condition

8.2.3.2.GDE: Effect of acid concentration

Another parameter that could be change in GDE configuration is the concentration of acid in the upper part of the cell, namely above the Nafion membrane. In theory changing the acid concentration will change the concentration at the interface between the catalyst layer and the membrane and therefore having an impact on the activity. Figure 8.7c and d show the evolution of impedance spectroscopy profile and of the ohmic drop of the system decay by increasing the acid concentration. Figure 8.7a shows the different voltametric response of material at the different concentration in argon while Figure 8.7b show voltammetry in oxygen (Ar-subtracted). It is possible to observed that at low concertation a limitation of current occur, similarly to RDE, while at higher concentration the expected curve (more discharge-like) is observed. The onset potential is not affected, while a clear effect of acid concentration is present at more negative potential. Figure 8.7a also shows that by increasing the acid concentration, the quinone-hydroquinone couple became more evident.

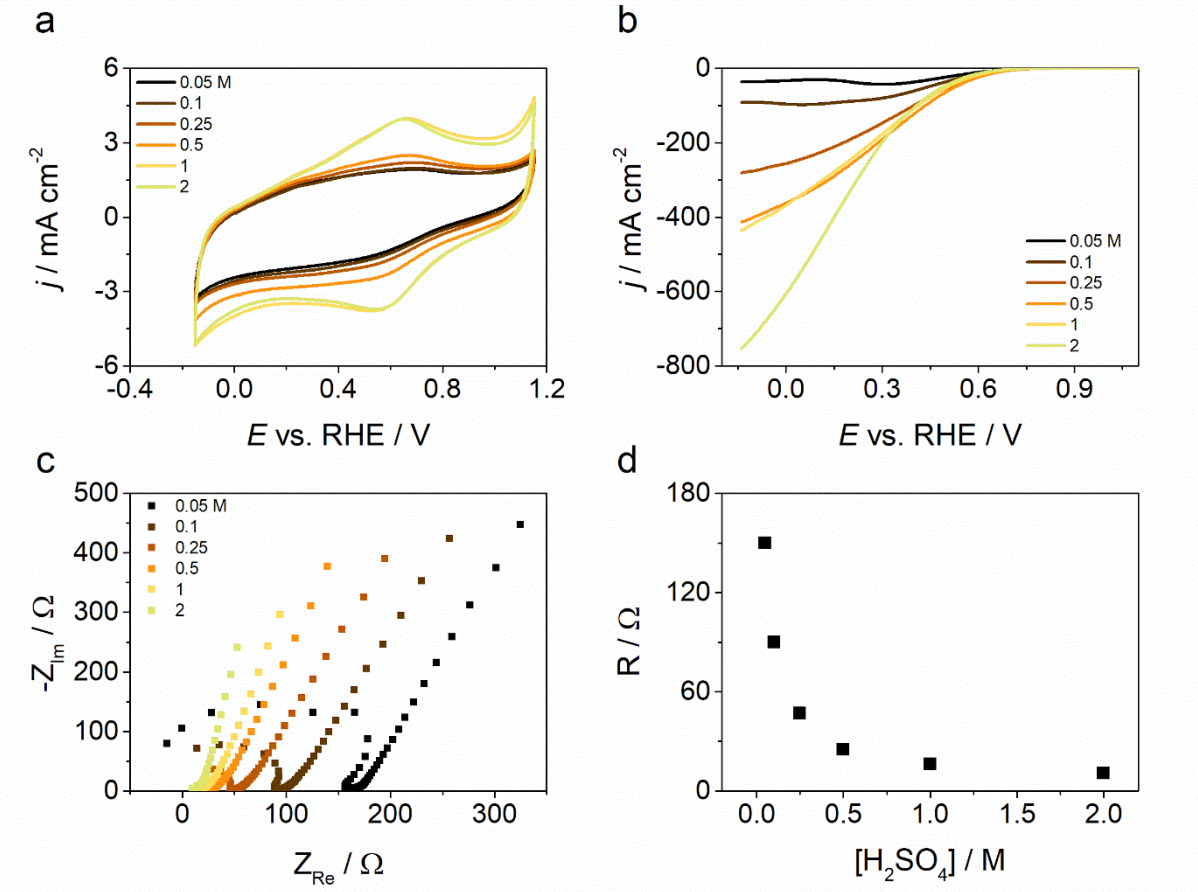

Figure 8.7. a) Cyclic voltammetry under Ar flux and b) voltametric response (cathodic run) at different acid concentration under oxygen flux. c, d) Variation of impedance profile and ohmic drop with the acid concentration

8.2.3.3.GDE: Effect of pH

As explained before, changing the pH has an influence on the activity recorded with RRDE, and therefore we investigate the same effect of the GDE configuration. In this case 0.5M H_2SO_4 was used as source of proton as in the other experiment, while in alkaline environment 1M KOH was as source of OH^-. In this case the Nafion membrane was replaced by an alkaline membrane.

As shown in Figure 8.8 also in this setup the activity in alkaline condition are better compared to acid environment. Looking at onset potential (taken at 2 mA cm^{-2} for GDE and 0.1 mA cm^{-2} for RRDE) and current (taken at 0.7 V for GDE and 0.8 V for RRDE) there is for the two setups respectively a difference of 70 mV and a threefold difference in favour of alkaline media.

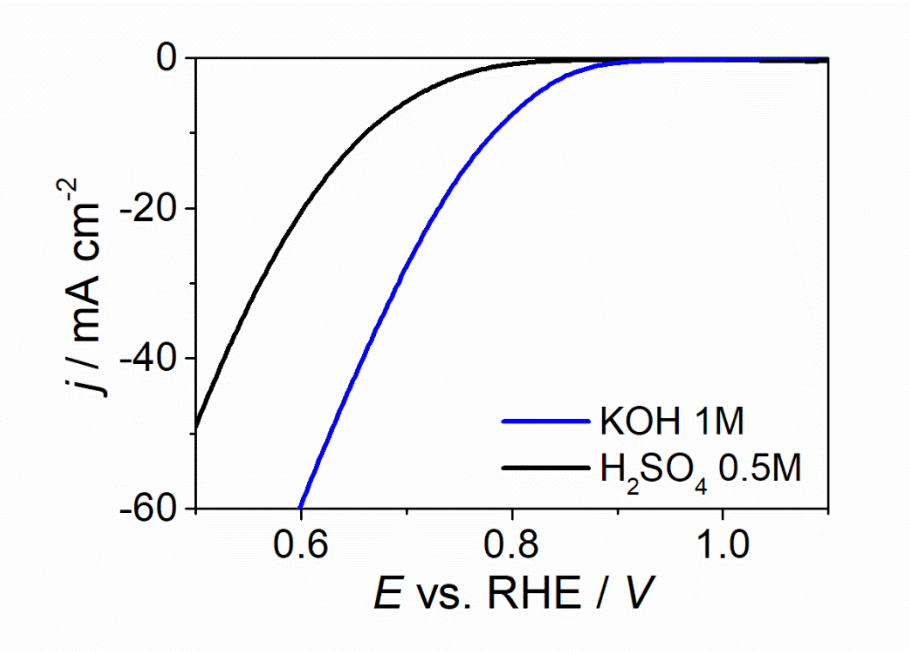

Figure 8.8. Comparison between measurement performed in acid and alkaline condition using GDE setup, the potential is converted vs. RHE

8.2.4. SD determination

As said, the determination of actual site density on the material is quite challenging but some quantitative analysis could be made. The above described NO_2 stripping method allow to electrochemically probe Fe-N_x sites giving an estimation which is probably a lower bound in determining the actual density of active site.

In Figure 8.9 the key measurements result are reported. From CV subtraction the stripping charge is obtained (Figure 8.9a ,b) which allow to calculate the SD, while the variation of current recorded at a certain potential (Figure 8.9c, d) could be used to evaluate the TOF at that potential since the overall activity at certain potential is proportional to the product of TOF and SD. More detail are given elsewhere in this thesis.

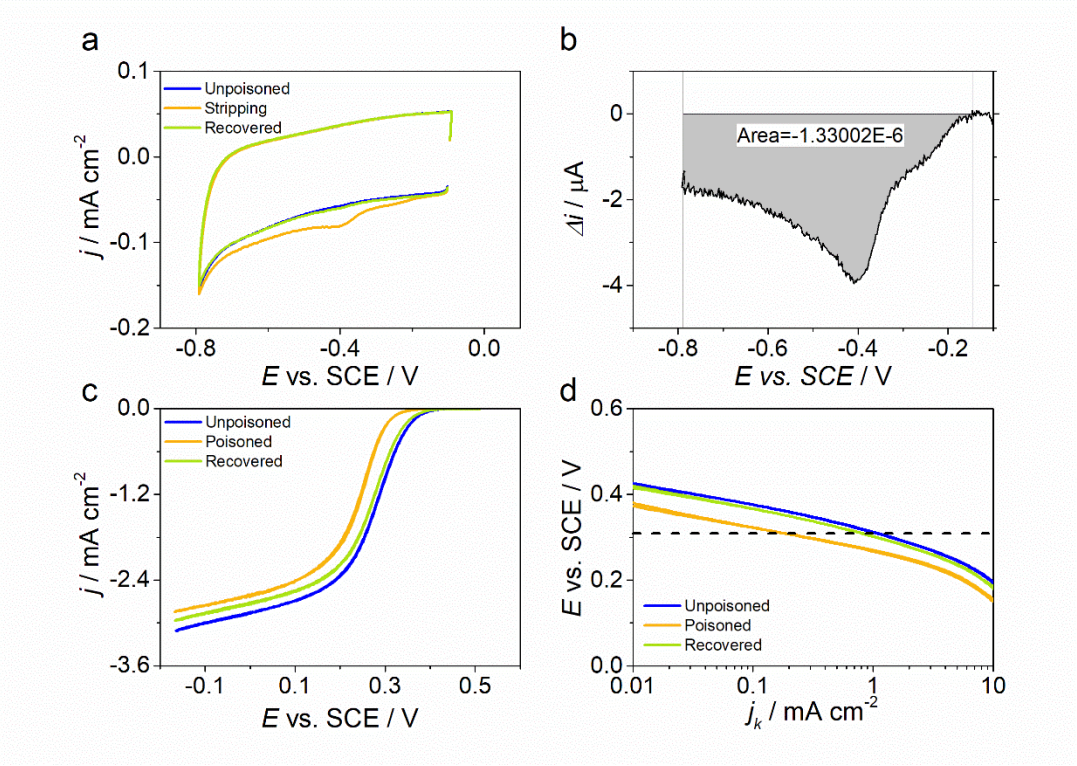

Figure 8.9. Voltametric response during a typical stripping analysis recorded in acetate buffer: a) CV in the stripping region before, during and after stripping in argon purged electrolyte, b) stripping charge area extrapolated from the CV showed in 'a', c) LSV at 1600 rpm and d) Tafel plot in O_2 saturated electrolyte.

8.2.5. Oxygen Reduction: Activity, Selectivity and Durability

8.2.5.1.R(R)DE

RDE is a very useful technique to perform different type of analysis. First of all is used in ORR activity determination by performing CVs and LSVs in static and hydrodynamic condition, but at the same time the RDE tip is very convenient for performing analysis such as accelerated stress test (AST), site density analysis, etc. RRDE as abovementioned is probably the most common technique after RDE to characterize material for ORR. In the classical configuration (disc → GC and ring → Pt) it is possible to work in many electrolytes since Pt is more or less inert.

Here we used two opposite conditions: pH = 0.3 of 0.5M H_2SO_4 and pH=13 of 0.1M KOH, which are very common in literature (sometimes 0.1 M H_2SO_4, 0.1 M $HClO_4$ or 0.5 M KOH are used). In Figure 8.10a the LSV recorded at 1600 rpm are reported for the two conditions, while in Figure 8.10b the peroxide yield is shown. It is evident that for the investigated material, as always append for Fe-N-C, the activity recorded in alkaline environment is higher, and also more stable, as result from AST (Figure 8.10c). A useful thing about RRDE is that it is possible to perform a stripping analysis after AST to evaluate changes, when we do that after AST in acid we observed that while the intrinsic activity of sites is similar (TOF), the SD became smaller, suggesting, as elsewhere demonstrate, during measurements in acid some sites are leached out, the remaining activity is due to more stable site. If the same is done in KOH not particular change in activity and site density was observed, so sites are more stable in this environment as suggested by lower shift of activity (Figure 8.10c), but probably the real active site are different as peroxide yield shows (Figure 8.10b). The variation in TOF is unexpected but should not play a central role in alkaline media, if Fe-N_x are not the central site.

The discrepancy between Figure 8.10a and c (curved obtained in AST) is due to the fact that the measurements were performed in different days, here form graphical reason only one measurement could be report, but when multiple analysis were done the value reported in table is meant as an average.

Table 8.1. Electrochemical parameter derived from CVs before and after AST

		$E_{1/2}$ V	$j_{L,0V}$ mA cm^{-2}	$j_{0.8\,V}$ mA cm^{-2}	$j_{k,0.8\,V}$ A g^{-1}	$\Delta E_{1/2}$ mV
H_2SO_4	Fe_2XC72	0.681	4.35	0.45	0.84	-
	after 7000 cycles	0.625	4.23	0.21	0.37	−56
KOH	Fe_2XC72	0.813	5.16	2.82	10.38	-
	after 7000 cycles	0.810	4.81	2.57	9.17	−3

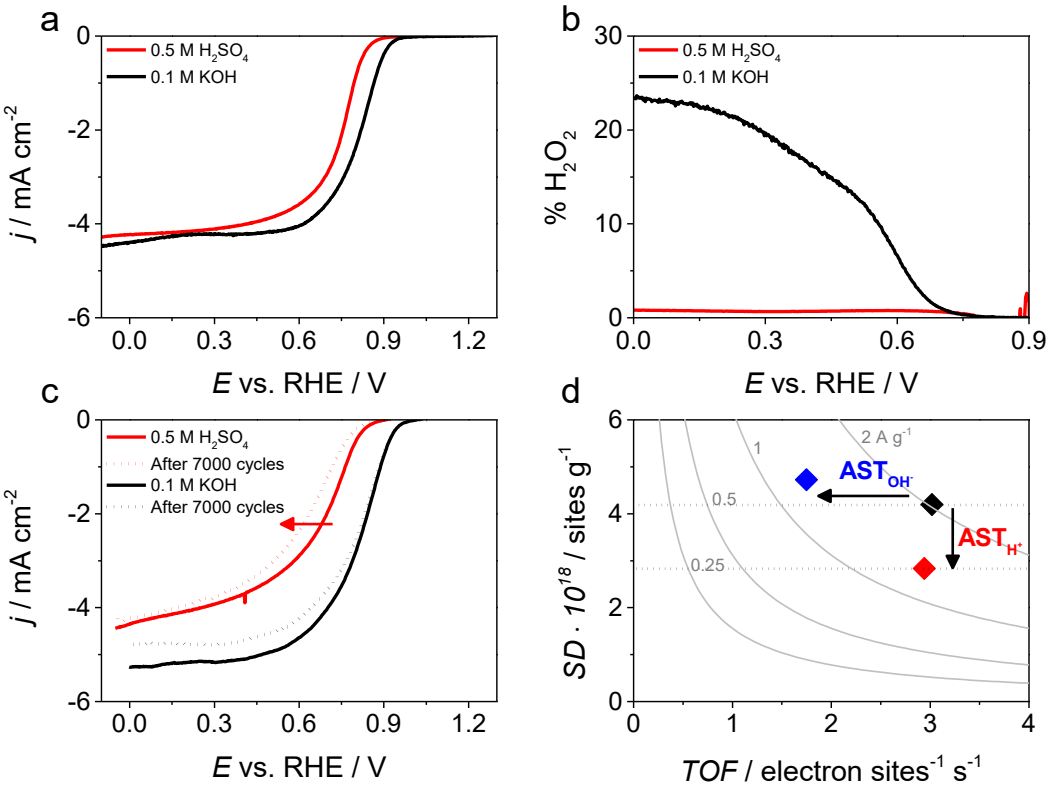

Figure 8.10. a) LSVs in acid and alkaline electrolyte and b) the production of peroxide (HO_2^- in KOH) in the same media. c) LSV evolution during AST in both electrolyte and d) variation of SD/TOF for the AST reported in an iso-current map.

8.2.5.2.GDE

The comfort and versatility that R(R)DE offers is to the detriment of truthfulness of result obtain, in the sense of how the recorded activity is actually translated to real device application. Approaching in laboratory test condition closer to fuel cell cathode without building an actual cell is therefore important and configuration as gas diffusion electrode helps in this way. As said, in this configuration the catalysis is no longer in direct contact with the electrolyte solution but is divided by a membrane (Nafion in the case of proton exchange membrane fuel cell mimicking) which allow the transfer of ions (proton) from the actual electrolyte solution. The device is therefore still a half-cell setup but should represent better what is seen by a catalyst when insert in a fuel cell assembly.

Figure 8.11a shows an example on what could be obtained by performing this kind of measurements. In Ar flow the CV resemble the one obtained in a traditional static RDE measurement, while when oxygen is fluxed under the catalysts layer, a discharge-like curve is observed. The current reached here are way higher that in RDE setup while generally the onset potential are lower.

Table 8.2. Electrochemical parameter derived from CVs before and after AST

	$E_{j=2}$ V	$j_{0.5\,V}$ mA cm^{-2}	$j_{0.7\,V}$ mA cm^{-2}	$\Delta j_{0.5}$ %
Fe_2XC72	0.782	48.23	9.00	-
after 8h	0.729	29.00	3.33	-39.9

This setup also allow to perform AST, in our case we chose to carry out a chronoamperometry protocol at 0.5 V vs. RHE for 8h recording a CV in O_2 after and before the AST. In Figure 8.11b, c are shown the chronoamperometry and the two CVs before and after the AST. The shift in current appears very clear, the potential at 2 mA cm^{-2} shifts from 0.782 to 0.729 V, the current at 0.5 is 19 mA cm^{-2} lower and the current at 0.7 is about 1/3. All this parameter shows that the activity is lowered in good accordance with the AST performed on RRDE where a decrease of 56 mV in half wave potential was observed after 7000 cycles between 0.55 and 1.05 V vs. RHE (Figure 8.10 and Figure 8.11)

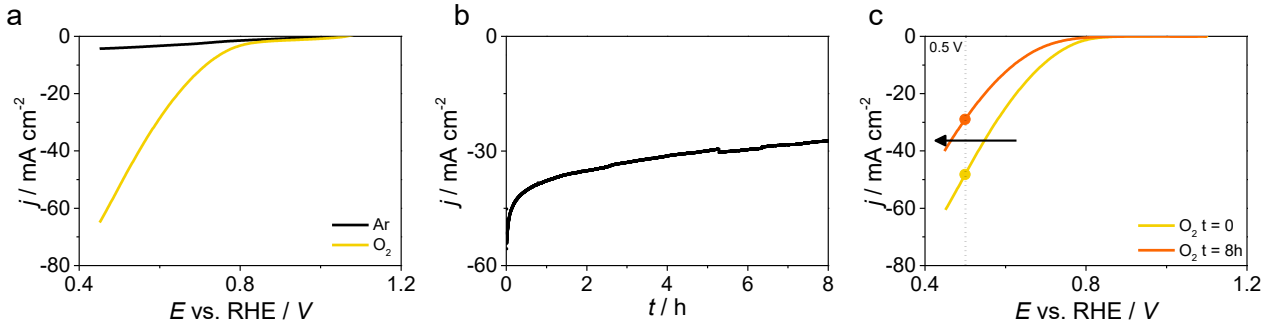

Figure 8.11. a) Cyclic voltammetry recorded under flow of Ar and O_2. b) Chronoamperometry at 0.5 V vs. RHE and c) CV shifting after the 8h of AST, here the curve are subtracted to the background.

8.2.5.3.Electrolysis in H-cell

The hydrogen peroxide yield is often calculated via RRDE analysis or sometimes with the less accurate Koutecky-Levich plot by RDE analysis at different rotation speeds. GDE setup previously described is closer to a real fuel cell setup but does not allow a quantification of hydrogen peroxide production, indeed a divided cell setup (or H-cell) coupled with a diffusion electrode setup (Figure 8.3) allow to evaluate the faradic efficiency on a setup with larger surface area which is in a certain way closer to practical device. This configuration is certainty more useful for electrolytic *in situ* production of H_2O_2, namely for catalysts specifically made for peroxide production, but could give a confirmation of how catalysts for fuel cell performed under different condition compared to RRDE.
More practically the catalyst was put on a carbon paper with a loading of around 0.6 mg cm^{-2} on an area of 3 cm^2 which is the active area under this setup. The electrolyte was as always 0.5 M H_2SO_4. Two cyclic voltammetry was recorded before and after 7 h of chronoamperometry at 0.2 V vs. RHE which also serves an AST (Figure 8.12).

Every hour the cell compartment directly facing the carbon paper was opened to sample the solution, 100 µL was taken added to Ti(IV) solution and UV-Vis recorded to calculate H_2O_2 concentration (see appendix 10.5.1, Figure 10.30). By the total amount produced a FE of 1.2 % was calculated which is perfectly in line with the amount derived from RRDE analysis. Certainly, under this configuration, part of the produced H_2O_2 could be further reduce, giving a certain underestimation.

Table 8.3. Electrochemical parameter derived from CVs before and after AST in divided cell

	$E_{j=2}$ V	$j_{0.5\,V}$ mA cm^{-2}	$j_{0.2\,V}$ mA cm^{-2}	$\Delta j_{0.5}$ %	$\Delta j_{0.2}$ %	FE %	rate mmol g^{-1} h^{-1}
Fe_2XC72	0.586	4.27	18.23	-	-	-	-
after 7h	0.556	3.37	17.41	-4.5	-21	1.2	5.0

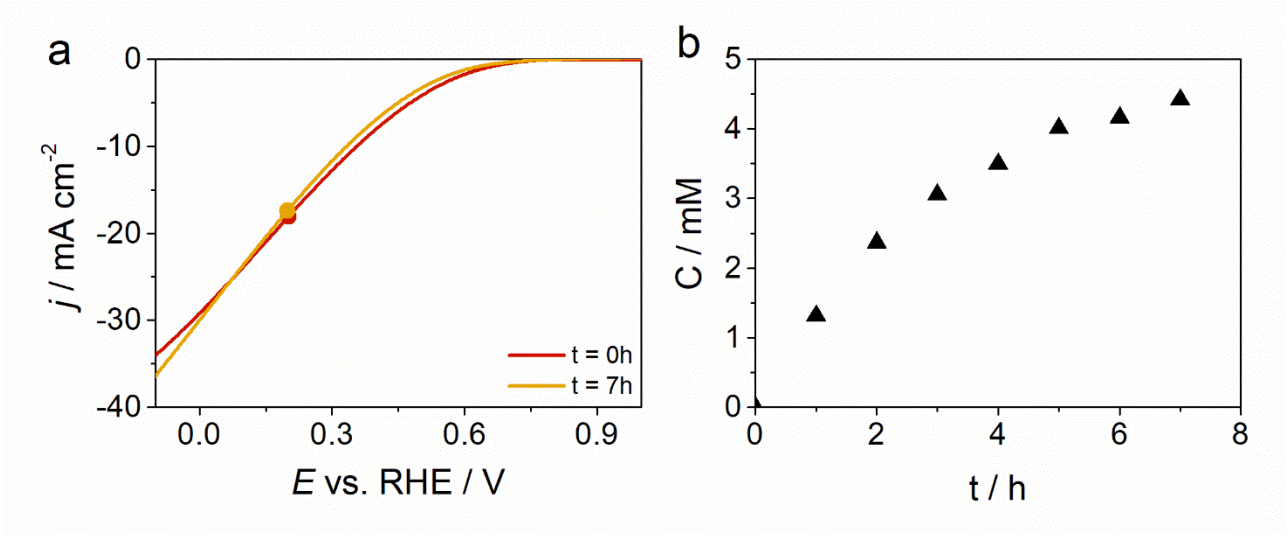

Figure 8.12. a) CV before and after chronoamperometry and b) peroxide concentration determined by titration method using Ti(IV).

8.2.6. Result comparison

If we compared the result obtained with the three setups, it is clear that GDE setups allow to reach higher current, and that no diffusion limitation occurs. Figure 8.13 report the curve with the current normalize for the area and loading to compare the three setups and Table 8.4 some parameter. The activity recorded in RRDE configuration is superior in the region of potential around 0.8 V vs. RHE followed by GDE configuration and finally by H-cell. At potential around 0.6 the RRDE is reaching is limiting current while the other two continue to grow due to the absence of the limit of diffusion, as said before. Dotted line in Figure 8.13b shows the RDE response after correction with Koutecky-Levich correcting the effect of mass transport, this is perfectly in line with the GDE profile, confirming that this setup eliminate this factor. These two setups are therefore perfectly interchangeable to gain more information.

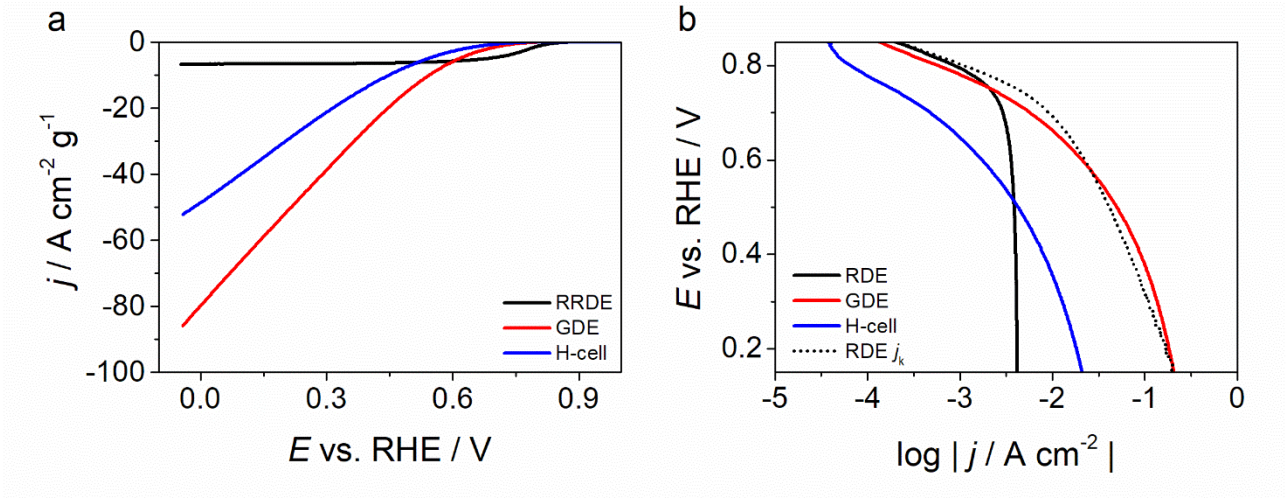

Figure 8.13. RDE vs. GDE vs. H-cell the scale is the current density normalized by loading

Table 8.4. Electrochemical parameter for the RDE, GDE and H-cell

	E_{onset} V vs. RHE	$j_{0.2V}$ A cm^{-2} g^{-1}	$j_{0.5V}$ A cm^{-2} g^{-1}	$j_{0.7V}$ A cm^{-2} g^{-1}
R(R)DE	0.871[a]	4.2	3.9	2.9
GDE	0.753[b]	183.3	49.9	5.8
H-cell	0.600[b]	18.2	4.3	0.5

[a] 0.1 mA cm^{-1}, [b] 2 mA cm^{-2}

8.3. Conclusion

In this chapter we explore more in detail several aspects of activity, durability tests under different setups, namely rotating ring disk electrode and gas diffusion electrode. All setups offer different way to understand the activity and durability of Fe-N-C catalysts, RRDE coupled with nitrite stripping allow a complete characterization of activity, selectivity, durability, and variation of site density. GDE offer more realistic condition, namely without mass transfer limitation, of both selectivity and durability by choosing the right setup. Using an “electrolyte free” cell, in which the catalyst is in contact with a membrane as in fuel cell, the result show a perfect agreement with mass transfer corrected RDE analysis showing that both setups are valid technique to characterize Fe-N-C to gain more information.

8.4. Bibliography

[1] D. Malko, A. Kucernak, T. Lopes, In situ electrochemical quantification of active sites in Fe-N/C non-precious metal catalysts, Nat. Commun. 7 (2016) 13285. https://doi.org/10.1038/ncomms13285.

[2] M.W. Chung, G. Chon, H. Kim, F. Jaouen, C.H. Choi, Electrochemical Evidence for Two Sub-families of FeN x C y Moieties with Concentration-Dependent Cyanide Poisoning, ChemElectroChem. 5 (2018) 1880–1885. https://doi.org/10.1002/celc.201800067.

[3] M.S. Thorum, J.M. Hankett, A.A. Gewirth, Poisoning the oxygen reduction reaction on carbon-supported Fe and Cu electrocatalysts: Evidence for metal-centered activity, J. Phys. Chem. Lett. 2 (2011) 295–298. https://doi.org/10.1021/jz1016284.

[4] N.R. Sahraie, U.I. Kramm, J. Steinberg, Y. Zhang, A. Thomas, T. Reier, J.-P. Paraknowitsch, P. Strasser, Quantifying the density and utilization of active sites in non-precious metal oxygen electroreduction catalysts, Nat. Commun. 6 (2015) 8618. https://doi.org/10.1038/ncomms9618.

[5] D. Malko, A. Kucernak, T. Lopes, Performance of Fe–N/C Oxygen Reduction Electrocatalysts toward NO_2^- , NO, and NH_2OH Electroreduction: From Fundamental Insights into the Active Center to a New Method for Environmental Nitrite Destruction, J. Am. Chem. Soc. 138 (2016) 16056–16068. https://doi.org/10.1021/jacs.6b09622.

[6] M. Primbs, Y. Sun, A. Roy, D. Malko, A. Mehmood, M.-T. Sougrati, P.-Y. Blanchard, G. Granozzi, T. Kosmala, G. Daniel, P. Atanassov, J. Sharman, C. Durante, A. Kucernak, D. Jones, F. Jaouen, P. Strasser, Establishing reactivity descriptors for platinum group metal (PGM)-free Fe–N–C catalysts for PEM fuel cells, Energy Environ. Sci. 13 (2020) 2480–2500. https://doi.org/10.1039/D0EE01013H.

[7] D. Malko, A. Kucernak, T. Lopes, In situ electrochemical quantification of active sites in Fe–N/C non-precious metal catalysts, Nat. Commun. 7 (2016) 13285–13292. https://doi.org/10.1038/ncomms13285.

[8] M. Mazzucato, G. Daniel, A. Mehmood, T. Kosmala, G. Granozzi, A. Kucernak, C. Durante, Effects of the induced micro- and meso-porosity on the single site density and turn over frequency of Fe-N-C carbon electrodes for the oxygen reduction reaction, Appl. Catal. B Environ. 291 (2021) 120068. https://doi.org/10.1016/j.apcatb.2021.120068.

[9] K. Kumar, L. Dubau, M. Mermoux, J. Li, A. Zitolo, J. Nelayah, F. Jaouen, F. Maillard, On the Influence of Oxygen on the Degradation of Fe-N-C Catalysts, Angew. Chemie. 132 (2020) 3261–3269. https://doi.org/10.1002/ange.201912451.

[10] M. Mazzucato, C. Durante, How Determinant is the Iron Precursor ligand in Fe-N-C Single-Site formation and activity for Oxygen Reduction Reaction?, Electrochim. Acta. 394 (2021) 139105. https://doi.org/10.1016/j.electacta.2021.139105.

[11] X. Shen, N. Sinclair, J. Wainright, R.F. Savinell, Methods—Analyzing Electrochemical Kinetic Parameters in Deep Eutectic Solvents Using an Extended Butler-Volmer Equation, J. Electrochem. Soc. 168 (2021) 056520. https://doi.org/10.1149/1945-7111/ac006a.

[12] K.J. Lee, C.T. Gruninger, K.M. Lodaya, S. Qadeer, B.E. Griffith, J.L. Dempsey, Analysis of multi-electron, multi-step homogeneous catalysis by rotating disc electrode voltammetry: Theory, application, and obstacles, Analyst. 145 (2020) 1258–1278. https://doi.org/10.1039/c9an02192b.

[13] C. Alemany, M. Aurousseau, F. Lapicque, P. Ozil, Cementation and corrosion at a RDE: Changes in flow and transfer phenomena induced by surface roughness, J. Appl. Electrochem. 32 (2002) 1269–1278. https://doi.org/10.1023/A:1021642327507.

[14] J.S. Prentice, H. Lee Craig, Rotating Disk Electrode Oxygen Sensor and Corrosion Rate Probe, IEEE J. Ocean. Eng. 4 (1979) 137–141. https://doi.org/10.1109/JOE.1979.1145435.

[15] A.A. Isse, A. Gennaro, Electrochemistry for Atom Transfer Radical Polymerization, Chem. Rec. 21 (2021) 2203–2222. https://doi.org/10.1002/tcr.202100028.

[16] F. Lorandi, M. Fantin, A.A. Isse, A. Gennaro, K. Matyjaszewski, New protocol to determine the equilibrium constant of atom transfer radical polymerization, Electrochim. Acta. 260

(2018) 648–655. https://doi.org/10.1016/j.electacta.2017.12.011.
[17] A. Goyal, G. Marcandalli, V.A. Mints, M.T.M. Koper, Competition between CO2Reduction and Hydrogen Evolution on a Gold Electrode under Well-Defined Mass Transport Conditions, J. Am. Chem. Soc. 142 (2020) 4154–4161. https://doi.org/10.1021/jacs.9b10061.
[18] K.H. Wu, Q. Zhang, Y. Lin, M.A. Ali, S. Zhao, S. Heumann, G. Centi, Real-Time Carbon Monoxide Detection using a Rotating Gold Ring Electrode: A Feasibility Study, ChemElectroChem. 7 (2020) 4417–4422. https://doi.org/10.1002/celc.202001263.
[19] M. Inaba, A.W. Jensen, G.W. Sievers, M. Escudero-Escribano, A. Zana, M. Arenz, Benchmarking high surface area electrocatalysts in a gas diffusion electrode: measurement of oxygen reduction activities under realistic conditions, Energy Environ. Sci. 11 (2018) 988–994. https://doi.org/10.1039/C8EE00019K.
[20] J. Schröder, V.A. Mints, A. Bornet, E. Berner, M. Fathi Tovini, J. Quinson, G.K.H. Wiberg, F. Bizzotto, H.A. El-Sayed, M. Arenz, The Gas Diffusion Electrode Setup as Straightforward Testing Device for Proton Exchange Membrane Water Electrolyzer Catalysts, JACS Au. 1 (2021) 247–251. https://doi.org/10.1021/jacsau.1c00015.
[21] S. Alinejad, J. Quinson, J. Schröder, J.J.K. Kirkensgaard, M. Arenz, Carbon-Supported Platinum Electrocatalysts Probed in a Gas Diffusion Setup with Alkaline Environment: How Particle Size and Mesoscopic Environment Influence the Degradation Mechanism, ACS Catal. 10 (2020) 13040–13049. https://doi.org/10.1021/acscatal.0c03184.
[22] M. De Jesus Gálvez-Vázquez, P. Moreno-García, H. Xu, Y. Hou, H. Hu, I.Z. Montiel, A. V. Rudnev, S. Alinejad, V. Grozovski, B.J. Wiley, M. Arenz, P. Broekmann, P. Moreno-García, Environment Matters: CO2RR Electrocatalyst Performance Testing in a Gas-Fed Zero-Gap Electrolyzer, ACS Catal. 10 (2020) 13096–13108. https://doi.org/10.1021/acscatal.0c03609.
[23] V. Perazzolo, G. Daniel, R. Brandiele, L. Picelli, G.A. Rizzi, A.A. Isse, C. Durante, PEO-b-PS Block Copolymer Templated Mesoporous Carbons: A Comparative Study of Nitrogen and Sulfur Doping in the Oxygen Reduction Reaction to Hydrogen Peroxide, Chem. - A Eur. J. 27 (2021) 1002–1014. https://doi.org/10.1002/chem.202003355.
[24] J. Li, S. Ghoshal, W. Liang, M.-T. Sougrati, F. Jaouen, B. Halevi, S. McKinney, G. McCool, C. Ma, X. Yuan, Z.-F. Ma, S. Mukerjee, Q. Jia, Structural and mechanistic basis for the high activity of Fe–N–C catalysts toward oxygen reduction, Energy Environ. Sci. 9 (2016) 2418–2432. https://doi.org/10.1039/C6EE01160H.
[25] A. Zitolo, V. Goellner, V. Armel, M.T. Sougrati, T. Mineva, L. Stievano, E. Fonda, F. Jaouen, Identification of catalytic sites for oxygen reduction in iron- and nitrogen-doped graphene materials, Nat. Mater. 14 (2015) 937–942. https://doi.org/10.1038/nmat4367.

9. Conclusion

In this work several aspects on the formation of active sites in Fe-N-C catalysts have been considered, focusing on the enhancement of FeN_x sites which are believed to be the main site for the reduction of oxygen to water. In addition, the use of GDE was exploited.

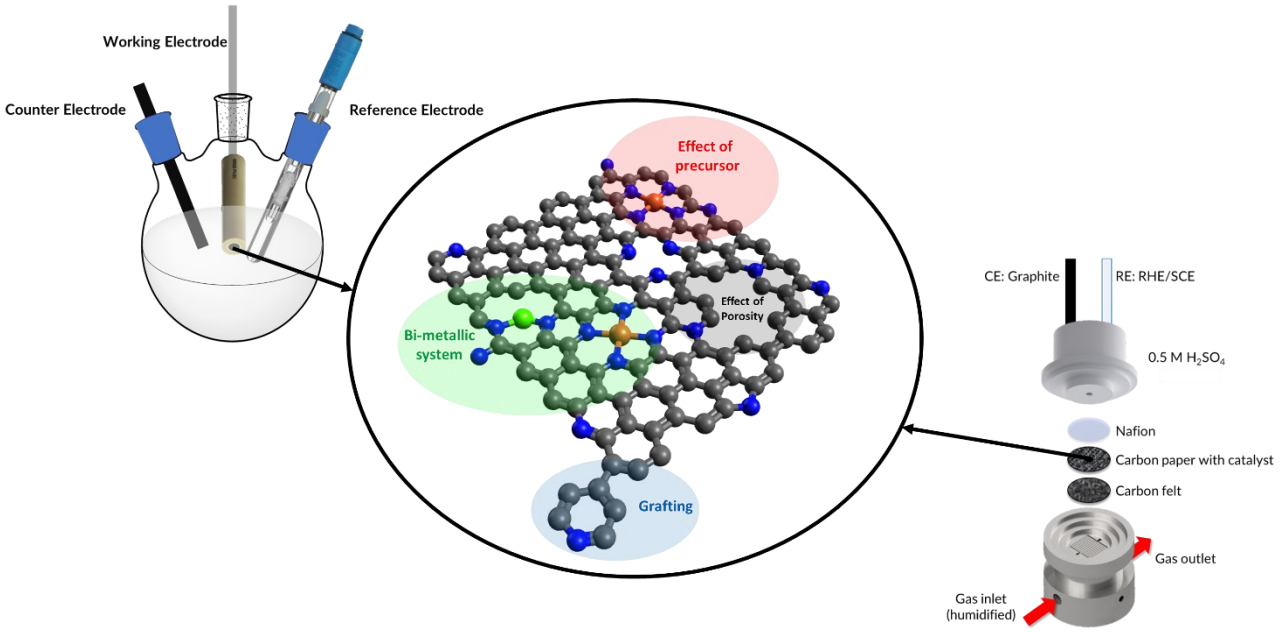

Firstly, the effect of the carbonaceous precursor was studied, in particular the effect of micropore and mesopore pre-existing on the carbon support on the site formation was investigated. CO_2 and Steam treatment were used to modulate the content of pore inside the material by changing the time and temperature of treatment. Interestingly the higher porosity, in particular of micropore, not only allow a better site formation, which was known, but also enhance the TOF, which means that other changes are happening on the surface that are able to also tune the intrinsic activity. CO_2 treatment leads to better activity, but with less control on final SD or TOF. In general, one order of magnitude of increment in activity was recorded (kinetic current) showing the importance of morphology of catalyst.

The research then moved to the optimization of iron-nitrogen precursor. In this case commercial Vulcan XC72 was used as support due to his availability and comparability with literature. Several Fe nitrogen-coordinating complexes were prepared with aromatic and non-aromatic ligand showing the importance of having and aromatic portion in order to favour the site formation, also interesting thing were observed, for example 2,2 bipyridine despite his similarity with 1,10-phenanthroline, lead to worst catalysts. The latter ligand was the best choice to achieve active catalysts. This study highlight that the decomposition of precursor leads to changes in morphology of catalyst, which is another parameter to consider.

Knowing the optimal precursor for our methodology of synthesis, we move to the addition of a secondary metal centre, namely Sn, to synthesize bimetallic catalysts. The effect of tin was marginal due to his low fixation induced by some competition in presence of Fe. Recent experiment shows that probably Sn is present as SnN_x but the fixation of that need optimization. In this contest GDE setup was used for the first time, up to our knowledge, to characterize M-N-C materials in activity and durability test, showing the validity of the method. This topic was fully investigated in late work

of this project showing the perfect interchangeability of RRDE and GDE to gain more information on M-N-C activity, durability, and selectivity.
As a spin-off of the main topic other active site were studied, namely the C-N ones. Grafting of pyridinic and pyrrolic structure on carbon surface were performed, showing increment of peroxide production that confirm their role, but some difficulty that ask for further work, make the study not straightforward.
In summary this work allows to evaluate a wide range of properties and aspect that influences the site formation and therefore the activity and selectivity of N-C, Fe-N-C and Sn/Fe-N-C catalysts for the ORR.
This project brings to the publication of 3 paper, 1 mini-review and a book chapter in the field of Oxygen reduction:

- **Mazzucato, M.**; Daniel, G.; Mehmood, A.; Kosmala, T.; Granozzi, G.; Kucernak, A.; Durante, C. Applied Catalysis B : Environmental Effects of the Induced Micro- and Meso-Porosity on the Single Site Density and Turn over Frequency of Fe-N-C Carbon Electrodes for the Oxygen Reduction Reaction. Appl. Catal. B Environ. 2021, 291, 120068. https://doi.org/10.1016/j.apcatb.2021.120068
- **Mazzucato, M.**; Durante, C. How Determinant is the Iron Precursor ligand in Fe-N-C Single-Site formation and activity for Oxygen Reduction Reaction? https://doi.org/10.1016/j.electacta.2021.139105
- **Mazzucato, M.**; Durante, C.; Insights on Oxygen Reduction Reaction to H_2O_2: The role of functional groups and textural properties on the activity and selectivity of doped carbon electrocatalysts Current Opinion in Electrochemistry 2022, 35:101051 https://doi.org/10.1016/j.coelec.2022.101051
- Durante, C.; **Mazzucato, M.**; Bellardita, M.; and Parrino, F. Book Chapter: Fundamental of photoelectrocatalysis, Photoelectrocatalysis: Fundamentals and Applications, Elsevier 2022
- **Mazzucato, M.**; Gavioli, G.; Balzano, V.; Rizzi, G.A.; Badocco, D.; Pastore, P.; Zitolo, A.; Durante, C. : Synergistic Effect of Sn and Fe in Fe-N_x site formation and activity in Fe-N-C Catalyst for ORR (submitted)

10. Appendix

10.1. Appendix chapter 2 – Theoretical background of electrochemistry measurement

10.1.1. Surface processes in heterogeneous electrocatalysis

In heterogeneous electrocatalysis, catalytic reactions take place thanks to the electronic properties of the catalysis sites present on the surface of the catalyst. A generic process characterized by an electronic transfer can be described by:

$$O_{ads} + ne^- \underset{k_a}{\overset{k_c}{\rightleftarrows}} R_{ads}$$

In the reversible process the cathodic component of the current is the one that describes the direction of the reduction reaction of the species O_{ads} to the species R_{ads}, with kinetic constant k_c, while the anodic component describes the inverse reaction with kinetic constant k_a.

In addition to the electrode process that occurs on the surface due to electron transfer, other phenomena due to displacement of species or chemical reactions in solution are encountered (Figure 10.1):

- Chemical reactions prior or successive to the electro transfer
- Adsorption/Desorption reaction of chemical species on the electrode
- Mass transfer processes: diffusion, migration, and convection.

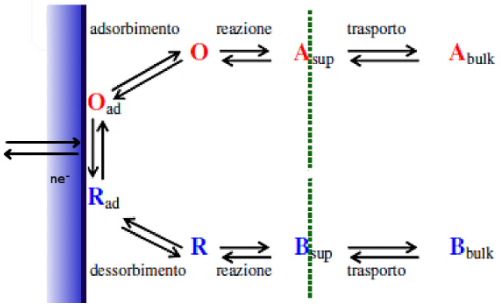

Figure 10.1: Diagram of the possible phenomena affecting the faradic current on the surface of an electrocatalyst.

In equilibrium conditions, the reaction described above has the same speed in both directions, while in non-equilibrium conditions, i.e., in the presence of a polarization of the electrode, there is a shift to the right or to the left. If the polarization is positive, the reduction is favoured, while if the polarization is negative, oxidation is favoured. The electrode potential is therefore different from the equilibrium one and this difference is called overpotential (η). The overpotential value necessary to make a given electrochemical process take place depends on the various phenomena described above, where the two main contributions are the electron transfer and that due to mass transport.

To experimentally determine η of an electrode, a potentiostat-galvanostat is used and it is useful to work with a three-electrode combination (Figure 10.2): the electrode under examination (working electrode or WE) whose overvoltage is to be determined, a counter electrode (CE) and a reference electrode (RE). Some analysis techniques, such as linear voltammetry on RRDE, require a second working electrode (WE2), in this case a bi-potentiostat is required to collect both signals.

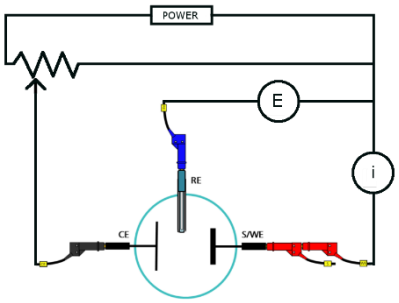

Figure 10.2 Electrical scheme in a 3-electrode configuration, the amperometric circuit is used to measure the current (*i*), while the potentiometric is used to measure the potential (*E*).

The system is characterized by two circuits: an amperometric one, in which WE and CE are connected where the current (*i*) is different from zero and recorded, and a potentiometric one, in which WE is connected to RE and the current is zero (negligible), here the measured quantity is the potential difference. This last electrode provides a constant equilibrium potential which is used as a reference. Second species electrodes are generally used as reference electrodes because they are characterized by redox processes that occur at well-defined and constant potentials, some examples are the calomel electrode (SCE), the Hg/HgO or the Ag/AgCl electrode. Other electrodes used as a reference are hydrogen ones such as RHE. The reference electrode cited were all used for electrochemical measurements in this project. The counter-electrode, on the other hand, is made up of an electronic conductor inert under the measurement conditions and has the function of closing the amperometric circuit that forms with the working electrode. In this thesis work a graphite counter-electrode was used, alternatively Pt can also be used. Finally, the working electrode is the one where electrochemical process to investigate takes place. These electrodes are characterized by a glassy carbon cylinder and an insulating outer coating of PEEK (Polyether Ether Ketone) or Teflon, both inert towards many organic and aqueous environments. In the case of RRDE electrodes there is also a platinum ring separated from the disc with a PEEK ring (Figure 10.3).

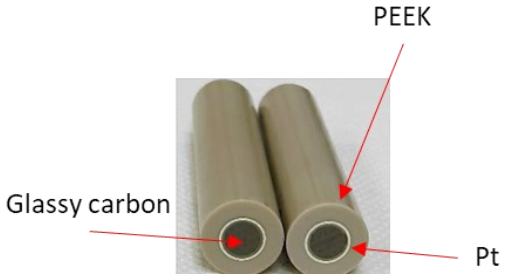

Figure 10.3 RRDE electrode used for ORR evaluation

As previously described, the overvoltage necessary to make the process take place is due to both the electronic transfer and mass transport processes, applying potentials very far from tends to favour the first process that bring to the condition in which the rate determining step is the mass transfer. The last contribution can be further divided into three contributions:

- Convention
- Diffusion
- Migration

Convection is the transport of mass due to density gradients and/or mechanical vibrations (natural convection) or due to forced agitation when using rotating electrodes, flow electrodes or flow cells. Generally, convection is controlled by thermostating the cell and/or by rotating the electrode.
The migration is instead due to the displacement of charges induced by an electric field, it is generally buffered with the addition of a support electrolyte that has the following characteristics:

to be a strong electrolyte in the solvent in use, to be electrochemically and chemically inert, to have an approximately unitary transport number (the transport number indicates the fraction of electric current carried by an ion with respect to the current carried by all the ions present in the electrolyte). Finally, diffusion is the phenomenon of movement of charges induced by a concentration gradient, in electrochemical systems gradients are generated as a result of reactions on the electrode surface. In the presence of a control of the other two components it is possible to work only in diffusive control. From a mathematical point of view, the flow of matter in the presence of the three contributions can be expressed through the Nernst-Planck equation (4.8), the first term is sufficient to described the case of rotating electrode, while time dependency of flux is needed in the case of stationary electrode.

$$J = -D\frac{dc}{dx} - \frac{zF}{RT}Dc\frac{d\emptyset}{dx} + cv \qquad (10.1)$$

• diffusion • migration • convection

10.1.2. Measurement with electrode in rotation (RDE)

Linear sweep voltammetry (LSV) is the technique in which the faradic current is recorded as a function of the electrode potential applied according to the relationship:

$$E = E_i - vt \quad con\ v = \frac{dE}{dt} \qquad (10.2)$$

When the electrode is in rotation (Figure 10.4a) with a certain angular velocity ω, a stationary region is created near the electrode surface, called Nernst diffusion layer (δ) (Figure 10.4b), where the species move by diffusion alone, the external zone is instead in agitation and guarantees a constant concentration of reactants (C*), provided that δ << cell size.

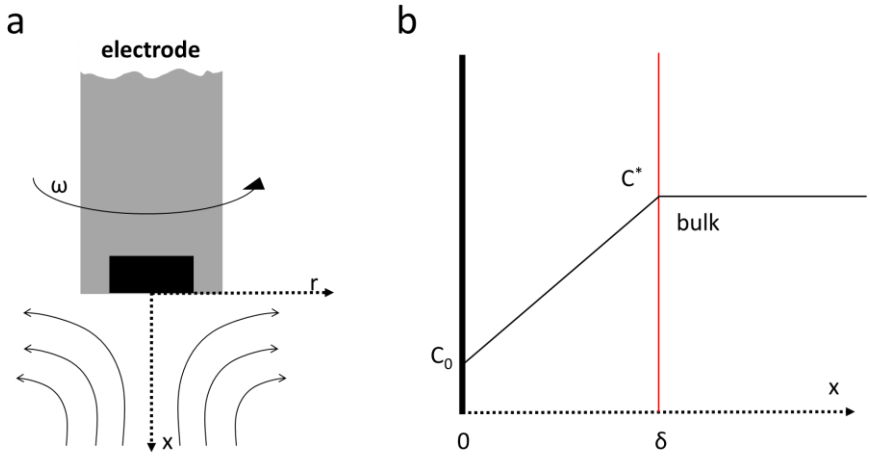

Figure 10.4 (a) electrode in rotation, solution flux is highlighted. (b) Concentration of O species profile as a function of the distance from the electrode surface, the linear section is the Nernst layer (δ)

The advantage of this setup it the dependency of Nernst layer with the sole rotation speed since the other are constant in a certain condition of electrolyte:

$$\delta = 1.61\ D_0^{1/3}\ v^{1/6}\ \omega^{-1/2} \qquad (10.3)$$

where D_O it's the diffusion coefficient of O species and v is the cinematic viscosity. Since the concentration is not time dependent, the fick equation could be solved giving the relationship of current with concentration and rotation of electrode

$$|j| = nF|J| = nFD_0 \frac{C_0^* - C_o(0)}{\delta} = nFD_0 \frac{C_0^* - C_o(0)}{1.61\, D_0^{1/3}\, v^{1/6}\, \omega^{-1/2}} \qquad (10.4)$$

The typical sigmoidal shape is obtained by increasing the overpotential namely reaching the condition in which the reaction rate is higher than the diffusion rate of the species towards the surface, the maximum gradient is obtained, and the expression is reduced to the Levich equation[1]:

$$|j_L| = 0.62nFD_0^{2/3}\, v^{-1/6}\, \omega^{1/2} C_0^* \qquad (10.5)$$

When this condition is reached, knowing certain kinetic parameter, allow a determination, for example of the number of transferred electron or the diffusion coefficient. In the event that the reaction kinetics is slower or comparable with the diffusive processes, there is no condition of cancellation of the concentration on the electrode surface and therefore the linear relationship between j and ω is lost. To take this effect into account, the Koutecky-Levich equation valid at a fixed potential (10.5) is used instead, this expression is generally used to calculate the number of electrons exchanged in the reaction known the other hydrodynamic parameters:

$$\frac{1}{j} = \frac{1}{j_K} + \frac{1}{j_L} = \frac{1}{j_K} + \frac{1}{0.62nFAD_0^{2/3}\, v^{-1/6}\, \omega^{1/2} C_0^*} \qquad (10.5)$$

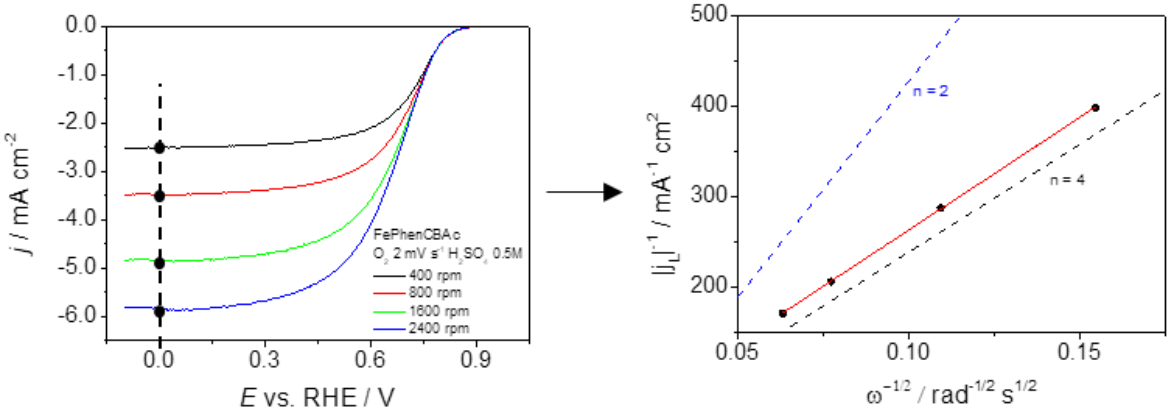

Figure 10.5 K-L analysis at 0V for a Fe-N-C catalyst

This expression also has limitations, in particular it is good to limit oneself to rotation speeds between 100 rpm and 10,000 rpm, the lower limit is imposed by the existence of the diffusion-convection layer, the upper one instead by the transition to the turbulent regime.
The shape of the current potential curve observable in Figure 10.5 can be derived from the Nernst equation (valid out of equilibrium if the electron transfer is fast), in the presence of only one species in solution (for example the O species) it is:

$$E = E^0 - \frac{2}{3}\frac{RT}{nF}\ln\left(\frac{D_O}{D_R}\right) + \frac{RT}{nF}\ln\left(\frac{j_L - j}{j}\right) = E_{1/2} + \frac{RT}{nF}\ln\left(\frac{j_L - j}{j}\right) \qquad (10.6)$$

[1] For a H_2SO_4 0.5 M at 25°C the value are: D_{O2} = 1.8 · 10^{-5} cm^2 s^{-1}, C_{O2}* = 1.1 · 10^{-6} mol cm^{-1}, v = 1.0 · 10^{-2} cm^2 s^{-1}.

where $E_{1/2}$ is an important parameter to determine since is linked to standard potential, and it is therefore linked to goodness of a catalysts (see later for more detail)
Of greater interest for the purpose of this project is the measurement with the RRDE electrode, in the presence of reactions that can give by-products it is useful to have a second electrode that allows to estimate the quantity produced. An example involving the ORR is the detection of the H_2O_2 formed in the disc which in part reaches the ring where it can be oxidized again to oxygen if an adequate potential is imposed. Depending on the construction parameters of the RRDE electrode only part of the peroxide reaches the ring and can actually react again, thus a quantity is defined that depends only on the geometry (Figure 10.6) of the tip: the collection efficiency N. measurement of the current that passes through the disk and the ring allow to obtain information on the number of exchanged electrons and on the quantity of hydrogen peroxide produced, it is therefore an alternative analysis to that of K-L (10.5).

$$n = \frac{4I_d}{NI_d + I_a} \quad \%H_2O_2 = 100\frac{4-n}{2} \tag{10.7}$$

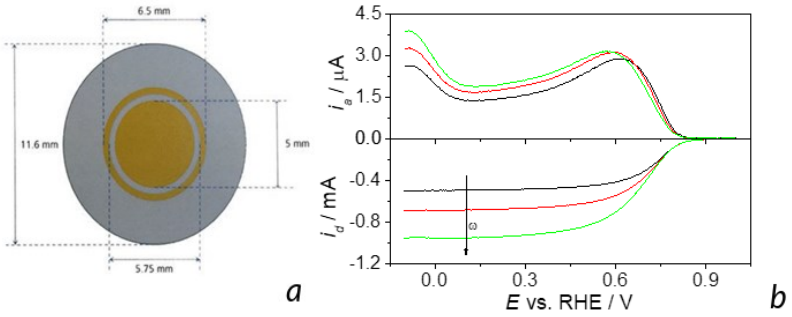

Figure 10.6 (a) RRDE geometry and (b) current measurement in O_2 of disk and ring

Operationally, an RRDE measurement is analogous to an RDE, with the foresight of having to use a bi-potentiostat for the independent control of the two potentials, what is observed are two different current-potential curves relating to one to the disk, in which the current read is a function of a potential made to vary over time, and the other to the ring whose applied potential is fixed and is expressed as a function of the disk potential (Figure 10.6b).

10.1.3. Measurement with stationary electrode

In the case of measurements with a stationary electrode, stationary conditions of concentration profile are not reached, the current will depend on time and the concentration profile evolves as shown in Figure 10.7:

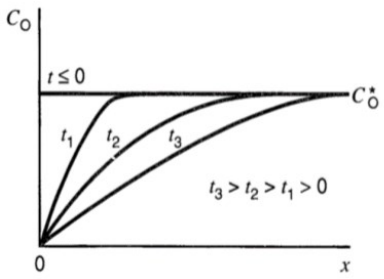

Figure 10.7. Temporal evolution of concentration in the case of stationary polarized electrode.

The two techniques used in this project are chronoamperometry (CA) and cyclic voltammetry (CV)

Chronoamperometry

It is a technique in which a potential far from the equilibrium is applied (thus imposing a very fast electronic transfer) and the evolution of the current over time is studied. The obtained profile could be expressed with the Cottrel equation. It is mainly used for the calculation of diffusion coefficients, during the thesis it was only to evolve hydrogen within the reference electrode and to long term analysis of oxygen reduction (accelerated stress test). The current profiles and the current expression are shown below (Figure 10.8), to note the dependence on the square root of time typical of diffusive phenomena.

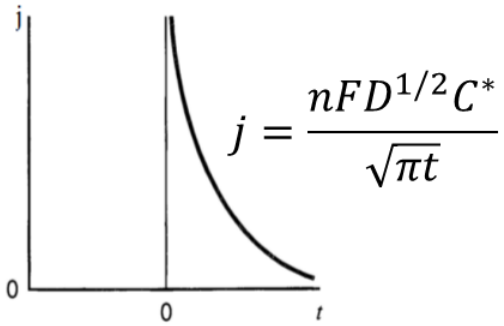

Figure 10.8. Relation and mathematical relation for the current profile density in a chronoamperometry

Cyclic voltammetry

In cyclic voltammetry, the potential is varied linearly from the initial value E_i to the final value E_f. The potentials E_i and E_f in this technique coincide. In detail, the linear scan starts from E_i and goes in the initial direction chosen, but at the value E_λ (at time t = λ) the direction is reversed until it returns to the initial value, as shown in Figure 10.9:

$$0 < t < \lambda \rightarrow E(t) = E_i - vt$$
$$t > \lambda \rightarrow E(t) = E_i - 2v\lambda + vt$$

Considering a reversible redox pair (O ⇄ R), during the scanning of the potential the system responds immediately by changing the concentrations. By applying the described potential program to a working electrode immersed in a solution containing only O, the voltammetric response shown in Figure 10.9 is obtained. The shape of the curve can be rationalized as follows: initially no process takes place and only capacitive current is measured, then the reduction process begins to occur, and a faradic current is also observed. The variation of the potential makes the reaction faster and faster until it enters the diffusive regime, and the current follows the Cottrel equation (it does not depend on the applied potential), the transition between the two regimes is highlighted by a peak (Ep, ip).

By inverting the potential at E_λ, the opposite process can occur if the reaction is reversible or quasi-reversible. The peak potential value is independent of the scan rate for a reversible process; however, the peak current varies with the square root of the scan rate, concentration and diffusion coefficient as shown by the Randles-Sevcik equation (10.8):

$$i_p^{rev} = 0.4436nFAC^*D^{1/2}\left(\frac{nF}{RT}\right)^{1/2}v^{1/2} \qquad (10.8)$$

The expression is valid for diffusive processes, while the dependence is linear on the velocity if the species are adsorbed on the surface.

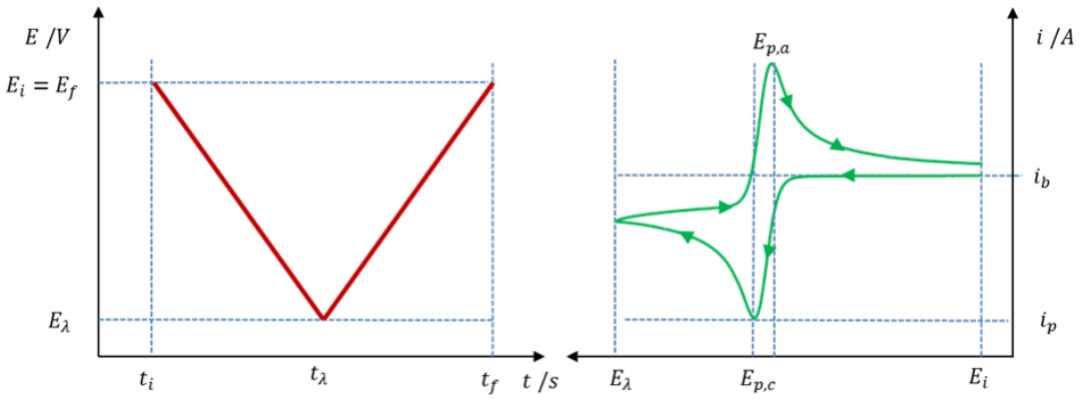

Figure 10.9. Voltammetric profile in green and in red the variation of the potential over time

In the case of irreversible processes, such as for the oxygen reduction reaction, only one of the two peaks is generally visible and the peak current has a different expression (10.9), in this case also the peak potential (10.10) has a dependence on scanning speed:

$$i_p^{irr} = 0.4958nFAC^*D^{1/2}\left(\frac{\alpha F}{RT}\right)^{1/2} v^{1/2} \qquad (10.9)$$

$$E_p = E^0 - \frac{RT}{\alpha F}[0.780 + \ln\left(\frac{D^{1/2}}{k^0}\right) + \frac{1}{2}\ln\left(\frac{\alpha F}{RT}v\right) \qquad (10.10)$$

10.2. Appendix chapter 4

10.2.1. Supporting Figures

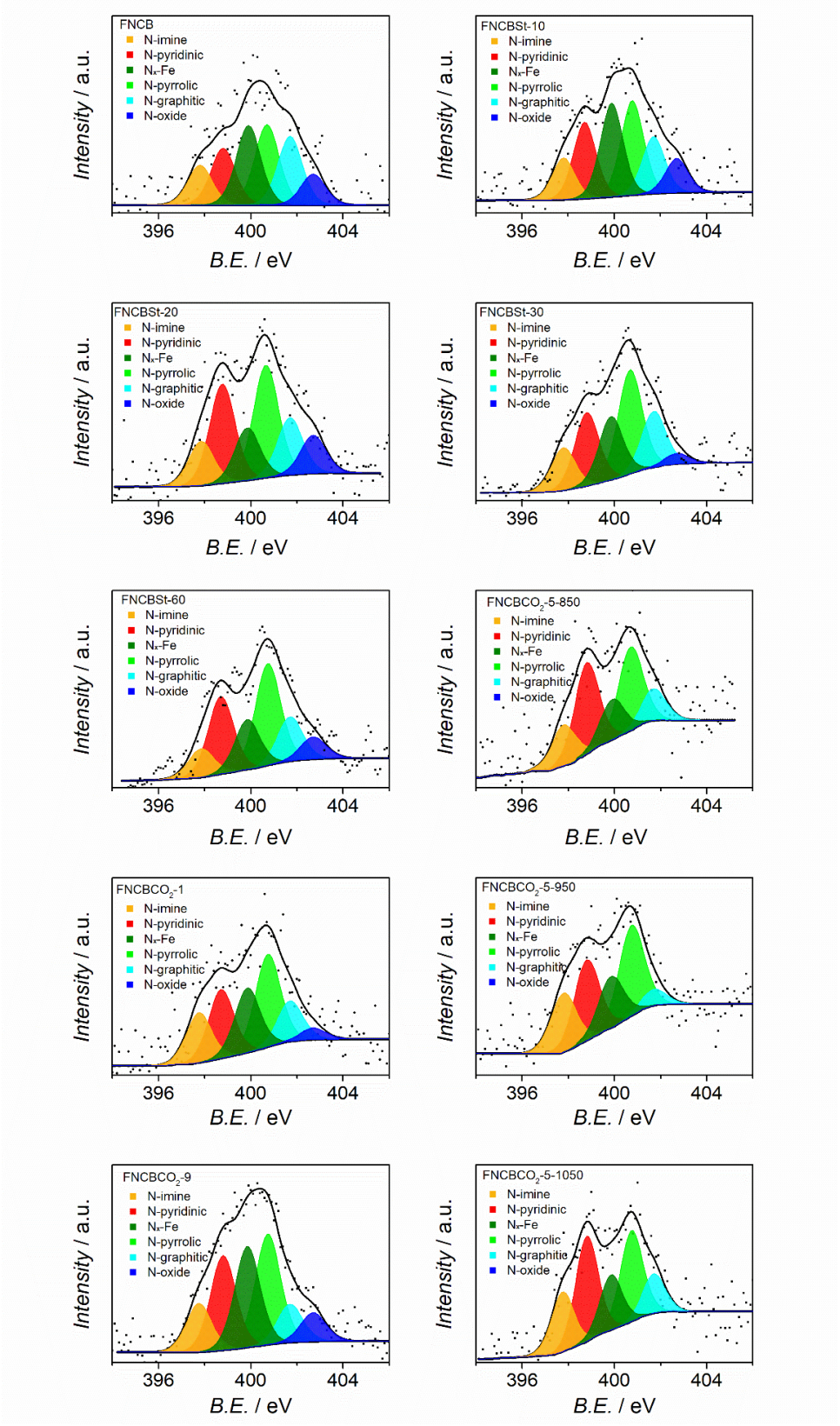

Figure 10.10. High-resolution core-level XPS spectra of N 1s regions and deconvolution into single chemical components for all the investigated F-N-C catalysts.

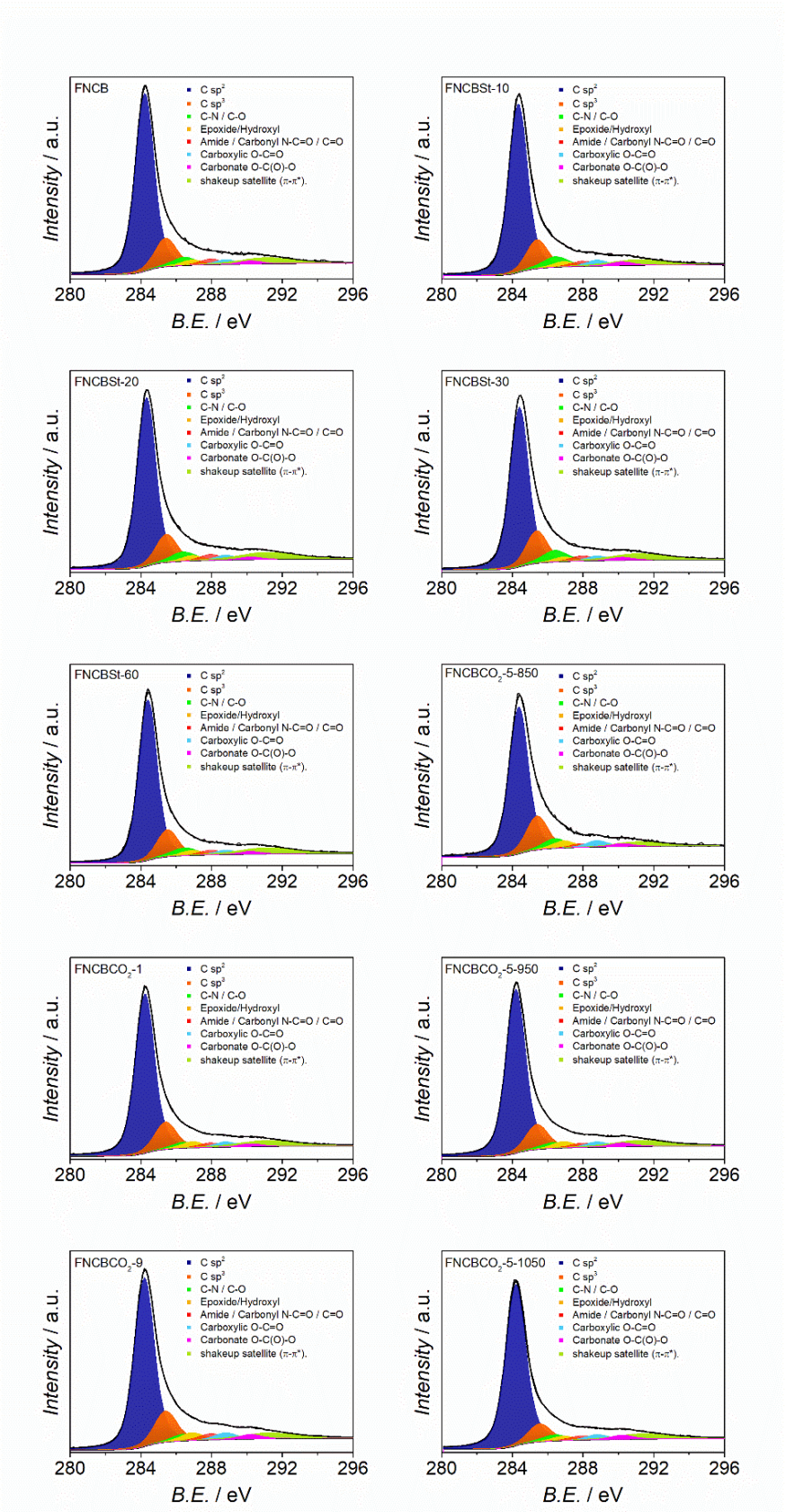

Figure 10.11. High-resolution core-level XPS spectra of C 1s regions and deconvolution into single chemical components for all the investigated F-N-C catalysts.

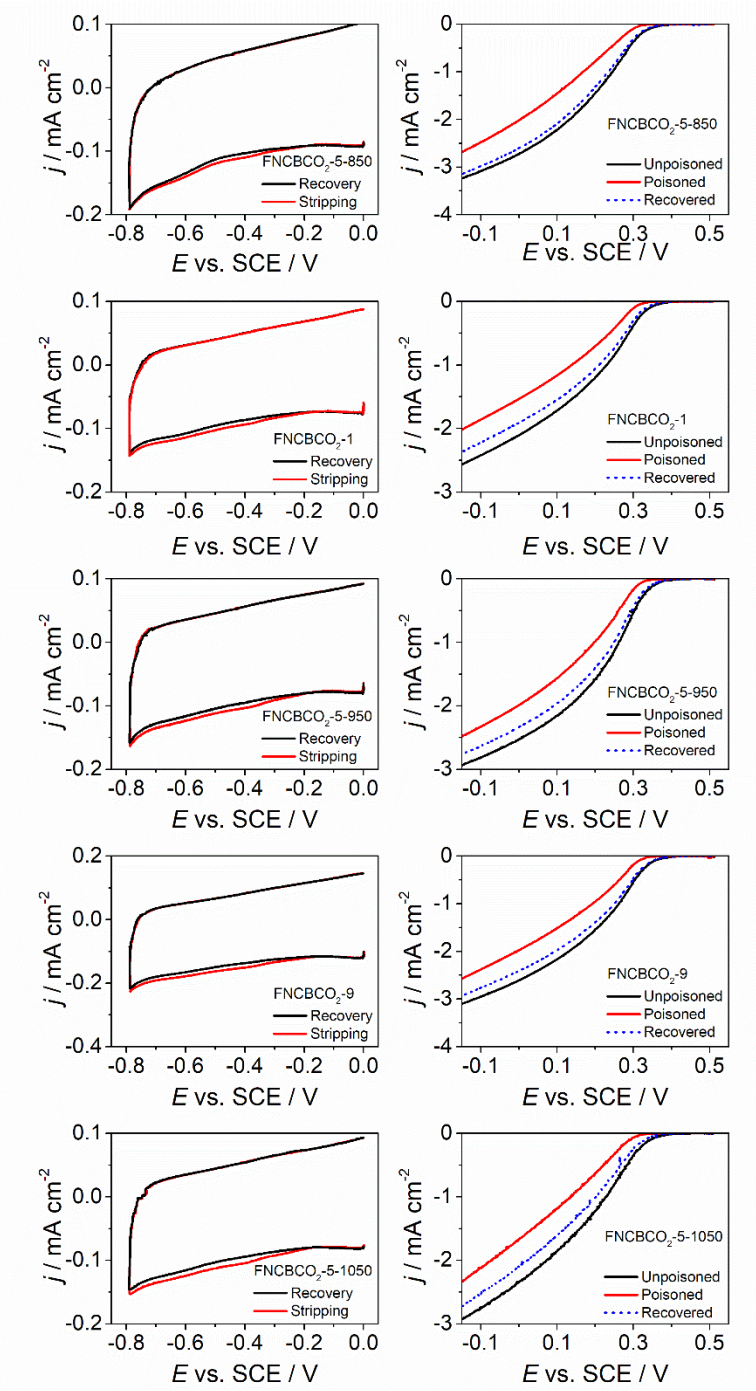

Figure 10.12. On the left nitrite stripping and recovered CVs of $FNCBCO_2$-5-Y and $FNCBCO_2$-X recorded in Ar-saturated electrolyte at 10 mV s^{-1}, on the left LSV recorded before, during and after poisoning at 1600 rpm and 5 mV s^{-1} in O_2-saturated electrolyte.

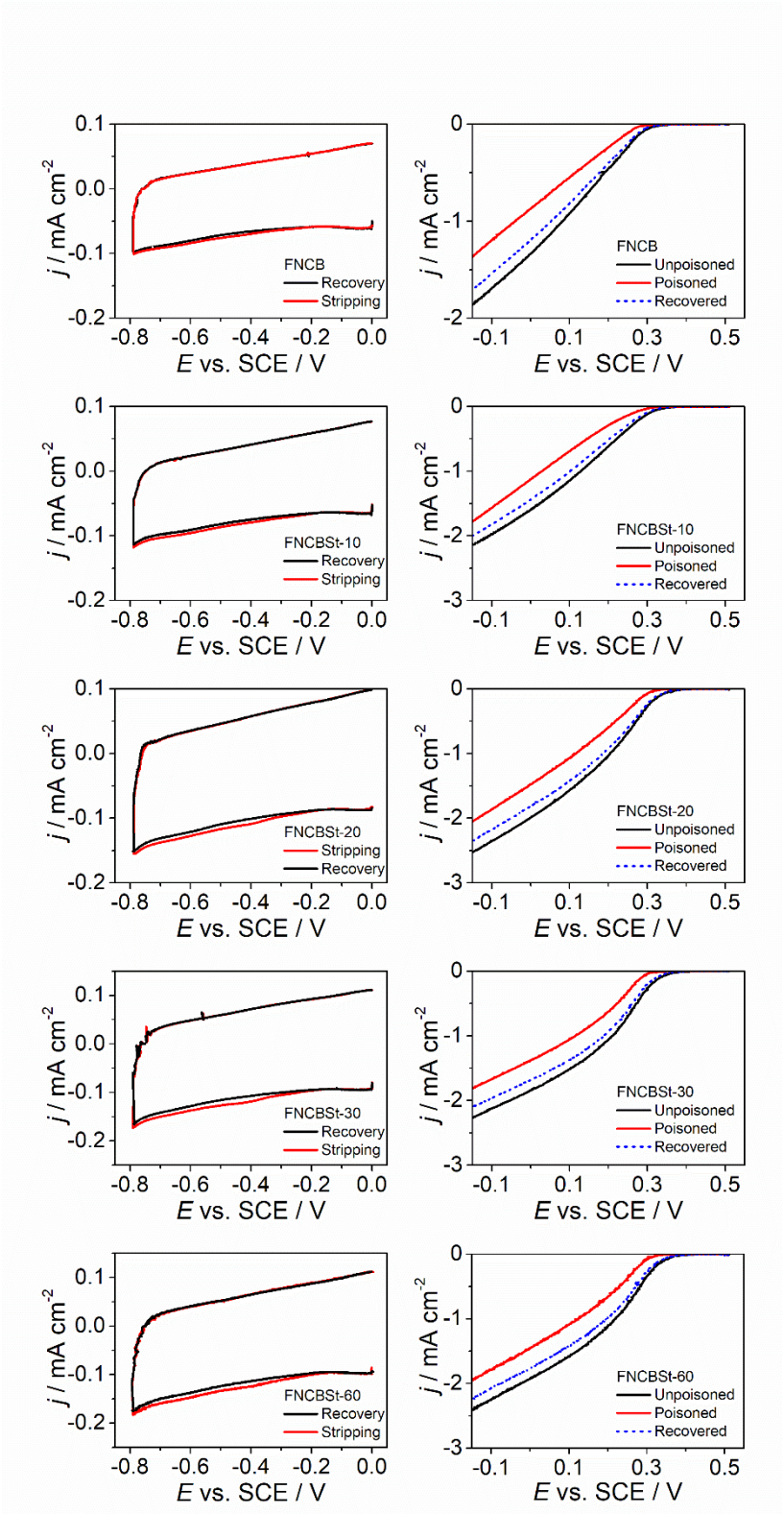

Figure 10.13. On the left nitrite stripping and recovered CVs of FNCBSt-X recorded in Ar-saturated electrolyte at 10 mV s-1, on the left LSV recorded before, during and after poisoning at 1600 rpm and 5 mV s-1 in O2-saturated electrolyte.

10.2.2. Supporting Tables

Table 10.1. First-order Raman bands and vibration modes

Band	Raman shift (cm^{-1})			Vibrational mode
	Soot	Disordered graphite	Highly oriented graphite	
G	~1580 cm^{-1}	~1580 cm^{-1}	~1580 cm^{-1}	Ideal graphite lattice (E_{2g})
D1	~1350 cm^{-1}	~1350 cm^{-1}	-	Disordered lattice (A_{1g}) : edge
D2	~1620 cm^{-1}	~1620 cm^{-1}	-	Disordered lattice (E_{2g}) : surface
D3	~1500 cm^{-1}	-	-	Amorphous carbon
D4	~1200 cm^{-1}	-	-	Disordered lattice (A_{1g}) : Polyene and ionic impurities

Table 10.2. Raman parameter derived from deconvolution of spectra

	D1 **cm^{-1}**	**I_{D1}** **a.u.**	***G*** **cm^{-1}**	**I_G** **a.u.**	**I_{D1} / I_G** **-**	***R2*** **-**
CB	1345	0.922	1588	0.732	1.3	0.58
CBSt-10	1343	0.906	1589	0.682	1.3	0.57
CBSt-20	1344	0.909	1590	0.689	1.3	0.55
CBSt-30	1342	0.909	1592	0.659	1.4	0.56
CBSt-60	1339	0.903	1591	0.639	1.4	0.54
$CBCO_2$-1	1345	0.911	1587	0.758	1.2	0.56
$CBCO_2$-5	1350	0.648	1593	0.663	1.0	0.52
$CBCO_2$-9	1347	0.677	1599	0.650	1.1	0.52
$CBCO_2$-5-850	1344	0.904	1587	0.692	1.3	0.60
$CBCO_2$-5-950	1350	0.648	1593	0.663	1.0	0.52
$CBCO_2$-5-1050	1342	0.952	1592	0.724	1.3	0.57

Table 10.3. Elemental analysis of samples at different iron initial loading

	C **wt.%**	**N** **wt.%**	**H** **wt.%**	**S** **wt.%**
$CBCO_2$-5	98.23	-	0.24	-
$FCBCO_2$-5-1%	91.24	0.20	0.32	0.15
$FCBCO_2$-5-2%	95.75	0.90	0.25	-
$FCBCO_2$-5-4%	87.31	0.66	0.56	-

Table 10.4. C1s peak deconvolution percentage with BE

	C sp^2	C sp^3	C-N/ C-O	Epoxide/ Hydroxyl	Amide / Carbonyl N-C=O / C=O	Carboxylic O-C=O	Carbonate O-C(O)-O
	284.3 eV	285.4 eV	286.4 eV	286.9 eV	288.0 eV	288.9 eV	290.2 eV
FNCB	72.3	13.6	4.9	2.5	2.7	2.4	1.6
FNCBSt-10	69.8	14.0	6.3	2.6	2.6	2.8	1.9
FNCBSt-20	71.0	14.0	5.4	2.8	2.9	2.5	1.4
FNCBSt-30	67.7	16.3	6.9	2.3	2.7	2.5	1.6
FNCBSt-60	71.4	14.2	5.3	2.7	2.5	2.4	1.5
FNCBCO$_2$-1	71.8	14.4	3.6	3.4	2.4	2.8	1.6
FNCBCO$_2$-5	72.7	13.0	3.8	3.3	2.3	2.9	2.0
FNCBCO$_2$-9	69.2	15.0	3.5	3.8	3.0	3.3	2.2
FNCBCO$_2$-5-850	66.0	17.9	5.4	3.7	2.0	3.4	1.6
FNCBCO$_2$-5-950	72.7	13.0	3.8	3.3	2.3	2.9	2.0
FNCBCO$_2$-5-1050	76.0	10.0	3.8	2.4	2.5	3.0	2.3

Table 10.5. Electrochemical data determined by RRDE measurements in 0.5 M H_2SO_4 and NO stripping in 0.5 M acetate buffer at pH 5.2.

	$E_{1/2}$ [a,b] V	j_K [b,c] A g^{-1}	$j_{0.8V}$ [b,c] mA cm^{-2}	H_2O_2 [d] %	Fe_{eff}
FNCBSt-0	0.60±0.01	0.16±0.05	0.11±0.01	3.9	2.65
FNCBSt-10	0.629±0.003	0.25±0.03	0.16±0.03	4.6	3.40
FNCBSt-20	0.640±0.006	0.44±0.04	0.26±0.04	3.0	4.36
FNCBSt-30	0.646±0.008	0.51±0.03	0.38±0.11	3.0	5.66
FNCBSt-60	0.654±0.009	0.50±0.04	0.34±0.07	4.8	11.01
FNCBCO$_2$-1	0.63±0.02	0.21±0.04	0.13±0.02	2.3	5.36
FNCBCO$_2$-5	0.67±0.02	0.39±0.06	0.23±0.05	0.7	8.08
FNCBCO$_2$-9	0.63±0.02	0.38±0.06	0.24±0.04	3.3	6.16
FNCBCO$_2$-5-850	0.66±0.01	0.37±0.01	0.1±0.05	3.6	1.78
FNCBCO$_2$-5-950	0.67±0.02	0.43±0.02	0.23±0.05	0.7	8.08
FNCBCO$_2$-5-1050	0.63±0.02	0.25±0.06	0.20±0.05	5.0	14.72
	Q_{STRIP} C g^{-1}	Δj_k [e] A g^{-1}	**SD** sites g^{-1}	**MSD** mol sites g^{-1}	**TOF** (0.8V) e^- $sites^{-1}$ s^{-1}
FNCBSt-0	0.94	0.14	1.17E+18	1.94E-06	0.76
FNCBSt-10	1.21	0.33	1.51E+18	2.51E-06	1.37
FNCBSt-20	1.72	0.78	2.14E+18	3.56E-06	2.27
FNCBSt-30	2.45	1.03	3.06E+18	5.08E-06	2.09
FNCBSt-60	2.61	1.30	3.26E+18	5.41E-06	2.48
FNCBCO$_2$-1	1.68	1.00	2.10E+18	3.48E-06	2.98
FNCBCO$_2$-5	1.91	1.49	2.38E+18	3.96E-06	3.90
FNCBCO$_2$-9	3.35	1.37	4.18E+18	6.95E-06	2.04
FNCBCO$_2$-5-850	1.31	1.00	1.63E+18	2.71E-06	3.84
FNCBCO$_2$-5-950	1.91	1.49	2.38E+18	3.96E-06	3.90
FNCBCO$_2$-5-1050	2.32	1.33	2.89E+18	4.80E-06	2.88

Table 10.6. Corrected data for stripping of Steam set

	Q_{STRIP} C g^{-1}	Δj_k A g^{-1}	SD sites g^{-1}	$TOF_{0.8V}$ e^- sites^{-1} s^{-1}	$Q_{STRIP,corr}$ C g^{-1}	SD_{corr} sites g^{-1}	TOF_{corr} e^- sites^{-1} s^{-1}
FNCB	0.94	0.14	1.17E+18	0.76	0.27	3.39E+17	2.57
FNCBSt-10	1.21	0.33	1.51E+18	1.37	0.54	6.75E+17	3.04
FNCBSt-20	1.72	0.78	2.14E+18	2.27	1.05	1.31E+18	3.70
FNCBSt-30	2.45	1.03	3.06E+18	2.09	1.78	2.22E+18	2.89
FNCBSt-60	2.61	1.30	3.26E+18	2.48	1.94	2.42E+18	3.35

10.2.3. Supporting Text

Chemicals

Iron(II) chloride (> 98%), Nafion (5 wt.% in a mixture of lower aliphatic alcohols and water), diethyl ether (>99.8%), Ethanol (HPLC grade >99.8%), THF (HPLC grade > 99.9%), Acetone (HPLC grade > 99.9%), Acetic Acid (> 99.8) were purchased from Sigma-Aldrich and used as received. Sodium acetate trihydrate and sodium nitrite were from Carlo Erba reagents and used without any purification. Carbon Black (Carbon black, Super P® Conductive, 99+%) and 1,10-phenanthroline were purchased from Alfa-Aesar. Highly pure H_2SO_4 (Fluka, 93-98%, TraceSELECT) was employed for electrochemical characterization.

Samples preparation for Raman analysis

To perform Raman measurements, samples were dispersed in milli-Q water and sonicated for 15-20 min. in order to efficiently disperse the powder; the dispersed solutions were then drop-casted onto a microscope slide previously heated. In table 10.1 the Raman shift for the first order region of carbonaceous materials.

Samples preparation for Physisorption analysis

To perform adsorption/desorption measurements each support was ball-milled and that placed in a glass tube. The amount of sample was chosen according to ideal range of surface area determination that is 40-120 m^2 for the instrument used (ASAP 2020 Plus). Each sample was then degassed at 300 °C for 20h and then the measurement was carried out.

Samples preparation for XPS analysis

To perform XPS measurements, samples were dispersed in milli-Q water and sonicated for 15-20 min. in order to efficiently disperse the powder; the dispersed solutions were then drop-casted onto electropolished polycrystalline copper (with a surface area of 1 cm^2). The samples were the dried on a hot plate. In figure 10.10 all the deconvolution of N1s peak are reported.

10.3. Appendix chapter 5

10.3.1. Direct pyrolysis of FePHEN3

As reference to highlight the importance of carbon black, we also prepared a catalyst made by the direct pyrolysis of $Fe(phen)_3Cl_2$, named $FePHEN_3py$. The idea was to show that the sole iron complex is not sufficient to both create a carbon matrix and Fe-N_x sites. The procedure was the same adopted for all the catalysts where the carbon black was omitted. In Table 10.7 and Figure 10.15 the results are shown, clearly the absence of carbon black is widely impacting the final activity, the low peroxide production is probably a consequence of low active sites density or a predominance of iron containing NP on the surface or under carbon shell.

10.3.2. *Hg/HgO electrode calibration*

The calibration of Hg/HgO reference electrode was performed in a standard three-electrode system with polished Pt wires as working and counter electrodes, and the Hg/HgO electrode as the reference electrode, the calibration curve is reported in Figure 10.14.

10.3.3. *Synthesis of Fe complexes*

FePHEN$_3$ / FeBPY$_3$ – Fe(phen)$_3$Cl$_2$ / Fe(bpy)$_3$Cl$_2$

Anhydrous $Fe^{II}Cl_2$ and 1,10-Phenanthroline (or 2,2'-Bipyridyl) were dispersed in the minimum useful volume of ethanol sufficient to dissolve the reagents, with a 1:3 molar ratio. The mixture was kept under stirring for 1h and then the complex was precipitated using diethyl ether and finally washed with diethyl ether again to give a yield of about 70% [45].

FePHEN$_2$ – Fe(phen)$_2$(SCN)$_2$

3×10^{-3} mole of $Fe^{II}SO_4(NH_4)_2SO_4\cdot6H_2O$ and 6×10^{-3} mole of 1,10-Phenanthroline were dissolved in 100 mL of distilled water. 1 mL of 6 M H_2SO_4 was added to the resulting solution along with an excess (about 5 eq.) of KSCN previously dissolved in 10 mL water. Upon the addition of KSCN a dark violet compound immediately forms and precipitate leaving a red solution. The mixture was aged 1 day under stirring and washed with isopropanol and dried in vacuo over P_2O_5 [46]. Contrary to cited reference we adopted isopropanol instead of ethanol and water for improving the complex yield since both ethanol and water easily dissolve the complex, which is then lost in the mother liquor, even during night tend to re-precipitate. Also the final colour of the complex seems to vary from purple to red as suggest also by Savage et al [47].

FePHEN$_1$ / FeBPY$_1$ – Fe(phen)Cl$_3$ H$_2$O / Fe(bpy)Cl$_3$ H$_2$O

A solution of anhydrous $Fe^{III}Cl_3$ (about 0.8 mmol) are dissolved in 10 mL of 10 M HCl in a 150 mL reaction flask. 10 mL of a solution made with 1 equivalent of 1,10-Phenanthroline (or 2,2'-Bipyridyl) and 10 M HCl was added to the resulting mixture. The ligand solution was added dropwise, upon which an orange colour was observed. The solution was stirred overnight at room temperature, and a yellow/orange precipitate formed. The solid was filtered and then recrystallized from ethanol [43]. The solid, yellow after filtration, became orange in EtOH where is slightly soluble, the recrystallization bring to a yield lower than 50%. The elemental composition for $FePHEN_1$ (and $FeBPY_1$), are in good agreement with the structure $Fe^{III}(phen)Cl_3$ (42 % C, 2.3 % H and 8.2 % N) and $Fe^{III}(bpy)Cl_3$ (36.8 % C, 2.7 % H and 8.4 % N) which could suggest that this complex formed instead of $[FeCl_4^-][H^+phen]\cdot2H_2O$ and $[FeCl_4^-][H^+bpy]\cdot2H_2O$ (also a colour change was observed) in disagreement to the synthesis procedure reported above, anyhow the synthesis of this complex

was described by Eckenhoff [44] in methanol, and other papers reports that these complexes exist with a solvent molecule (e.g. water or DMF [48–50]). On the base of these consideration, we retain that the complex $Fe^{III}(phen)Cl_3$ and $Fe^{III}(bpy)Cl_3$ formed coordinating a molecule of water or ethanol for which the elemental analysis is still fitting.

FeTPMA – [Fe(TPMA)Cl_2][$FeCl_4$] and FeBPMA – Fe(BPMA)Cl_3

$Fe^{III}Cl_3 \cdot 6H_2O$ (0.370 mmol) and 0.5 (for TPMA) or 1 (for BPMA) equivalent of complexing ligand were dissolved in 5.0 mL of methanol. After 15 min of stirring at ambient temperature, diethyl ether (for FeTPMA) was added to precipitate the complex, which was filtered and dried under vacuum [44]. Conversely to what reported in literature, diethyl ether was not needed for FeBPMA which is evidently insoluble in MeOH.

FeIM – [$FeCl_2$(im)$_4$]Cl

Anhydrous $Fe^{III}Cl_3$ (0.5 mmol) was added to a flask containing 8 mL acetonitrile and the solution was heated to 50 °C. After the $FeCl_3$ was dissolved, imidazole (3 eq.) in 40 mL acetonitrile was added dropwise to the mixture, which was then stirred for 1 h at 50 °C. Orange/red crystals precipitated after cooling during night at −18 °C. The resulting [$FeCl_2(im)_4$]Cl was isolated on a filter, washed with acetonitrile, and dried in vacuo at 40 °C [51]. The under stoichiometric amount of imidazole used we think is to avoid formation of higher coordinated complexes.

10.3.4. Supporting Figures

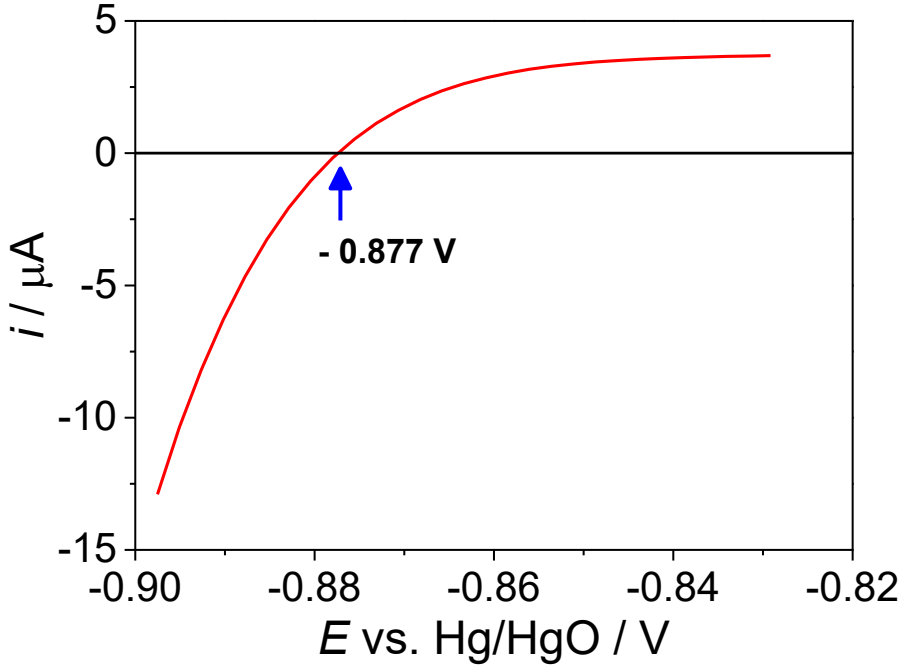

Figure 10.14. Calibration curve of Hg/HgO reference LSV at 0.5 mV s^{-1}

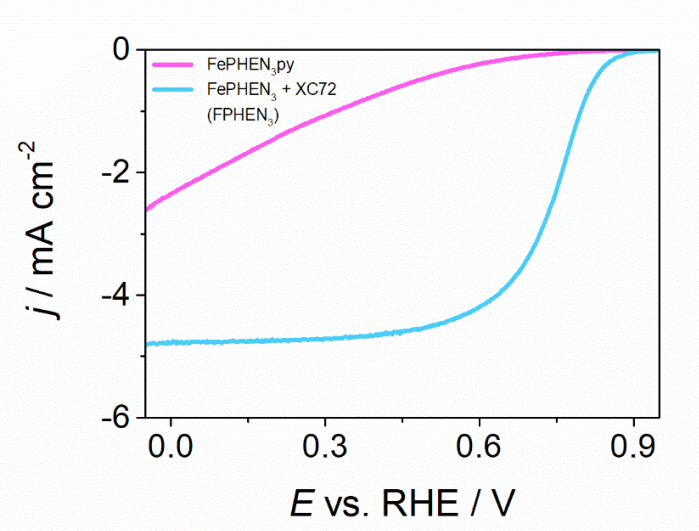

Figure 10.15. LSV 2mV s^{-1}, 1600 rpm, 0.5 M H_2SO_4 for the two samples.

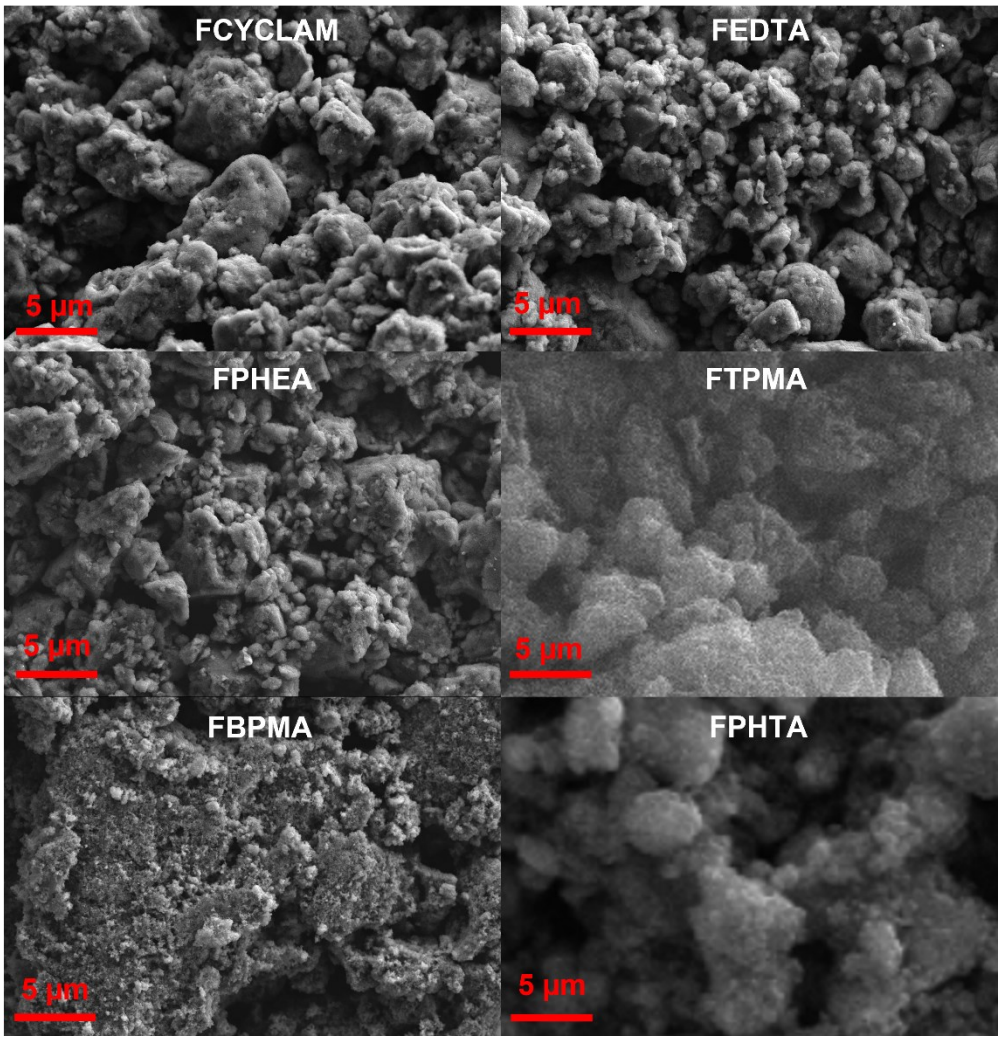

Figure 10.16. SEM images of the 6 sample not shown in the main text

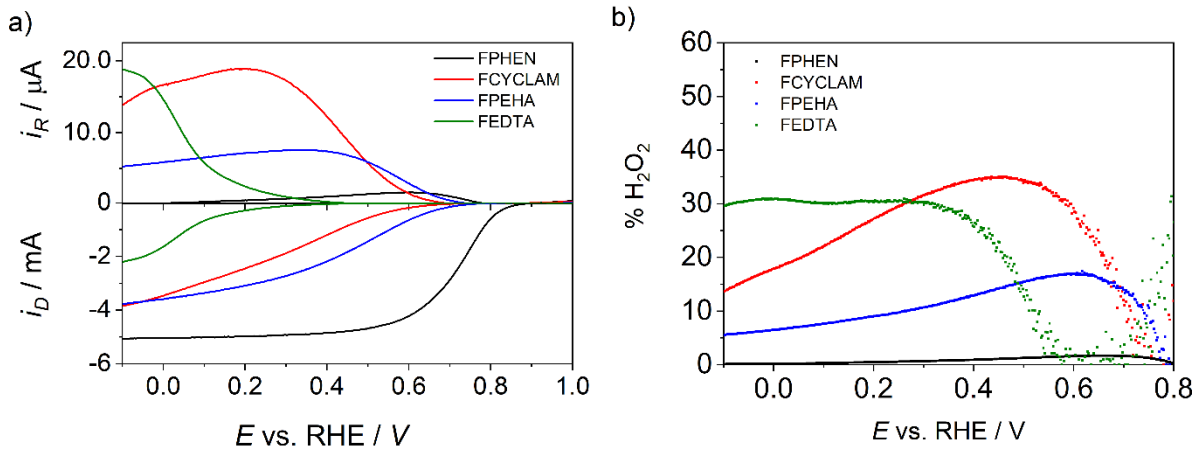

Figure 10.17. Electrochemical data of Fe-N-C catalysts prepared from Fe complex bearing non-aromatic nitrogen ligands (EDTA, CYCLAM, PEHA) in O_2 saturated 0.5 M H_2SO_4 a) LSV at 1600 rpm, 2 mV s^{-1}, b) H_2O_2 yield.

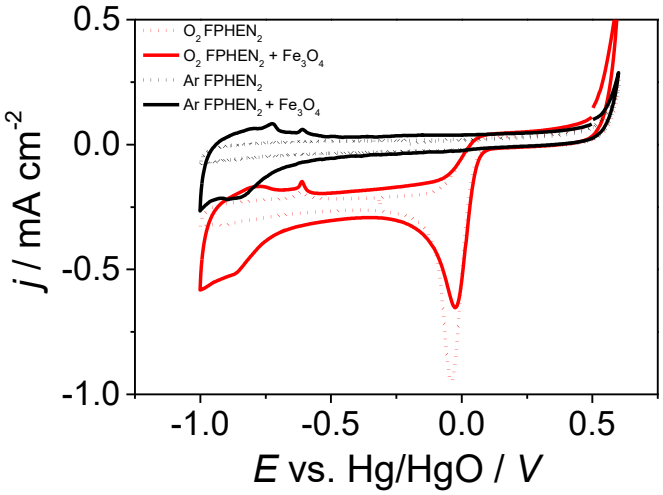

Figure 10.18. CV in Ar purged and O_2 saturated 0.1 M KOH in the absence and in the presence of Fe_3O_4 mixed with a Fe-N-C catalysts and loaded on the GC support. The peaks that appears in O_2 saturated electrolyte were already present in Ar-saturated solution. We do not claim the presence of magnetite inside our catalysts, but the formation of some oxide or hydroxide in oxygen saturated alkaline solution is plausible.

10.3.5. Supporting tables

Table 10.7. Composition and elemental analysis of complexes

								Calculated				Founded			
	Name	Formula	C	N	H	S	MM	C	N	H	S	C	N	H	S
	-	-	#	#	#	#	g mol^{-1}	%	%	%	%	%	%	%	%
1	**FePHEN$_3$**	$Fe(C_{12}H_8N_2)_3Cl_3 \cdot 7H_2O$[a]	36	6	31	0	**792.8**	54.5	10.6	4.8	-	53.9	10.3	4.2	-
2	**FePHEN$_2$**	$Fe(C_{12}H_8N_2)_2(SCN)_2$	26	6	16	2	**531.9**	58.7	15.8	3.0	12.0	56.6	15.3	3.1	12.6
3	**FePHEN$_1$**	$FeCl_3(C_{12}H_9N_2)H_2O$	12	2	13	0	**414.7**	34.8	6.8	3.1	-	41.4	7.9	2.8	-
4	**FeBPY$_3$**	$Fe(C_{10}H_8N_2)_3Cl_3 \cdot 7H_2O$[a]	30	6	31	0	**720.8**	50.0	11.7	5.3	-	50.9	11.6	4.7	-
5	**FeBPY$_1$**	$FeCl_3(C_{10}H_9N_2)H_2O$	10	2	13	0	**390.7**	30.7	7.2	3.3	-	36.8	8.4	2.7	-
6	**FeIM**	$FeCl_2(C_3N_2H_4)_4Cl \cdot H_2O$[a]	12	8	17	0	**452.2**	31.9	24.8	4.0	-	31.9	24.1	3.7	-
7	**FeTPMA**	$Fe_2C_{18}H_{18}N_4Cl_6$	18	4	18	0	**614.4**	35.2	9.1	2.9	-	35.7	9.0	2.9	-
8	**FeBPMA**	$FeC_{12}H_{13}N_3Cl_3$	12	3	13	0	**361.2**	39.9	11.6	3.6	-	39.9	11.2	3.7	-
9	**FePHTA**	$FeC_{32}H_{16}ClN_8$	32	8	16	0	**603.8**	63.6	18.5	2.6	-	-	-	-	-

[a]The H_2O of hydration in some complexes was added according to literature [46]

Table 10.8. Onset potential, half-wave potential, kinetic current and hydrogen peroxide production for the Fe-N-C catalyst prepared with $FePHEN_3$ complex and with or without Vulcan XC72

	precursors	$E_{j=0.1}$ V vs. RHE	$E_{1/2}$ V vs. RHE	j_K A g^{-1}	$H_2O_2^{0V}$ %
FPHEN$_3$py	**FePHEN$_3$**	0.668	0.257	0.04	0.3
FPHEN$_3$	**FPHEN$_3$ + Vulcan XC72**	0.871	0.748	1.84	0.6

Table 10.9. chemical composition and Electrochemical data for catalysts made with iron complexes coordinating non-aromatic ligands

	Elemental analysis					E_{onset}	j_L		n	% H_2O_2	
	C	H	N	S	Fe[a]		-0.2 V[b]	0.0 V[b]	0.2 V[b]	0.2 V[b]	0.7 V[b]
FPEHA	95.81	0.08	0	0	0	0.676	-	-3.60	3.81	9.0	13.9
FEDTA	97.65	0.01	0	0	0	0.159	-2.46	-	3.39	30.4	-
FCYCLAM	96.78	0	0	0-	0.08	0.584	-4.16	-3.47	3.45	27.3	-

[a] determined by XPS analysis, [b] all potentials are vs RHE

Table 10.10. Electrochemical data for different loading of $FPHEN_3$ on GC

loading mg cm^{-2}	$j_{0.8\,V}$ mA cm^{-2}	j_L mA cm^{-2}	j_K A g^{-1}	$E_{1/2}$ V vs. RHE
0.2	0.37	2.8	2.2	0.72
0.4	0.59	3.7	1.8	0.73
0.6	0.88	4.3	1.8	0.75
0.8	0.98	4.6	1.6	0.75

Table 10.11. Electrochemical data for Fe-N-C catalysts in O_2 saturated 0.1 M KOH electrolyte

		$E_{j=0.1}$ V vs. RHE	$E_{1/2}$ V vs. RHE	$j_{L,0V}$ mA cm^{-2}	$j_{0.8\,V}$ mA cm^{-2}	$j_{K,\,0.8V}$ A g^{-1}	n_{0V} -	$\%H_2O_2^{\,0.7V}$ -
1	**FPHEN$_3$**	0.937	0.80 ± 0.01	4.39	2.37	8.7 ± 2.1	3.53	1.0
2	**FPHEN$_2$**	0.928	0.81 ± 0.04	5.92	3.39	8.5 ± 5.5	3.54	1.9
3	**FPHEN$_1$**	0.938	0.825 ± 0.007	4.87	3.07	13.9 ± 2.1	3.40	4.2
4	**FBPY$_3$**	0.905	0.754 ± 0.002	4.55	1.46	3.6 ± 0.1	3.21	7.1
5	**FBPY$_1$**	0.909	0.779 ± 0.006	5.03	3.11	13.7 ± 1.9	3.29	1.5
6	**FIM**	0.893	0.775 ± 0.001	4.49	1.61	4.2 ± 0.2	3.27	9.3
7	**FTPMA**	0.912	0.809 ± 0.007	4.71	2.65	10.2 ± 1.9	3.40	3.4
8	**FBPMA**	0.923	0.828 ± 0.004	4.89	3.36	17.9 ± 2.7	3.45	2.4
9	**FPHTA**	0.897	0.775 ± 0.005	4.04	1.46	3.8 ± 0.4	3.41	10.9

Table 10.12. ORR and Stripping data for the samples at different initial Fe amount

	$E_{j=0.1}$ V	$E_{1/2}$ V	$j_{L,0V}$ mA cm^{-2}	$j_{0.8V}$ mA cm^{-2}	j_K A g^{-1}	n -	H_2O_2 %	SD 10^{18} sites g^{-1}	TOF s^{-1}	Δj_K A g^{-1}
C	0.380	0.170	1.81	-	-	3.48	26.0	0	0	0
Fe$_1$CB	0.743	0.471	3.09	0.03	0.04	3.70	14.9	1.11	0.24	0.04
Fe$_1$CB*	0.812	0.640	4.13	0.15	0.26	3.95	2.7	2.23	1.83	0.65
Fe$_2$CB	0.822	0.669	4.63	0.23	0.41	3.95	2.7	2.38	3.90	1.49
Fe$_4$CB	0.842	0.666	4.28	0.37	0.68	3.92	4.2	2.27	2.21	0.80

10.4. Appendix chapter 6

10.4.1. Supporting Text

10.4.1.1. Synthesis of $Fe(phen)_3Cl_2$ (Fe-phen) complex

Anhydrous $Fe^{II}Cl_2$ and 1,10-phenantroline were dissolved in a small volume of EtOH (to facilitate the further precipitation we use the lowest necessary amount to completely dissolve the precursor) with a 1:3.1 molar ratio. The mixture was kept under stirring for 1 h and then the complex was precipitated using diethyl ether and finally washed with diethyl ether to give a yield of about 70% [34] (Elemental analysis: C_{calc} 54.5%, N_{calc} 10.6%, H_{calc} 4.8%; C_{found} 53.9%, N_{found} 10.3%, H_{found} 4.2%). The structure is shown in Figure 10.19

10.4.1.2. Synthesis of $Sn(phen)Cl_2$ (Sn-phen) complex

A proper synthesis procedure was not available in literature using 1,10-phenathroline, so, it was adopted a similar procedure as for $Fe(phen)_3Cl_2$. The starting Sn compound was $Sn^{II}Cl_2 \cdot 2H_2O$, so the oxidation state of Sn in the complexes is +2 as compared to iron-phenanthroline synthesis. Therefore, $SnCl_2 \cdot 2H_2O$ and 1,10-phenantroline (1:2 molar ratio in EtOH solution) were mixed. A yellow precipitate was immediately formed, the solution was filtered within 5-10 min to avoid decomposition product to form as observed for N oxide-phenanthroline by Owens [35]. The product was finally washed with ice-cold ethanol and the dried overnight at 40 °C. In alternative the same synthesis works also in isopropanol. The yield was 92% and the product was characterized by elemental analysis assuming the final formula of the compound is $Sn(phen)Cl_2$ as reported by Owens et al.[35]. The found percentage seemed to confirm that assumption (C_{calc} 38.96%, N_{calc} 7.58%, H_{calc} 2.16%; C_{found} 36.83%, N_{found} 6.82%, H_{found} 2.09%). The suggested structure is shown in Figure 10.19**.** We emphasize that for the use of the complex, namely a precursor to pyrolyze, was not of primary importance the understanding of complex structure, the main objective is to have both the metal centre and a nitrogen source within the same compound, even knowing that it could influence the fixation efficiency [17].

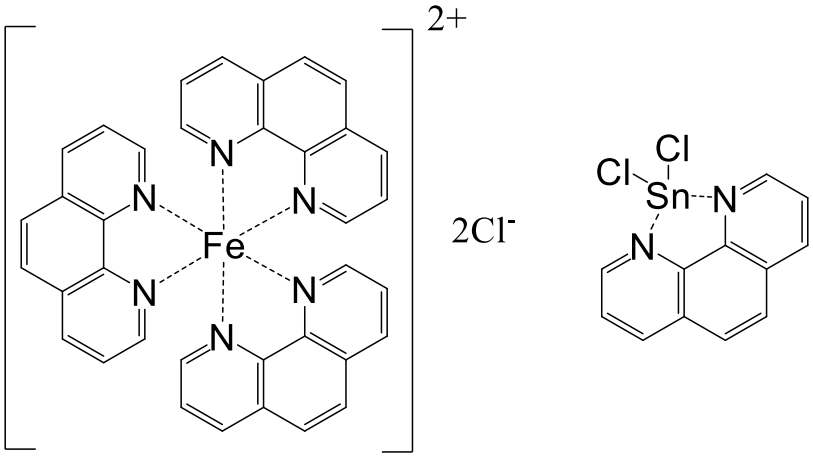

Figure 10.19. Fe-phen and Sn-phen complexes structures.

10.4.1.3. Effect of different acid leaching condition

The presence of Sn NP in Sn_4XC72 suggested that the acid leaching (see experimental section) is not able to dissolve Sn or to convert it in a soluble salt (which remain after vacuum filtration)

preventing the effectiveness of this treatment. In order to remove the NP, we try several conditions also looking at literature work where Sn was used [3]:

- HCl 4M for 6h in Ar-saturated solution at 90°C
- HNO_3 2M for 6h in Ar-saturated solution at 90°C
- H_2SO_4 2M for 6h in Ar-saturated solution at 90°C

For each sample after washing a fraction was set aside and the rest was submitted to the second heat treatment. The sample was labelled: Sn_4X (where *X* = acid used) after acid leaching and Sn_4W2T (where *W* = S for H_2SO_4, N for HNO_3 and C for HCl).
In Table 10.15 we report the elemental analysis for each step and in Figure 10.21 and Figure 10.22 respectively the SEM-EDX analysis and the electrochemical performances.
Sn_4C2T has a higher percentage of carbon which might suggest that higher Sn has been leached out but looking at SEM-EDX analysis appear that the sample with the highest leaching, namely with the lower evidence of NPs (Figure 10.22), is the sample treated in 2 M sulphuric acid (Sn_4S2T), while nitric acid is the less effective. In any case the prolonged acid treatment (6 h vs. 3 h) and the higher concentration of the acid allow for all 3 considered leaching bath formulation a better leaching compare with the Sn_4XC72.
Compared to the original Sn_4XC72 the sample leached with HNO_3 shows better performance, while Sn_4C2T and Sn_4S2T shows very similar activity with the latter that perform very similar to the other sample leached in H_2SO_4. The same is not true in alkaline electrolyte where Sn_4XC72 outperformed the other sample and also shows a different LSV profile where a clear double sigmoidal shape is present, in correspondence of the second step the amount of peroxide produced decrease where for the other sample remain almost constant (the same is also true for Sn_2XC72, see main text)

10.4.1.4. *Electrochemical test*

Cyclic voltammetry (CV) and linear sweep voltammetry (LSV) were carried out on a rotating ring-disc electrode (RRDE, Metrohm: ∅ = 5 mm GC disk and a Pt ring for acid measurements and RRDE, Pine Instrument: ∅ = 5.61 mm GC disk and a Pt ring for alkaline measurements), in both Ar-purged and O_2-saturated 0.5 M H_2SO_4 and 0.1 M KOH solution. All the measurements were done in a three-electrode cell thermostated at 25 °C. The RRDE tip was used as working electrode, a graphite rod was used as counter-electrode and, for acidic electrolyte, a homemade RHE as reference electrode prepared before each experiment according to literature procedure [36].
For the measurements in KOH, a Hg/HgO (AMEL instruments for Electrochemistry) reference electrode (E_{RHE} = 0.098V + 0.059pH + $E^0_{Hg/HgO}$) was adopted. The calibration of Hg/HgO reference electrode was described in previous chapter. A gas diffusion electrode cell design by Arenz et al. [19] was used to evaluate the activity in a more realistic condition since in this apparatus the catalysts is casted on a carbon paper and covered with a Nafion membrane. The electrolyte serves as a source of proton and is not in direct contact with the catalyst layer, while the oxygen gas comes from under the layer mimicking the fuel cell cathode. The electrolyte container was filled with a 0.5 M H_2SO_4 as for the RRDE measurements, graphite serves as counter electrode and RHE as reference; the working electrode is the catalysts loaded carbon paper supported by the steel body of the cell. The scheme of GDE cell is reported in Figure 10.20. To evaluate the catalysts site density, nitrite (NO_2^-) poisoning and electrochemical stripping were performed following the procedure described by Malko et al. [22,37,38]. Stability tests were performed using an extensive

cycling between 0.55 and 1.05 V as reported in literature [39], which is a variation on the procedure reported by Ohma et al. [40] for the start and stop stress test for Pt/C fuel cells catalysts and extended also to M-N-C [3].

10.4.1.5. XRD analysis

XRD analysis was performed on Sn_4XC72 in order to understand the nature of Sn NP, Figure 10.23 does not show any peak related to SnO_2 while almost all sharp peaks are associable with metallic Sn, 3 additional peaks were not related with tin species but assigned to Si, probably gives by the substrate. This means that if tin oxide is present in the outer layer of nanoparticles isn't in a crystalline form. Lastly two very broad peak at around 25 and 45° (very broad and almost superimposable with the background) are associated to the crystalline part of carbon support, as typical for M-N-C materials. Materials with Fe and Sn/Fe does not show peaks associated with inorganic crystalline phases due to confirming the effectiveness of acid leaching, remembering that, as said, in presence of iron no NPs were observed.

10.4.1.6. EXAFS data analysis

The EXAFS data analysis was performed with the GNXAS code, which is based on the decomposition of the EXAFS χ(k) signal into a summation over n-body distribution functions γ(n) calculated by means of the multiple-scattering (MS) theory. Details of the theoretical framework of the GNXAS approach are described in refs [41,42]. The Fe coordination shells have been modelled with Γ-like distribution functions which depend on four parameters, namely, the coordination number N, the average distance R, the mean-square variation σ^2, and the skewness β. Note that β is related to the third cumulant C_3 through the relation $C_3=\sigma^3\beta$.

10.4.1.7. Additional investigation

The sample Sn_2XC72 and a metal free prepared with only phenanthroline [17] in the mixture were used to show that Sn_2XC72 shows a non-negligible stripping charge from NO_2 stripping analysis (Figure 10.25), which means that something in the sample gives a response to NO_2. We think that is unlikely that this is due to NP since the amount is very high, so we cannot exclude that some SnN_x are present in the sample.

To verify that also an effect of the sole additional phenanthroline is present a sample with $1\%_{mol}$ of initial amount of Fe was prepared and another one with an additional amount of phenanthroline to reach the same quantity added for the 2% (marked as 1*); for more detail see reference [17].

Fe_1 as expected is worse than the sample with the 2, but the sample prepared with 1% of Fe and additional phenanthroline well perform, suggesting that also a simple effect of Sn-phen complex as phenanthroline source could be present, indeed the activity of Sn_1Fe_1 was only slightly better. This at the end means that the amount of Fe in the precursor is sufficient at 1%, but additional N-source is necessary to fix more sites to reach better acidity and selectivity (comparing 1 and 1* in Figure 10.30)

10.4.2. Supporting Table

Table 10.13. N_2 Physisorption result for the four supports under analysis

	S_{tot} [a] $m^2\ g^{-1}$	$S_{0.5\text{-}40nm}$ [b] $m^2\ g^{-1}$	S_{μ} [b] $m^2\ g^{-1}$	S_{meso} [b] $m^2\ g^{-1}$	V_{μ} [b] $cm^3\ g^{-1}$	V_{meso} [b] $cm^3\ g^{-1}$	V_{tot} [c] $cm^3\ g^{-1}$
$CBCO_2$-5	199	197	129	68	0.055	0.457	0.791
MC	207	186	7	179	0.002	0.427	0.444
XC72	233	234	179	55	0.075	0.231	0.380
EC300J	806	779	423	356	0.172	0.671	1.494

[a]BET Model, [b]QSDFT Model, [c]Gurvich rule at 0.98

Table 10.14. Electrochemical result for the 4 sample prepared for choosing the best support

	$E_{j=0.1}$ V vs. RHE	$E_{1/2}$ V vs. RHE	E_p V vs. RHE	$j_k^{0.8V}$ A g^{-1}	n_{0V} -	$\%H_2O_2^{0.7V}$ -
$Sn_1Fe_1CBCO_2$-5	0.839	0.683	0.755	0.59	3.98	1.1
Sn_1Fe_1MC	0.850	0.692	0.756	0.87	3.97	2.3
Sn_1Fe_1XC72	0.857	0.719	0.771	1.16	3.98	2.2
Sn_1Fe_1EC300J	0.856	0.722	0.769	1.08	3.98	2.3

Table 10.15. Elemental analysis and Sn content (EDX) for the 3 sample washed in different acidic solution, the elemental analysis is reported for each step while the EDX only on the final catalyst

	C_{EA} wt.%	N_{EA} wt.%	H_{EA} wt.%	Sn_{EDX} wt.%
$Sn(phen)Cl_2$ + XC72	63.93	3.86	1.37	-
After 1° thermal tret.	80.72	1.64	0.21	-
Sn_4HCl	78.97	1.40	0.38	-
Sn_4HNO_3	84.19	1.74	0.56	-
$Sn_4H_2SO_4$	86.11	1.69	0.34	-
Sn_4C2T	91.68	1.17	0.21	1.17
Sn_4N2T	83.27	0.96	0.22	4.89
Sn_4S2T	86.14	1.31	0.25	0.90

Table 10.16. Electrochemical result for the 4 sample prepared from the 3 acid leaching in 0.5 M H_2SO_4

	$E_{j=0.1}$ V vs. RHE	$E_{1/2}$ V vs. RHE	$j_{L,0V}$ mA cm^{-2}	$j_{0.8\ V}$ mA cm^{-2}	$j_k^{0.8V}$ A g^{-1}	n_{0V} -
Sn_4XC72	0.803	0.548	3.72	0.11	0.19	3.97
Sn_4C2T	0.774	0.498	3.72	0.06	0.11	3.97
Sn_4N2T	0.831	0.624	4.84	0.25	0.44	3.98
Sn_4S2T	0.815	0.592	3.86	0.14	0.25	3.97

Table 10.17. Electrochemical result for the 4 sample prepared from the 3 acid leaching in 0.1 M KOH

	$E_{j=0.1}$ V vs. RHE	$E_{1/2}$ V vs. RHE	$j_{L,0V}$ mA cm^{-2}	$j_{0.8\ V}$ mA cm^{-2}	$j_k^{0.8V}$ A g^{-1}	n_{0V} -
Sn_4XC72	0.933	0.790	3.78	1.75	5.44	3.65
Sn_4C2T	0.912	0.762	4.18	1.46	3.75	3.11
Sn_4N2T	0.909	0.779	3.77	1.52	4.25	3.32
Sn_4S2T	0.916	0.766	4.16	1.58	4.26	3.10

Table 10.18. Best-fit parameters obtained from the EXAFS analysis of Fe_2XC72, Sn_1Fe_2XC72, and Sn_2Fe_2XC72. R (Å) is the interatomic distance, σ^2 (10^{-3} Å^2) is the Debye-Waller factor and N is the coordination number. Errors are given in parentheses, *e.g.*, 2.04(2) means 2.02-2.06

	R_{Fe-N} (Å)	σ^2 (10^{-3} Å^2)	N_{Fe-N}	R_{Fe-O} (Å)	σ^2 (10^{-3} Å^2)	N_{Fe-O}
Fe_2XC72	2.04(2)	8.2(4)	3.7(4)	1.89(2)	10(2)	2.0(2)
Sn_1Fe_2XC72	2.04(2)	12(1)	3.8(3)	1.90(2)	10(2)	2.0(3)
Sn_2Fe_2XC72	2.03(2)	7.0(3)	4.0(4)	1.86(2)	9.3(5)	2.0(2)

Table 10.19. Stripping data for the analysed samples

	Q_{STRIP} C g^{-1}	Δj_k A g^{-1}	*SD* sites g^{-1}	*MSD* mol sites g^{-1}	*TOF (0.8V)* s^{-1}
Sn_1Fe_1XC72	2.92	4.11	3.64E+18	6.04E-06	7.04
Sn_2Fe_2XC72	6.40	2.11	7.99E+18	1.33E-05	1.81
Sn_2Fe_1XC72	3.35	4.81	4.18E+18	6.94E-06	7.06
Sn_3Fe_1XC72	3.86	0.57	4.82E+18	8.01E-06	0.75
Sn_1Fe_2XC72	3.70	4.08	4.62E+18	7.67E-06	6.20
Sn_4XC72	1.44	0.66	1.80E+18	2.98E-06	2.31
Sn_2XC72	1.37	0.34	1.71E+18	2.84E-06	1.23
Fe_2XC72	3.39	4.52	4.24E+18	7.03E-06	6.66
NC	0.16	0.00	1.95E+17	3.23E-07	0.00

Table 10.20. Electrochemical result for the all catalysts in GDE cell

	$E_{j=2}$ V vs. RHE	j_{0V} mA cm^{-2}	$j_{0.7\,V}$ mA cm^{-2}
Sn_1Fe_1XC72	0.767	180.00	7.79
Sn_2Fe_2XC72	0.752	170.00	6.03
Sn_2Fe_1XC72	0.760	303.00	7.06
Sn_3Fe_1XC72	0.776	175.00	9.09
Sn_1Fe_2XC72	0.789	245.00	11.00
Sn_4XC72	0.721	103.00	2.76
Sn_2XC72	0.519	25.54	0.07
Fe_2XC72	0.748	279.00	5.42

10.4.3. Supporting Figure

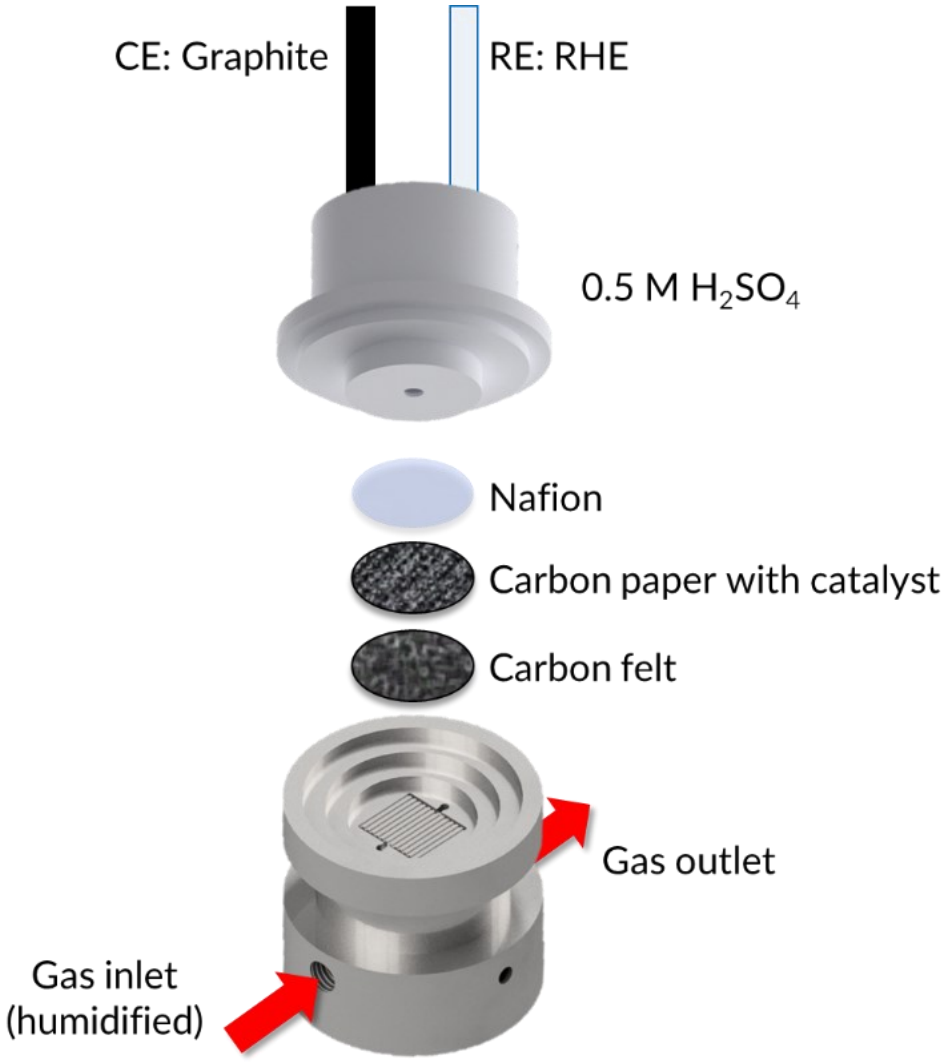

Figure 10.20. GDE cell set-up of our cell based on the scheme proposed by the inventor and seller [43,44]

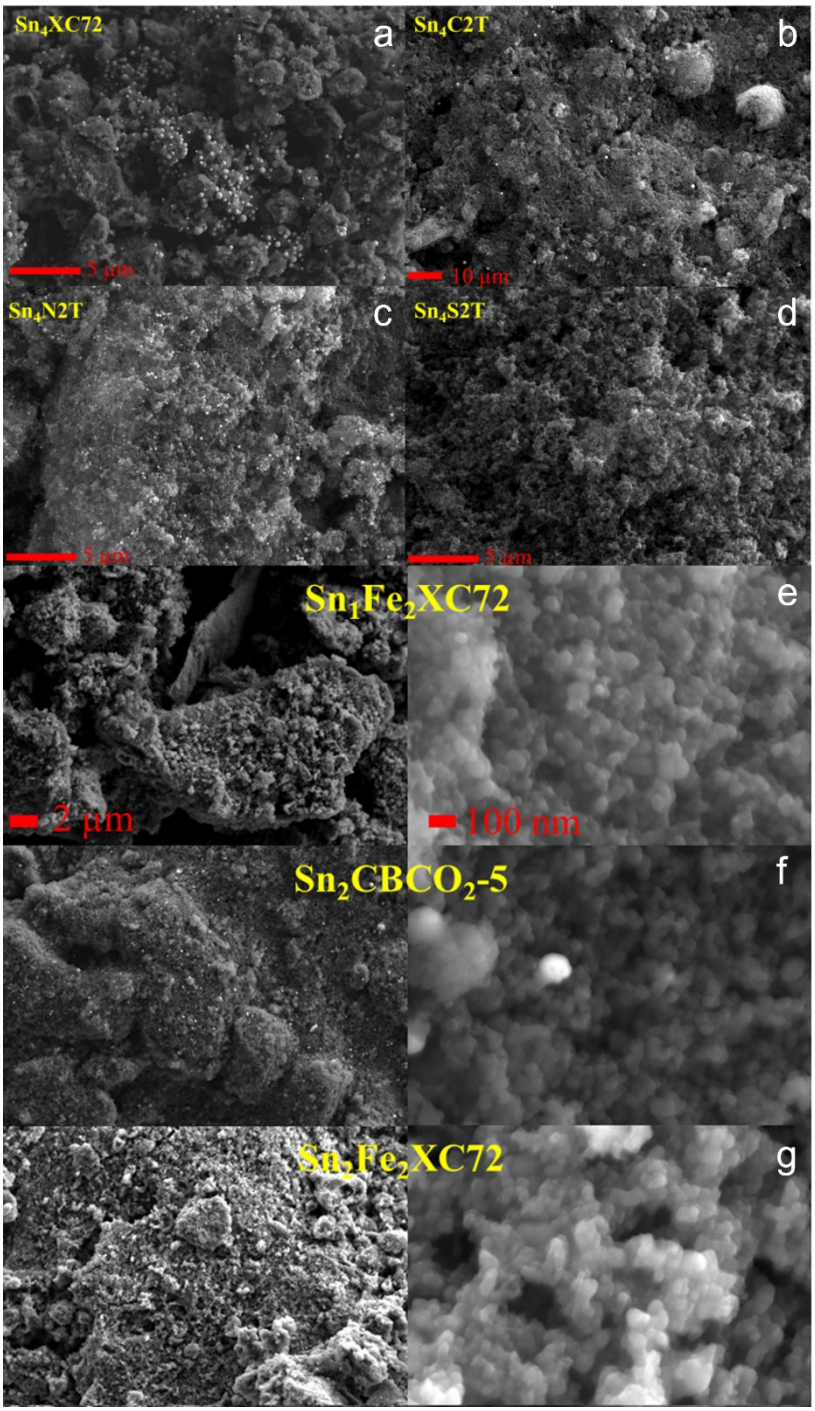

Figure 10.21. SEM image of a) Sn_4XC72, b) Sn_4C2T, c) Sn_4SNT, d) Sn_4S2T, e) Sn_1Fe_2XC72, f) Sn_2CBCO_2-5 and g) Sn_2Fe_2XC72

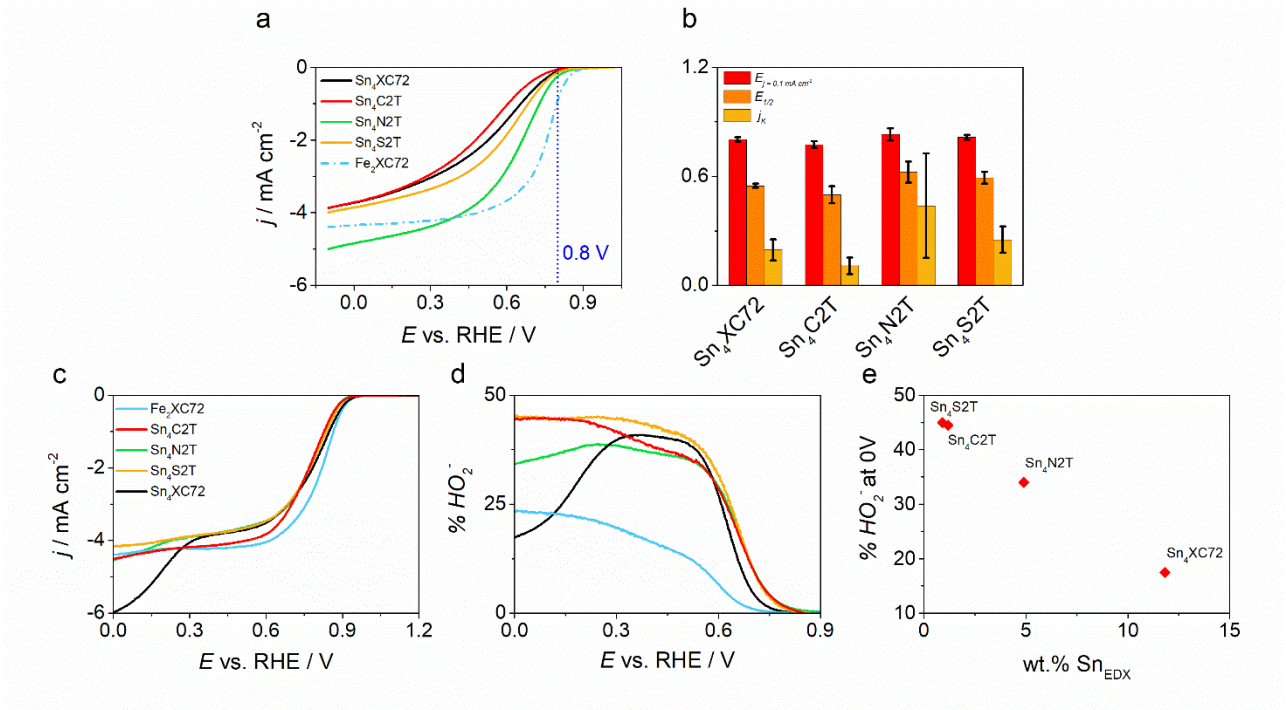

Figure 10.22. a, b) LSV and activity summary for measurement in acid electrolyte for Sn_4XC72, Sn_4C2T, Sn_4SNT and Sn_4S2T. For the same sample c) LSV, d) peroxide production in alkaline electrolyte and e) variation of peroxide yield as a function of Sn content. Fe_2XC72 was left only as comparison.

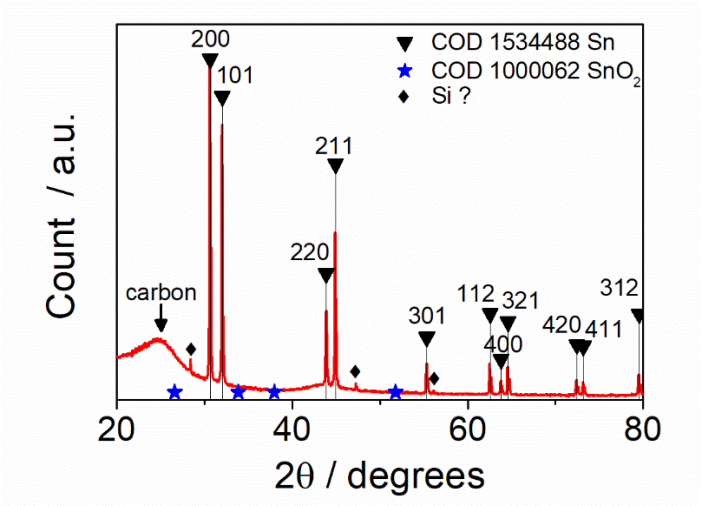

Figure 10.23. XRD response for Sn_4XC72, diamond shaped labelled peak could be due to the silicon sample holder.

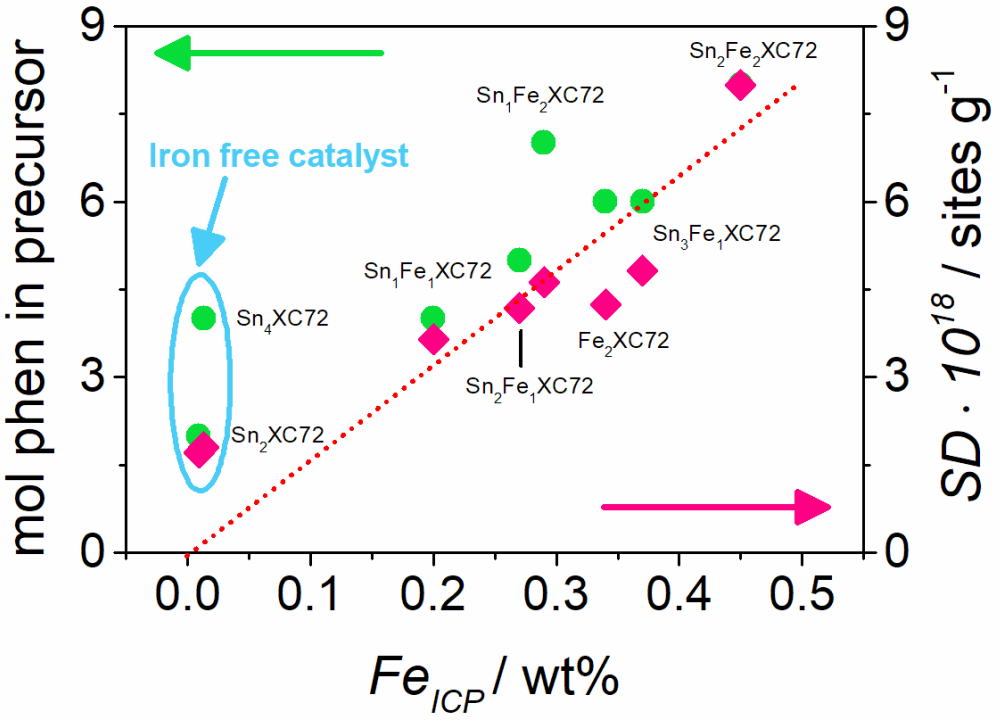

Figure 10.24. Correlation between phenanthroline in the precursor mixture and SD vs. the amount of iron detected by ICP-MS.

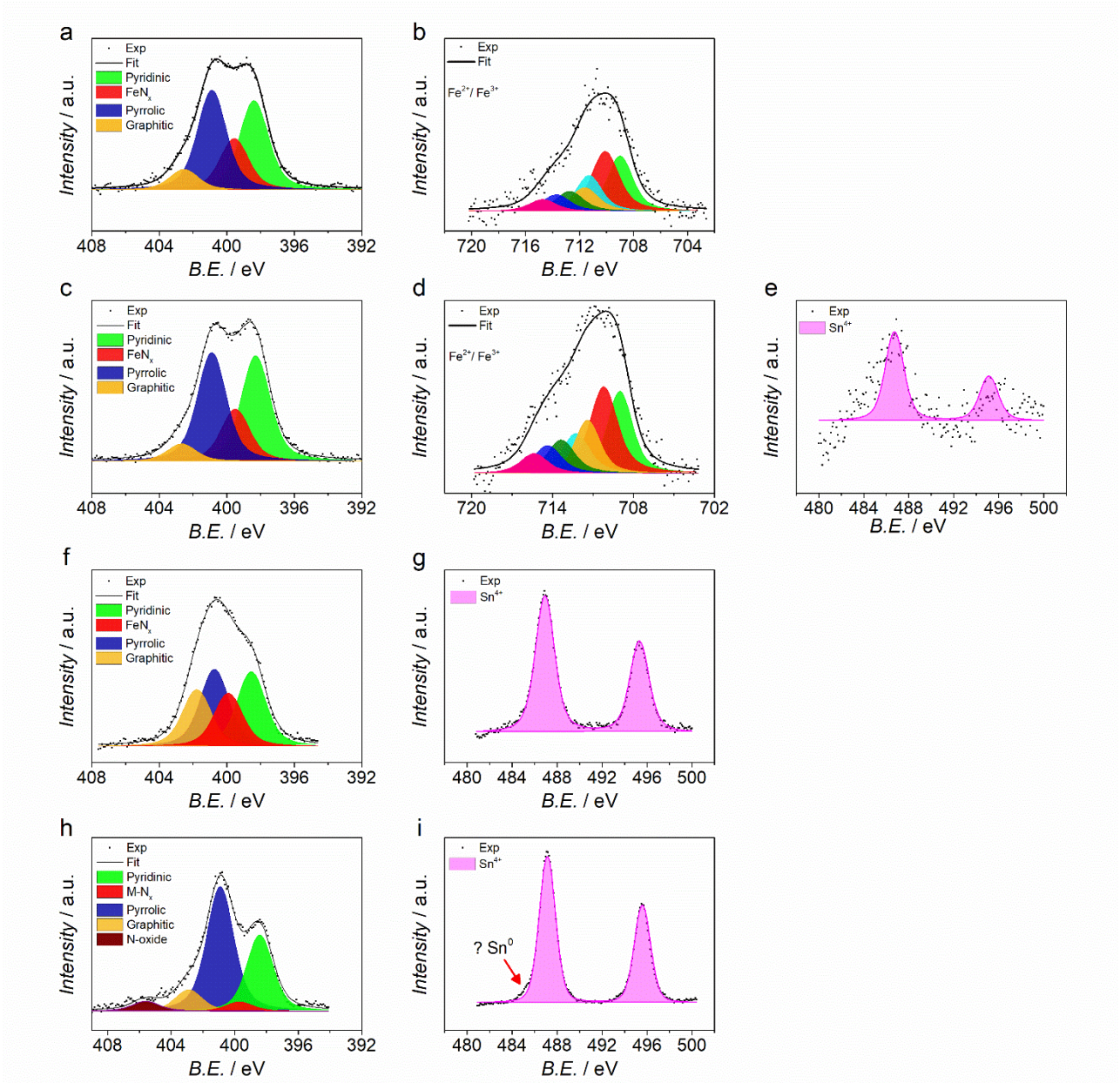

Figure 10.25. High resolution XPS peaks and deconvolution for (a,b) Fe_2XC72, (c,d,e) Sn_1Fe_2XC72, (f,g) Sn_2Fe_2XC72 and (h,i) Sn_4XC72. a, c, f, h) N 1s, b, d) Fe 2p e, g, i) Sn 3d.

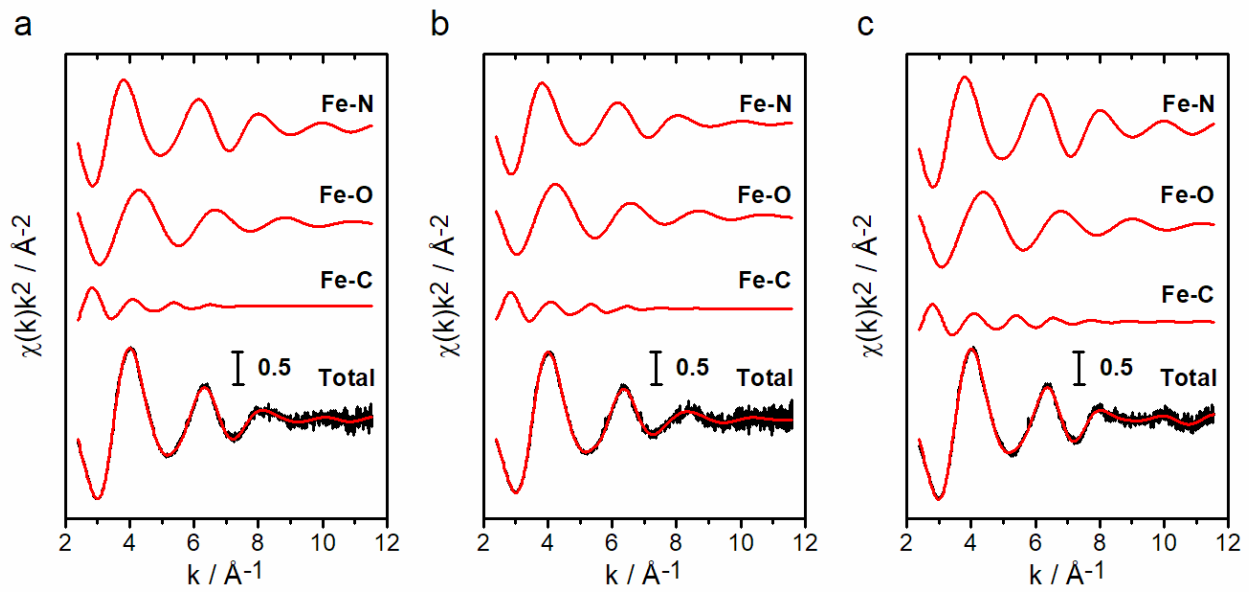

Figure 10.26. Fe K-edge EXAFS analysis of a) Fe_2XC72, b) Sn_1Fe_2XC72 and c) Sn_2Fe_2XC72 via the GNXAS program. From top to bottom: Fe-N, Fe-O, and Fe-C contributions included in the fit, and the total theoretical signal (red line) superimposed to the experimental one (black line).

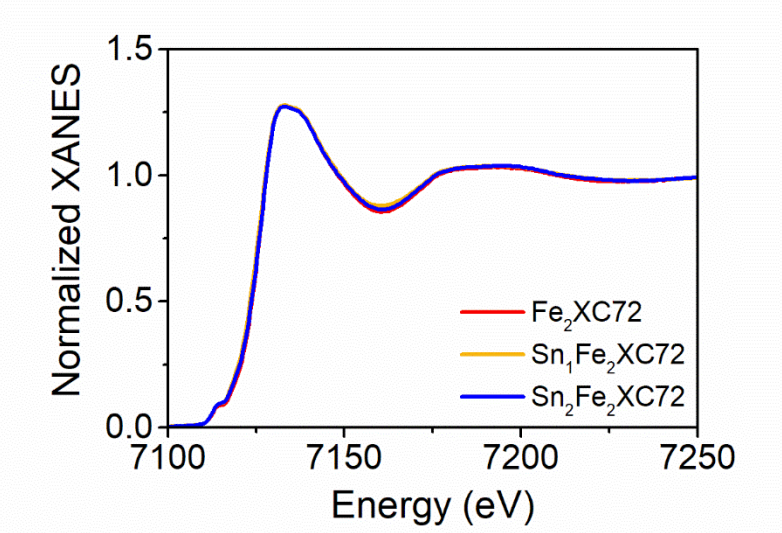

Figure 10.27. Fe K-edge XANES spectra of Fe_2XC72 (red line), Sn_1Fe_2XC72 (orange line) and Sn_2Fe_2XC72 (blue line).

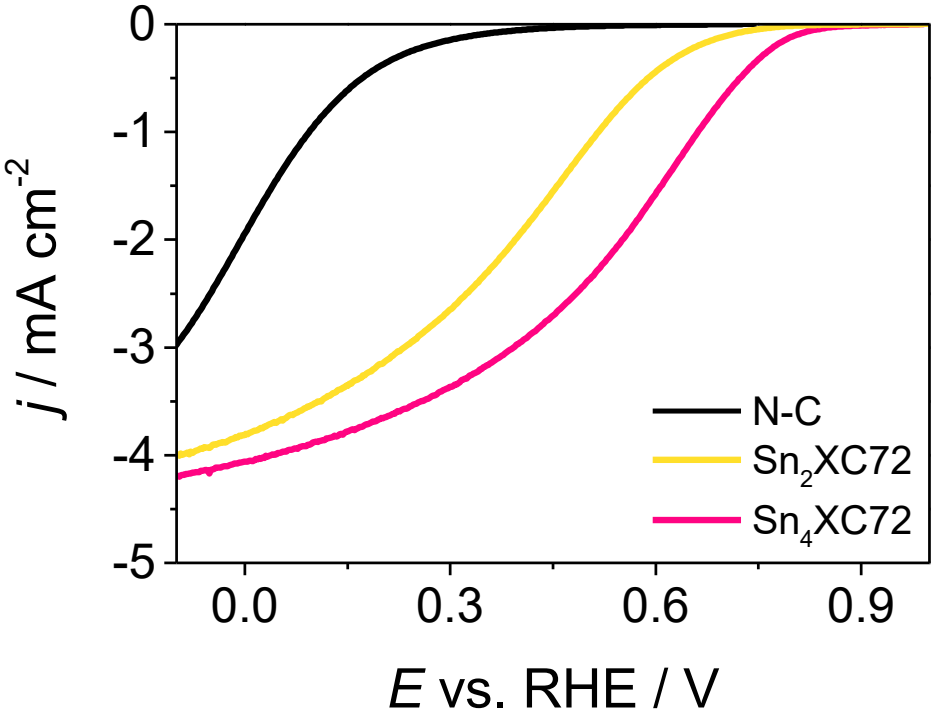

Figure 10.28. Comparison between Sn_x samples and a metal-free-N-doped carbon in 0.5 M H_2SO_4

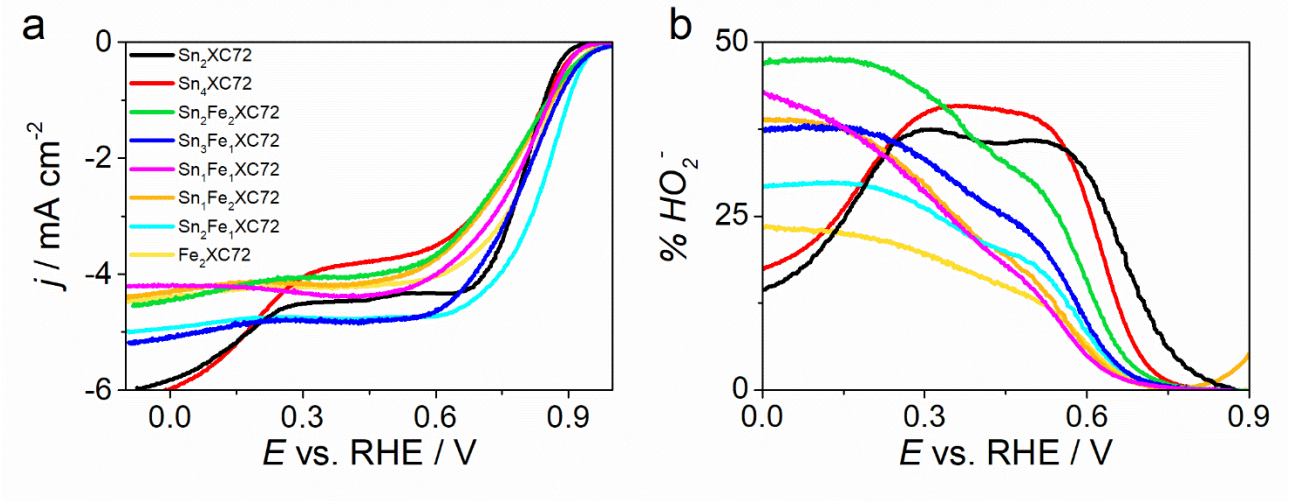

Figure 10.29. a) LSVs and b) Peroxide yield in 0.1 M KOH

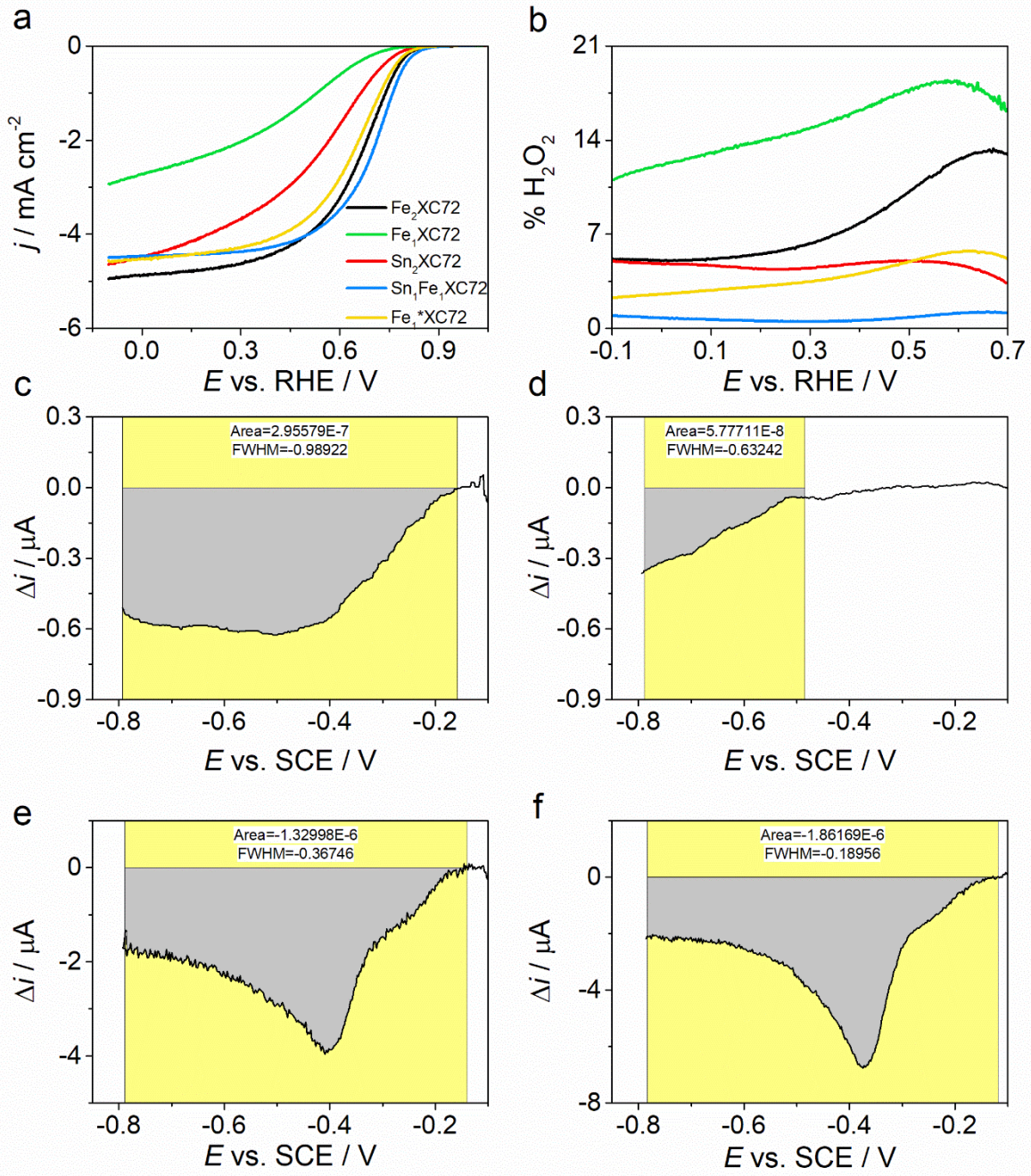

Figure 10.30. a) Effect of Sn and phenanthroline on activity and b) hydrogen peroxide production for Fe_xXC72; c-f) Stripping for Sn_2XC72, metal-free catalyst (N-C), Fe_2XC72 and Sn_2Fe_1XC72.

10.5. Appendix chapter 7

10.5.1. Raman deconvolution

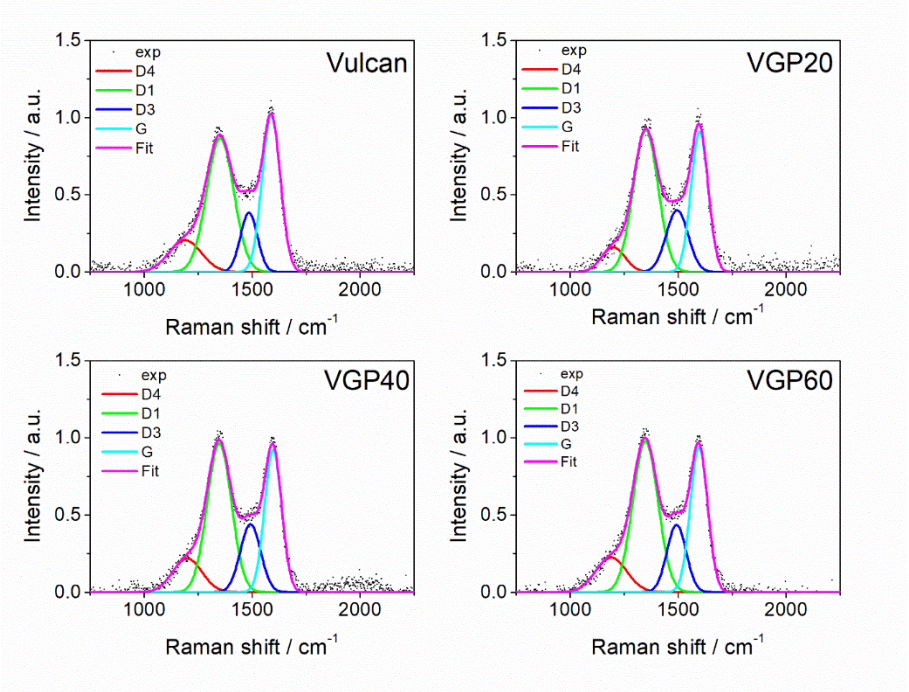

Figure 10.31. Raman deconvolution of pyridine functionalized Vulcan

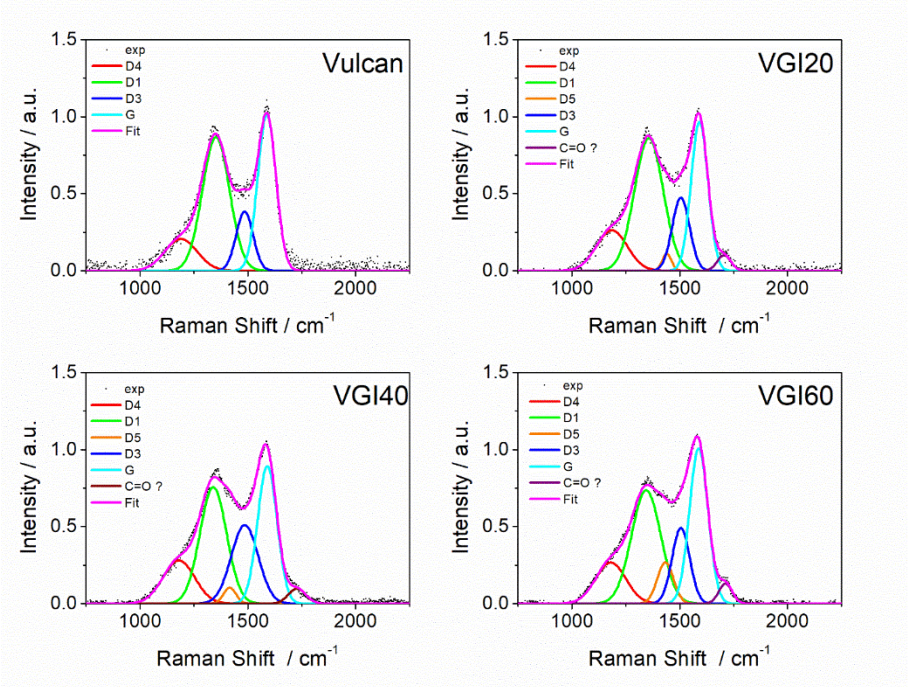

Figure 10.32. Raman deconvolution of indole functionalized Vulcan

10.6. Appendix chapter 8

10.6.1. UV-Vis determination of Hydrogen peroxide using $Ti^{IV}OSO_4$

The amount of produced H_2O_2 was evaluated by a spectrophotometric method involving the complexation of the peroxide with potassium titanium oxide sulphate ($TiOSO_4$ xH_2O) and its detection at 410 nm. A 0.02 M Ti(IV) standard solution was prepared in a 100 mL round bottom flask through dissolution of the proper amount of the salt in 30 mL of MilliQ H2O and 27.2 mL of H_2SO_4 and further addition of MilliQ H_2O to a final volume of 100 mL. The calibration solutions were prepared in 2 mL graduated flasks containing Ti(IV) reagent (0.02 M) and a proper amount of H_2O_2 added as pure reagent or diluted solution. In Figure 10.33 the spectra and calibration curve are reported. The obtained equation was A = 0.81381 [H_2O_2 / mM] + 0.00601

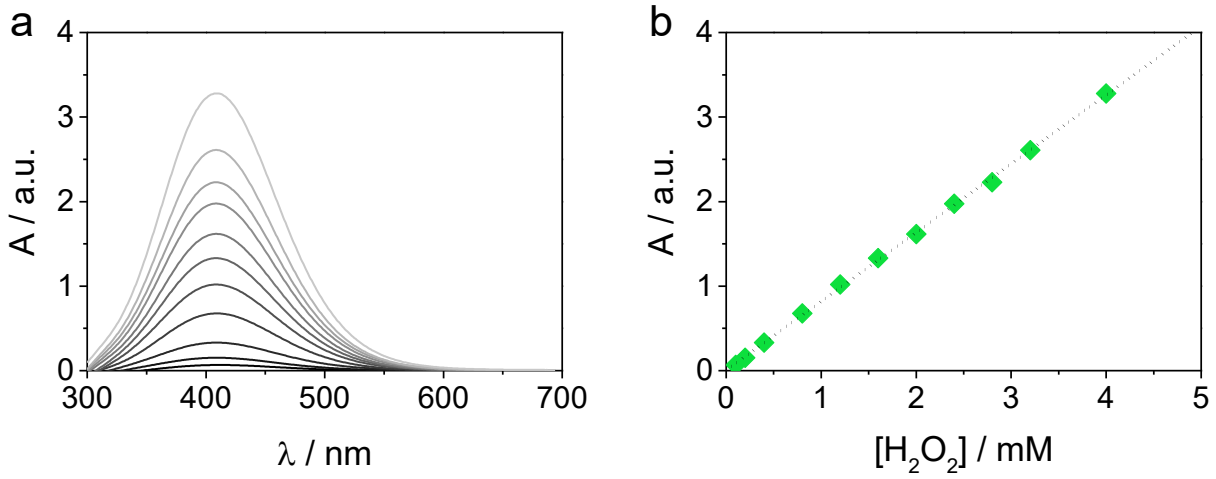

Figure 10.33. a) Uv-Vis spectra at different concentration of hydrogen peroxide and b) calibration curve

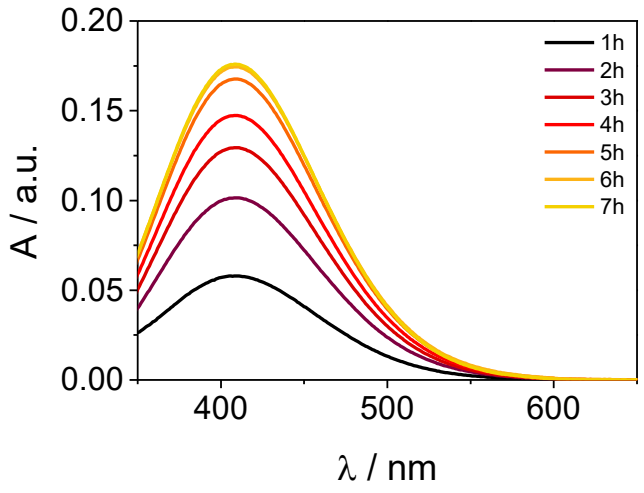

Figure 10.34. Experimental UV-Vis spectra for each sampling

10.6.2. XAS Analysis

Fe K-edge X-ray absorption spectroscopy (XAS) spectra were measured at the SAMBA beamline (Synchrotron SOLEIL), at room temperature in fluorescence mode, using a Ge 33-pixel detector. The beamline is equipped with a sagittally focusing Si 220 monochromator and two Pd-coated mirrors that were used to remove X-rays harmonics. The catalysts were pelletized as disks of 10 mm diameter using boron nitride as a binder.

XAS measurements were performed at the Fe K-edge. A detailed extended X-rays absorption fine structure (EXAFS) analysis show that the Fe atoms are atomically dispersed on the carbon matrix in all the samples (Figure 10.35), with the Fourier transform (FT) of the EXAFS signal characterized by a first peak at ca 1.5 Å assigned to the Fe-N first coordination shell, and a minor peak at 2.6 Å assigned to Fe-C backscattering from the second coordination shell. The EXAFS spectra were fitted assuming the presence of in-plane nitrogen atoms, and also oxygen atoms as axial ligands. The structural parameters obtained from the analysis are summarized in Table 10.21, and they show a Fe-N coordination number around 4 for all the catalysts, demonstrating that iron forms Fe-N_4 moieties. Moreover, an axial signal between Fe and a light atom can be probed, suggesting that two O atoms are adsorbed on top of the Fe-N_4 moieties, as previously found in other Fe-N-C catalysts.[24,25] No Fe-Fe backscattering is detectable in all the EXAFS spectra, thus confirming the absence of metal NPs. As far as the X-ray absorption near edge structure (XANES) region of the spectrum is concerned.

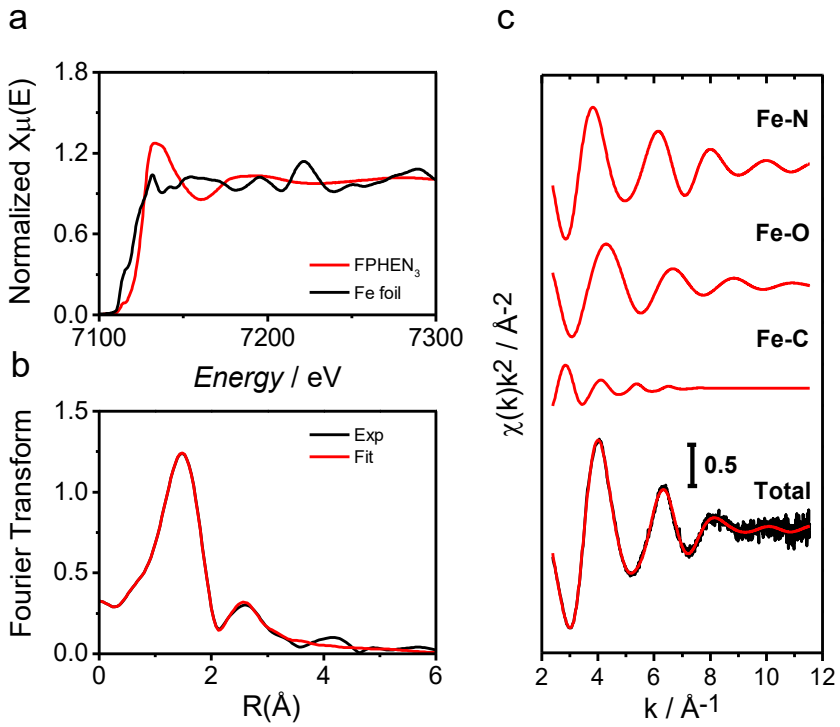

Figure 10.35. a) Fe K-edge XANES spectra of Fe_2XC72, b) Fe K-edge EXAFS analysis in the Fourier transformed space, c) Fe K-edge EXAFS analysis. From top to bottom: Fe-N, Fe-O, and Fe-C contributions included in the fit, and the total theoretical signal (red line) superimposed to the experimental one (black line).

Table 10.21. Best-fit parameters obtained from the EXAFS analysis . R (Å) is the interatomic distance, σ^2 (10^{-3} Å^2) is the Debye-Waller factor and N is the coordination number. Errors are given in parentheses, *e.g.*, 2.04(2) means 2.02-2.06

	R_{Fe-N} (Å)	σ^2 (10^{-3} Å^2)	N_{Fe-N}	R_{Fe-O} (Å)	σ^2 (10^{-3} Å^2)	N_{Fe-O}
Fe_2XC72	2.04(2)	8.2(4)	3.7(4)	1.89(2)	10(2)	2.0(2)